Doctoral Thesis

Sabril Haris

ISBN 978-82-471-4531-9
ISBN 978-82-471-4532-6
ISSN 1503-8181

Doctoral theses at NTNU, 2013:208

Sabril Haris

Damage interaction analysis of ship collisions

NTNU
Norwegian University of Science and Technology
Thesis for the degree of Philosophiae Doctor
Faculty of Engineering Science and Technology
Department of Marine Technology

NTNU – Trondheim
Norwegian University of
Science and Technology

Doctoral theses at NTNU, 2013:208

NTNU – Trondheim
Norwegian University of
Science and Technology

Sabril Haris

Damage interaction analysis of ship collisions

Thesis for the degree of philosophiae doctor

Trondheim, May 2013

Norwegian University of Science and Technology
Faculty of Engineering Science and Technology
Department of Marine Technology

NTNU – Trondheim
Norwegian University of
Science and Technology

NTNU
Norwegian University of Science and Technology

Thesis for the degree of philosophiae doctor

Faculty of Engineering Science and Technology
Department of Marine Technology

ISBN 978-82-471-4531-9
ISBN 978-82-471-4532-6
ISSN 1503-8181

Doctoral Theses at NTNU, 2013:208

Printed by Skipnes Kommunikasjon as

To my beloved family

Abstract

During its lifetime, a ship may encounter accidents, such as collision and grounding, for which damage consequences in the forms of loss of human life, pollution of the environment, and economic losses may be substantial. This thesis focuses on the damage analysis of two deformable colliding ships using simplified analytical methods and numerical simulations.

In the simplified analytical methods, the ship structure is divided into several basic elements. Typical basic elements include the L-section (angle), T-section, X-section (cruciform), web girder, and shell plating. The resistance of each basic element is evaluated, and all resistances are added to obtain the total response of the entire structure. Numerical simulations using the non-linear finite element software LS-DYNA 971 are conducted to provide virtual experimental data, especially when physical experiments are unavailable. Finite element analysis is also useful in observations of the contribution of each structural part to the total resistance.

A new formula to calculate the resistance of shell platings is proposed. Derivation of the formula is based on a kinematically admissible displacement field, which is obtained from observations of the characteristic deformation modes in physical experiments and numerical simulations. The shell plating is subjected to a rigid indenter, whose shape is modelled as an elliptical parabolic surface; the surface is parameterized by the curvatures α and β in the transverse and vertical direction. The elliptical parabolic surface is more suitable for idealizing the actual shape of the striking bow than the existing approach, which models the indenter as a sharp point or with a circular surface. By partitioning the plate girder intersection on a side structure of a ship, the effective width of the cruciform is determined. The contribution of the stiffeners to the resistance of their parent elements is also analysed. New formulae for determining the total resistance of a ship side struck by a rigid bow and a bow that has collided with a rigid wall are proposed. These formulae are utilized in the simplified analysis of a collision between two deformable ships.

Numerical simulations of right-angle collisions between two real ships are performed for several collision scenarios. The finite element model, in which a fine mesh is applied in the vicinity of the collision area, consists of 660,000 elements. Three types of collision behaviour are identified: Collision Type 1—a relatively rigid bow striking a deformable ship side, Collision Type 2—a relatively rigid side colliding with a deformable bow, and Collision Type 3—a case in which both ships deform.

A new simplified procedure for analysing a right-angle ship-ship collision is proposed. Calculation of the resistance of each ship is based on the proposed formulae; their values are subsequently compared to identify the type of collision that will occur. For Collision Types 1 and 2, in which the resistance of one ship is relatively dominant to the resistance of the other ship, the analysis is simplified to a collision between a rigid structure and a deformable ship. Otherwise, a damage interaction analysis between two deformable ships should be conducted (Collision Type 3). During the collision process, the structural damage may switch between the two ships. Updating curvatures α and β of the bow shape due to the damage of the ships is a unique step in this new procedure. The predicted contact force and the internal energy dissipated during the collision demonstrate good agreement with the reference data provided by the numerical simulations.

Acknowledgement

Praises be to Allah, God the Almighty. Without His will and blessings, none of achievements in my life would ever happen.

I would like to express my sincere gratitude to my supervisor, Professor Jørgen Amdahl, for his guidance throughout the years of my doctoral study. His great patience and support always encourage my motivations, so that I could accomplish this comprehensive work.

My appreciation goes to all professors and PhD students, as well as staffs in the Department of Marine Technology, NTNU. Especially to the members of the ScenaRisC&G project: Dr. Hagbart Alsos, Dr. Lin Hong, Dr. Mohammad Tavakoli, Dr. Zhenhui Liu, and Dr. Tan-Hoi Nguyen who have shared their ideas and thoughts. Also, I would like to thank Dr. Yasuhira Yamada from the National Maritime Research Institute of Japan for his valuable discussions and supporting experimental data.

My life in Trondheim would never be as colourful and enjoyable without interactions with Indonesian student organization (PPIT) and Indonesian families (KT) in Trondheim. Special appreciation is given to Muslim-fellows in the Indonesian Muslim Community in Trondheim (KMIT); our brotherhood has made my life easier and meaningful in every situation.

The greatest honour to my parents, H. Gazali Samad and Hj. Nurzaida Zein; their love and prayers had been true source of God's blessings. Though they are no longer here to celebrate this achievement, may the fruits of this accomplishment be heavenly rewards to both of them. My sincere gratefulness is addressed to my parents-in-law, H. Mulia Hanifah and Hj. Yarmis Ilyas, for their unconditional support and care. To my wife, Yenita Mulia, with whom I share the ups and downs along this journey, I dedicate this thesis for her patience, love, and endless support. Last but not least, I would like to thank my brother, sisters, and extended family in Indonesia.

This work has been financed by the Research Council of Norway through the Strategic University Programme—Scenario-based Approach to Risk Analysis of Ship Collision and Grounding (ScenaRisC&G) Project. The financial support is gratefully acknowledged and appreciated.

Sabril Haris
May, 2013
Trondheim, Norway

List of appended papers

[Paper I]

Haris S., Amdahl J. Crushing resistance of a cruciform and its application to ship collision and grounding. Ships and Offshore Structures, 2012, 7(2):185-195.

[Paper II]

Haris S., Amdahl J. An analytical model to assess a ship side during a collision. Ships and Offshore Structures, 2012, 7(4):431-448.

[Paper III]

Haris S., Amdahl J. Analysis of ship–ship collision damage accounting for bow and side deformation interaction. Marine Structures, 2013, 32:18-48.

List of notations

b	[m]	half span of a web girder
db	[m]	indentation on the bow
dRB	[m]	global displacement
ds	[m]	indentation on the ship side
k	[MPa]	strength coefficient - a constant in the steel material model
n	-	hardening exponent - a constant in the steel material model
t_c	[m]	thickness of identical flanges of cruciform
$t_{cf\text{-}i}$	[m]	thickness of flange *i*-th of cruciform
t_p	[m]	plate thickness
$t_{px,y}$	[m]	equivalent plate thickness for x and y directions of the shell plating
t_t	[m]	thickness of identical flanges of T-section
$t_{tf\text{-}i}$	[m]	thickness of flange *i*-th of T-section
t_w	[m]	thickness of web girder
x, y, z	[m]	coordinates on the elliptical parabolic surface
C_c	[m]	width of identical flanges of cruciform
$C_{cf\text{-}i}$	[m]	width of flange *i*-th of cruciform
C_{eff}	[m]	effective width of cruciform
C_t	[m]	width of indentical flanges of T-section
$C_{tf\text{-}i}$	[m]	width of flange *i*-th of T-section
$\dot{E}_{int}$	[Nm/s]	the rate of internal energy
L	[m]	height of a cruciform
M_0	[Nm/m]	plastic moment capacity for a unit plate width
$M_{0\text{-}i}$	[Nm/m]	plastic moment capacity of flange *i*-th for a unit plate width
P	[N]	applied external load
P_{bow}	[N]	total resistance of a bow
P_c	[N]	resistance of cruciform with four identical flanges
P_{cf}	[N]	resistance of cruciform with different thickness and width flanges
P_s	[N]	resistance of shell plating
P_{side}	[N]	total resistance of a side of a ship

P_t	[N]	resistance of T-section with three identical flanges
P_{tf}	[N]	resistance of T-Section with different thickness and width flanges
P_w	[N]	resistance of web girder which its span is $2b$ and supported at both ends
P_{wf}	[N]	resistance of web girder which its span is b and supported at one end
S_x, S_y	[m]	half dimension of shell plating in x and y directions
T, t	[s]	time of simulation
V	[m^3]	volume of the solid body
α, β	-	indenter curvatures for x and y directions on the elliptical parabolic surface
α_i, β_i	-	updated indenter curvatures
α_l	-	reduction factor for curved shell plating on the bow cross section
δ	[m]	displacement of indenter, indentation on the shell plating
$\dot{\delta}$	[m/s]	velocity in the direction of loading
δ_f	[m]	displacement of failure
$\dot{\varepsilon}^p_{eq}$	[1/s]	the rate of equivalent plastic strain
ε_f	-	failure strain
$\dot{\varepsilon}^p_{ij}$	[1/s]	the rate of plastic strain tensor
ε^p	-	effective plastic strain
ε_{yp}	-	elastic strain at yield point
λ	-	effective length factor of crushed section
θ	[deg]	angle between tangential line of shell curve and crushing direction at bow cross section
σ	[MPa]	flow stress in the material model in the numerical simulation
σ_{eff}	[MPa]	the effective stress
σ_{ij}	[MPa]	stress tensor
σ_0	[MPa]	constant flow stress in the simplified analytical method, $\sigma_0 = (\sigma_y + \sigma_u)/2$
σ_y	[MPa]	engineering yield stress, initial yield stress in the steel material model
σ_u	[MPa]	engineering ultimate stress

Contents

Chapter 1

Introduction

1.1 Background and Motivation

Although the probability of ship accidents such as collision and grounding is low, their consequences are high, notably for accidents that involve ship tankers (ISSC 2006). An analysis of 20 reports of marine accidents by Rømer et al (1995) indicated that the total frequencies of collisions ranged from 0.5 to 13 cases per 10^6 ship miles. However, the impact of ship accidents on loss of life, environmental pollution, and financial cost is remarkable.

In December 1987 near the Philippines, a collision between the passenger ferry Dona Paz and the oil tanker Vector caused the ferry to burn and sink; 4,341 people died. This accident is recorded as the deadliest maritime disaster in peace-time history. It surpasses the sinking of the memorable passenger vessel RMS Titanic, which collided with an iceberg on her maiden voyage in 1912. The Atlantic Empress, which transported 276,000 ton of crude oil, collided with the oil tanker Aegean Captain on July 19, 1979 in the Caribbean Sea. Although the Aegean Captain was under control, the bow part of the tanker was flamed; the majority of her cargo was transferred safely to other vessels. Unfortunately, the Atlantic Empress burned continuously for 15 days prior to the sinking and disappearance of her remaining parts. Twenty six crew members perished. Recent ship accidents, e.g., the grounding of the cruise line Costa Concordia off the shore of Isola del Giglio, which is an Italian island, in January 2012; a collision between the tanker Norgas Cathinka and the ferry

Bahuga Jaya in September 2012 in the Sunda Strait, in Indonesia; and a collision between the car carrier vessel Baltic Ace and the container Corvus J in the North Sea in December 2012; indicate that the risk of accidents persists.

Major ship accidents can stimulate improvements in naval safety to prevent similar events and future consequences. The tragedy of the Titanic prompted the first International Convention for the Safety of Life at Sea (SOLAS), which was adopted in 1914 and enforced in July 1915. After the disaster of the tanker Torrey Canyon in 1967, from which 120,000 tons of crude oil spilled, the International Maritime Organization (IMO) introduced the International Convention for the Prevention of Pollution from Ships (MARPOL) in 1973; however, the convention did not enter into force. The modified 1978 MARPOL Protocol was established as a response to a series of tanker accidents from 1976-1977; the convention known as MARPOL 73/78 entered into force in 1983. The Oil Pollution Act of 1990 (OPA 90) was approved by the US Congress after the grounding accident of Exxon Valdez, which caused an environmental disaster due to the wide spreading of 600,000 barrels of crude oil. The regulation requires all tankers that sail on US waters after 2015 to possess double hull structures or achieve an equivalent level of safety.

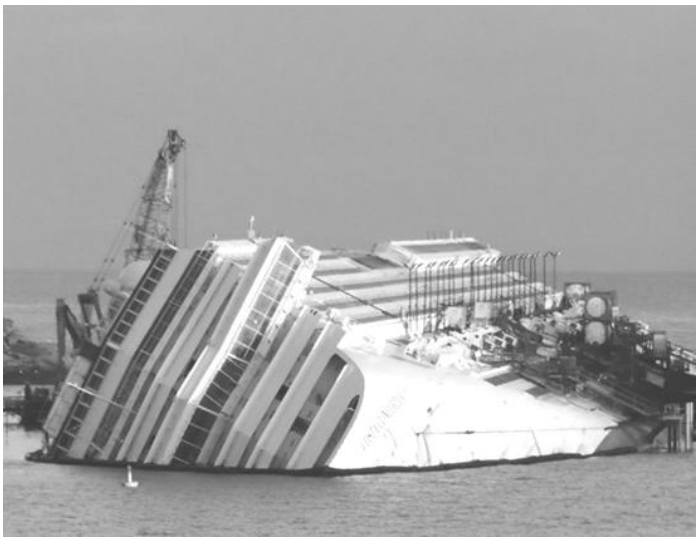

Figure 1.1: The Grounded Costa Concordia (source: www.news.yahoo.com)

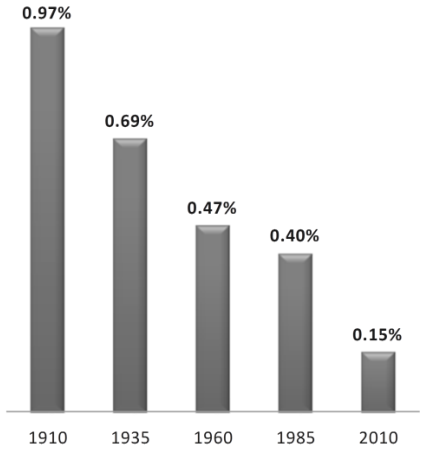

Figure 1.2: Total percentage losses of world fleet for interval 25 years (AGCS 2012)

Combined with improvements in ship navigation systems, all of these efforts have succeeded in reducing the number of fatalities and the economic losses in ship transportation. For shipping in the UK, the rate of fatal accidents was 11 per 100,000 seafarer-years from 1996 to 2005. This rate declined from 39 and 53 per 100,000 seafarer-years in the two previous decades (AGCS 2012). In the case of total ship losses, the number has reduced significantly, from about 1 ship per 100 in 1910 to 1 ship per 670 in 2010 (Figure 1.2)

Despite continuous efforts to minimize the probability of accidents, analyses of ship crashworthiness for appropriate accident scenarios must be addressed to reduce the consequences of accidents. Amdahl et al (1995) proposed a potential design procedure for ship collision, as shown in Figure 1.3.

Ship parameters and accident scenarios are defined in the initial step. The ship parameters which focus on the struck ship, consist of the loading conditions (i.e., full load and ballast conditions), the speed, and the hull girder loads. The accident scenarios include the size and speed of the striking ships, the shape and structural arrangement of the bow, and the collision geometry (i.e., striking location and impact angle). To determine the scenarios, databases of actual ship accidents are good sources of data (ISSC 2003); the data should be used carefully when they are applied to future scenarios (ISSC 2006). Definitions of characteristic accident scenarios can be found in Laubenstein et al (2001), Tagg et al (2001), Lutzen (2001), Skjong and Vanem

(2004), and Samuelides et al (2008). In addition, artificial data for various collision scenarios (i.e., ship size, speed, and collision angle) can be generated, as demonstrated by Pedersen et al (1996) and Brown and Chen (2002).

The second step consists of the analysis of external dynamics for estimating collision energy and contact force. The colliding ships are analysed as two rigid bodies using the hydrodynamic parameters and initial ship data (i.e., mass and speed) from the first step, as demonstrated by Pedersen and Zhang (1998) and Liu and Amdahl (2010).

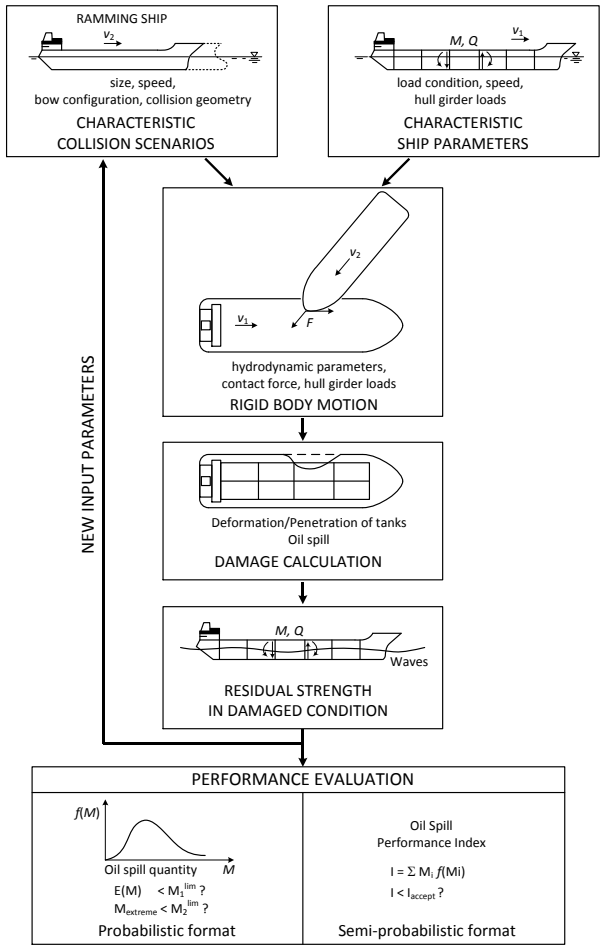

Figure 1.3: Design procedure for ship collision (Amdahl et al 1995)

The third step involves the internal mechanics analysis, which is used to evaluate the damage to ships. The damage corresponds to the amount of collision energy estimated in the second step. Rupture of the hull plating and cargo tank caused by the damage is a primary concern because potential oil spills or water ingresses cause a loss of hydrostatic stability.

The residual strengths of damaged ships are assessed in the next step. This step is important for decision support tools to ensure minimal consequences. Research on ship strength in damaged condition is discussed in (ISSC 2009) and (ISSC 2012), particularly by, e.g., Zhang et al (1996), Paik et al (1998), Wang et al (2000b, 2002), Fang and Das (2005), and Khan and Das (2007). In the last step, the performance of the ship is checked against relevant acceptance criteria, e.g., oil spill quantity. The integrity of the structures should achieve a minimum level for rescue or normal operation (ISSC 2003).

This thesis focuses on the analysis of internal mechanics to calculate the structural damage in the collided ships, which is a crucial step in the design procedure. Both ships, the struck ship and the striking bow, are assessed. In the following section, an overview of the analysis and existing research are presented.

1.2 An overview of damage analysis of ship collision

Research on the behaviour of ship structures during collision was initially applied to nuclear ships in the 1950s. Although the research focused on nuclear ships, the methods that were developed are useful for other types of ships, i.e. oil tankers and LNG carriers. In a pioneering study by Minorsky (1959), an empirical formula that relates the volume of the damaged material of the ships and the energy absorbed during collision was proposed.

Three methods for ship collision analysis: experiments, numerical simulations, and simplified analytical methods are reviewed in the following sections.

1.2.1 Experiments

Results from a series of experimental tests conducted from the 1960s -1970s in Japan, Germany, and Italy were compared with Minorsky's formula. Akita and Kitamura (1972) conducted a series of tests for a side model of nuclear powered ship and stem models of conventional ships. The stem contained transverse or longitudinal frames with different plate thicknesses, which resulted in six different stem models. All the specimens had a scale of 1:10. Different damage modes and distributions of

energies were found on the side and the stem; they were dependent on the relative strength of the stem and the side. The absorbed energies were compared to Minorsky's formula using conversions (see also Akita et al 1972). Suhara et al (1970) conducted a collision test between rigid bow models and a side tank model using a scale of 1:15. The predicted energy dissipation on the struck side was compared with the experimental results.

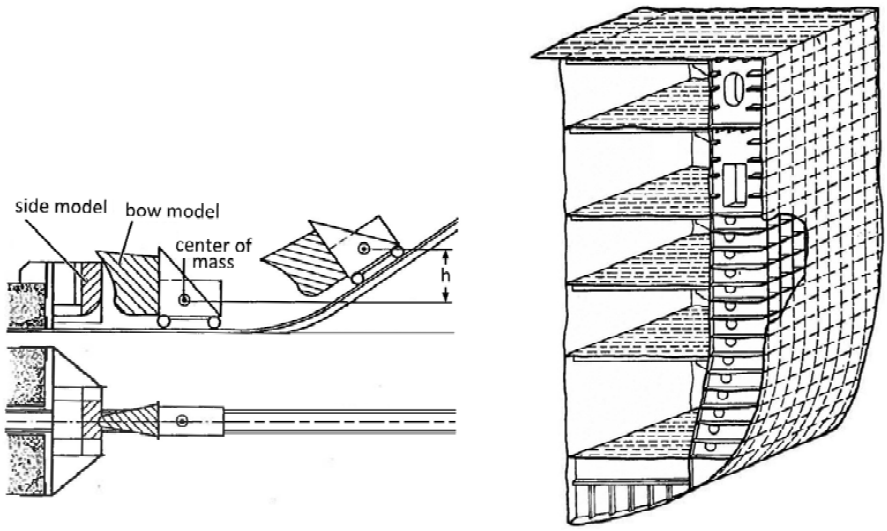

(a) (b)

Figure 1.4: (a) Test set up for bow collision in Germany, (b) Design of the penetration protection side of the resisting barrier type (Woisin 1979).

Woisin (1979) reported 12 tests conducted in Germany from 1967–1976. The models had scales of 1:7.5 and 1:12. The bow ran down through an inclined railway and struck the side of the ship, which exhibited a resisting barrier type (Figure 1.4). Based on the test results, he proposed modification and limitation to the Minorsky's formula. A series of tests in Italy was mentioned in Woisin (1979) and Zhang (1999). The series included 24 specimens on scales of 1:10 and 1:15 for various types of side structures and striking bows. Similar to the tests conducted in Germany, the bows ran down a slope.

The empirical methods by Minorsky did not specify the effect of structural configuration; the absorbed energy was only a function of damaged material volume. Considering the configuration of the structures, knowledge of the local and global structural behaviours became crucial due to the increasing number of new ships with different scantling systems. Experiments conducted after the 1980s placed extra concern on the detail response and damage pattern/mechanism of structures. Test evidence became a suitable means of establishing alternative methods: simplified analytical methods and numerical simulations. The collision tests were generally classified into two types: a side model subjected by a rigid bow and a deformable bow versus a rigid wall.

Collision tests between a rigid bow and the side of a double hull ship were conducted by Ito et al (1984 and 1985). The estimated scale of the models was 1:10. Based on the experimental results, the authors developed a simplified method to calculate the resistance of the side. The first type exhibits similarity with the grounding process; thus, data from grounding tests can be included in this type. Other collision tests, involving a side or bottom model and a rigid indenter, were reported by Hagiwara et al (1983), Arita and Aoki (1985), Amdahl and Kavlie (1992), Wang et al (2000a), and Endo et al (2002).

Amdahl (1983) conducted crushing tests for different types of bows: normal bows, ice-strengthened bows, bulbous bows, and stern structures. Tests were also conducted for a simple plate intersection of a cruciform. Other tests for a deformable bow versus a rigid wall were conducted by Ohnisi et al (1982), Hagiwara et al (1983), Endo and Yamada (2001), and Tautz et al (2010).

Endo et al (2002) conducted a series of collision tests with various bow models. One of the test cases consisted of collisions between a deformable bow and a deformable side. The test revealed separate indentations between the bow and the side. The deformations were initially imposed on the side until a certain indentation occurred, in which the increased resistance of the side was greater than the resistance of the bow. The indentation then switched to the bow for the remainder of the test.

Experiments with basic elements were also performed. The experiments were intended to obtain a picture of the representative deformation mechanisms, which were subsequently used to determine the resistance of the element through the use of simplified analytical method (see, e.g.: Amdahl 1983, Abramowicz and Jones 1984a, 1984b, and 1986, Hayduk and Wierzbicki 1984, Abramowicz 1994, Wierzbicki 1995, Wierzbicki and Driscoll 1995, Wang et al 1998, Zhang 1999, Simonsen and Ocakli 1999, Simonsen and Lauridsen 2000, Abramowicz and Simonsen 2003).

1.2.2 Numerical simulations

Physical experiments, especially with large-scale models, are usually too costly and risky to conduct. Numerical simulation using the finite element method (FEM) becomes a suitable alternative to analyse various structural problems. The use of finite element methods has been reported by Chang et al (1980) and Valsgård and Jorgensen (1983). Ohtsubo et al (1994) compared the results of numerical studies completed by Lenseling and Thung (1992) with existing experimental data of collisions reported by Vredevelt and Wevers (1992). The tests were conducted for a scale model of VLCC and a non-deformable bow. Regarding the damage pattern, the results from numerical simulations exhibited good agreement with experimental data; however, the maximum collision force was over-predicted by 20%. A similar study was conducted by Kitamura (1997). He performed numerical simulations of collisions between the side of a double hull ship and a rigid bow and verified the results by comparison with experiments. The simulations were extended by varying the side configuration. Based on the results of the numerical simulations and physical experiments, a new concept for a VLCC side structure was proposed. The experimental data for collision between a scale model of a double-hull tanker and a rigid bow were also used by Lehmann and Peschmann (2002) to validate the results of their numerical simulation; acceptable correlations were achieved. Further simulations were conducted for a full-scale ship, in which the shell plating was strengthened by austenitic material.

Numerical simulations of a collision between a deformable bow and a rigid wall were executed by Endo et al (2004). They employed their experimental tests for verification (Endo et al 2002). They conducted further simulations for two deformable colliding ships to investigate the effectiveness of a new buffer bow concept. In addition, Yamada and Endo (2004) presented the results of numerical simulations of oblique collision.

On the smaller scale, Wu et al (2004) conducted numerical simulations for the experimental tests conducted by Wang et al (2000a). The specimens consisted of double hull models indented by a rigid cone fitted with a spherical nose. The indenters had variable nose diameters and contact positions. Double bottom tests with a hexagonal truncated cone were used by Amdahl et al (1995) to verify their numerical simulations. Two models contained an even number of girder intersections and predominantly one-way transverse frames. They also extended the simulation to a grounding case with actual hull dimensions.

Some numerical studies for full-scale of structures and rigid indenters include the following: Naar et al (2002) conducted a stranding analysis for various bottom

structures subjected to a rounded-tip conical indenter, and Alsos and Amdahl (2007) and Nguyen et al (2011) conducted stranding analyses in which they studied one type of bottom structure but varied the indenter shape and contact position.

Other researchers conducted numerical simulations for collisions between two deformable ships. Kitamura (2000) used six different bows for collision with a side structure of a VLCC. He used a coarse element size for both colliding ships. Shibue et al (2001) simulated a full-scale collision between the double hull of a VLCC and the bow of a similar vessel. However, deformation of the bow was not significant and tended to be rigid. Moan et al (2003) conducted a simulation between a ship bow and an FPSO tank side structure. Three types of simulation were performed: two deformable structures, a rigid bow versus the deformed side, and a rigid side versus the deformed bow.

1.2.3 Simplified analytical method

A simplified analytical method is preferably developed along model experiments and subsequently with numerical simulations. The methods are typically based on plastic mechanism analysis, which requires the development of kinematically admissible displacement mechanisms. The simplified analytical methods are fast, cheap, and good for risk analysis and parametric studies; they need, however, to be verified against experiments or numerical simulations. The methods have often proved to give good results for idealised collision situations, but for more complex scenarios the accuracy may deteriorate.

The mechanisms can be created from observations of experiments and/or numerical studies. Experiments of basic structures were conducted to determine the resistance of the individual element; the experimental results were utilized to validate the total resistance predicted with simplified methods. When experimental data are unavailable for full-scale ship collisions, numerical simulations can serve as alternatives.

Resistance formulae for basic elements have been proposed by many researchers. For plate intersections, i.e., L-, T-, X-sections, simple expressions have been formulated by Wierzbicki and Abramowicz (1983), Amdahl (1983), Hayduk and Wierzbicki (1984), Yang and Caldwell (1988), Santosa and Wierzbicki (1998), and Abramowicz and Simonsen (2003). The following authors have proposed formulae to calculate the resistance of web girders: Choi et al (1994), Wierzbicki and Driscoll (1995), Wang and Ohtsubo (1997), Simonsen (1997a), Simonsen and Ocakli (1999),

Zhang (1999), and Hong and Amdahl (2008). Zhang (1999) defined the resistances of the shell plating subjected to a concentrated point load and a circular parabolic indenter. Wang and Ohtsubo (1997), Simonsen and Lauridsen (2000), and Wang et al (2000a) derived the resistance for a spherical indenter.

Amdahl (1983) applied a simplified analytical method to calculate the resistance of complete bows. The predictions were compared with experimental results. Yang and Caldwell (1988) conducted a similar analysis but used different resistance formulae for the basic elements. Pedersen et al (1993) modified the formulations by Amdahl (1983) and Yang and Caldwell (1988) and estimated the collision force as a function of the size and speed of the vessel, the bow shape, and the angle of the collision. Simplified methods to predict the resistance of a bow that collides with a rigid structure were also applied by Kierkegaard (1993), Lehmann and Yu (1995), Wang et al (1995), Endo et al (2002), and Yamada and Pedersen (2008). The resistance of a double hull structure subjected to penetration by a rigid indenter was proposed by Wang et al (2000). Experiments with small scale models were used to verify the predictions.

A procedure that considers the mutual interaction between the striking ship and the struck ship was proposed by Lutzen et al (2000). They used force displacement curves obtained from the collisions of a bow with a rigid wall and a rigid bow with a deformable side of a ship, respectively. Interaction between the two deformable ships was considered by applying the ratio of the bow cross-sectional areas at two different stages of the penetration of the bow. The results were not verified by experiments or numerical simulations. Yamada and Pedersen (2007) performed similar analyses of collisions between deformable sides and bow structures. In studies by Lutzen et al (2000) and Yamada and Pedersen (2007), the contribution of the shell plating to the total side resistance was calculated for a plate subjected to a point load.

1.2.4 Summary of the methods

The existing research on ship collision analysis can be summarized as follows:

- Although numerous experiments have been conducted, they have been limited to small- to medium-scale of structures. The majority of experiments have been conducted for collisions between a deformable specimen and a rigid structure.

- Numerical methods have been used widely to simulate ship collisions, from basic structural element to full-scale ship structures. Existing experimental data were used to validate the numerical methods.
- Simplified analytical methods are based on the observations of experimental evidence and the results of numerical simulations. These methods can be suitable alternatives to analysis of ship collisions. On a global level, procedures have been proposed for the case in which a deformable bow or the side of a ship collides with a rigid structure. Collision analyses of two deformable structures remain very rare; as a result, improving existing methods and developing new procedures for such analyses remain challenging.

1.3 Objectives and Scope of Work

This study has been performed as part of the Strategic University Programme—Scenario-based Approach to Risk Analysis of Ship Collision and Grounding (ScenaRisC&G) Project. The project began in 2005 and was financially supported by the Research Council of Norway. The project aimed to develop rational methods for the analysis of the risks involved in ship grounding and collisions in restricted waters. Another objective was to develop a procedure for the evaluation of consequences in terms of structural damage, environmental pollution, and loss of human life, once an accident has occurred.

The focus of this thesis is the damage analysis of ships during collisions using numerical simulations and simplified analytical methods. The main objective of this study is to propose a new procedure for analysing ship which considers simultaneously both ships as deformable bodies. The procedure is based on simplified analytical methods and verified by data from numerical simulations. The main objective is constituted by the following subtasks:

- To identify and analyse the existing resistance formula for basic elements of typical ship structures, i.e., cruciforms, web girders, T-sections, and shell plating, which will be used as representative formulae in damage analysis of ship collisions. Particularly, the effective width of a cruciform will be analysed in detail.
- To develop a resistance formula for a shell plating that is suitable for the shape of the striking bow and to verify the proposed formula with experimental data and numerical simulation results.
- To establish resistance formulae for the collision of a deformable ship with a rigid ship, i.e., the side of a ship struck by a rigid bow or a bow striking a rigid wall. The

proposed formulae are verified by existing experimental data and numerical simulation.

- To conduct numerical simulations of ship collision involving two deformable bodies, which will be used as virtual experimental data.
- To propose a procedure for a simplified analysis of a ship-ship collision in which both ships are deformable. The procedure should be verified against results from numerical simulations.

1.4 Thesis Organization

This thesis comprises five chapters which are described below:

Chapter 1 presents an overview of ship accidents, the methods of analysis, and the motivations and objectives of the study.

In **Chapter 2**, the methods of ship collision analysis are presented. Focus is placed on the assessment of internal mechanics using two methods: simplified analytical methods and numerical simulations. The principles of the methods and the use of existing experimental data as references for the numerical simulations and simplified methods are discussed.

Resistance formulae for basic elements are reviewed in **Chapter 3**. Paper I and Paper II are associated with this chapter. In Paper I, the effective width of a cruciform is defined; this term is applied to the total resistance of the side of a ship, which is discussed in Chapter 4. A new resistance formula for a shell plating subjected to an indenter with a general shape is proposed (Paper II). The resistance formulae for the other basic elements are selected from the existing formulae in the literature. The contribution from the stiffeners is discussed in the last part of Chapter 3.

In **Chapter 4**, ship collision analyses are presented. The first step is to establish an analytical formula to calculate the total resistance of the ship side and the bow (Paper II and Paper III). The formulae are verified by comparison with experimental data and the numerical results. Numerical simulations are established as virtual experiments and used as a reference for the proposed simplified analysis. Analyses of several ship collisions scenarios involving two deformable ships are executed. Three types of collisions are identified: a collision between a relatively rigid bow and a deformable ship, a collision between a very strong side of a ship and a deformable bow, and a

collision between two deformable ships. A new procedure for the analysis is described considering an updated parameter for the bow shape.

Conclusions of this study and recommendations for future studies are provided in **Chapter 5**.

Chapter 2

Methods in Ship Collision Analysis

2.1 Introduction

Analysis of ship collisions can be divided into two parts: the external dynamics and the internal mechanics (Pedersen and Zhang 1998). In the external dynamics, the rigid body motion of two collided ships is analysed to determine the amount of kinetic energy that is absorbed through deformation and friction. The principles of conservation of momentum and conservation of energy are utilized. The internal mechanics concern the response of the ship structures and the related energy absorbed during a collision. The response and the energy can be represented by force-deformation relationships of the deformed structures.

The analysis of ship collisions was pioneered by Minorsky (1959). Using data from twenty-six ship collisions, he calculated the lost kinetic energy for each collision by means of external dynamic analysis. The structural damage to the collided ships was also assessed. Minorsky (1959) proposed an empirical formula that relates the lost kinetic energy and the volume of the damaged ship material. Pedersen and Zhang (2000) improved the parameters of the damaged volume in Minorsky's formula to accommodate different structural arrangements of the newer ships. The material properties and the failure modes were also included in their revision. This modification is considered a substantial improvement of Minorsky's formula (Hong 2009).

Decoupling of the external dynamics and the internal mechanics is commonly used to simplify the analysis. Brown (2002) demonstrated that the total dissipation energy in the struck ship was similar if coupled or decoupled analysis was applied.

This study focuses on the internal mechanics of ship collisions. The deformation pattern, force-displacement history, and dissipation energy of the collided ships are examined. The current approach to analysis of the internal mechanics of ship collisions can be generally categorised into three methods: experiments, numerical simulations, and simplified analytical methods. All methods can be applied from the basic element level to the level of small-scale ship substructures. Experimental results are preferably used as a reference against which the two other methods must be verified. If experiments are impracticable and costly, such as experiments on a global structure level, the use of numerical and simplified methods should be considered.

The analysis methods adopted in this thesis are based on numerical simulations and simplified analysis; existing experimental data are used for verification. In the following sections, the numerical simulations and simplified analytical methods are described. The last section in this chapter discusses the use of existing experimental data and their importance to the two other methods.

2.2 Numerical Simulation

Numerical simulations using non-linear finite element software have been widely used in the analysis of ship accidents since the 1990s (Ohtsubo et al 1994, Amdahl et al 1995, Kitamura 1996, Kuroiwa 1996, Sano et al 1996). Improvements in computer capability and the modelling of structure and material behaviour have enabled more practicable and reliable computations. Although a large ship structure requires considerable effort for model preparation and a relatively long simulation time, nonlinear finite element analysis can be an acceptable alternative to physical experiments at a reasonable cost. If conducted skilfully, they may be considered virtual experiments (Kitamura 2002). One of the main issues in numerical simulation is material modelling, which should represent the reality as close as possible. For this purpose, recent investigations have been performed by Bao and Wierzbicki (2004), Simonsen and Törnqvist (2004), Lee et al (2004), Servis and Samuelides (2006), Alsos et al (2008), Ehlers et al (2008), Alsos et al (2009), and Hogström et al (2009). A review of the existing material models was conducted by Samuelides (2011).

In this thesis, numerical simulations are performed using the advanced non-linear finite element software LS-DYNA 971 (Hallquist 2006, 2007). Belytschko-Tsay

shell elements (Belystchko et al 2006) with five integration points over the thickness are selected in the model. Explicit time integration with small time steps is applied to comply with stability requirements for solving equations. Finite element size and material modelling, including fracture criteria, should be addressed to achieve reliable simulation results (ISSC 2003).

2.2.1 Element mesh size

Discretisation and modelling of the structures are challenging steps. A trade-off is associated with the size of the element mesh (l_e). The mesh should be as coarse as possible to reduce the computation time; however, a mesh that is too coarse will affect the folding pattern and severely hamper the fracture prediction. The use of excessively fine meshes should be avoided if the effect on the resistance and energy dissipation is marginal. Paik (2007) recommended a practical technique to determine the element size that is based on the folding length, i.e., using eight elements for one half-fold. Törnqvist and Simonsen (2004) suggested an approximate element length-to-thickness ratio (l_e/t_p) of five to accurately capture the stress and strain fields. Alsos and Amdahl (2007) used an element size-to-thickness ratio of approximately l_e/t_p = 10 to obtain a reasonably accurate prediction of fracture, which resulted in a consistent internal energy.

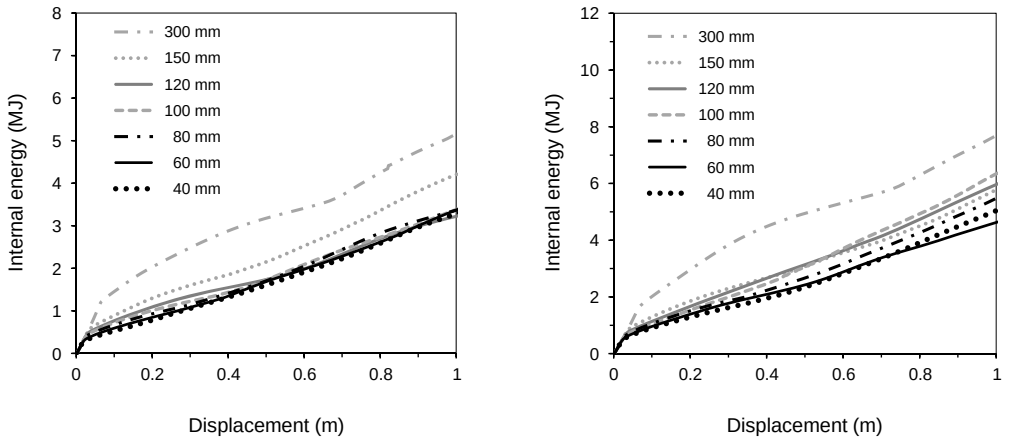

Figure 2.1: Internal energy for different mesh sizes:
plate thickness t_p of (a) 12 mm and (b) 16 mm.

A test of element mesh sensitivity has been conducted for a simple structure. The structure is a cruciform with two different plate thicknesses: t_p = 12 and 16 mm; the width and height are identical, i.e., 1200 mm and 2400 mm, respectively. The results are presented in the form of internal energy-displacement curves in Figure 2.1. For a plate thickness of 12, consistency is attained for a mesh size of 40–120 mm ($l_e/\ t_p$ = 3.3–10). Approximately identical results are obtained for the 40–150-mm mesh size ($l_e/\ t_p$ = 2.5–9.4) for a 16-mm plate thickness; only the results for the 300-mm mesh size deviate significantly. In this simple case, the use of a 40-mm mesh size demands four times more CPU than the 60-mm mesh size.

For large ship collision models, e.g., two deformable collided ships, applying different element mesh sizes can achieve optimum computation times and reliable results. In the main investigated area, a fine mesh is selected within the suggested range, usually in the vicinity of the collision point. In the area with no significant deformation or stress gradients, coarse meshes, i.e., $l_e/\ t_p$ = 20 – 40, are employed. Transitional mesh sizes are applied between the fine mesh and the coarse mesh. However, the coarsest mesh size is less than the limit mesh size suggested by Kitamura (1997) and Lee and Kim (2001), i.e., $l_e/\ t_p$ = 60. In the current simulation, the total number of elements can be reduced from approximately two million elements, if a uniform element size is applied, to approximately 660,000 elements, if a variable mesh size is used. The total computation time of two deformable colliding ships on a high-performance computer is three days (two Intel Xeon X5690 3.46 GHz, 24 GB RAM).

2.2.2 Steel material model

The steel material is characterised by a power law stress-strain relationship as

$$\sigma = k\left(\varepsilon_{yp} + \varepsilon^p\right)^n, \tag{2.1}$$

where $\varepsilon_{yp} = \left(\sigma_y/k\right)^{1/n}$ is the elastic strain to yield, ε^p is the effective plastic strain, k is strength coefficient, and n is hardening exponent. The modulus of elasticity (E) is 207,000 MPa. A nominal yield stress (σ_y) of 235 MPa is used in the majority of the simulations. Simulations using different material properties are also conducted with augmented yield stresses of σ_y = 285, 355, and 460 MPa. The strength coefficient k and hardening exponent n are adopted from Alsos and Amdahl (2007) and Alsos et al (2009), see Table 2.1. The Poisson´s ratio and steel density are μ = 0.3 and ρ = 7850

kg/m^3, respectively. The friction coefficient between the striking and the struck ships is set to 0.3; the same friction coefficient is applied to the internal structure contacts.

Table 2.1: The power law material properties

σ_y (MPa)	k (MPa)	n (-)
235	670*)	0.24
285	740	0.24
355	760	0.225
460	820	0.13

*) erroneous number given in Paper II and Paper III

Material failure is established according to the Rice-Tracey and Cockcroft-Latham (RTCL) model developed by Törnqvist (2003). The RTCL model is stress state dependent and may provide more realistic failure prediction than a conventional criterion, i.e., a critical plastic strain. Implementation of the failure model in LS-DYNA subroutines was conducted by Alsos (2008).

2.2.3 Supports and loads

Appropriate boundary conditions are needed to simulate the actual process of a ship collision. Because it is not easy to identify them properly, a simplified but acceptably accurate model must be generated.

In the case studies, the struck ship is defined as being in a standstill condition: no initial velocity and no motion occur during collision. The latter condition is in accordance with the recommended assumption of the ISSC 2003 report, which states that during the contact stage, the struck ship tends to move insignificantly. The striking ship hits the side of the struck ship in a right-angle collision and moves forward with a constant velocity; the movement generates a contact force between the collided ships.

Numerical simulations have also been conducted for collisions between a rigid ship and a deformable ship: a rigid bow striking the side of a ship or a deformable bow crushing a rigid wall. These simulations are idealizations of cases in which one of the ships is much stronger than the other ship; thus, only the weaker ship will deform and absorb the collision energy.

Numerical simulations of several ship collision cases are presented in Chapter 4.

2.3 Simplified Analytical Methods

Analysis of the behaviour of basic elements in ship structures is a primary building block in simplified analytical methods. Typical basic elements in ship structures include the L-section (angle), T-section, X-section (cruciform), web girder, and shell plating. Each basic element is scrutinized to identify its characteristic deformation pattern and to determine its resistance to deformation. The deformation characteristics of the basic elements will be used to predict the resistance of the ships on a global level.

Very large strains and deformations are involved in a ship collision process; therefore, plastic analysis is applied to the deformed structures. The plastic analysis is based on "the upper bound theorem" (or kinematic theorem), which requires kinematically admissible mechanisms of the structure. The collapse load can be obtained by equating the rate of external work from the applied load and the rate of internal energy from the strain of elements as

$$P(\delta)\dot{\delta} = \dot{E}_{int}, \tag{2.2}$$

where $P(\delta)$ is the applied external load, $\dot{\delta}$ is the velocity in the direction of loading, and $\dot{E}_{int}$ is the rate of internal energy.

For a continuous solid body, the rate of internal energy dissipation is determined by the volume integral as

$$\dot{E}_{int} = \int_v \sigma_{ij}\, \dot{\varepsilon}_{ij}^{p}\, dV, \tag{2.3}$$

where σ_{ij} is the stress tensor, $\dot{\varepsilon}_{ij}^{p}$ is the rate of plastic strain tensor, and V is the volume of the solid body that undergoes plastic deformation. The integrand in Eq. 2.3 can be replaced by a scalar multiplication between the effective stress σ_{eff} and the rate of equivalent plastic strain $\dot{\varepsilon}_{eq}^{p}$ as follows:

$$\sigma_{ij}\, \dot{\varepsilon}_{ij}^{p} = \sigma_{eff}\, \dot{\varepsilon}_{eq}^{p}\,. \tag{2.4}$$

Based on the von Mises yield criterion, the effective stress σ_{eff} is equal to the flow stress. Because a perfectly rigid plastic material is assumed in the analysis, the flow

stress can be represented by the constant value σ_0. The rate of internal energy dissipation is defined by

$$\dot{E}_{int} = \int_v \sigma_0 \, \dot{\varepsilon}_{eq}^p \, dV \,, \tag{2.5}$$

where the rate of equivalent plastic strain $\dot{\varepsilon}_{eq}^p$ is formulated as follows:

$$\dot{\varepsilon}_{eq}^p = \sqrt{\frac{2}{3} \, \dot{\varepsilon}_{ij}^p \, \dot{\varepsilon}_{ij}^p} \,, \tag{2.6}$$

Various assumptions for the flow stress have been employed for different types of materials and structures, e.g., Hayduk and Wierzbicki (1984), Yang and Caldwell (1988), Abramowicz and Simonsen (2003), Yamada and Pedersen (2008), and Hong and Amdahl (2008). One of the most practical formulations, which has been widely used for steel material, is adopted in this thesis

$$\sigma_0 = \frac{\sigma_y + \sigma_u}{2} \,, \tag{2.7}$$

where σ_y and σ_u are the yield and ultimate engineering stresses, respectively. Eq. 2.7 is a simple formula and is easy to apply when information about the material properties is limited.

Kinematically admissible mechanisms are predominantly inspired by deformation patterns observed in experiments. On the level of basic elements, physical experiments can be conducted at a reasonable cost and with low risk. In addition, extensive results from numerical simulations can support the experimental data used in determining the most suitable deformation pattern. Once the mechanism is selected, the rate of plastic strain $\dot{\varepsilon}_{ij}^p$ can be evaluated, and the rate of internal energy dissipation can be obtained.

Many researchers have analysed deformation mechanisms for typical basic elements based on experimental evidence and defined the resistance of the elements using simplified analytical methods. For plate girder intersections, Wierzbicki and Abramowicz (1983) classified the internal energy in the junction area by two types: the energy associated with the plate material being rolled over moving hinge lines and the energy dissipated on the toroidal surface at the meeting side of the angle section. These definitions were subsequently adopted by many researchers to evaluate other

types of girder intersections, i.e., T-section and cruciform (see, e.g.: Amdahl 1983, Hayduk and Wierzbicki 1984, Yang and Caldwell 1988, Santosa and Wierzbicki 1998, and Abramowicz and Simonsen 2003).

Resistance formulae for a web girder have been proposed by many researchers based on experimental data (Choi et al 1994, Wierzbicki and Driscoll 1995, Wang and Ohtsubo 1997, Simonsen 1997a, Zhang 1999, and Simonsen and Ocakli 1999). For instance, the deformation mechanism based on the experimental results conducted by Zhang (1999) is shown in Figure 2.2. More recently, Hong and Amdahl (2008) summarized these results and proposed another formulation based on the previous mechanisms.

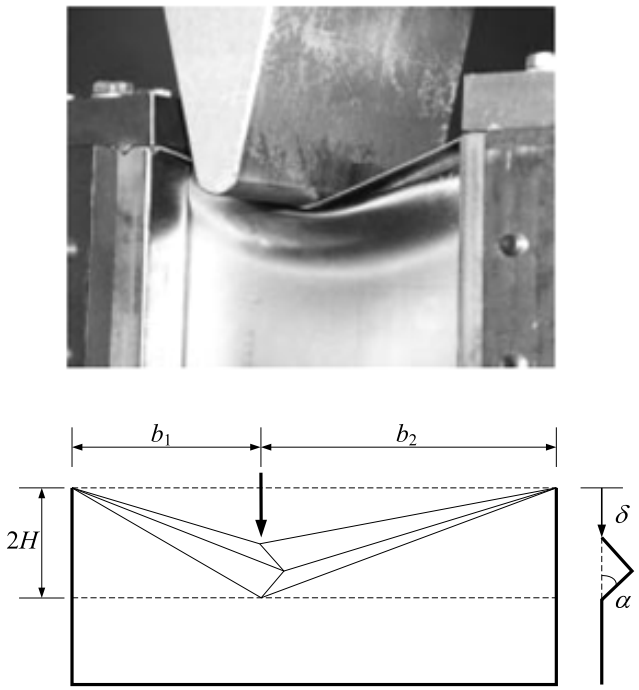

Figure 2.2: Crushing test of the web girder and its deformation mechanism model (Zhang 1999).

The resistance of the shell plating was defined by Zhang (1999). The shell plating was subjected to a concentrated point load and a circular parabolic indenter. Wang and Ohtsubo (1997), Simonsen and Lauridsen (2000), and Wang et al (2000) derived the resistance for a spherical indenter.

The entire damage process for ship structures is established by combining all of the deformation mechanisms of the structural elements. For this purpose, it is assumed that the different structural elements contribute independently to the total structures and that the interaction effects are minor. In the analysis of marine structures, these assumptions are valid and provide results with satisfactory accuracy (Hong 2009).

Several tests of small- to medium-scale models have been conducted to verify the various proposed analytical methods; the majority of the tests were performed for collisions between a deformable structure and a rigid object (for a deformable bow striking a rigid wall, see e.g., Amdahl 1983, Yamada and Pedersen 2008; for a deformed side of a ship indented by a rigid bow, see e.g., Ito et al 1984&1985, Amdahl and Kavlie 1992, and Wang et al 2000a). The same procedures for determining the resistance of the ship side and the bow have been applied to real ship collision scenarios (see, e.g., Zhang 1999 and Lutzen et al 2000).

2.4 Use of Existing Experimental Data

As mentioned in Sections 2.1 and 2.3, experimental data are very important as a reference for simplified analytical methods and numerical simulations. In this thesis, relevant experimental results are employed to assure that the methods and the simulations are reliable and legitimate. Within the possible range of physical experiments (from simple basic elements to scale models of ship structures), the numerical simulations should be consistent with the results of the experiments. Provided that numerical simulations are well verified against available model tests, they can be used to generate virtual experimental data where physical experiments are unavailable and, thus, can be used as references for simplified analytical methods.

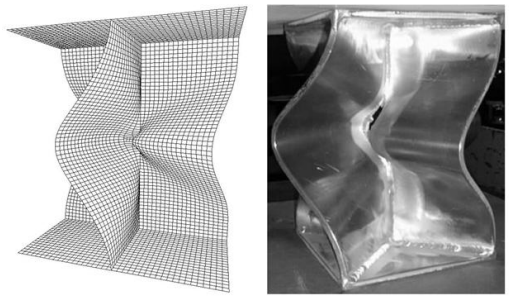

(a)

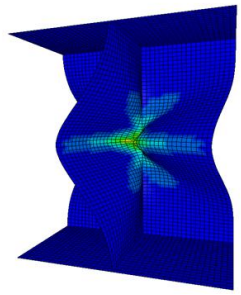

(b)

Figure 2.3: Deformation of cruciform: (a) simulation and test by Urban (2003), and (b) present numerical simulation.

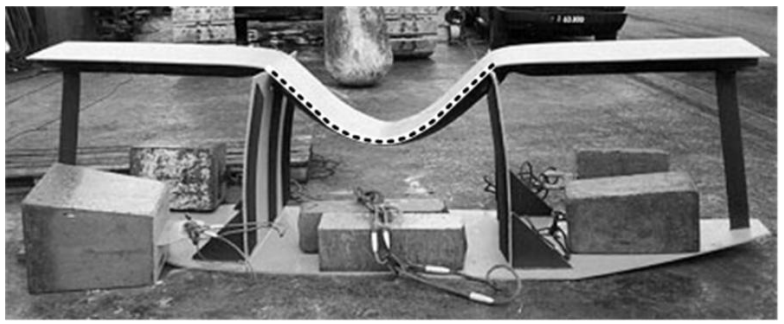

Figure 2.4 Deformation pattern of a one-way plate (Qvist et al 1995). The dashed line depicts the deformation.

An example of a comparison of experimental data with numerical simulation on the level of simple basic elements is shown in Figure 2.3. Similar deformation patterns are obtained. Large stresses and strains in the vicinity of the plate intersection indicate that this part contributes significantly to the energy dissipation. In Figure 2.4, the experimental evidence is utilized to define the deformation mechanism of a one-way stiffened plate subjected to a rigid indenter. This test is employed to propose a new resistance formula for shell platings (Section 3.4).

For the side model and the bow model, existing experimental data are applied to a comparison of the force-displacement curves from three different methods (Section 4.2).

Chapter 3

Resistance Formula of the Basic Elements

To analyse a ship collision, we can divide the structure of a ship into a number of basic elements. The resistance of each basic element is evaluated, and all resistances are added to obtain the total response of the entire structure. The most common basic elements in the analysis include the cruciform, web girder, T-section, L-section, and shell plating. The resistance formulae are derived from energies which are related to deformation; friction energy is not treated because it has minor contribution to the total energy for all cases presented in Chapter 4.

In the following section, the resistance formulae of the basic elements used in this thesis are discussed.

3.1 Cruciform

(Paper I)

Existing formulae to determine the mean crushing force of the cruciform have been reviewed by Yamada and Pedersen (2008). Previously, Abramowicz and Simonsen (2003) summarized the formulae and compared them with experimental results. The formula was derived from the kinematic admissible deformation mode for a cruciform with a fixed bottom support (Figure 3.1).

The effective width of a cruciform is determined by analysing the internal energy distribution. The analysis is conducted for a single cruciform, which is divided into a number of plate strips to determine the distribution of the internal energy over the flange width. A cruciform with a 2000-mm height, 15-mm thickness, and 4000-mm width is divided into 40 plate strips of equal width, i.e., a 100-mm width. The numbering extends from the junction to the free end (as shown in Figure 3.2) for one flange of the cruciform.

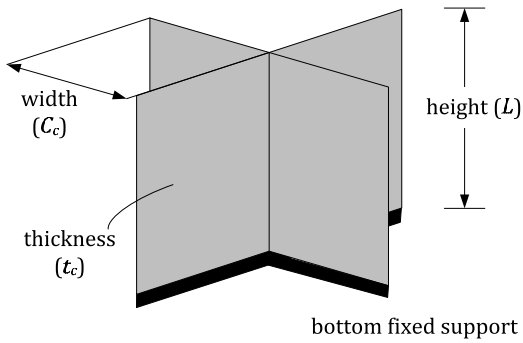

Figure 3.1: Cruciform model

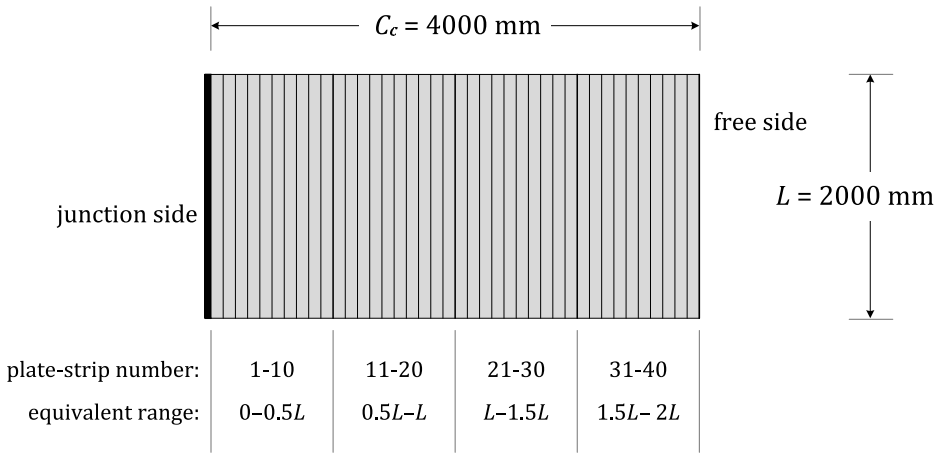

Figure 3.2: Partition of the cruciform

The deformation patterns of the selected cross-sections of the cruciform are shown in Figure 3.3. Plate strip number 1 crumples in more folds than the other plate strips because the junction side is constrained during the crushing process. Both membrane and bending energies develop during this folding process; therefore, more energy is dissipated. For the remaining plate strips, the number of folds decreases. For the end plate strip, only one large wave exists; for this deformation process, the bending energy is dominant.

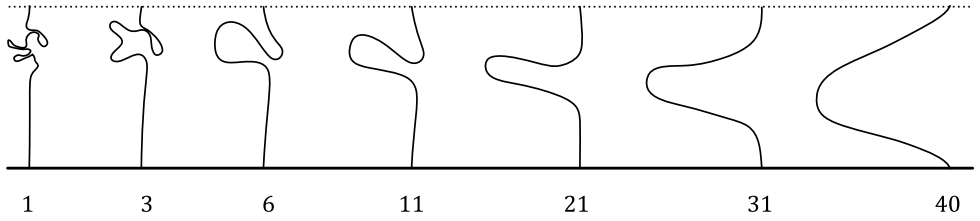

Figure 3.3: Deformation of a cross-section at an indentation of 1.0 m. The numbers refer to the plate strip numbers.

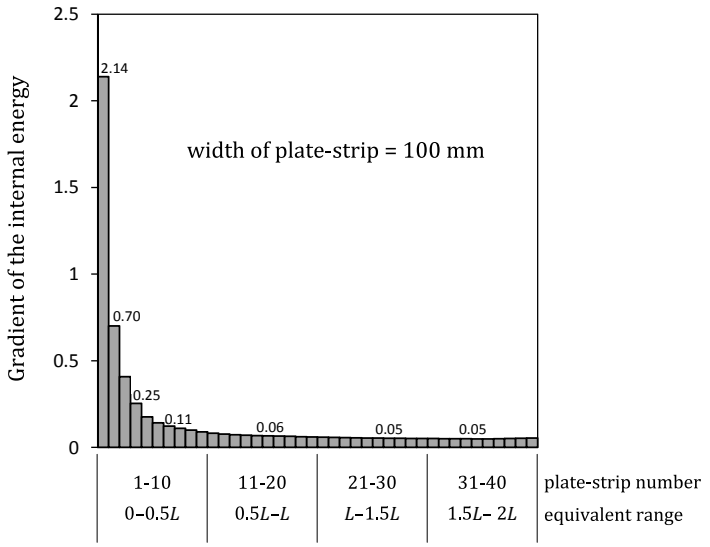

Figure 3.4: Distribution of the internal energy in the cruciform

The different folding patterns cause a variation in the internal energy dissipation. The gradient of the internal energy curve in the steady state is presented in Figure 3.4. A significant contribution to the internal energy derives from the first plate strip, which is located at the junction. The contribution decreases asymptotically for the next plate strips and tends to be constant for those located far from the junction. Other simulations with longer cruciform breadths show the same tendency; the plate strips far from the junction have trivial contributions to the total internal energy.

The analytical formula should comply with the numerical results. For this purpose, the energy dissipation for the groups of plate strips is shown in Figure 3.5. The internal energy that is absorbed by the plate strips within the range of 0–0.5 L is distinctly dominant, whereas the energy dissipation for the other groups is either similar or significantly smaller.

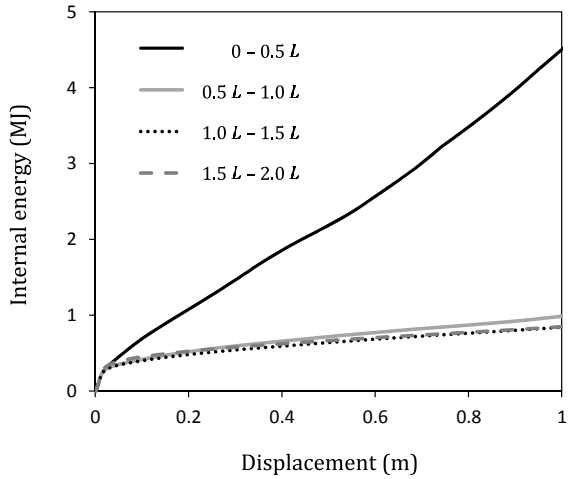

Figure 3.5: Internal energy for the various parts of the cruciform

Based on the results shown in Figure 3.4 and Figure 3.5, the cruciform has a certain width that efficiently dissipates strain energy. The effective width was considered to be half of the height of the cruciform as follows:

$$C_{eff} = 0.5\ L \qquad 3.1$$

It was determined that the most suitable formula for the average crushing force of a cruciform, with its width equal to half of the height of the cruciform, is the formula proposed by Hayduk and Wierzbicki (1984)

$$P_c = \frac{20.05}{\lambda} M_0 \left(\frac{C_c}{t_c} \right)^{1/2} , \tag{3.2}$$

where M_0 is the plastic moment capacity for a unit plate width, and C_c and t_c are the width and thickness of the cruciform, respectively. The effective length factor λ is set to 0.73. The plastic moment capacity is defined as follows:

$$M_0 = \frac{\sigma_0 \cdot {t_c}^2}{4} , \tag{3.3}$$

The cruciform resistance, P_c, in Eq. 3.2 applies to cruciforms with four identical flanges. In ship structures, cruciforms typically consist of flanges with different widths and thicknesses. The formula is therefore modified, assuming each flange contributes one-fourth of the amount associated with a cruciform with uniform flanges. The modified formula yields the following expression

$$P_{cf} = \sum_{i=1}^{4} \left[\frac{5.01}{\lambda} M_{0i} \left(\frac{C_{cf-i}}{t_{cf-i}} \right)^{1/2} \right] , \tag{3.4}$$

where P_{cf} is the cruciform resistance with unequal flanges, and $C_{cf\text{-}i}$ and $t_{cf\text{-}i}$ are the width and thickness of cruciform flange *i*, respectively.

3.2 Web girder

Resistance formulae for a web girder have been suggested by many researchers (Wang and Ohtsubo 1997, Simonsen 1997a, Simonsen and Ocakli 1999, Zhang 1999, and Hong and Amdahl 2008). Haris and Amdahl (2009) achieved good agreement with a formula proposed by Zhang (1999)

$$P_w = \frac{11.26}{\lambda} M_0 \left(\frac{b}{t_w} \right)^{1/3} , \quad 3.5$$

where b is half the span of the web girder and t_w is the thickness. The effective length factor λ is set to 0.73 and the plastic moment capacity M_0 is analogous to the definition in Eq. 3.3. Figure 2.2 displays the deformation mode of the web girder modelled by Zhang (1999).

The formula in Eq. 3.5 applies to web girders with fixed supports at both ends that are loaded at mid span. For a web girder with length b that is only supported at one end, the formula becomes

$$P_{wf} = \frac{5.63}{\lambda} M_0 \left(\frac{b}{t_w} \right)^{1/3} . \quad 3.6$$

3.3 T-Section

A formula by Amdahl (1983) is used for the T-section. The formula is similar to the formula proposed by Yang and Caldwell (1998) for their Mode-ii of a T-section. The crushing force is given by Eq. 3.7 as

$$P_t = \frac{10.98}{\lambda} M_0 \left(\frac{C_t}{t_t} \right)^{1/2} , \quad 3.7$$

where C_t and t_t are the width and thickness of the T-section, respectively, and λ and M_0 are as defined in Eq. 3.2 and 3.3.

For T-sections with different flanges, the formula in Eq. 3.7 is modified as

$$P_{tf} = \sum_{i=1}^{3} \left[\frac{3.66}{\lambda} M_{0i} \left(\frac{C_{tf-i}}{t_{tf-i}} \right)^{1/2} \right] , \quad 3.8$$

where P_{tf} is the resistance of the T-section, and $C_{tf\text{-}i}$ and $t_{tf\text{-}i}$ are the width and thickness of T-section flange i, respectively.

3.4 Shell Plating

(Paper II)

A new formula to determine the resistance of a shell plating is proposed. The plate is subjected to an indenter, whose shape is represented by an elliptical parabolic surface. The elliptical parabolic indenter is given as

$$z = \frac{x^2}{(\alpha \cdot S_x)} + \frac{y^2}{(\beta \cdot S_y)} \tag{3.9}$$

where α and β are the curvatures on the x and y axes, respectively, and the indenter is applied on the middle of the plate sizes $2S_x \times 2S_y$. The elliptical parabolic surface in the x-z plane is illustrated in Figure 3.6.

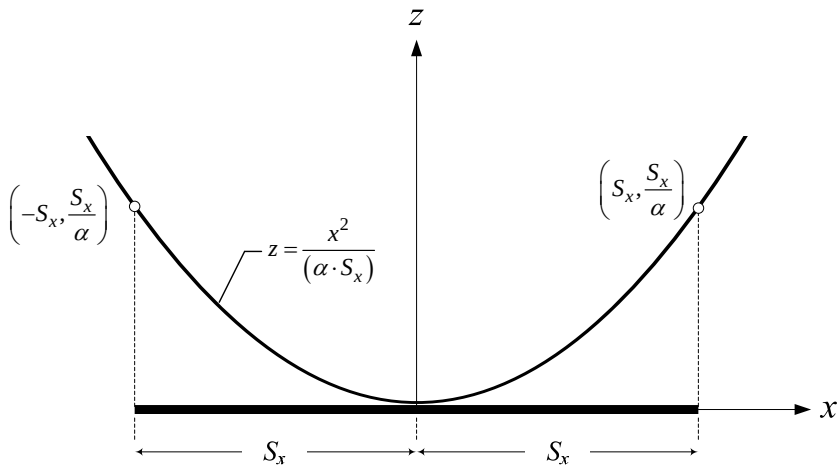

Figure 3.6: Elliptical parabolic surface in the x-z plane

The deformation pattern of the plate is defined on the basis of experimental evidence provided by Qvist et al (1995), Kuroiwa (1993), and Zhang (1999) for a strip plate. The results from the strip plate are subsequently adopted for the two-way plate. The resistance of the shell plating due to indentation of the elliptical parabolic indenter is given by Eq. 3.10 as

$$P_s(\delta) = \frac{8}{3\sqrt{3}} \cdot \sigma_0 \left(t_{px} \cdot \frac{S_y}{S_x} \left(1 - \frac{\alpha\delta}{S_x} \right)^{-1/2} + t_{py} \cdot \frac{S_x}{S_y} \left(1 - \frac{\beta\delta}{S_y} \right)^{-1/2} \right) \delta \qquad 3.10$$

where t_{px} and t_{py} are the equivalent plate thicknesses determined by smearing the stiffener area in the x and y directions, respectively, and δ is the indentation in the middle of the plate. The detailed derivation of the formulae and its application to a real bow shape can be found in Appended Paper II. For the bow that is crushed during a collision, the effective curvatures of the bow should be determined as shown in Figure 3.7.

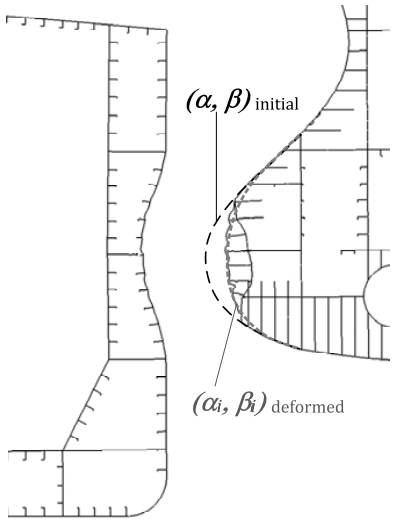

Figure 3.7: The effective curvatures of the crushed bow.

The failure displacement of the shell plating subjected to a circular paraboloid indenter, i.e., $\alpha = \beta$, is given as

$$\delta_f = \left[1.316 \frac{S_x S_y}{\sqrt{S_x{}^2 + S_y{}^2}} \sqrt{\varepsilon_f} \right] \times \sqrt{\alpha} \qquad 3.11$$

where ε_f is the failure strain. If indenter curvatures vary for each axis, the function $\sqrt{\alpha}$ is modified by applying linear multiplication for the curvatures and the total order is maintained by using the square root. For example, if $\alpha \neq \beta$, it will be replaced by $\left(\sqrt{\alpha} \times \sqrt{\beta}\right)^{1/2}$.

3.5 Stiffener

Ship structures typically consist of stiffened plate panels. The stiffeners may be attached on the shell plating, girders, stringer, transverse frame, and bulkhead. To determine whether the stiffeners should be considered in the analysis, numerical simulations are conducted to observe their contribution relative to the main plate.

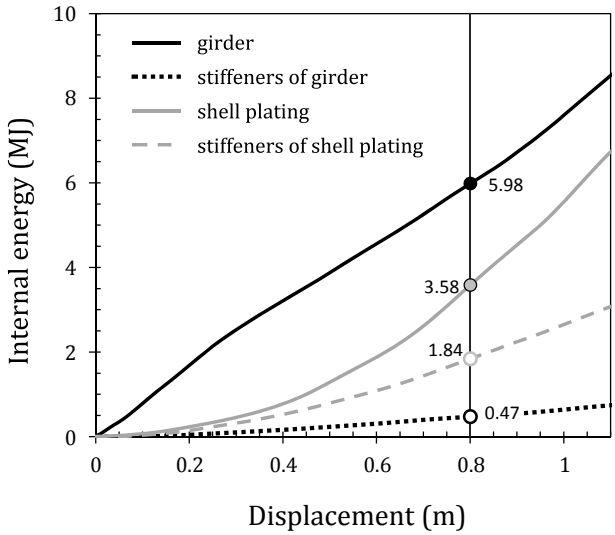

Figure 3.8: Contribution of the stiffeners on the struck side of the ship

Observations from the results of numerical simulations of an actual side of a ship hit by a rigid sharp bow indicate different contributions from the stiffeners on the shell plating and on the girders, as shown in Figure 3.8. For a certain displacement, stiffeners on the girder contribute approximately 7% to the total internal energy dissipation. The internal energy of the stiffeners attached to the shell plating is half of the internal energy of the shell plating. Other simulations for different conditions of

the struck side of a ship and the striking bow show equivalent tendencies: a minor contribution from the stiffener on the girder and significant contributions from the stiffeners on the shell plating.

Thus, for the girder on the struck side of a ship, only the main plate girder will be considered in the analysis. Regarding the shell plating, the stiffeners have to be included in the calculations, and the stiffened plate panel will be considered to have an equivalent plate thickness (refer to Section 3.4 for the equivalent plate thickness).

In the analysis of the crushing bow, the cross-section of the bow between two transverse frames or on the transverse frame is used to calculate the resistance of the bow. The stiffeners, with the bulkhead, stringer, and the shell plating, establish three common types of plate intersections: L-section, T-section, and cruciform. Therefore, all stiffeners are included in the calculation. The contribution of the stiffeners to the analysis of the bow is discussed in Chapter 4.

Chapter 4

Ship Collision Analysis

In this chapter, the resistance formulae for basic elements are applied to the structural components of the ships that are involved in the collision. The actual structure for the struck ship is the ship side, and the actual structure for the striking ship is the bow. The simplified formulae are initially assumed to be governing for a simple double hull and a transverse section of the simple bow model, which are models for the side of the ship and the bow, respectively. The formulae are verified with experimental data as well as numerical simulation. Subsequent analyses are performed for actual ship collision scenarios.

4.1 Resistance Formulae

(Paper II), (Paper III)

A typical side of a double hull ship is illustrated in Figure 4.1. The structure can be divided into the shell plating, the cruciform constituting the intersection of girders, and the web girders. For the shell plating, the outer shell, which is in direct contact with the striking bow, is the primary focus (Figure 4.1b). Eq. 3.10 is used to calculate the resistance of the shell plating as a function of the displacement of the contact point. The cruciform consists of the girder intersection, and the width is assumed to be half of the girder height (Figure 4.1c). The remainder of the plate girder is analysed as a web girder with no intersection (Figure 4.1d). For these plate girder elements, a constant resistance is assumed using Eqs. 3.4 and 3.6.

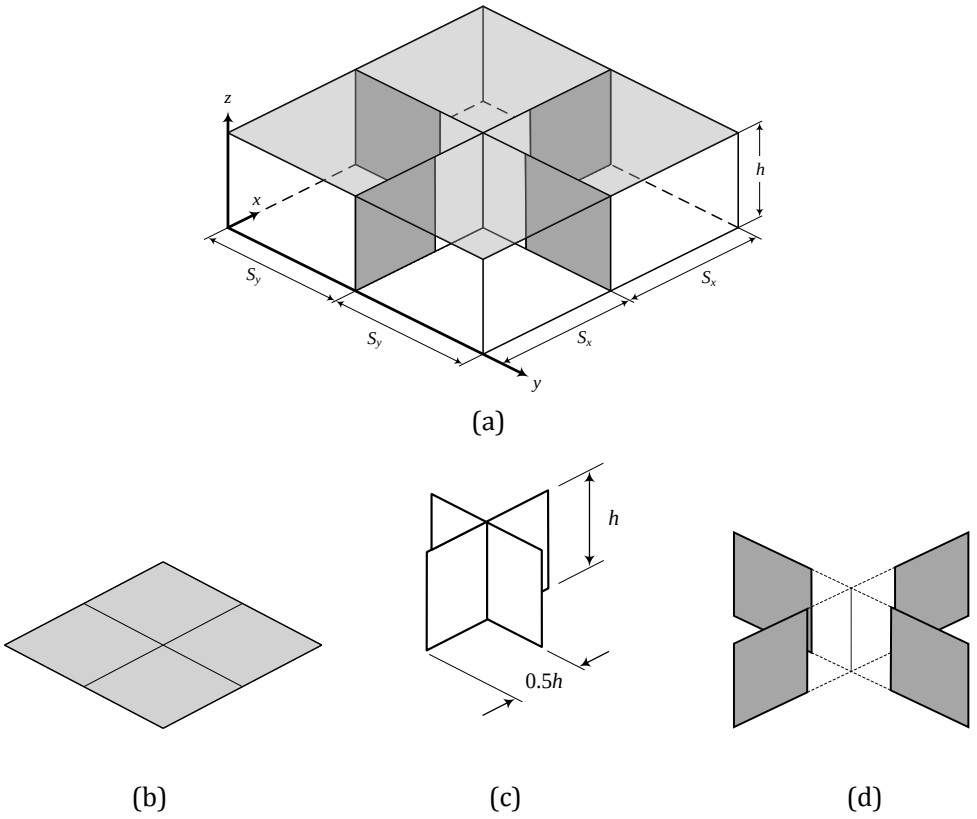

Figure 4.1: (a) An example of the structure of the side of a ship: shell plating and one plate girder intersection, (b) shell plating, (c) cruciform with a height equal to the girder height, and (d) four remaining sections form web girder.

The total resistance for a typical side of a double hull ship is determined as

$$P_{side} = P_{cf} + \sum_{i=1}^{4} P_{wf} + P_s \ , \qquad 4.1$$

where P_{cf}, P_{wf} and P_s are the resistances of the cruciform, the web girder and the shell plating, as described in Eqs. 3.4, 3.6, and 3.10, respectively. In an actual ship collision, the deformation on the side of the ship may continue and include additional panels.

The striking ship may have additional contact with the struck ship beyond the area spanned by the first panel. Alternatively, the significant tension forces of the non-ruptured shell plating may cause collapse of the next girder intersections. Eq. 4.1 can be utilized to calculate the resistance by updating the number of cruciforms and web girders, as well as the size of the panel.

In the analysis of ship bows, the structure is partitioned into basic elements for transverse sections. Longitudinal frames, including longitudinal bulkheads and stringers, the bow shell plating, and its longitudinal stiffener are included in the calculations. The basic elements of a partitioned structure are simplified to consist of only cruciforms and T-sections. L-sections, which consist primarily of L-stiffeners, are modelled as equivalent flat bars with the same height and correct cross-section area. Furthermore, if the plate is curved, it can be simplified as a straight plate. An example of a bow transverse section is shown in Figure 4.2. The total resistance is calculated by summing the resistances of all cruciforms and T-sections.

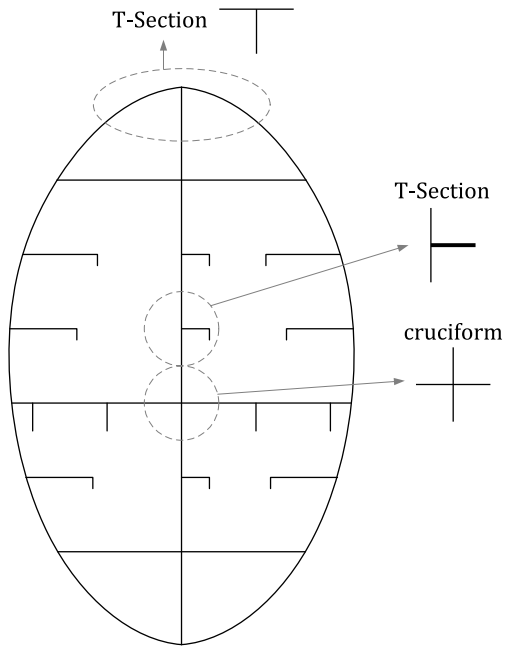

Figure 4.2: An example of transverse section of bow

The effect of a shell plating that is curved in the longitudinal and transverse directions is considered in the calculation. Due to the shell inclination, the crushing force is reduced. A reduction factor developed by Wang et al (1995) is adopted. The reduction factor, α_I, is expressed as

$$\alpha_I = \frac{1-\sqrt{\sin^2\theta+(1-\lambda)^2\cos^2\theta}}{\lambda\cos\theta}, \tag{4.2}$$

where θ is the angle between the tangential line of the shell curve and the crushing direction at the instantaneous bow section, and λ is defined as in Eq. 3.2.

The total resistance of the bow for a given transverse section is calculated using the following formula as

$$P_{bow} = \sum_{i=1}^{m}\left[\sum_{j=1}^{4}\left[\frac{5.01}{\lambda}M_{0j}\left(\frac{C_{cf-j}}{t_{cf-j}}\right)^{1/2}\right]\right]_i + \sum_{p=1}^{n}\left[\sum_{q=1}^{3}\left[\frac{3.66}{\lambda}M_{0q}\left(\frac{C_{tf-q}}{t_{tf-q}}\right)^{1/2}\cdot\alpha_{I-q}\right]\right]_p \tag{4.3}$$

where m and n are the numbers of cruciforms and T-sections, respectively.

4.2 Application of the Formula to Simple Structures

4.2.1 Application in a double hull of ship side model

The resistance of the side of a ship, as defined by Eq. 4.1, was applied to a simple model of the side of a ship as described by Wang et al (2000a). The ship side model consists of a double hull with a depth of 200 mm and equal girder spacing in both directions, i.e., 200 mm. For the entire model, a plate thickness of 2.3 mm was used. The experimental test was conducted using a rigid conical indenter with a nose radius of 200 mm.

The shape of the indenter is approximated by an elliptical parabolic surface. In the beginning of the indentation, only 400x400 mm of the side panel is involved. The

elliptical parabolic is determined for size panel S_x = S_y = 200 mm. By using Eq. 3.9 and the coordinates of the cone located 200 mm from the collision point, the curvatures are defined as α_1 = β_1 = 1.707. These curvatures are updated to α_2 = β_2 = 0.854 if deformation involves a larger panel, i.e., 800x800 mm size. The model is illustrated in Figure 4.3.

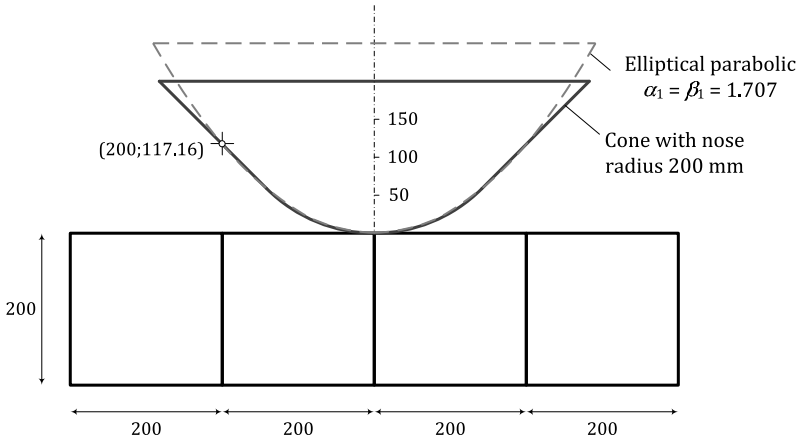

Figure 4.3: A double ship side model that is focused on the panels at the collision point and one neighbour panel for each side.

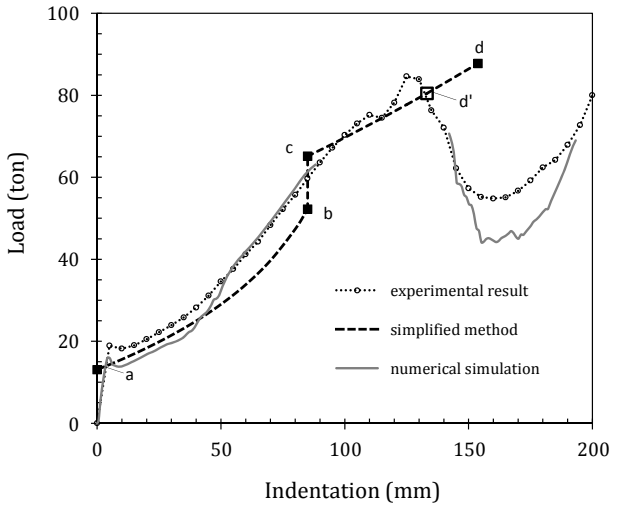

Figure 4.4: Load-indentation curves for the double ship side model

The results for the load indentation are shown in Figure 4.4. The simplified method provides a good prediction of the experimental results. Stage a-b on the curve for the simplified method signifies the resistance when contact occurs within the panel with dimensions 400x400 mm. The penetration continues without failure on the outer shell plating and the next girder intersections begin to deform. They involve a larger panel and more cruciforms and web girders. Eq. 4.1 is applied by considering the new panel size, the updated curvatures (α_2, β_2), and the number of cruciforms and web girders. The calculation ceases when failure occurs on the shell plating (point d in Figure 4.4) using the assumed failure strain by Wang et al (2000a), i.e., ε_f = 20%.

Various values of failure strain have been used, e.g., in the range of 5–10% (Amdahl 1995, Zhang 1999, McDermott et al 1974, and Paik et al 1999). A better prediction can be achieved if a moderate value of strain failure is used (point d', in Figure 4.4). Detailed calculations are provided in Appendix B-1.

4.2.2 Application on a bow model

(Paper III)

Experimental data from Yamada and Endo (2005) and Yamada and Pedersen (2008) were used to verify the resistance formula of the bow. The model tests consisted of two bows with different stiffener systems: one bow with transverse stiffeners (Type–BCG) and one bow with longitudinal stiffeners (Type–BCL). Note that both bow models had the same configuration of the cross-section from the tip of the bow to ring frame 1 (Section 1). The bows are illustrated in Figure 4.5.

The experimental data, the simplified analyses, and the numerical results for the resistance and the internal energy dissipation are presented in Figure 4.6 and Figure 4.7. The curves show that the results of the simplified analysis and the finite element simulation are similar to the experimental results. A detailed analysis and discussion are included in Paper III and Appendix B-2.

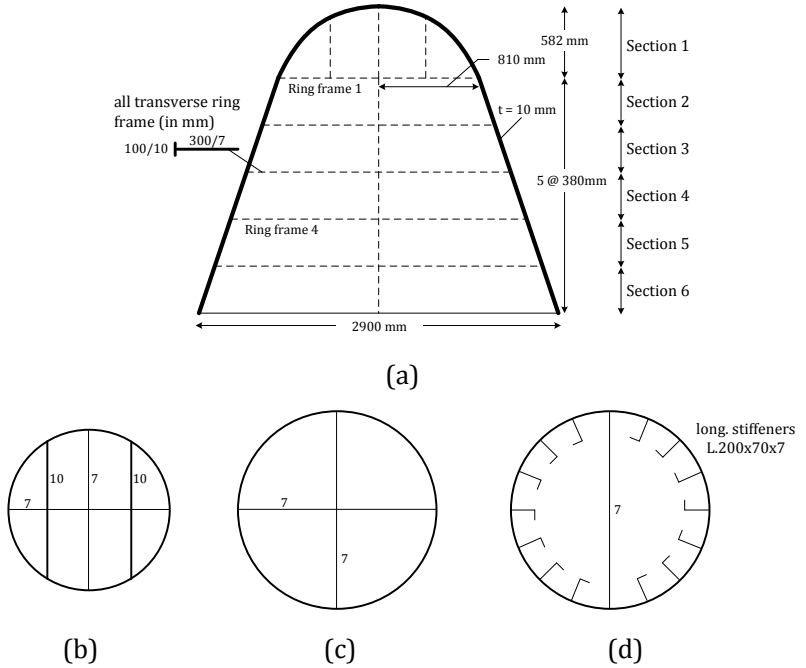

Figure 4.5: Bow model tests: (a) Vertical cross-section at centre line, (b) Horizontal cross-section for Section 1, (c) Horizontal cross-section for BCG model, and (d) Horizontal cross-section for BCL model.

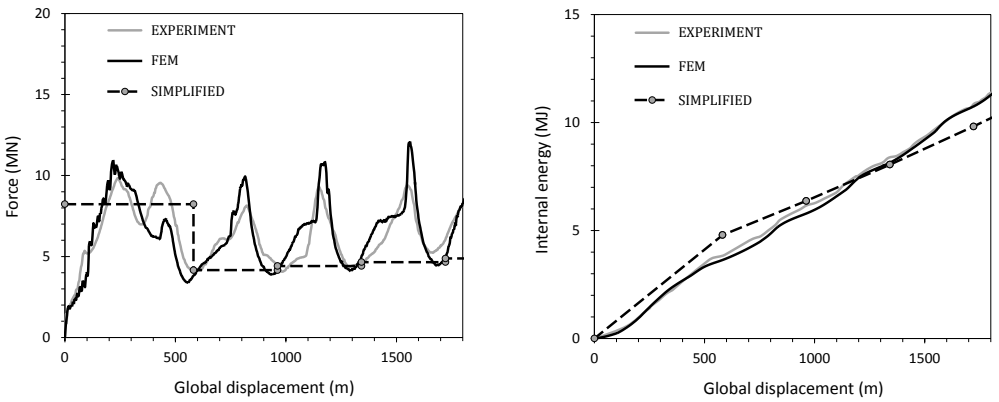

Figure 4.6: Results for BCG-Model

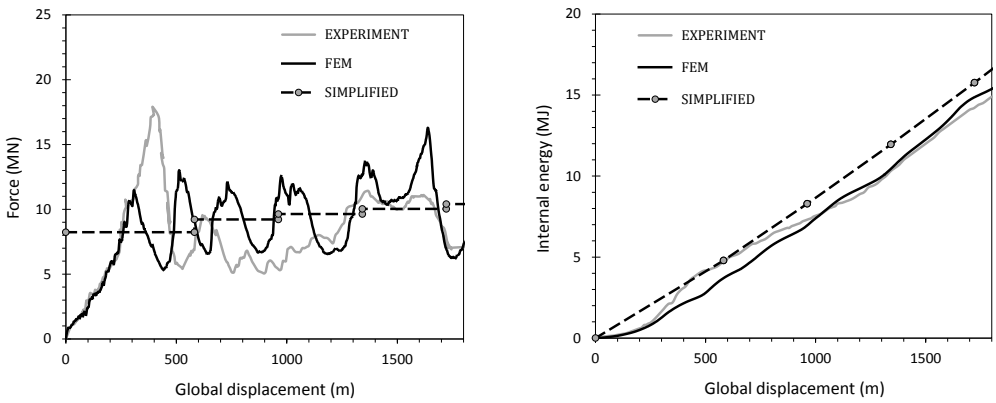

Figure 4.7: Results for BCL-Model

4.3 Ship Collision Scenarios

Several ship collision scenarios are simulated using the non-linear finite element software LS-DYNA 971. The numerical results are compared with the results of the simplified method using the proposed analytical formula.

The struck ship is a 120,000 DWT shuttle tanker with six double hull tanks, as illustrated in Figure 4.8. The main dimensions are presented in Table 4.1.

Table 4.1: The main dimensions of the struck ship (in m).

Length P.P.	256.60
Breadth moulded	42.50
Depth moulded	22.00
Design draft	15.00
Tank length	32.00
Frame spacing	4.00
Double side width	2.56
Outer shell plating (mm)	17
Horizontal stringer (mm)	12

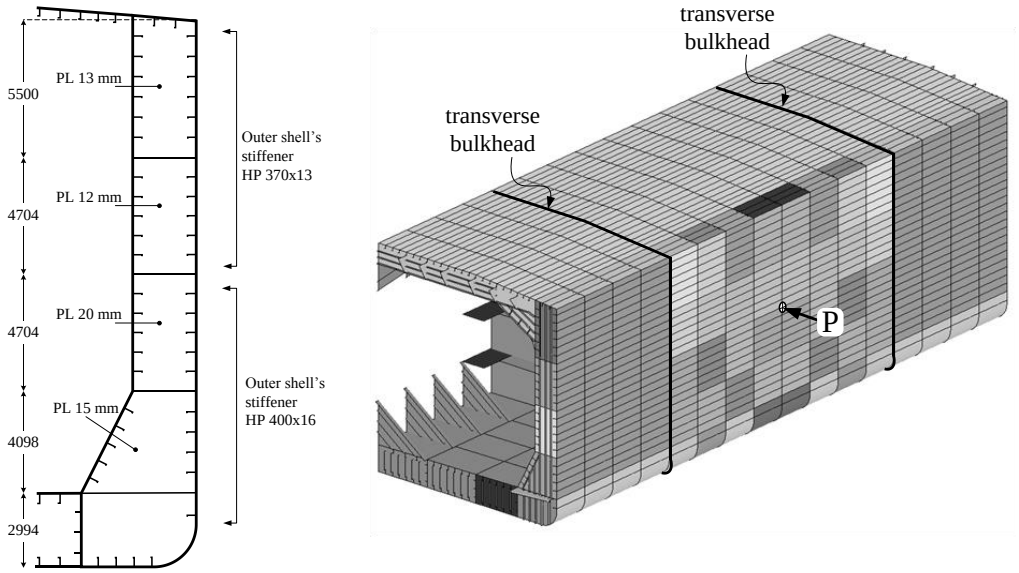

Figure 4.8: The struck ship model: (a) Cross-section, (b) The middle tank of the ship, with two half tanks as the focus of the analysis. Point P is the first contact point with the uppermost point of the striking bow

Two real ships with different bow shapes are used to simulate the striking ships. They are denoted by *the Sharp Bow* and *the Blunt Bow*. The ship with the sharp bow has a displacement of 126,000 DWT, whereas the ship with the blunt bow has a displacement of 148,000 DWT (Figure 4.9 and Figure 4.10). The principal properties of the two bows are listed in Table 4.2.

Table 4.2: The main properties of the striking ships.

	Sharp Bow	Blunt Bow
DWT (ton)	126 000	148 000
Length BPP (m)	251.26	262.00
Breadth moulded (m)	40.79	46.00
Depth moulded (m)	22.20	26.60
Draught (m)	16.76	17.00
web frame 1 to contact point		
Distance (m)	1.24	4.38
Thickness of shell plating (mm)	16 & 18.5	20
web frame 2 to web frame 1		
Distance (m)	3.10	3.20
Thickness of shell plating (mm)	18 & 18.5	20

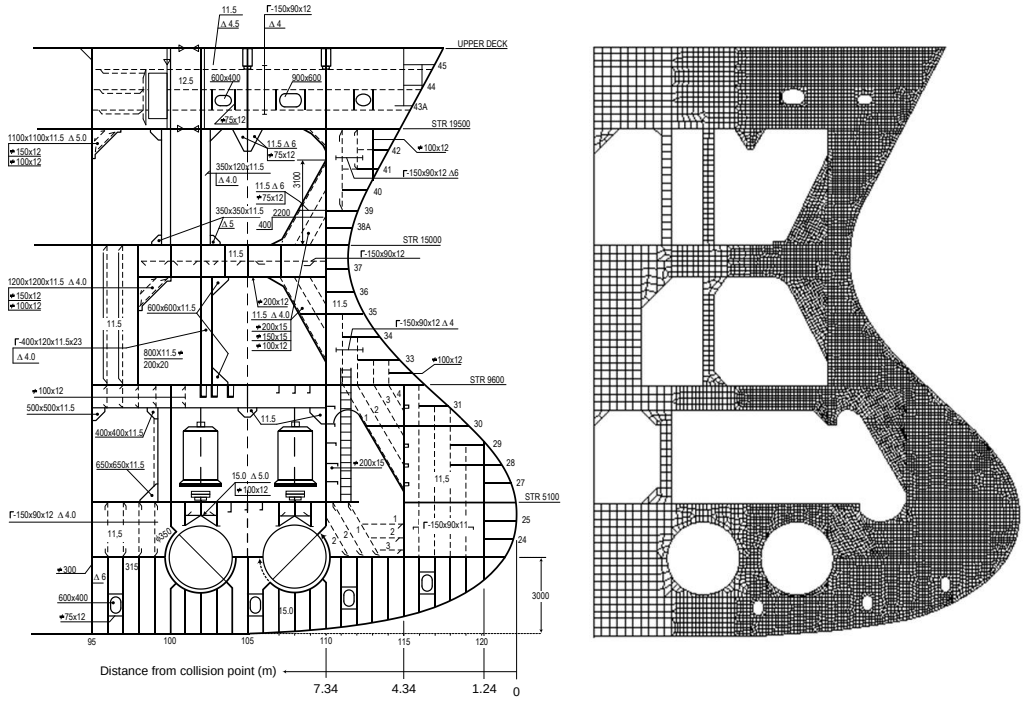

Figure 4.9: The Sharp Bow and its numerical model

The striking ships have a constant velocity of 5 m/s when they hit the struck ship at a right angle. The first contact point is located at the intersection of the web frame and the stringer, as illustrated in Figure 4.8b. For the struck ship, the area in the vicinity of the contact point is focused. If the striking bow is substantially crushed, the investigated area may be expanded. The energy dissipated by the structural elements that are directly involved is considered.

The collision scenarios are described as follows:

a. Collision between a very strong bow and a deformable side of the ship. In this scenario, the side of the ship is hit by a rigid bow, and all energy will be dissipated by the struck side of the ship.
b. Collision between a very strong side of the ship and a deformable bow. A rigid wall is used to mimic the strong side of the ship.
c. Collision between two deformable ships.

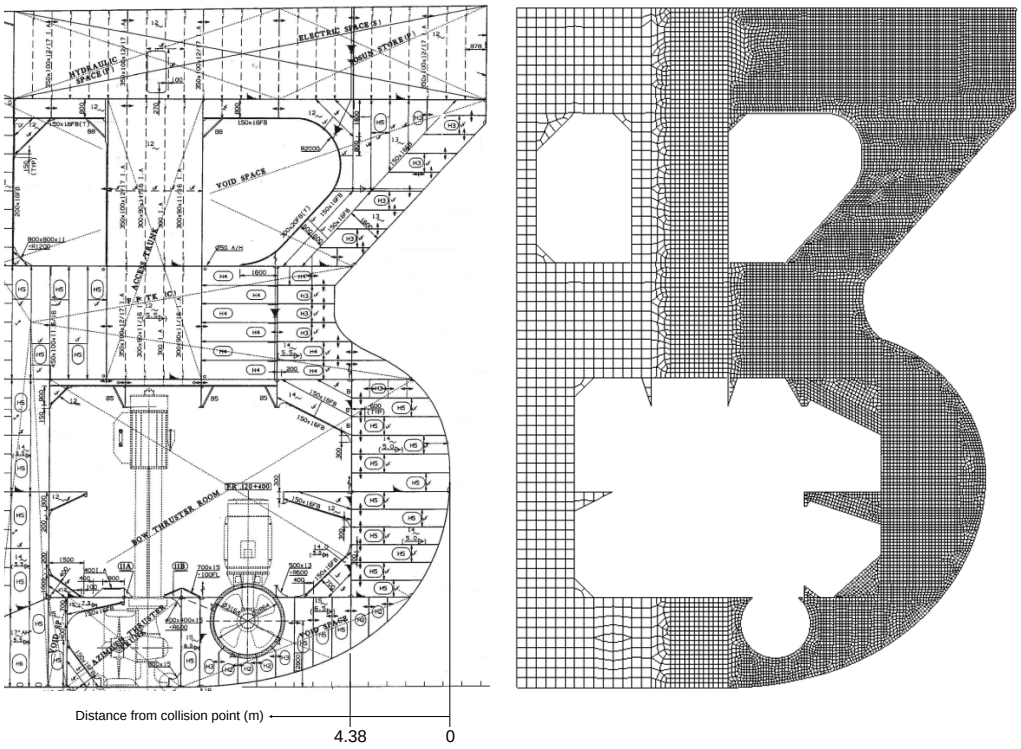

Figure 4.10: The Blunt Bow and its numerical model

4.3.1 Collision between a rigid bow and a deformable side of the ship

(Paper II)

This scenario constitutes an advanced case for indentation of the side of a double hull ship by a rigid cone, as discussed in Section 4.2.1. The shuttle tanker (Figure 4.8) is used to represent the struck ship. The striking structures are the Sharp Bow and the Blunt Bow, which are modelled as rigid and, consequently, absorb no energy. For this purpose, it is sufficient to include only the fore shell plating. For this type of collision, the simplified formula that is used to calculate the resistance is given by Eq. 4.1.

The response of the struck side of the ship is heavily dependent on the resistance of the shell plating. A significant resistance may develop if the shell plating does not experience fracture. The contact between the ramming bow and the struck side may extend over a large area. In that case, many parts of structures contribute to the resistance force. In the opposite case, early fracture may obstruct the distribution of the external load. The force may concentrate in the area in direct contact and cause early failure of the structure. Force-indentation curves for different striking rigid bows are presented in Figure 4.11.

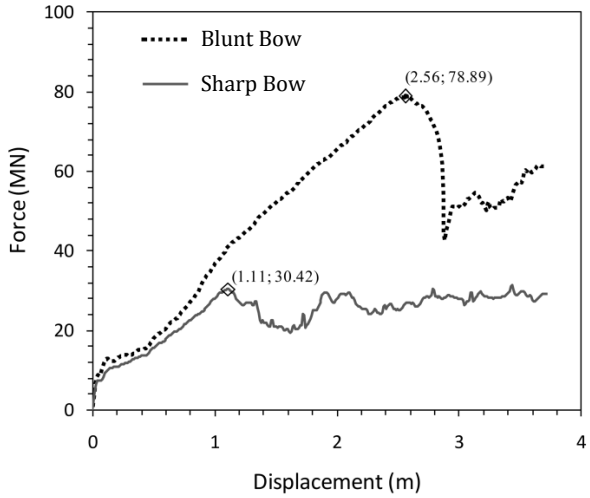

Figure 4.11: Force-displacement curves for different bows. The points indicate failure of the outer shell.

To analyse the deformation pattern and load distribution during penetration, the side of the struck ship is divided into two zones: the main zone, which is composed of the panel near the first contact point between the bow and side of the ship, and the extended zone, which is adjacent to the main zone (Figure 4.12). The main zone is forced to deform during penetration because it is in direct contact with the striking bow. The extended zone may also begin to deform because it cannot support the forces from the main zone or because the striking bow is in direct contact.

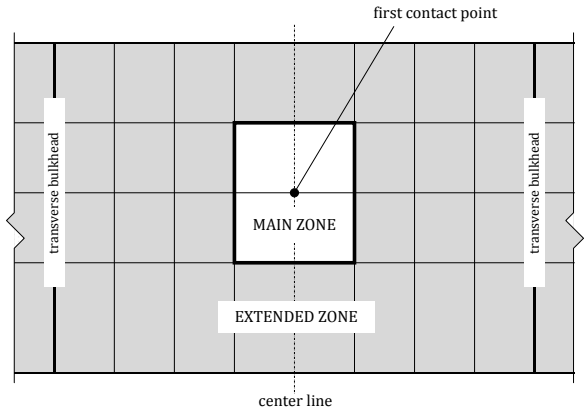

Figure 4.12: Main zone and extended zone of the side of struck ship

For the side of the ship struck by the Sharp Bow, the deformations are limited to the main zone. The extended zone undergoes very small deformations. When fracture occurs in the outer shell, the curvature of the striking bow is too small to create direct contact with the extended zone; thus, the striking bow only penetrates the main zone. When the side of the ship is indented by the Blunt Bow, both the main zone and the extended zone are mobilised prior to rupture of the outer shell. The plastic strain distribution in the outer shell indicates that three transverse frames from the striking point undergo significant plastic strain. Detailed analyses of the deformation patterns and load distributions are included in Appended Paper II.

The estimated resistance and the predicted point of failure for both cases are plotted with the numerical result. For the Sharp Bow case, the analytical curve lies above the numerical curve (Figure 4.13). The displacement at failure is estimated very well, whereas the prediction of the ultimate resistance is 15% greater than the numerical result.

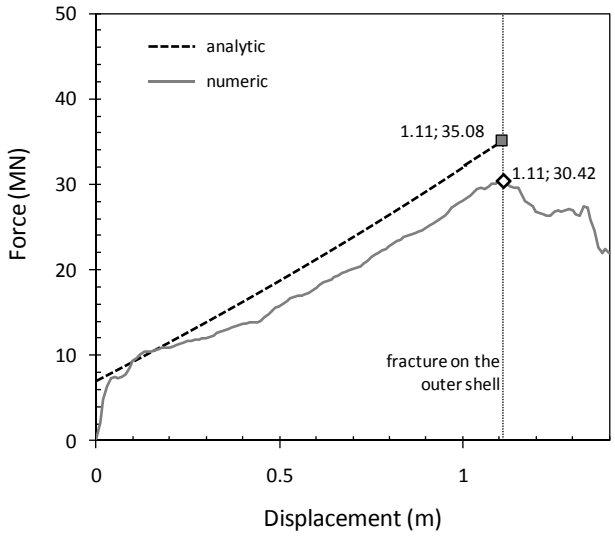

Figure 4.13: Force-displacement curve for the Sharp Bow case

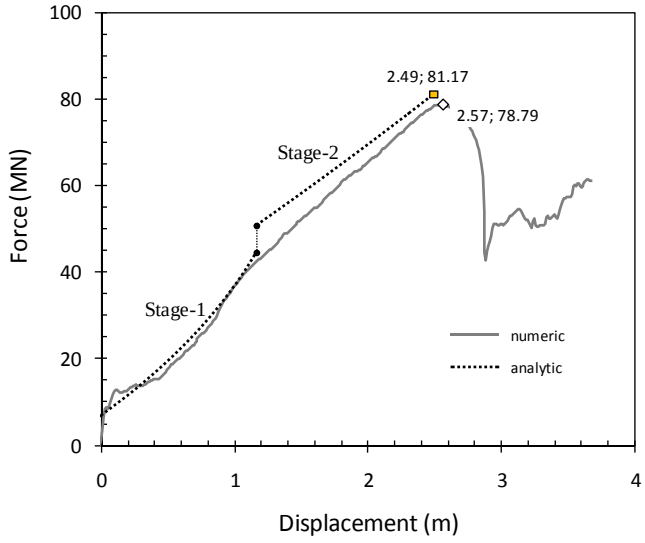

Figure 4.14: Force-displacement curve for the Blunt Bow case

The results for the Blunt Bow case are presented in Figure 4.14. The estimated resistance is defined in two stages: Stage 1 represents the resistance when deformation is in the main zone; and Stage 2 represents the resistance when deformation is continuous in the extended zone. The predicted ultimate resistance at the onset of failure is 81.17 MN, which deviates from the numerical results by less than 3%. The prediction of failure displacement by the analytical formula is less than 3% of the prediction of failure displacement by the numerical results.

4.3.2 Collision between a deformable bow and a rigid wall

(Paper III)

The second scenario serves to verify the accuracy of Eq. 4.3, which is the formula for the bow crushing force. Complete models of the Sharp Bow and the Blunt Bow are subjected to collision with a rigid wall. To reduce computational time, a fine element mesh was only applied to the front part of the bow. A coarse mesh was employed for the remainder of the structure.

The results for the Sharp Bow are presented in Figure 4.15. The average force and internal energy dissipation, as estimated by the simplified method, are in agreement with the numerical results. The error for the internal energy dissipation is in the range of 7–8%.

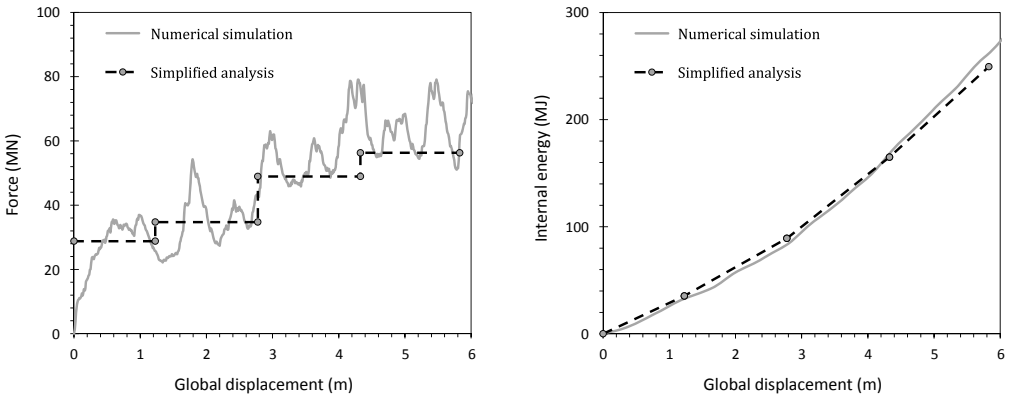

Figure 4.15: Results for the collision of the Sharp Bow with a rigid wall

The resistance and the internal energy curves for the Blunt Bow are shown in Figure 4.16. The results of the simplified method are similar to the results of the numerical simulation, with a difference of 7–10%.

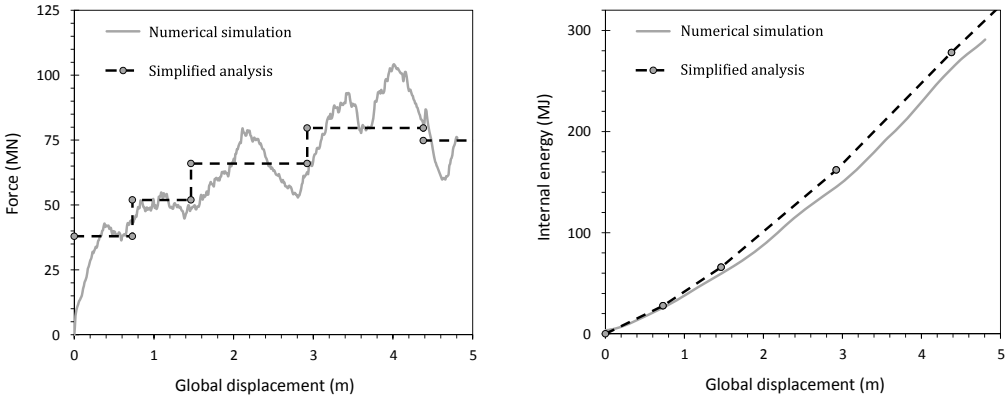

Figure 4.16: Results for the collision of the Blunt Bow with a rigid wall

Detailed calculations of the predicted resistances of the Sharp Bow are provided in Appendix B-3.

4.3.3 Collision between two deformable ships

The shuttle tanker shown in Figure 4.8 is struck by two ships: the Sharp Bow and the Blunt Bow (Figure 4.9 and Figure 4.10). The ships are deformable, and all components are included in the numerical model. The mesh size was sufficiently large to obtain a practical simulation time and sufficiently small to capture the major deformation modes.

A nominal yield stress (σ_y) of 235 MPa was used in most of the simulations, with associated constants k = 670 MPa and n = 0.24. To vary the relative strengths of the striking and the struck ships, analyses were also conducted with augmented yield stresses of σ_y = 355 MPa and σ_y = 460 MPa.

During the collision process, both ships are presumed to undergo crushing. Therefore, defining the indentation and crushing of each ship is essential. The displacement of the contact point of collision is defined as the reference for indentations (Figure 4.17).

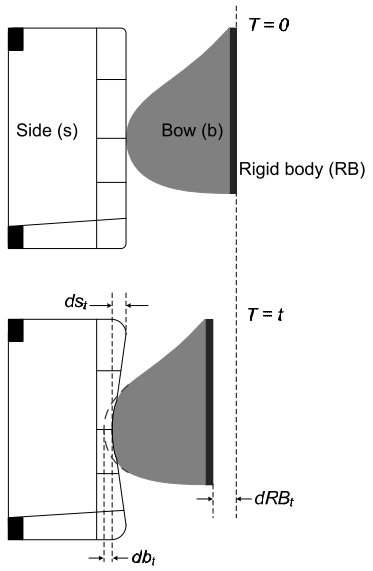

Figure 4.17: Indentation measurement for the deformed collided structures

The collision begins at $T = 0$. At time $T = t$, the rigid body attached on the aft side of the striking bow has moved forward a distance dRB_t, which is equal to the global displacement. If both the bow and the struck side of the ship are deformed and indented, as represented by db_t and ds_t, respectively, a simple relationship between the two indentations is obtained as follows:

$$db_t + ds_t = dRB_t \tag{4.4}$$

If one of the colliding structures is relatively stronger than the other colliding structure, the stronger structure undergoes no deformation. Thus, the indentation on the weaker structure is equal to the global displacement dRB_t.

The Sharp Bow

Figure 4.18 displays the damage process for the collision with the Sharp Bow. In general, the collision process can be categorised into four main stages according to the distribution of damage and the indentations of the striking bow and the struck ship. The deformations of the ships are illustrated in Figure 4.19, and the stages are denoted by numbers 1–4.

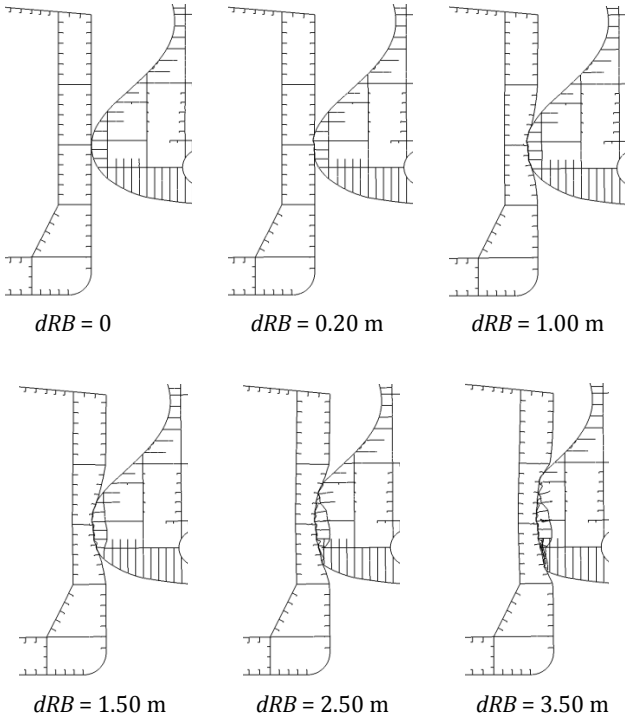

Figure 4.18: Longitudinal section of deformed structures for the Sharp Bow impact

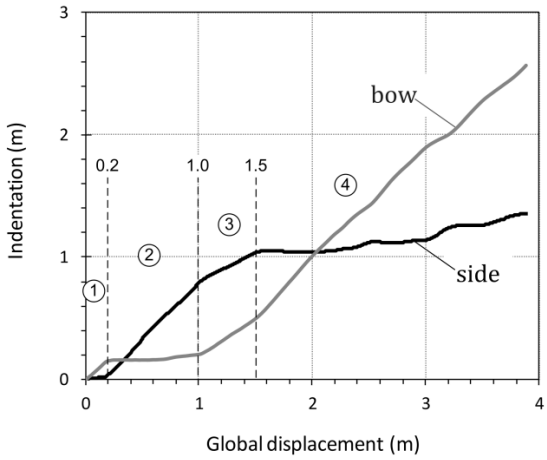

Figure 4.19: Indentation histories for the Sharp Bow case

In this scenario, deformation occurs in both ships, and the damage process switches between the two structures. The stages of indentation can be described as follows:

- Stage 1, small deformation of the bow;
- Stage 2, indentation of the side;
- Stage 3, deformation of both ships; and
- Stage 4, massive crushing on the bow.

The force–indentation histories are displayed in Figure 4.20.

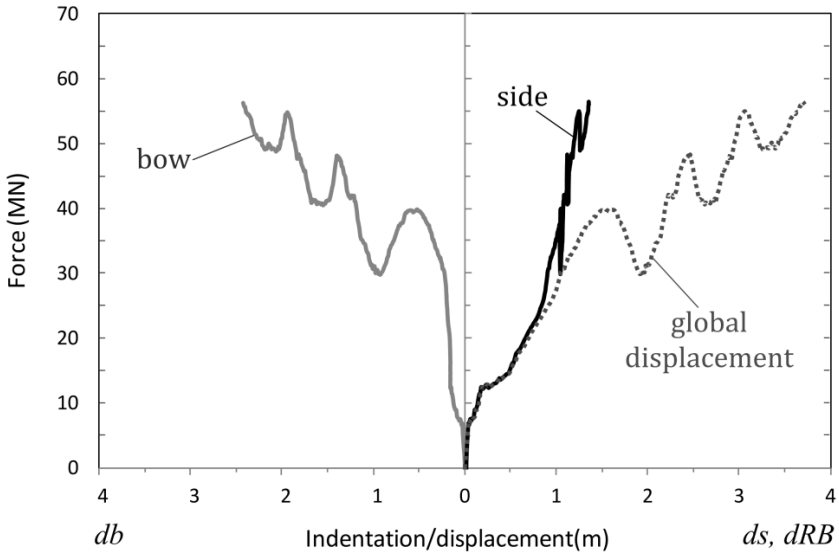

Figure 4.20: Force-deformation histories for the Sharp Bow case

Simulations with a relatively stronger bow are conducted by replacing the actual yield strength of the bow, σ_y = 235 MPa, with a higher yield stress σ_y = 355 and 460 MPa. The new simulations demonstrate that the bow becomes virtually rigid for both yield stresses and penetrates the side with minor damage to the bow.

Another simulation is conducted to obtain a relatively rigid side of the ship by applying a higher yield stress of 460 MPa and by increasing the thicknesses of the shell plating and the web girders to 24 mm. The results of this scenario are used as an example of a collision between a relatively rigid side of a ship and a deformable bow.

The Blunt Bow

The damage process for the Blunt Bow collision is shown in Figure 4.21, and the indentation histories for each ship are presented in Figure 4.22. The bow is much stronger than the side and undergoes minor deformations at the beginning of the collision. The subsequent collision process is dominated by indentations on the side. During subsequent stages of the collision, a global collapse mechanism occurs on the struck side.

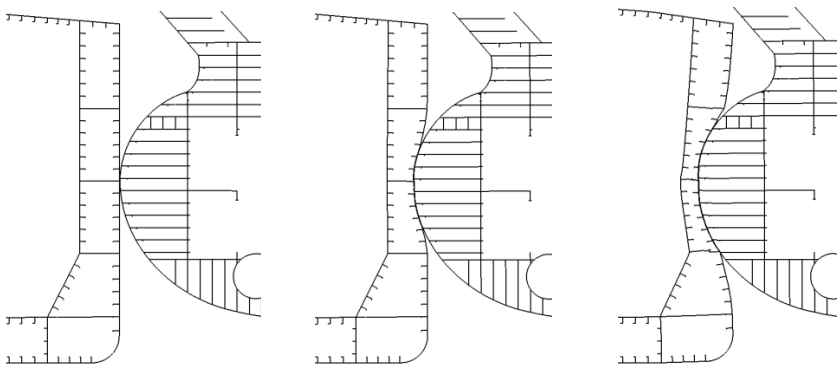

Figure 4.21: Collision process of the Blunt Bow

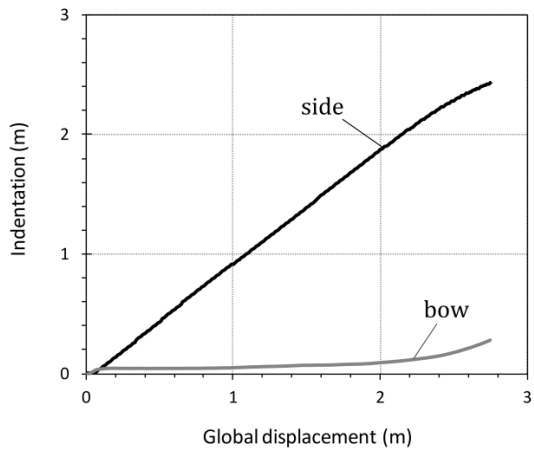

Figure 4.22: Indentation history for the Blunt Bow case

As shown in Figure 4.23, the force-indentation history of the struck side is similar to the force-total displacement history because the striking bow can resist the collision forces and behaves like a rigid body.

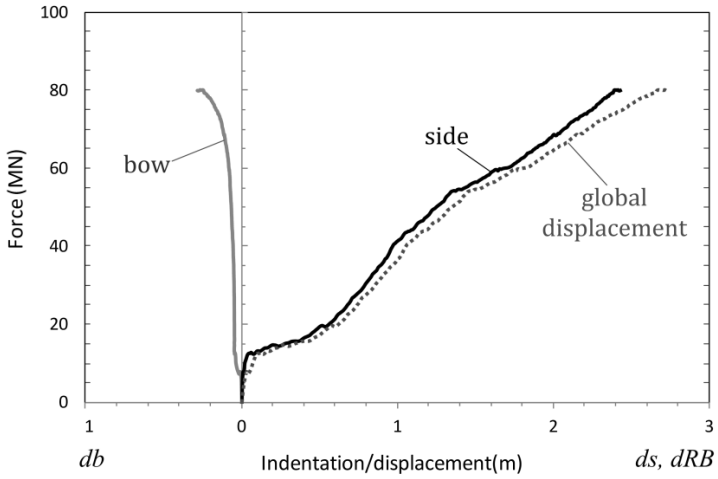

Figure 4.23: Force-indentation history for the Blunt Bow case

A new simulation, in which the yield stress of the side structure is increased to 355 MPa, is conducted to obtain a better balance between the resistance to deformation of the bow and the side. The collision process is similar to the first case with the Sharp Bow, and both structures are damaged.

All numerical simulation results from this section are utilized in application of the simplified analytical method for the ship collision.

4.4 Type of Ship Collision

The collision processes obtained in the numerical simulations can be categorised into three types:

a. Type 1: a relatively rigid bow colliding with a deformable side. This type is denoted as *ductile design* in the NORSOK N-004 (2004) for the design of offshore structures against ship impacts.

The bow suffers a minor indentation. The force indentation of the side is similar to the force global displacement. This type is observed in the simulations with the Blunt Bow and the side with actual yield stresses and with the Sharp Bow with increased yield stresses.

b. Type 2: a relatively rigid side colliding with a deformable bow (*strength design* according to NORSOK N-004 (2004))

   Small deformations occur in the side. The force-deformation of the bow is similar to the force-global displacement. The collision between the Sharp Bow and the side with the increased yield stress resulted in this type of collision.

c. Type 3: a deformable bow colliding with a deformable side (s*hared energy design* according to NORSOK N-004 (2004))

   Both ships are deformed, and the striking and the struck ships deform simultaneously. This category includes the cases in which the damage process may switch between the two structures. The simulation with the Sharp Bow and the side, both with the actual yield stresses, is an example of this collision type.

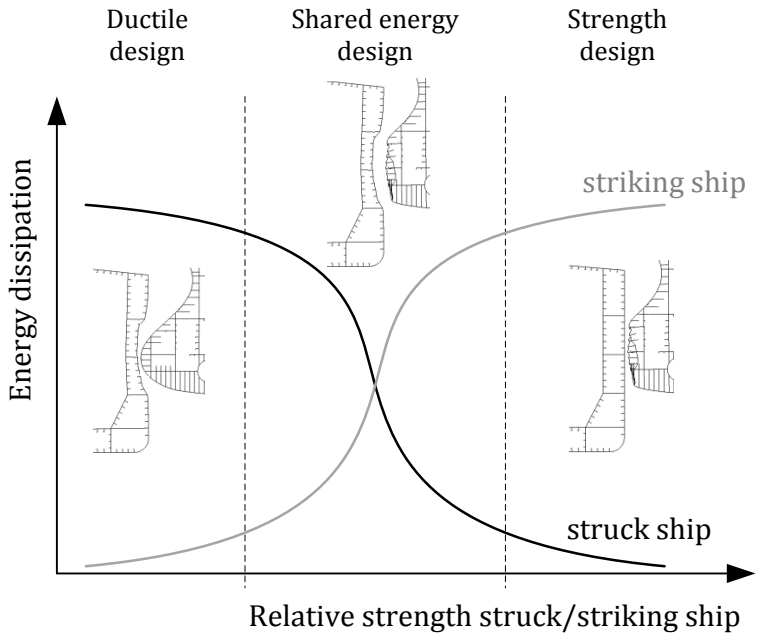

Figure 4.24: Type of ship collision

The types of collision are illustrated in Figure 4.24. The terms in these classifications are concerned with the strength of the side of the ship relative to the strength of the striking bow. In the ductile type, the side of the ship is designed to absorb the majority of the energy during collision when the strong bow hits the side. The energy dissipated by the side will decrease when the relative strength increases. In the strength design, the strong side deforms modestly and dissipates minimal energy. In the shared-energy design, the side and the bow contribute mutually.

4.5 Application of Simplified Analytical Method for Real Ship Collision Scenarios

4.5.1 Determining type of collision

The collision process is characterised by mutually dependent deformations of the colliding ships. The deformation of each ship is determined by the relative resistance to additional deformations. One of the ships may consistently dominate, resulting in Collision Types 1 or 2. Otherwise, if the resistance of the ships switches from one ship to the other during collision, Collision Type 3 is expected.

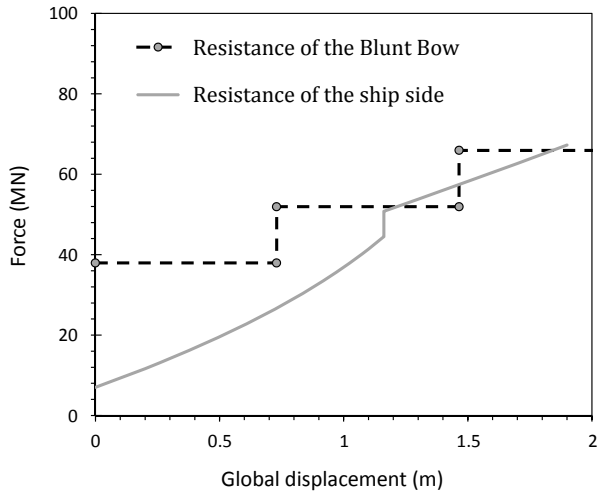

Figure 4.25: Resistance of the Blunt Bow striking a rigid wall and resistance of the side of the ship indented by the rigid Blunt Bow.

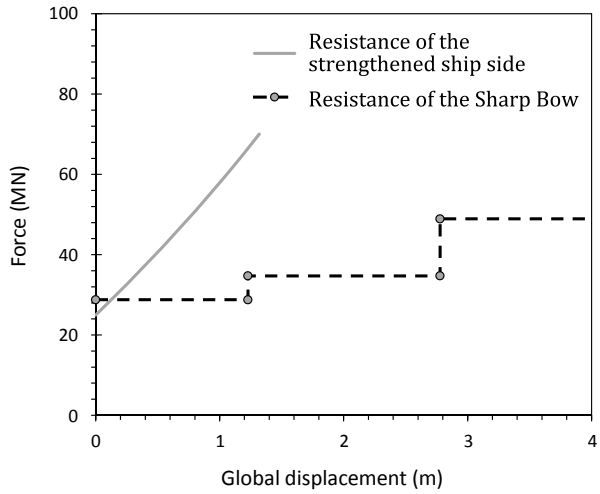

Figure 4.26: Resistance of the Sharp Bow striking a rigid wall and resistance of the strengthened ship side indented by the rigid Sharp Bow

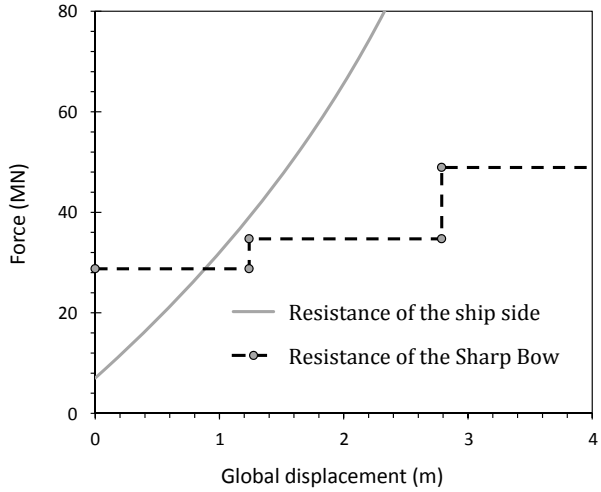

Figure 4.27: Resistance of the Sharp Bow striking a rigid wall and resistance of the ship side subjected by the rigid Sharp Bow

The resistance for each of the ships can be determined by conducting independent simulations of collision for the deformable bow with a rigid wall and the ship side with a rigid bow. The simplified analytical formulae, i.e., Eq. 4.1 and 4.3, are used to calculate the resistance of the deformable ship. The resistances of the collided ships for three different scenarios are presented in Figure 4.25–Figure 4.27.

Domination of the striking bow is shown in Figure 4.25. Until approximately 1.0 m of indentation, the resistance of the side of the ship is distinctly less than the resistance of the bow; deformation will occur on the side of the ship within this range. Due to this deformation, the contact area between the two ships varies and the resistance of the bow increases. The resistance of the bow shifts to a higher level when the ship side is indented by 1.0 m; as a result, the resistance of the bow becomes greater than the resistance of the side of the ship. For further penetration, the side of the ship becomes slightly stronger than the bow, and the bow may deform. However, the deformation of the bow will cease when the contact area increases and the resistance of the bow is greater than the resistance of the side of the ship. In general, the major indentation occurs in the side of the ship. For simplicity, we assume that only the ship side is deformed and that the striking bow exhibits no deformation during the collision process. For this case, the collision is defined as involving a relatively rigid bow and a deformable side of the ship, i.e., Collision Type 1.

The second scenario, in which the resistance of the side of the ship is significantly higher than the resistance of the bow, is illustrated in Figure 4.26. At the beginning of the collision, the resistance of the side of the ship is less than the resistance of the bow. After short indentation, the resistance of the side of the ship becomes higher than the resistance of the bow, which continues for the remainder of the collision. For this case, the collision occurs between a relatively rigid side of the ship and a deformable bow, i.e., Collision Type 2.

In Figure 4.27, the resistances of the ships in the third scenario are presented. The bow has a greater resistance than the side of the ship in the initial stages of collision; thus, the side of the ship is indented. The resistance of the side of the ship increases as a function of indentation; after approximately 0.9 m, it becomes greater than the resistance of the bow. The indentation, which is switched to the striking bow, tends to continue for the remainder of the collision. Because there is a distinct change in resistance dominance between the bow and the side of the ship, this last scenario is categorized as Collision Type 3, i.e., both ships deform.

4.5.2 Simplified Analysis

(Paper III)

An application for each type of collision is presented as follows: Collision Types 1 and 2, in which one of the ships involved is relatively rigid, are simplified to consider the collision of a fully rigid ship with a deformable ship. For Collision Type 3, in which both ships are deformed, a simplified calculation model is used for the striking bow and the struck ship. The virtual experimental data from the FE simulations, which are described in Section 4.3, are used as the reference.

Collision Type 1

The case of collision between the Blunt Bow and the realistic side using FE simulation is presented as an example. In the simplified method, the bow is assumed to be rigid. The side dissipates all collision energy through plastic deformations. The predicted resistance force refers to the results from Figure 4.14 (i.e., the analytic curve) and is compared to the reference curve presented in Figure 4.23 (i.e., the global displacement curve). The results of the comparison are provided in Figure 4.28. The force predicted with the analytical method concurs with the FE results. The outer shell fails at a global displacement of 2.83 m. The displacement predicted by the simplified method is 12% smaller than the displacement predicted by the numerical simulation, i.e., 2.49 m. The resistance, which is predicted well, is 4% larger than the resistance of the numerical simulation. The estimated energy dissipation differs by only 2% from the energy dissipation of the simulation.

Collision Type 2

The collision between the strengthened side and the Sharp Bow with the actual yield stress is used as an example of Collision Type 2. A higher yield stress of 460 MPa and shell plating and web girders with thicknesses of 24 mm are applied to obtain a relatively rigid side of the ship.

The predicted resistance of the bow in Figure 4.15 is compared to the results from the FE simulation. The force-displacement histories from both methods are displayed in Figure 4.29, which shows that the simplified method yields a relatively accurate estimate of the mean crushing force. Regarding the internal energy, the difference between the results of the simplified method and the FE results is 3%.

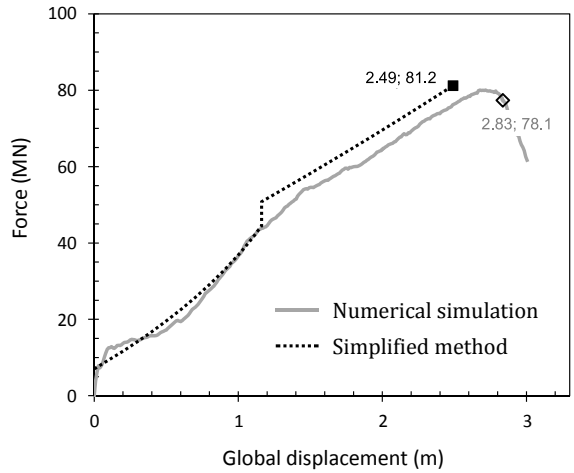

Figure 4.28: Collision Type 1: Comparison of the resistance of the side of the ship from numerical simulation with the resistance of the side of the ship from simplified analysis.

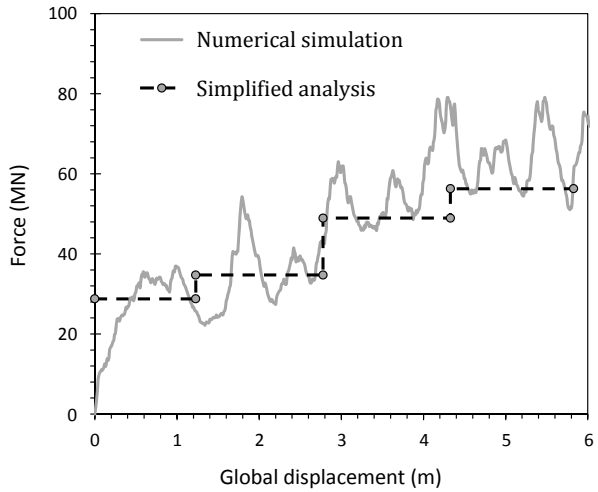

Figure 4.29: Collision Type 2: Comparison of the resistance of the bow from numerical simulation with the resistance of the bow from simplified analysis.

Collision Type 3

In Collision Type 3, deformation occurs in both ships, and the simplified analysis is applied in several stages. In each stage, the deformation is defined as occurring only on the weaker ship. The force-displacement curve of the weaker structure is used as the contact force of the collision.

In the simulation example of collision between the Sharp Bow and the side of the ship, four stages of indentation are identified, as shown in Figure 4.19. A comparison of the resistance of the side with the resistance of the bow, as presented in Figure 4.27, indicates that the side exhibits lower resistance than the resistance of the bow in the initial stage; the side will be indented by the bow. Therefore, a small indentation of the bow, as demonstrated by the simulation in the initial stage, is disregarded in the simplified analysis. The deformation changes from the side to the bow after some indentation, and both ships are deformed during this transition. Because the damage process is very complicated in this stage, we simplify the process by establishing that deformation only occurs on the side when the resistance of the side is lower than the resistance of the bow and that deformation of the bow only occurs when the resistance of the side is greater than the resistance of the bow. The damage processes are identified by two stages of indentation, i.e.,

- the first stage, which is denoted by deformation of the side of the ship
- the second stage, which is denoted by deformation of the bow.

The indentation processes are illustrated in Figure 4.30. For each ship, its indentations are plotted against the global displacement *dRB*.

Initially, the resistance of the side is less than the resistance of the bow, i.e., 28.8 MN. The resistance of the side increases as its indentation increases, and the resistance attains the value 28.8 MN at 0.88 m indentation. In the figure, an inclined line is plotted on the SIDE curve and the horizontal line for the BOW; displacement on the side equals the global displacement.

After 0.88 m, deformation switches to the bow because the resistance of the side becomes greater than the resistance of the bow. As shown in Figure 4.27, the resistance of the bow increases to 34.7 MN if it has been indented for 1.24 m. The indentation can switch back to the side because the resistance of the side is 28.8 MN (using initial bow curvatures). The curvatures change significantly after indentation of the bow. The resistance of the side of the ship is calculated as 35.3 MN for the current indentation and curvatures, which is slightly greater than the resistance of 34.7 MN for the bow. The side is still stronger than the bow, and the deformation process for the bow is continued for the remainder of the collision.

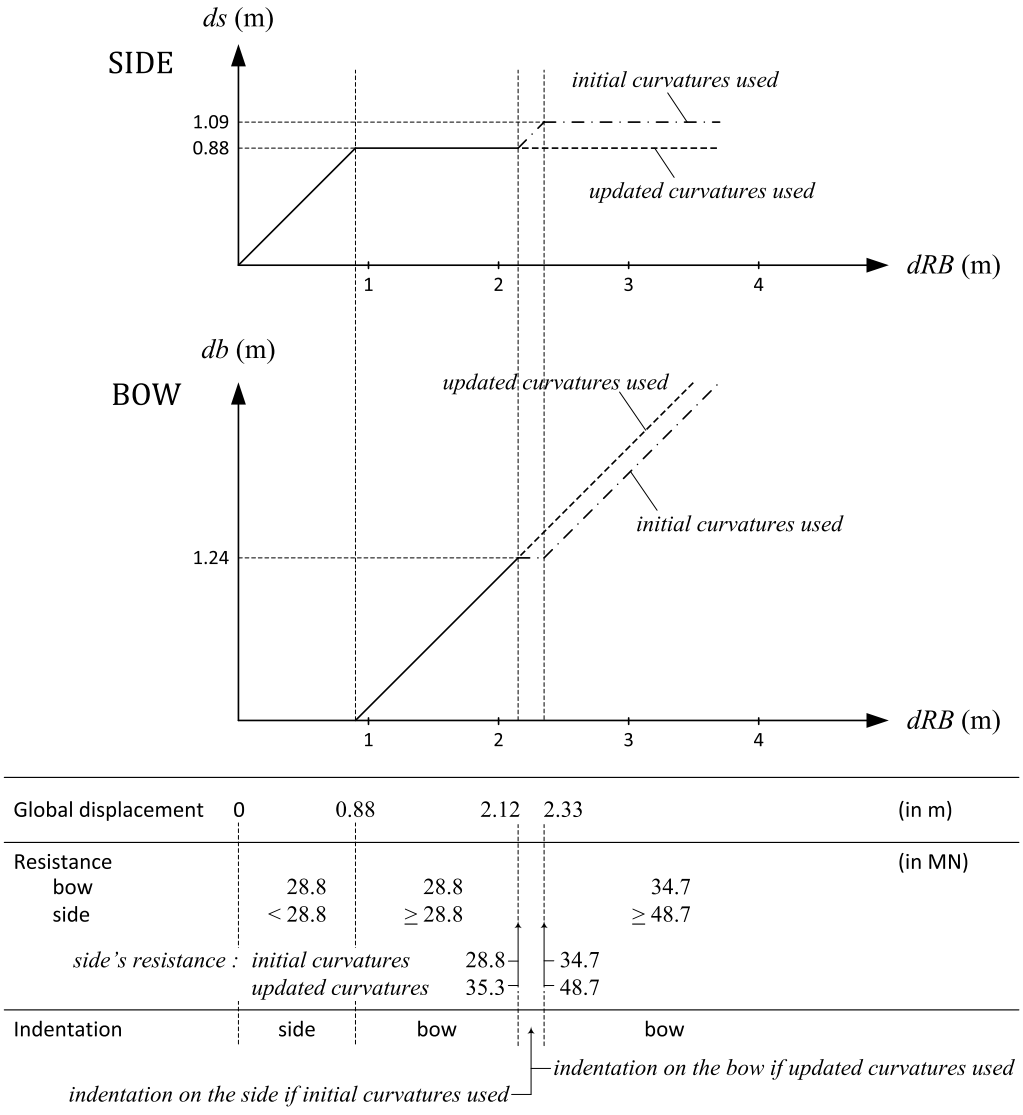

Figure 4.30: Indentation process in Collision Type 3

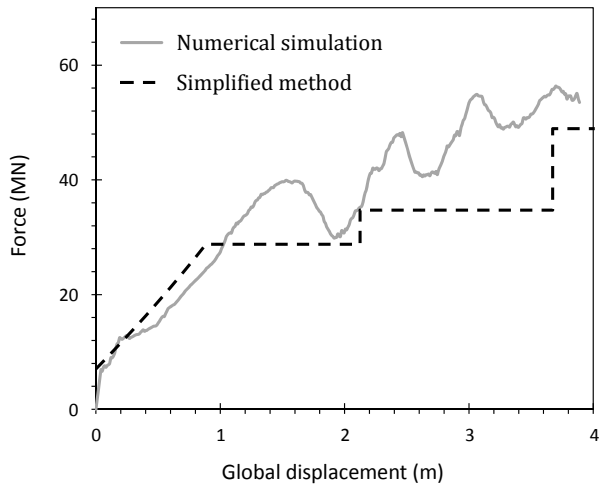

(a)

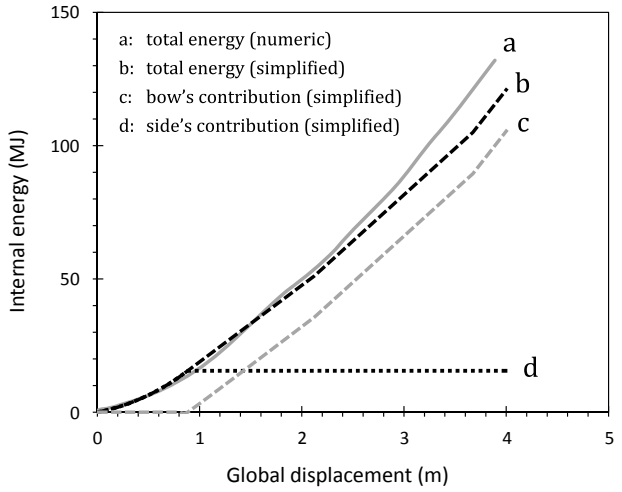

(b)

Figure 4.31: Collision Type 3: a. Force-displacement curve and b. Internal energy curve

The contact force during collision is plotted against the global displacement in Figure 4.31(a). The contact forces for each stage are taken as the minimum values of the resistances of the side and the bow. In the first stage, the contact force is equal to the resistance of the side, and the bow is stronger than the side and exhibits no indentation. The bow begins to deform after the first stage, and the side is rigid, which results in a contact force that is equivalent to the resistance of the bow. In Figure 4.31(b), the internal energies from the numerical simulation and the simplified method are presented. The side contributes to energy dissipation only at the beginning of the collision; it stops after 0.88 m of displacement. After this point, only the bow contributes to energy dissipation. The side does not absorb any energy.

In general, the two methods perform consistently, especially for global displacements of less than 2.00 m. The predictions deviate for larger displacements because the side undergoes some indentations in the numerical simulations. At the end of the simulation, the simplified method underpredicts the energy by approximately 13%.

Chapter 5

Conclusions and Recommendations

5.1 Conclusions

This doctoral thesis focuses on right-angle ship collision analyses using simplified analytical methods and numerical simulations. Assessment of the internal mechanics was conducted on the level of basic elements, the side of the ship and the bow, and for collisions involving real ship configurations through a step-by-step process. The novel with the procedure is that the force of striking ship and the resistance of struck ship are updated after each step, and deformation in the next step is directed to the current weaker structure. By contrast to the procedures commonly used, the damage interaction between the collided ships is taken into account. The research results have been published in selected journals, with a significant focus on the structural analysis of ships during extreme actions.

The main contributions from this study to the field of ship collision analysis can be summarised as follows:

1. Numerical simulations using a nonlinear finite element method were compared with several existing experimental data; good agreement was achieved. The numerical methods were employed in parametric studies on the level of basic elements to the real scale of ship collision. The numerical simulations were considered virtual experiments, and the generated data were utilized as references for the simplified analytical methods.
2. Representative formulae for calculations of the resistances of basic ship structural elements were assessed. Existing expressions for cruciform, T-section, web girder,

and shell plating were collected and compared with available experimental data; the validation was also supported by extensive numerical simulation results. From the validation studies, the most suitable formulae for cruciform, T-section and web girder were selected. The development of a new formula for the shell plating was considered necessary.

3. A thorough study was conducted to determine the effective widths of cruciforms with respect to the energy dissipation. Numerical observations of the internal energy distribution along the cruciform flanges showed that the most significant contribution to the energy dissipation was generated from the vicinity of the intersection with a trivial contribution from areas located further from the junction. The effective width of the cruciform is half of the cruciform height. In the analysis of the resistance of the side of the ship, this effective width was applied. The girder sections between the cruciform were considered to be simple web girders.

4. A new formula to determine the resistance of a shell plating was proposed. The formula was derived for a shell plating subjected to a rigid indenter, whose shape was modelled as an elliptical parabolic surface. The elliptical parabolic surface is more suitable for idealizing the real shape of the striking bow than the existing approach, which models the indenter as a sharp point or with a circular surface. The curvature parameters in the new formula, i.e., α and β, were uniquely defined for different ship side structures. The curvatures should be updated when the bow and/or the side are deformed to ensure appropriate contact force between the colliding ships. A procedure to update the curvatures was proposed.

5. The contribution of the stiffeners to the resistance of their parent elements was examined carefully. The internal energy dissipations obtained from the numerical simulations were used as the basis for the analysis. For the side of the ship, the stiffeners attached to the shell plating should be included in the assessment of the total resistance; the shell plating is assumed to have equivalent thickness using a thickness smearing technique. Any stiffeners on the plate girder, typically longitudinal stiffeners, should be disregarded. For the bow, all of the stiffeners placed on the shell plating, the stringers and the bulkheads should be considered. The stiffeners, the shell plating, and the plate girder constitute numerous T-sections and cruciform, and the total resistance of the bow was calculated based on the resistance of these basic elements.

6. New formulae to calculate the resistance of a side of a ship struck by a rigid bow and the collision of a bow with a rigid wall were proposed. The proposed formulae were examined by applying them to the existing model tests. Agreement was achieved. Numerical simulations were also performed. Consistent results from the experiments, the simplified analytical methods, and the numerical methods provided a strong foundation for the conclusion that numerical simulations can be considered virtual experiments and, thus, represent a reference for simplified analytical methods that are used for quick assessment of more complex structures.

7. Numerical simulations using the nonlinear FEM software LS-DYNA 971 were conducted for several ship collision scenarios. The struck ship was a double hull tanker. Two real ships with different bow shapes, denoted *The Sharp Bow* and *The Blunt Bow*, were used as the striking ships. All ships were in the same size range of 120 000–150 000 DWT. The collision scenarios were as follows: between the ship side and the two rigid bows, between the bows and a rigid wall, and between two deformable ships. For the collisions between a deformable ship and a rigid ship, the predicted resistance of the deformed ship was satisfactory.

8. Three types of ship collision behaviour were identified from the simulations with two deformable ships. They are as follows: Collision Type 1, a relatively rigid bow hitting a deformable ship side, denoted as *ductile design type*; Collision Type 2, a relatively rigid side colliding with a deformable bow, denoted as *strength design type*; and Collision Type 3, a case involving two deformable ships, denoted as *shared energy design type*. All collision types are consistent with the classification NORSOK N-004 (2004), which is employed in the design of offshore structures against accidental ship collision.

9. A new simplified procedure to analyse a right-angle ship-ship collision was proposed. The first step was to determine the resistance of each collided ship and subsequently compare their values. If one resistance was dominant to the other resistance, the analysis was then simplified as Collision Type 1 or Collision Type 2; the stronger ship was assumed to be rigid. Deformation only occurred in the weaker ship, and the contact force was determined by the resistance of this ship.

10. In Collision Type 3, a damage interaction analysis was conducted when the resistances of the two ships were relatively balanced. The damage was limited to the weaker ship, and it could switch between ships during collision. The contact force was based on the resistance of the weaker ship. The curvatures of the bow were updated during the damage interaction analysis due to deformation of the

side or deformation of the bow. The indentations of each ship were plotted against the global displacement. The global force-displacement curve was constructed and compared with the numerical simulations. The force and energy predictions proposed by the simplified analytical methods demonstrated satisfactory results.

5.2 Recommendations

In this section, considerations and recommendations for future studies are presented.

1. Numerical simulations were conducted for only one side of a ship and two different collision types. Additional simulations of ship collisions should be conducted with varying bow shapes, sizes and contact positions. The generated data should be compared with the results of simplified analytical methods.
2. The study was limited to right-angle collisions. The proposed simplified method should be further developed to consider varying collision angles. The models should be supported by sufficient data from numerical simulations.
3. The new resistance formula of the shell plating can be used for similar ship accidents, e.g., ships in a stranding condition. The seafloor topologies by Alsos and Amdahl (2007) and adopted by Nguyen et al (2012) are similar to the bow shape, which is represented by an elliptical parabolic surface. However, Nguyen et al (2012) used the resistance formula by Simonsen (1997b) for a spherical indenter, which was not appropriate for the elliptical parabolic surface. The proposed formula for crushing the shell plating can be employed as an alternative in the evaluation of ship damage during stranding.
4. Proper prediction of the imitation of fracture is crucial, notably for shell platings subjected to significant tensile membrane stresses. Fracture models that consider the effect of strain concentrations near welds and notches and are applied in conjunction with shell finite element analysis remain uncertain. Additional studies should be conducted to develop acceptable fracture models for simplified methods.
5. The resistance of shell plating after fracture is not included in the formulation. The collision process in the present analysis is limited by failure of the outer shell plating. The failure mechanism is similar to the plate-tearing mode suggested by Wang et al 2000a. A formula proposed by Ohtsubo and Wang (1995) is a candidate for calculation of the tearing resistance. It is recommended that future studies focus on the tearing behaviour of shell plating

6. The present study focused mainly on the internal mechanics of ship collisions. The procedures developed in this study may be coupled with external dynamic analyses as tools for rapid assessment of collision damage or implementation using available tools, e.g., SIMCOL (Chen 2000, Brown et al 2000), GRACAT (Friis-Hansen and Simonsen 2002) and an improved MCOL (Sourne 2007).

Bibliography

Abramowicz W., 1994. Crush resistance of 'T' 'Y' and 'X' sections. Joint MIT-Industry Program on Tanker Safety. Report No.24.

Abramowicz W., Jones N., 1984a. Dynamic axial crushing of square tubes. International Journal of Impact Engineering, 2(2):179-208.

Abramowicz W., Jones N., 1984b. Dynamic axial crushing of circular tubes. International Journal of Impact Engineering, 2(3):263–281.

Abramowicz W., Jones N., 1986. Dynamic progressive buckling of circular and square tubes. International Journal of Impact Engineering, 4(4):243–270.

Abramowicz W., Simonsen B.C., 2003. Effect of fracture on crushing of ship structures. Journal of Ship Research, 47(3):194–207.

AGCS, 2012. Safety and Shipping 1912 - 2012, From Titanic to Costa Concordia. Allianz Global Corporate & Specialty (AGCS) and the Seafarers International Research Centre (SIRC) Report.

Akita Y., Kitamura K., 1972. A study on collision by an elastic stem to a side structure of ships. Journal of The Society of Naval Architects of Japan, 131:307-317.

Akita Y., Ando N., Fujita Y., Kitamura K., 1972. Studies on collision-protective structures in nuclear powered ships. Nuclear Engineering and Design, 19(2):365-401

Alsos H.S., 2008. Ship grounding: Analysis of ductile fracture, bottom damage and hull girder response. Ph.D thesis. Department of Marine Technology, Norwegian University of Science and Technology. Trondheim, Norway.

Alsos H.S., Amdahl J., 2007. On the resistance of tanker bottom structures during stranding. Marine Structures, 20(4):218–237.

Alsos H.S., Amdahl J., Hopperstad O.S., 2009. On the resistance to penetration of stiffened plates, part II: numerical analysis. International Journal of Impact Engineering, 36(7):875–887.

Alsos H.S., Hopperstad O.S., Törnqvist R., Amdahl J., 2008. Analytical and numerical analysis of sheet metal instability using a stress based criterion. International Journal of Solids and Structures, 45(7-8):2042–2055.

Amdahl J., 1983. Energi absorption in ship-platform impacts. Ph.D thesis. Department of Marine Technology, Norwegian University of Science and Technology, Trondheim, Norway.

Amdahl J., 1995. Side Collision. 22nd WEGEMT Graduate School. Technical University of Denmark.

Amdahl J., Kavlie D., 1992. Experimental and numerical simulation of double hull stranding. DNV – MIT Workshop on "Mechanics of Ship Collision and Grounding", Oslo, Norway.

Amdahl J., Kavlie D., Johansen A., 1995. Tanker grounding resistance. In: Proceedings of the Sixth International Symposium on Practical Design of Ships and Mobil Units (PRADS'95), Seoul, Korea.

Arita K., Aoki G., 1985. Strength of ship bottom in grounding (1st Report), an investigation into the case of a ship stranded on a rock. Journal of the Society of Naval Architecture of Japan, 158:359-367.

Bao Y., Wierzbicki T., 2004. A comparative study on various ductile crack formation criteria. Transactions of the ASME, 126(3):314-324.

Belytschko T., Liu W.K., Moran B., 2006. Nonlinear finite elements for continua and structures. Chichester (England): JohnWiley & Sons.

Brown A.J., 2002. Collision scenarios and probabilistic collision damage. Marine Structures, 15(4-5):335-364

Brown A.J., Chen D., 2002. Probabilistic method for predicting ship collision damage. Oceanic Engineering International, 6(1):54-65.

Brown A.J., Tikka K., Daidola J.C., Lutzen M., Choe H.C., 2000. Structural design and response in collision and grounding. SNAME - Transactions, 108:447-473

Chang P.Y., Seibold F., Thasanatorn C., 1980. A rational methodology for the prediction of structural response due to collisions of ships. SNAME - Transactions, 88:173-193

Chen D., 2000. Simplified collision model. Master thesis. Department of Ocean Engineering, Virginia Technology, USA.

Choi S.K., Wierzbicki T., Driscoll C.J., 1994. Crushing strength of a web girder. Joint MIT-Industry Project on Tanker Safety. Report No. 23.

Ehlers S., Broekhuijsen J., Alsos H.S., Biehl F., Tabri K., 2008. Simulating the collision response of ship side structures: A failure criteria benchmark study. International Shipbuilding Progress, 55(1):127–144 127.

Endo H., Yamada Y., 2001. The performance of buffer bow structures against collision, 1st report: Collapse strength of the simplified structure models. Journal of the Society of Naval Architecture of Japan, 189:209-217.

Endo H., Yamada Y., Kawano H., 2004. Verification on the effectiveness of buffer bow structure through FEM simulation. In: Proceedings of the 3rd International Conference on Collision and Grounding Proceedings, Izu, Japan.

Endo H., Yamada Y., Kitamura O., Suzuki K., 2002. Model test on the collapse strength of the buffer bow structures. Marine Structures, 15(4–5):365-381.

Fang C., Das P.K., 2005. Survivability and reliability of damaged ships after collision and grounding. Ocean Engineering, 32(3–4):293-307.

Friis-Hansen P, Simonsen BC. 2002. GRACAT: software for grounding and collision risk analysis. Marine Structures. 15(4-5):383–401.

Hagiwara K., Takanabe H., Kawano H., 1983. A proposed method of predicting ship collision damage. International Journal of Impact Engineering, 1(3):257-279.

Hallquist J.O., 2006. LS-DYNA theory manual. Technical report. Livermore, CA: Livermore Software Technology Corporation.

Hallquist J.O., 2007. LS-DYNA keyword user's manual. Technical report. Livermore, CA: Livermore Software Technology Corporation.

Haris S., Amdahl J., 2009. Crushing mechanics of girder intersections in ship collision and grounding. In: Proceedings of the 3rd International Conference on Computational Methods in Marine Engineering (MARINE), Trondheim, Norway.

Haris S., Amdahl J., 2012a. Crushing resistance of a cruciform and its application to ship collision and grounding. Ships and Offshore Structures, 7(2):185-195.

Haris S., Amdahl J., 2012b. An analytical model to assess a ship side during a collision. Ships and Offshore Structures, 7(4):431-448.

Haris S., Amdahl J., 2013. Analysis of ship–ship collision damage accounting for bow and side deformation interaction. Marine Structures, 32:18-48.

Hayduk R.J., Wierzbicki T., 1984. Extensional collapse modes of structural members. Computer Structures, 18(3):447–458.

Hogström P., Ringsberg J.W., Johnson E., 2009. An experimental and numerical study of the effects of length scale and strain state on the necking and fracture behaviours in sheet metals. International Journal of Impact Engineering, 36(10-11):1194-1203.

Hong L., 2009. Simplified analysis and design of ships subjected to collision and grounding. Ph.D thesis. Department of Marine Technology, Norwegian University of Science and Technology, Trondheim, Norway.

Hong L., Amdahl J., 2008. Crushing resistance of web girders in ship collision and grounding. Marine Structures, 21(4):374–401.

ISSC, 2003. Committee V.3: Collision and grounding. 15th International Ship and Offshore Congress, San Diego, Vol.2:71-107.

ISSC, 2006. Committee V.1: Collision and grounding. 16th International Ship and Offshore Congress, Southampton, Vol.2:1-60.

ISSC, 2009. Committee V.1: Damage assessments after accidental events. 17th International Ship and Offshore Congress, Seoul, Vol.2:1-72.

ISSC, 2012. Committee V.1: Damage assessment following accident. 18th International Ship and Offshore Congress, Rostock, Vol.2:1-65.

Ito H., Kondo K., Yoshimura N., Kawashima M., Yamamoto S., 1984. A simplified method to analyse the strength of double hulled structures in collision. Journal of The Society of Naval Architects of Japan, 156:283-296.

Ito H., Kondo K., Yoshimura N., Kawashima M., Yamamoto S., 1985. A simplified method to analyse the strength of double hulled structures in collision (2nd Report). Journal of The Society of Naval Architects of Japan, 158:420-434.

Khan I.A., Das P.K., 2007. Structural safety assessment of damaged ships. In: Proceedings of 26th International Conference on Offshore Mechanics and Arctic Engineering (OMAE), San Diego, California, USA.

Kierkegaard H., 1993. Ship bow response in high energy collisions. Marine Structures, 6(4):359-376.

Kitamura O., 1996. Comparative study on collision resistance of side structure. In: Proceedings of the International Conference on Design and Methodologies for Collision and Grounding Protection of Ships, San Francisco.

Kitamura O., 1997. Comparative study on collision resistance of side structures. Marine Technology, 34(4):293–308.

Kitamura O., 2000. Buffer bow design for the improved safety of ships. IMO [MEPC45/INF.5, Annex].

Kitamura O., 2002. FEM approach to the simulation of collision and grounding damage. Marine Structures, 15(4–5):403-428.

Kuroiwa T., 1993. Dynamic experiments and numerical simulations of failure of ship's side structure. In: Proceedings of the International Conference on Prediction Methodology of Tanker Structural Failure and Consequential Oil Spill, Tokyo, Japan.

Kuroiwa T., 1996. Numerical simulation of actual collision and grounding experiments. In: Proceedings of the International Conference on Design and Methodologies for Collision and Grounding Protection of Ships, San Francisco.

Laubenstein L., Mains C., Jost A., Tagg R., Bjoemeboe N, 2001. Updated probabilistic extents of damage based on actual collision data. In: Proceedings of the 2nd International Conference on Collision and Grounding Proceedings, Copenhagen, Denmark.

Lee J., Kim J., 2001. A comparative study of the double hull structures for the collision energy absorption systems. Journal of Ship and Ocean Technology, 5(4):19-28.

Lee Y.W., Woertz J.C., Wierzbicki T., 2004. Fracture prediction of thin plates under hemi-spherical punch with calibration and experimental verification. International Journal of Mechanical Sciences, 46(5):751–781.

Lehmann E., Peschmann J., 2002. Energy absorption by the steel structure of ships in the event of collisions. Marine Structures, 15(4-5):429–441

Lehmann E., Yu X., 1995. Progressive folding of bulbous bows. In: Proceedings of the Sixth International Symposium on Practical Design of Ships and Mobil Units (PRADS'95), Seoul, Korea.

Lenselink H., Thung K.G., 1992. Numerical simulations of the Dutch-Japanese full-scale ship collision tests. In: Proceedings of the First Conference on Marine Safety and Environment/Ship Production, Delft, Netherlands.

Liu Z., Amdahl J., 2010. A new formulation of the impact mechanics of ship collisions and its application to a ship–iceberg collision. Marine Structures, 23(3):360-384.

Lutzen M, 2001. Ship collision damage. Ph.D thesis. Department of Mechanical Engineering, Technical University of Denmark, Lyngby, Denmark.

Lutzen M., Simonsen B.C., Pedersen P.T., 2000. Rapid prediction of damage to struck and striking vessels in a collision event. In: Ship Structure Symposium on Ship Structures for the New Millennium: Supporting Quality in Shipbuilding, Arlington, VA.

Minorsky V.U., 1959. An analysis of ship collisions with reference to nuclear power plants. Journal of Ship Research, 3(2):1-4.

Moan T., Amdahl J., Wang X.Z., Spencer J., 2003. Risk assessment of FPSOs with emphasis on collision. SNAME - Transactions, 110:307-338.

Naar H., Kujala P., Simonsen B.C., Ludolphy H., 2002. Comparison of the crashworthiness of various bottom and side structures. Marine Structures, 15(4-5):443–460

Nguyen T.H., Garre L., Amdahl J., Leira B.J., 2011. Benchmark study on the assessment ofship damage conditions during stranding. Ships and Offshore Structures, 7(4):431-448.

NORSOK N-004, 2004. Design of Steel Structures, Appendix A, Design against accidental actions.

Ohnishi T., Kawakami H., Yasukawa W., Nagasawa N., 1982. On the ultimate strength of bow construction. Journal of the Society of Naval Architecture of Japan, 151:174-186.

Ohtsubo H., Kawamoto Y., Kuroiwa T., 1994. Experimental and numerical research on ship collision and grounding of oil tankers. Nuclear Engineering and Design, 150 (2-3):385-396.

Ohtsubo H., Wang G., 1995. An upper-bound solution to the problem of plate tearing. Journal of Marine Science and Technology,1:46-51.

Paik J.K., 2007. Practical techniques for finite element modeling to simulate structural crashworthiness in ship collisions and grounding (part II: verification). Ships and Offshore Structures, 2(1):81–85.

Paik J.K., Thayamballi A.K., Wang G. et al., 1999. On the rational design of double hull tanker structures against collision. SNAME - Transactions, 107:323-363.

Paik J.K., Thayamballi A.K., Yang S.H., 1998. Residual strength assessment of ships after collision and grounding. Marine Technology, 35(1):38-54.

Pedersen P.T., Hansen P.F., Nielsen L.P., 1996. Collision risk and damage after collisions. In: Proceedings of the International Conference on the Safety of Passenger RoRo Vessels, RINA, London.

Pedersen P.T., Valsgård S., Olsen D., Spangenberg S., 1993. Ship impacts: bow collisions. International Journal of Impact Engineering, 13(2):163–187.

Pedersen P.T., Zhang S., 1998. On impact mechanics in ship collisions. Marine Structures, 11(10): 429-49.

Pedersen P.T., Zhang S., 2000. Absorbed energy in ship collision and grounding-Revising Minorsky's empirical method. Journal of Ship Research, 44(2):140-54.

Qvist S., Brian K., Schmidt M.H., Madsen S.H., 1995. Ship Collision – Experimental and numerical analysis of double hull models. In: Proceeding of 9th DYMAT Technical Conference Material and Structural Modelling in Collision Research, Munich, Germany.

Rømer H., Petersen H.J.S., Haastrup P., 1995. Marine accidents frequencies – Review and recent empirical results. Journal of Navigation, 48(3):410-424.

Samuelides M.S., 2011. Designing for protection against collision. In: Soares C.G., Garbatov Y., Fonseca N., Teixeira A.P. (Eds.), Marine Technology and Engineering (Vol. 2, pp. 955-977). Leiden: CRC Press, Taylor & Francis Group.

Samuelides M.S., Tabri K., Incecik A., Dimou D., 2008. Scenarios for the assessment of the collision behaviour of ships. International Shipbuilding Progress, 55(1-2):145-162.

Sano A., Muragishi O., Yoshikawa T., Motoi T., Murakami A., 1996. Strength analysis of a new double hull structure for VLCC in collision. In: Proceedings of the International Conference on Design and Methodologies for Collision and Grounding Protection of Ships, San Francisco.

Santosa S.,Wierzbicki T., 1998. On the modeling of crush behavior of closed-cell aluminum foam structure. Journal of the Mechanics and Physics of Solids. 46(4):645–669.

Servis D., Samuelides M., 2006. Implementation of the T-failure criterion in finite element methodologies. Computers and Structures, 84(3-4):196–214.

Shibue T., Abe A., Fujita K., 2001. The effect of the strut arrangement on the energy absorption of side structure in collision. In: Proceedings of the 2nd International Conference on Collision and Grounding Proceedings, Copenhagen, Denmark.

Simonsen B.C., 1997a. Ship grounding on rock – I. theory. Marine Structures, 10(7): 519–562.

Simonsen B.C., 1997b. Mechanics of ship grounding. Ph.D thesis. Department of Naval Architecture and Offshore Engineering, Technical University of Denmark, Lyngby, Denmark.

Simonsen B.C., Lauridsen L.P., 2000. Energy absorption and ductile failure in metal sheets under lateral indentation by a sphere. International Journal of Impact Engineering. 24(10):1017-1039.

Simonsen B.C., Ocakli H., 1999. Experiments and theory on deck and girder crushing. Thin-walled Structures, 34(3):195–216

Simonsen B.C., Törnqvist R., 2004. Experimental and numerical modelling of ductile crack propagation in large-scale shell structures. Marine Structures, 17(1):1-27.

Skjong R., Vanem E., 2004. Damage stability evaluation in collision and grounding of ships. In: Proceedings of the 3rd International Conference on Collision and Grounding Proceedings, Izu, Japan.

Sourne H.L., 2007. A ship collision analysis program based on super-element method coupled with large rotational ship movement analysis tool. In: Proceedings of the 4th International Conference on Collision and Grounding of Ships, Hamburg, Germany; 2007. p. 117-22.

Suhara T., Ando S., et al., 1970. Strength of huge tankers in collision. Journal of the Society of Naval Architecture of Japan (Zosen Kyokai), 128:281-294.

Tagg R., Bartzis P., Papanikolaou A., Spyrou K., and Lutzen M, 2001. Updated vertical extent of collision damage. In: Proceedings of the 2nd International Conference on Collision and Grounding Proceedings, Copenhagen, Denmark.

Tautz I., Schöttelndreyer M., Fricke W., Lehmann E, 2010. Experimental investigations on collision behaviour of bow structures. In: Proceedings of the 5th International Conference on Collision and Grounding of Ships, Espoo, Finland.

Törnqvist R., 2003. Design of crashworthy ship structures. Ph.D thesis. Department of Naval Architecture and Offshore Engineering, Technical University of Denmark. Lyngby, Denmark.

Törnqvist R., Simonsen B.C., 2004. Safety and structural crashworthiness of ship structures - Modelling tools and application in design. In: Proceedings of the 3rd International Conference on Collision and Grounding of Ships, Izu, Japan.

Urban J., 2003. Crushing and fracture of lightweight structures. Ph.D thesis. Department of Mechanical Engineering, Technical University of Denmark. Lyngby, Denmark.

Valsgård S., Jorgensen L., 1983. Evaluation of ship collision damage using a simplified nonlinear finite element procedure. In: Proceedings of the Second International Symposium on Practical Design in Shipbuilding, Tokyo and Seoul.

Vredevelt A.W., Wevers L.J., 1992. Full-scale ship collision tests. In: Proceedings of the First Conference on Marine Safety and Environment/Ship Production, Delft, Netherlands.

Wang G., Arita K., Liu D., 2000a. Behavior of a double hull in a variety of stranding or collision scenarios. Marine Structures, 13(3):147-187.

Wang G., Chen Y., Zhang H., Peng H., 2002. Longitudinal strength of ships with accidental damages. Marine Structures, 15(2):119-138.

Wang G., Chen Y., Zhang H., Shin Y., 2000b. Residual strength of damaged ship hull. In: Ship Structure Symposium on Ship Structures for the New Millennium: Supporting Quality in Shipbuilding, Arlington, VA.

Wang G., Katsuyuki S., Ohtsubo H., 1995. Predicting collision strength of bow structure. In: Proceedings of the International Conference on Technologies for Marine Environment Preservation, Tokyo, Japan.

Wang G., Ohtsubo H., 1997. Deformation of ship plate subjected to very large load. In: Proceedings of the 16th International Conference on Offshore Mechanics and Arctic Engineering (OMAE), vol. 2:173–180. Yokohama, Japan.

Wang G., Ohtsubo H., Arita K., 1998. Large deflection of a rigid-plastic circular plate pressed by a sphere. Journal of Applied Mechanics, 65(2):533–535.

Wierzbicki T., 1995. Concertina tearing of metal plates. International Journal of Solids and Structures, 32(19):2923-2927.

Wierzbicki T., Abramowicz W., 1983. On the crushing mechanics of thin-walled structures. Journal of Applied Mechanics, 50(4a):727–734.

Wierzbicki T., Driscoll J.C., 1995. Crushing damage of web girders under localized static loads. Journal of Constructional Steel Research, 33(3):199–235.

Woisin G., 1979. Design against collision. In: Proceeding of International Symposium on Advances in Marine Technology, Trondheim, Norway.

Wu F., Spong R., Wang G., 2004. Using numerical simulation to analyze ship collision. In: Proceedings of the 3rd International Conference on Collision and Grounding Proceedings, Izu, Japan.

Yamada Y., Endo H., 2004. Collapse strength of the bulbous bow structure in oblique collision. In: Proceedings of the 3rd International Conference on Collision and Grounding Proceedings, Izu, Japan.

Yamada Y., Endo H., 2005. Collapse mechanism of the buffer bow structure on axial crushing. International Journal of Offshore and Polar Engineering, 15(2):147–154.

Yamada Y., Pedersen P., 2007. Simplified analysis tool for ship-ship collision. In: Proceedings of the 17th International Offshore and Polar Engineering Conference (ISOPE), Lisbon, Portugal.

Yamada Y., Pedersen P., 2008. A benchmark study of procedures for analysis of axial crushing of bulbous bows. Marine Structures, 21(2–3):257–93.

Yang P.D.C., Caldwell J.B., 1988. Collision energy absorption of ship's bow structures. International Journal of Impact Engineering, 7(2):181–96.

Zhang S., 1999. The mechanics of ship collisions. Ph.D thesis. Department of Naval Architecture and Offshore Engineering, Technical University of Denmark, Lyngby, Denmark.

Zhang S., Yu Q., Mu Y., 1996. A semi-analytical method of assessing the residual longitudinal strength of damaged ship hull. In: Proceedings of International Offshore and Polar Engineering Conference (ISOPE), Golden, Colorado, USA.

Appendix A

Appended papers

Paper I

Haris S., Amdahl J.

Crushing resistance of a cruciform
and its application to ship collision and grounding

Published in:

Ships and Offshore Structures
Volume 7, Issue 2, pages 185-195, 2012

Ships and Offshore Structures
Vol. 7, No. 2, 2012, 185–195

Taylor & Francis
Taylor & Francis Group

Crushing resistance of a cruciform and its application to ship collision and grounding

Sabril Haris* and Jorgen Amdahl

Department of Marine Technology, Norwegian University of Science and Technology, Trondheim, Norway

(*Received 13 August 2010; final version received 14 October 2010*)

On ships, cruciforms are girder intersections that possess significant resistance to indentation during collision and grounding. Hence, an understanding of the energy that is absorbed by the cruciform during accidents is important. In this study, the crushing resistance of the individual cruciforms is analysed by using a non-linear finite element program LS-DYNA. The results are compared with existing plastic analytical formulas and experimental data in the literature. On the basis of scrutinisation of the internal energy, an effective width for the cruciform is proposed and applied to the ship's girder with realistic boundary conditions and real striking structures. The energy dissipation of the cruciform at the girders' intersection that is subjected to a flat indenter and a large radius rigid bow shows a difference of less than 6% in comparison with the analytical formula for a single cruciform. The deviation increases as the radius of the bow decreases. The material's fracture also has a moderate influence on energy dissipation in the analysed case. By adopting the proposed concept of the cruciform's effective width, the internal energy that is absorbed by the ship structure during the collision and grounding can be estimated accurately using an analytical method.

Keywords: cruciform; girder intersection; crushing resistance; ship collision and grounding; analytical method; non-linear FEM

Introduction

Ship structures typically consist of stiffened plate panels that are supported by a system of transverse and longitudinal girders and stringers. These systems are normally designed in the elastic zone to carry shear and bending moments that are caused by functional and environmental loads. During collision or grounding, girders and stringers are subjected to actions (typically transverse crushing) that are significantly different from the loads for which they were designed. Plate girder intersections in double hulls consist of joints between stringers and transverse frames in the ship's side as well as longitudinal girders and transverse frames in the ship's bottom (Figure 1).

The energy that is absorbed by ship structures during collision and grounding can be estimated by means of plastic analysis methods and by the non-linear finite element method. Both methods have been used by many researchers (Amdahl 1983; Simonsen 1997; Zhang 1999; Tornqvist 2003; Urban 2003; Alsos 2008; Hong 2009). From the crushing assessment point of view, intersections between transverse frames and stringers, which constitute cruciforms, play a significant role in dissipating external energy during these accidents. Therefore, a thorough understanding of the cruciform's crushing resistance is necessary to estimate the total internal energy that is dissipated during collision or grounding.

Existing formulas to determine the mean crushing force of the cruciform have been reviewed by Yamada and Pedersen (2008). Previously, Abramowicz and Simonsen (2003) summarised formulas, which were derived from the kinematic admissible model of an individual cruciform with a fixed bottom support (Figure 2a), to compare their experimental results. However, an individual cruciform with a fixed bottom support that is subjected to a flat indentation does not properly characterise the real condition of a girder intersection during a collision and grounding. In the real case, the cruciform is not supported at the bottom but is supported by the adjacent girders as part of a structural system (Figure 2b). The bottom support replaces the adjacent elements, and a transverse shear mechanism develops. The shape of the indentations also depends on the strength of the striking ship during the collision or the seabed's surface in the case of grounding; hence, the assumption of a flat indentation is not always appropriate.

Another important issue that should be addressed is how to determine the effective width of the cruciform as a part of the girder intersection system. This issue becomes vital because the analytical method's purpose is to accurately subdivide the ship's structure into basic structural components by both estimating the energy dissipation that is associated with the deformation of each component and summing the energies for the complete structure.

*Corresponding author. Email: sabril.haris@ntnu.no

ISSN: 1744-5302 print / 1754-212X online

http://dx.doi.org/10.1080/17445302.2010.536392
http://www.tandfonline.com

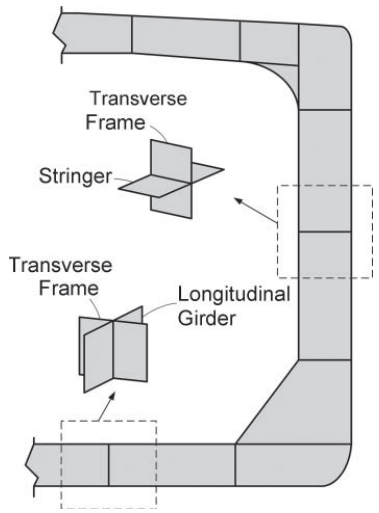

Figure 1. Types of plate girder intersections in double hull amidships.

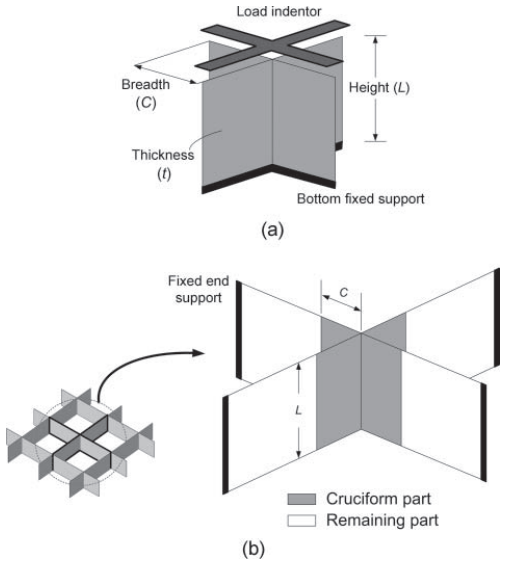

Figure 2. (a) A cruciform supported at the bottom and the definition of its dimensions: breadth (C), height (L) and thickness (t). (b) A typical girder intersection that is taken out of the girder system. The typical girder intersection, which is fixed along the vertical end side, consists of a cruciform and the remaining parts.

In this paper, a plastic analytical method is reviewed in brief, and representative formulas will be selected to provide adequate estimates of the cruciform's mean crushing force, e.g. unique formulas by Amdahl (1983) and Abramowicz (1994). An extensive numerical work that uses a non-linear finite element program LS-DYNA is carried out to produce numerous virtual experimental results. The dimensions of the cruciforms are realistic for typical tanker girder systems; they are varied immediately over and under the existing range to cover adequate data. Experimental data are also presented to support numerical results and analytical formulas.

The internal energy dissipated by the girder intersection is then scrutinised to determine the significant part of the energy dissipation that can be considered to be associated with the cruciform's deformation. The results of the individual cruciforms are applied to real ship girders with realistic boundary conditions and also to real striking structures. The finite element results for both the individual cruciform and the girder intersection are compared with existing analytical formulas.

Plastic analysis method and review of the existing analytical formula

In the analytical methods, the internal energy is assessed on the basis of a kinematically admissible displacement field for the deformed structure. During the crushing process, the material is assumed to be rigid, perfectly plastic with a constant flow stress σ_0; the elastic energy is disregarded. Various assumptions for the flow stress have been used for different types of materials and structures (Hayduk and Wierzbicki 1984; Yang and Caldwell 1988; Abramowicz and Simonsen 2003; Hong and Amdahl 2008; Yamada and Pedersen 2008). One of the most practical formulations, which has been widely used for steel material, is adopted in this study:

$$\sigma_0 = \frac{\sigma_y + \sigma_u}{2}, \tag{1}$$

where σ_y and σ_u are the yield and ultimate engineering stresses, respectively. Equation (1) is a simple formula and easy to apply when information about the material properties is limited.

Most authors split internal energy dissipation in cruciforms into two categories: the bending energy along the horizontal stationary hinge lines and the energy dissipated around the intersecting zone, which is the so-called *junction area*. Wierzbicki and Abramowicz (1983) considered the internal energy in the junction area for the angle section to consist of two types: the energy rolling over moving hinge lines and the energy dissipated on the toroidal surface at the meeting side of the angle section. These definitions have been adopted by many researchers. Some cruciform deformation models are constituted by the angle section and two other flanges with a specific definition of the internal energy. However, the kinematical deformation model

for the rest of the flanges generally follows the same idea, where the deformed junction area is treated as a triangle (Amdahl 1983; Hayduk and Wierzbicki 1984; Santosa and Wierzbicki 1998; Yang and Caldwell 1988; Abramowicz and Simonsen 2003).

The analytical formula for the crushing mechanics of a cruciform is frequently presented in terms of the mean crushing force (P_m), which is derived through equilibrium of the external and internal energy dissipation rates as follows:

$$P_m = \frac{E_t}{\lambda \cdot 2H}, \tag{2}$$

where P_m, E_t, λ and $2H$ are the mean crushing force, the total internal energy that is dissipated during one plastic folding, the effective crushing factor and the folding depth, respectively. By collecting existing formulas from previous studies, it is concluded that all of the formulas are located in a range in which the 'lower' limit is given by Abramowicz (1994) for his *mix folding mode-II* and the 'upper' one by Amdahl (1983) for his *symmetric mode*. In the intermediate range, there exist many closed formulas, but the formula proposed by Hayduk and Wierzbicki (1984) for their *Mode-II* is preferred.

The formulas are listed below:

$$\text{The 'lower' limit: } \frac{P_m}{M_0} = \frac{19.67}{\lambda}\left(\frac{C}{t}\right)^{0.445}, \tag{3}$$

$$\text{The intermediate: } \frac{P_m}{M_0} = \frac{20.05}{\lambda}\left(\frac{C}{t}\right)^{1/2}, \tag{4}$$

$$\text{The 'upper' limit: } \frac{P_m}{M_0} = \frac{1}{\lambda}\left[22.78\left(\frac{C}{t}\right)^{1/2} + \pi^2\right], \tag{5}$$

where M_0 is the plastic bending moment per unit width, whereas C and t are the breadth and thickness of the cruciform, respectively. Furthermore, the plastic bending moment is defined as follows:

$$M_0 = \frac{\sigma_0 t^2}{4}. \tag{6}$$

Another issue that should be addressed in the crushing analysis is the effective crushing distance. In reality, the structures cannot be fully compressed. On the basis of the experimental results, Wierzbicki (1983) estimated the crushing distance to be 2/3 of the panel's height. Abramowicz (1983) performed an analytical calculation to define the effective crushing factor for axially crushed box columns and found that the effective crushing factors are 0.70 and 0.60 for the box column without and with stiffeners, respectively. While deriving the cruciform's mean crushing force, Abramowicz (1994) used a factor of 0.73 for the effective crushing factor. Amdahl (1983) defined the effective crushing distance as a function of the plate thickness and the curvature of the folded plate. Abramowicz and Jones (1984) used an effective crushing factor of 0.73 for the symmetric collapse mode and 0.77 for both the extensional collapse mode and the asymmetric mixed collapse mode. Zhang et al. (2009) reported a series of axially crushed square tubes with effective crushing factors in the range of 0.728–0.744. Overall, previous data for the effective crushing factor are in the range 0.67–0.77. In this paper, a value of $\lambda = 0.73$ is used.

Crushing analysis of the cruciform

Modelling

Numerical simulations are conducted by using finite element software LS-DYNA (Hallquist 2006, 2007) and are considered to be *virtual experiments*. To build confidence in the numerical simulations, experimental and numerical results from a cruciform test conducted by Urban (2003) are utilised for verification. The height of the specimen was 340 mm, the width was 140 mm and the thickness was 8 mm. The material was aluminium 5083-T2. Material properties and imperfections are modelled as specified in the thesis. Figure 3 shows that the force–displacement curve obtained by the present analysis virtually coincides with that of Urban. The folding pattern is very similar, and fracture is initiated at the same place (Figure 4).

The single cruciform is modelled as shown in Figure 5. The cruciform is fixed at the bottom; however, the top is free to displace axially but is fixed against rotation and lateral deformation. The load is applied by a flat rigid indenter that moves downward with a constant speed ramped up in 0.01 sec.

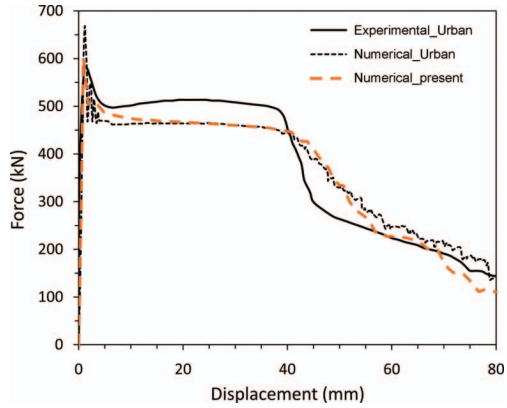

Figure 3. Force–displacement curve from tests and simulation (Urban 2003) and present analysis. (This figure is available in colour online.)

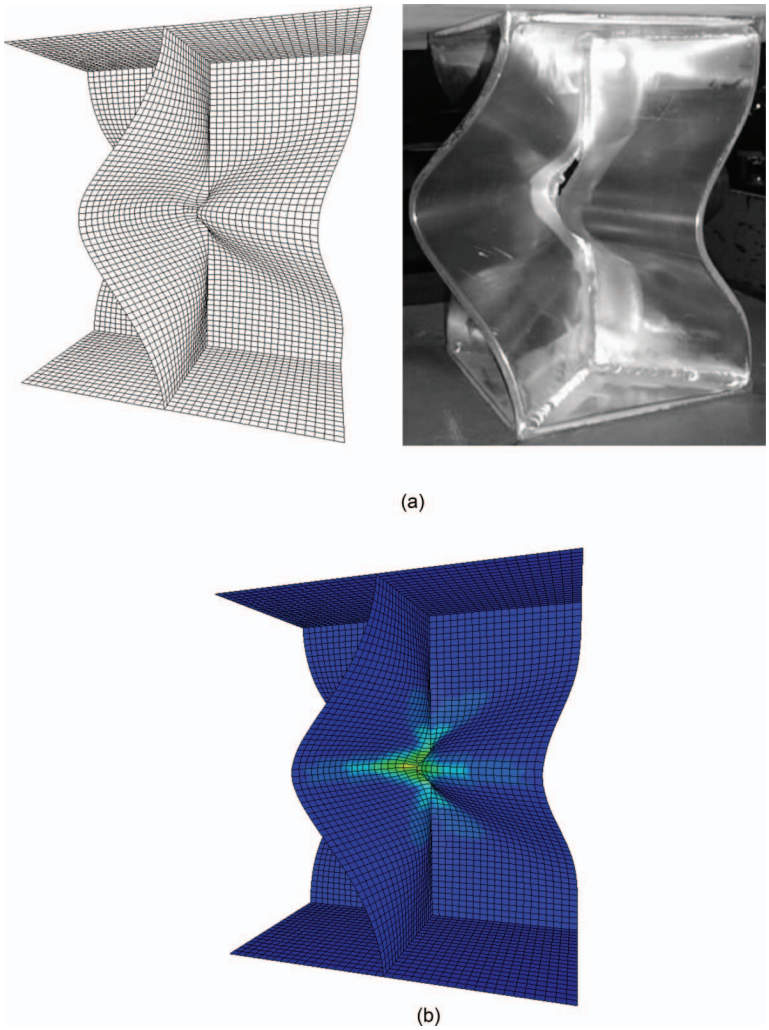

Figure 4. Partly crushed configuration of aluminium cruciform: (a) simulation and test by Urban (2003) and (b) present analysis. (This figure is available in colour online.)

The material behaviour is represented by *power-law plasticity,* which is defined by the following formula:

$$\sigma = k\left(\varepsilon_{yp} + \varepsilon^{p}\right)^{n} \tag{7}$$

where $\varepsilon_{yp} = (\sigma_y / E)^{1/n}$ is the elastic strain at the yield point and ε^p is the effective plastic strain. The material constants that are used in this study refer to data from Alsos et al. (2009). The values in the formula are given as $k = 740$ and $n = 0.24$, while the elastic modulus and yield stress are $E = 207{,}000$ MPa and $\sigma_y = 285$ MPa, respectively. The effect of fracture is disregarded; thus, there is no limit to the strain.

Mesh size sensitivity

There is a trade-off associated with the size of the element mesh (l_e). The mesh should be as coarse as possible to reduce the computation time but not so coarse that the fracture prediction and folding pattern is severely hampered.

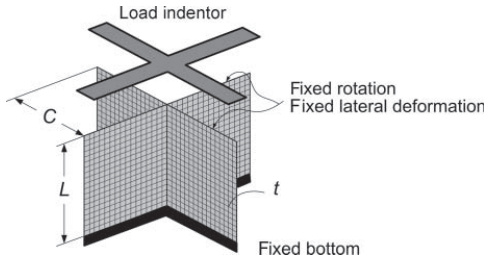

Figure 5. Model of the single cruciform.

Use of excessively fine meshes should be avoided if the effect on the resistance and energy dissipation is marginal. Paik (2007) recommended a practical technique to determine the element size that was based on the folding length, i.e. by using eight elements for one half-fold (H). Alsos and Amdahl (2007) used the element size ratio of about $l_e/t = 10$ which resulted in a consistent internal energy. Furthermore, Tornqvist (2003) suggested that the element length to thickness ratio should be around five to capture the stress and strain fields accurately.

A cruciform with an initial breadth $C = 1200$ mm and height $L = 2400$ mm is selected for the element mesh sensitivity test, while two plate thicknesses $t = 12$ and 16 mm are applied. The results are presented in the internal energy–displacement curves in Figure 6. For the 12 mm plate thickness, consistency is attained for a mesh size of 40–120 mm ($l_e/t = 3.3$–10). Approximately identical results are obtained for the 40–150 mm mesh size ($l_e/t = 2.5$–9.4) and 16 mm plate thickness; only the results for the 300 mm mesh size diverge significantly.

Ideally, the size/thickness ratio should be less than about five, which is in agreement with Tornqvist's suggestion; however, the results are considered to be reasonably consistent up to $l_e/t \sim 10$ because there is no significant variation in the results in comparison with the computational costs. For illustration, using a 40 mm mesh size demands four times more processing time than the 60 mm mesh size. This issue is important to be considered when non-linear finite element analyses are conducted for a huge structural model of a ship–ship collision, in which several million elements may be involved.

The formula that was proposed by Hayduk and Wierzbicki (1984) to determine the folding height (i.e. $H = 0.983\sqrt[3]{t(2C)^2}$) yields Paik's recommended element size of ~50 mm for the 12 mm thickness and ~54 mm for the 16 mm thickness. These recommendations are within the range of the numerical results. However, owing to simplification and the small size of the structures in this study, an element size of $l_e = 50$ or 60 mm is used to ensure mesh-size-independent results.

Mean crushing force

From the numerical analyses, the cruciform initially behaves as a column before it buckles and starts to fold. This phenomenon is observed by the typical force–displacement curve that starts with a high-impact force and then drops dramatically to a somewhat constant force or a moderate fluctuation curve (Figure 7a). In terms of internal energy dissipation, the curve increases rapidly in the beginning and then increases steadily for the crushing range (Figure 7b).

The initial buckling level depends on several factors, such as initial imperfections, welding residual stresses and

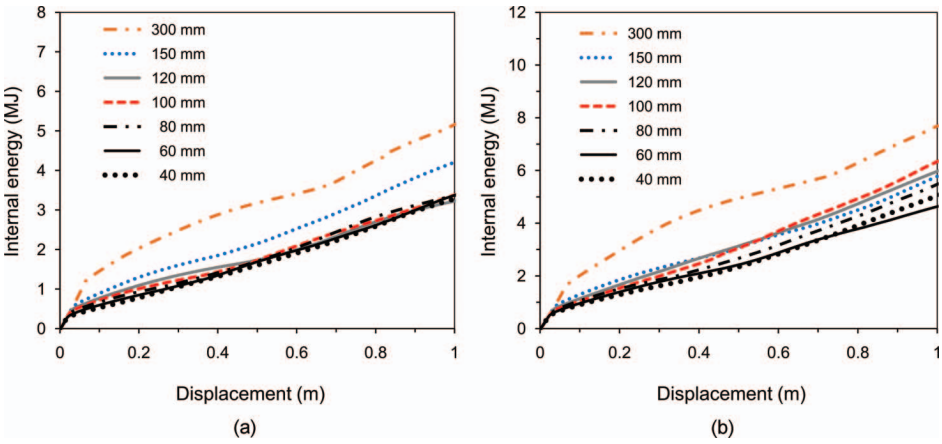

Figure 6. Internal energy for different mesh sizes: plate thickness of (a) $t = 12$ mm and (b) 16 mm. (This figure is available in colour online.)

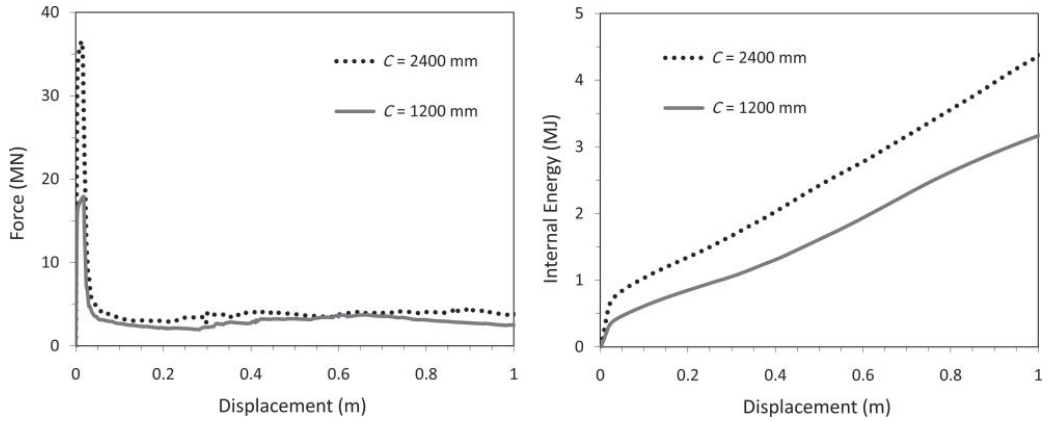

Figure 7. Force–displacement curve and the internal energy of the cruciform for a height and thickness of 2400 mm and 12 mm, respectively.

uncertain factors. Fortunately, the buckling phase has an insignificant effect on the average crushing force because it occurs in a very short period. Hence, the mean crushing force is only taken into account after the initial buckling phase, when the folding process is formally started; the definition for this mean crushing force is equivalent to the gradient of the internal energy curve in the steady state phase.

The numerical results, analytical formulas and experimental data are presented for the mean crushing force. For this purpose, Equations (3)–(5) are utilised, and a number of experimental data from Amdahl (1983), Abramowicz (1994) and Abramowicz and Simonsen (2003) are plotted. As shown in Figure 8, a good agreement is achieved. Most of the points are located between the intermediate and the lower limit formulas. For smaller breadth–thickness ratios (C/t), e.g. less than 100, the data are very close to the intermediate formula. For large ratios, the numerical results lie fairly close to the lower limit.

Thus, the numerical results agree with the experimental data and the analytical formula. The intermediate formula [Equation (4)] with an effective crushing factor λ of 0.73 is considered to be a representative analytical formula to estimate the mean crushing force of the cruciform; in the real case, the breadth–thickness ratio of the cruciform are usually less than 100.

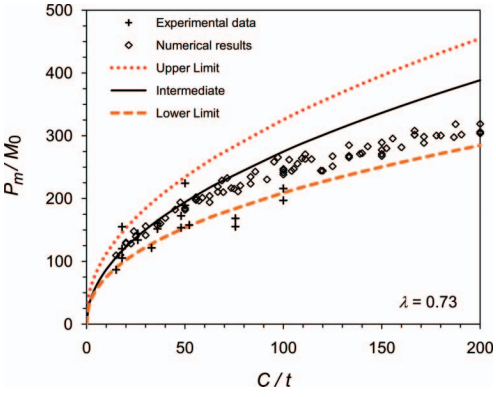

Figure 8. Plotting the numerical results, experimental data and the existing analytical formula. (This figure is available in colour online.)

Crushing analysis of the girder intersection

The objective of this task is to investigate the application of the individual cruciform model to estimate the energy dissipation in a girder intersection, i.e. to identify the effective width of the cruciform. Energy dissipation in the remaining parts of the girder is not addressed.

Effective width of the cruciform

The effective width of a cruciform is determined by analysing the internal energy distribution. The analysis is

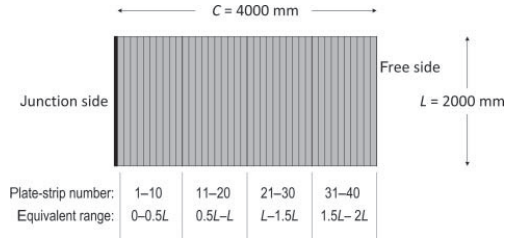

Figure 9. Partition of the cruciform.

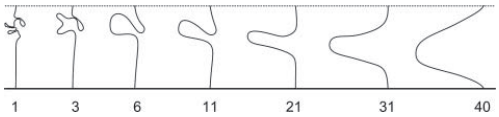

Figure 10. Deformation of cross section at an indentation of 1.0 m. The numbers refer to the plate strip number.

conducted for a single cruciform, which is divided into a number of plate strips, to determine the distribution of the internal energy over the flange's breadth. A cruciform with a 2000 mm height, 15 mm thickness and 4000 mm breadth is split into 40 equal width plate strips, i.e. 100 mm width. The numbering runs from the junction to the free end, as shown in Figure 9 for one flange of the cruciform.

The deformation patterns of the selected cross sections of the cruciform are shown in Figure 10. Apparently, plate strip number 1 crumples in more folds than the other ones because the junction side is constrained during the crushing process. Both the membrane and bending energies develop during this folding process; hence, more energy is dissipated. For the next plate strips, the number of folds decreases. For the end plate strip, only one large wave exists; in this deformation process, the bending energy is dominant.

The different folding patterns cause a variation in the internal energy dissipation; the gradient of the internal energy curve in the steady state is presented in Figure 11. A significant contribution to the internal energy comes from the first plate strip, which is located at the junction. The contribution decreases asymptotically for the next plate strips and tends to be constant for those located far from the junction. Other simulations with longer cruciform breadths show the same tendency; the plate strips far away from the junction have trivial contributions to the total internal energy.

In the analytical models, the area in the vicinity of the junction experiences axial and shear straining; thus, significant membrane energy is involved, which is in accordance

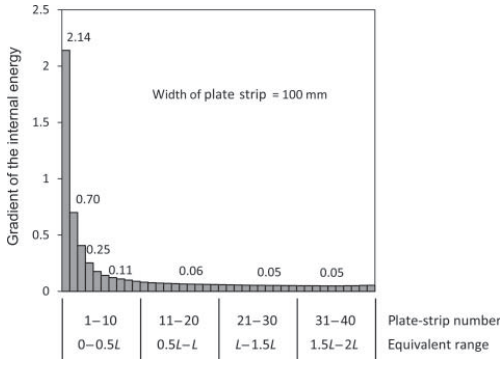

Figure 11. Distribution of the internal energy in the cruciform.

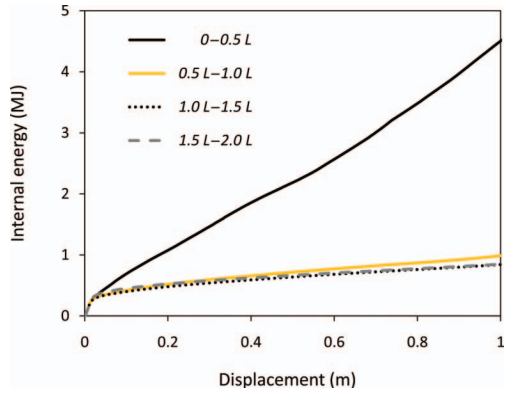

Figure 12. Internal energy for the parts of the cruciform. (This figure is available in colour online.)

with the numerical results. However, in the analytical models, bending occurs uniformly along the width of the cruciform, which indicates that the number of folds is similar for the whole cross section of the deformed cruciform. Thus, regarding the number and pattern of the folds, the analytical model does not capture the actual deformation mode entirely and correctly.

The analytical formula should comply with the numerical results. For this purpose, the energy dissipation for the groups of plate strips is shown in Figure 12. The internal energy that is absorbed by the plate strips within the range of 0–0.5L is clearly dominant, whereas the energy dissipation for the other groups is similar or much smaller.

On the basis of the results shown in Figures 11 and 12, the cruciform has a certain width that efficiently dissipates

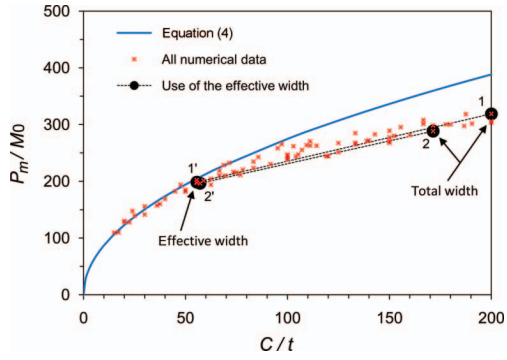

Figure 13. The effect of using the effective width for the cruciform ($C_{eff} = 0.5L$). The original dimensions for point 1 are $t = 18$, $C = 3600$ and $L = 2000$ mm, and point 2 are $t = 21$, $C = 3600$ and $L = 2400$ mm. (This figure is available in colour online.)

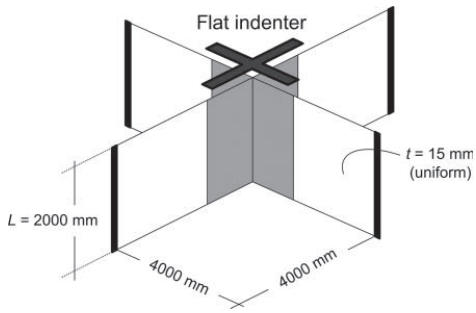

Figure 14. Model for the girder intersection that is subjected to a flat indenter.

most of the strain energy. The effective width may be taken as half of the cruciform's height:

$$C_{eff} = 0.5L. \tag{8}$$

Various girder geometries have been analysed: three different heights, $L = 2000$ mm, 2400 mm and 2500 mm, and varying width to thickness ratios. The analyses confirm that the energy dissipation follows the typical trend of an asymptotic curve as shown in Figure 11.

By using the effective width instead of the total width, a better estimate of the mean crushing force is obtained. Several points based on the total width now move to the left and come very close to the intermediate curve given by Equation (4). This is illustrated in Figure 13. If the effective width–thickness ratio is very large, the data points remain close to the lower limit as before. However, in most cases such points correspond to very thin plates, which are not representative for typical ship structures.

Girder intersection subjected to a flat indenter

The single cruciform is supported at the bottom; however, the girder intersection is free to move vertically at the bottom, while the vertical ends are fixed. To analyse the influence of the boundary conditions, a plain girder intersection is subjected to a flat indenter (Figure 14). Equation (8) is used to define the effective width of the cruciform; it is 1000 mm.

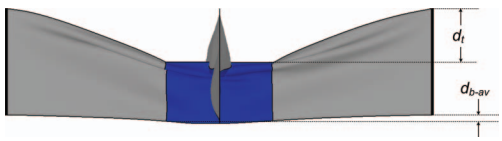

Figure 15. Deformed structure and definition for the net crushing displacement (d_n), i.e. d_t = top indentation and d_{b-av} = average bottom displacement. (This figure is available in colour online.)

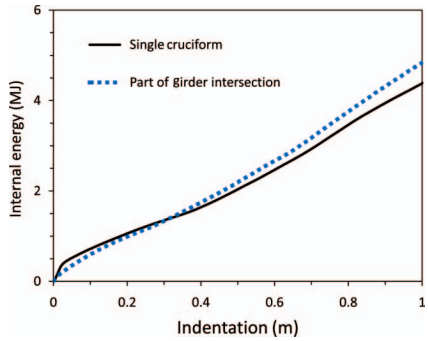

Figure 16. Comparison of the internal energy between a single cruciform and the cruciform as part of a girder intersection with a flat indenter. (This figure is available in colour online.)

The plate flanges are attached to both the top and bottom of the girder intersection to achieve the real condition between the girder intersection and the shell plating (the flanges are not shown in the figure). In the real case, considerable energy will be dissipated by membrane action in the outer shell when the deformation becomes finite, eventually limited by fracture in the shell. Likewise, when the inner bottom starts to deflect, membrane forces will develop in the inner bottom plating. The contribution to the resistance of the membrane forces is not taken into account because the purpose of the present work is to study the energy dissipation in the girder webs only.

The deformed structure is shown in Figure 15, which emphasises the cruciform part. Because the bottom is free to move vertically, the top indentation (d_t) is not identical to the displacement of the crushed cruciform. Hence, it is more appropriate to use the net crushing displacement (d_n) that is obtained by subtracting the average bottom displacement from the top displacement.

The histories of the internal energy dissipation are illustrated in Figure 16. For small indentations, the energy dissipation that is based on the net crushing distance agrees very well with that of the single cruciform, but it is somewhat

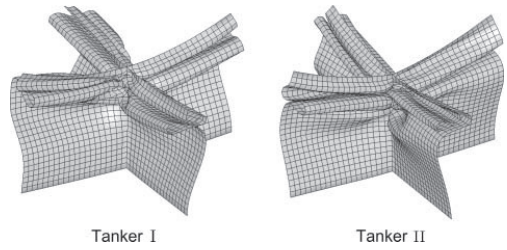

Figure 17. Deformed configuration of the cruciform part of the girder intersection for different ship bows.

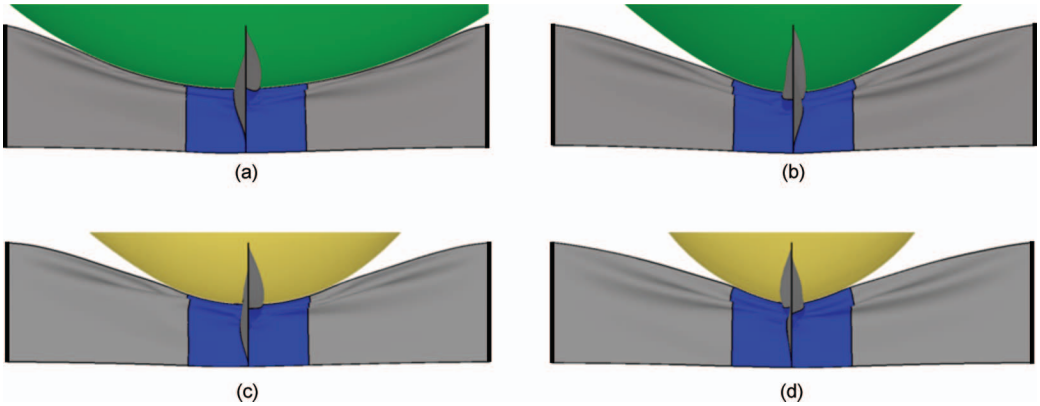

Figure 18. Deformation of the girder intersections at about 1.20 m from the top indentation for two different ship bow shapes. Tanker I: (a) vertical direction and (b) horizontal direction; tanker II: (c) vertical direction and (d) horizontal direction. (This figure is available in colour online.)

higher for large indentations. However, by applying the effective breadth of the cruciform and by taking into account the net crushing displacement, the influence of the boundary conditions is minor.

Girder intersection subjected to ship bows

By replacing the flat indenter in the previous section, two different tanker bow shapes are applied to the girder intersection, in which the bow radius of tanker I is larger than that of tanker II. The bow is modelled as a rigid indenter and dissipates no energy. The aim of this analysis is to investigate the influence of the indenter's shape on the crushing resistance of the girder intersection. Deformed configurations of the cruciform part of the girder intersection for different ship bows are shown in Figure 17. In general the folding patterns are similar, although the direction of folds is not exactly same. Figure 18 shows the deformation of the girder intersection at about 1.20 m from the top indentation in the horizontal and vertical planes.

In Figure 19, the internal energy curves are illustrated for both indenter shapes that used the net crushing displacement. The responses are almost linear and similar up to about 0.5 m of displacement; a small variation then initiates for the next increment.

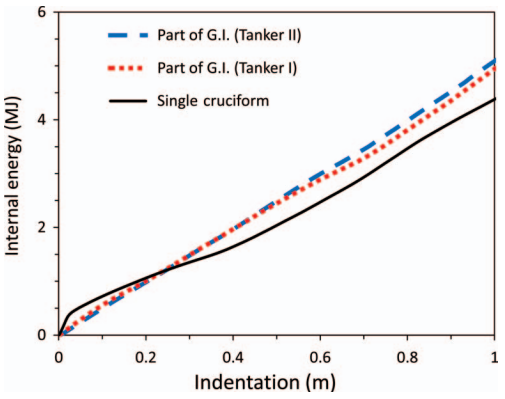

Figure 19. Internal energy curves for the cruciform parts of the girder intersection (G.I.) that are subjected to two ship bows. (This figure is available in colour online.)

Discussion

The internal energy curves that are shown in Figures 16 and 19 are utilised to assess the crushing resistance of the cruciform parts. The results are listed in Table 1 and compared with the analytical formula of the individual cruciform.

Table 1. Results for the mean crushing force.

Case	P_m (MN)	Difference Δ^*
Individual cruciform		
Analytical formula [Equation (4)]**	4.519	–
Part of girder intersection		
Flat indenter	4.766	5.5%
Tanker I (large radius of bow)	4.783	5.8%
Tanker II (small radius of bow)	5.047	11.7%

*Δ: values are compared with the analytical formula.
**Flow stress $\sigma_0 = 358$ MPa, plate thickness $t = 15$ mm and $\lambda = 0.73$.

The girder intersections which are subjected to indentation by a flat indenter and a tanker I ship bow have similar mean crushing forces. By focusing on the cruciform part, the impact of a blunt bow on a girder intersection creates a deformation pattern that is somehow similar to the one caused by a flat indenter in the vertical plane (Figure 18a); however, a concave deformation (like the shape of a bow) occurs in the other plane (Figure 18b). By comparing the numerical results with the analytical formula, the estimates are very good with a deviation less than 6%. Thus, the cruciform model with a flat indenter can be applied to girder intersections that are struck by a bow with a large radius.

For a bow with a small radius, the mean crushing force is large. Both in the horizontal and vertical directions, the contact area is small, and the cruciform deforms as a curved surface. Observation of some elements in the vicinity of the junction shows that the strains are somewhat larger in comparison with those for a blunt surface impact. Thus, the internal energy and the mean crushing force will be higher than those for an impact by a large radius bow. For the small radius, the deviation to the analytical value is about 12%.

To study the influence of fracture, the Rice–Tracey and Cockcroft–Latham (RTCL) material model that was proposed by Tornqvist (2003) is applied to the actual bow collision case. The simulation shows that fracture occurs in elements mostly on the fixed end side and not in the junction area. Because focus is placed on the cruciform, fracture does not influence the internal energy dissipation of the cruciform (Figure 20). On the basis of the gradient of the internal energy curve for the RTCL model, the mean crushing force becomes 4.637 MN, which is only 3.0% different from that of a material without fracture (see the nominal value in Table 1 for tanker I); the result is even closer to the analytical formula. Hence, fracture has a minor effect for the case presented in this study.

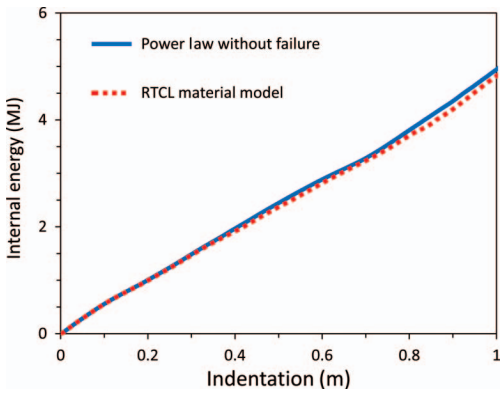

Figure 20. Internal energy curves for the larger radius of the tanker I bow by using different material models: taking into account the failure (RTCL) and power law without failure. (This figure is available in colour online.)

Conclusion

The cruciform's crushing resistance, which can be applied to analyse the girder intersections during ship collision and grounding, has been studied in this paper. The plastic method of analysis is briefly reviewed, and existing formulas for the mean crushing force of a cruciform are adopted. The effective flow stress and the effective crushing factor to be used with the formulas are discussed. The crushing resistance of individual cruciforms is analysed by using LS-DYNA. The numerical results and experimental data from the literature are compared with the analytical formulas, and a very good agreement is obtained.

On the basis of close scrutiny of the distribution of strain energy dissipation, an effective cruciform width may be defined, in which the major part of the energy is dissipated. The effective width is proposed to be half of the girder height. This proposed width is subsequently applied to analyse the girder intersections.

The crushing resistance models for single cruciforms apply quite well to ship girder intersections with realistic boundary conditions (support at far end) when the net crushing displacement is used.

The crushing resistance formulas, which are developed for impacts by flat indenters, are also used for the case of collisions with rigid ship bows with realistic shapes. The numerical results are compared with the formula that was proposed by Hayduk and Wierzbicki (1984), and the agreement is good, especially for the large bow radius. When fracture is taken into account, the analytical formula is still appropriate.

In the real case, where the ship bow is not rigid and will deform during collision, the contact area increases and approaches the condition of a flat surface. Thus, the analytical formula is expected to be in a better agreement with the numerical results.

By adopting the effective cruciform width in a girder intersection system, an analytical method can be applied with good accuracy to assess the internal energy that is absorbed by the ship's structure during collision and grounding.

Acknowledgement

The authors wish to thank the Research Council of Norway for financial support through the Strategic University Program (SUP) 'ScenaRisC&G', Norwegian University of Science and Technology.

References

Abramowicz W. 1983. The effective crushing distance in axially compressed thin-walled metal columns. Int J Impact Eng. 1(3):309–317.

Abramowicz W. 1994. Crush resistance of 'T', 'Y' and 'X' sections. Cambridge, MA: Joint MIT-Industry Program on Tanker Safety. Report No.: 24.

Abramowicz W, Jones N. 1984. Dynamic axial crushing of square tubes. Int J Impact Eng. 2(2):179–208.

Abramowicz W, Simonsen BC. 2003. Effect of fracture on crushing of ship structures. J Ship Res. 47(3):194–207.

Alsos HS. 2008. Ship grounding: analysis of ductile fracture, bottom damage and hull girder response [PhD thesis]. [Trondheim (Norway)]: Department of Marine Technology, Norwegian University of Science and Technology.

Alsos HS, Amdahl J. 2007. On the resistance of tanker bottom structures during stranding. Mar Struct. 20(4):218–237.

Alsos HS, Amdahl J, Hopperstad OS. 2009. On the resistance to penetration of stiffened plates, part II: numerical analysis. Int J Impact Eng. 36(7):875–887.

Amdahl J. 1983. Energy absorption in ship-platform impacts [PhD thesis]. [Trondheim (Norway)]: Department of Marine Technology, Norwegian University of Science and Technology.

Hallquist JO. 2006. LS-DYNA theory manual. Technical report. Livermore, CA: Livermore Software Technology Corporation.

Hallquist JO. 2007. LS-DYNA keyword user's manual. Technical report. Livermore, CA: Livermore Software Technology Corporation.

Hayduk RJ, Wierzbicki T. 1984. Extensional collapse modes of structural members. Comput Struct. 18(3):447–458.

Hong L. 2009. Simplified analysis and design of ships subjected to collision and grounding [PhD thesis]. [Trondheim (Norway)]: Department of Marine Technology, Norwegian University of Science and Technology.

Hong L, Amdahl J. 2008. Crushing resistance of web girders in ship collision and grounding. Mar Struct. 21(4):374–401.

Paik JK. 2007. Practical techniques for finite element modeling to simulate structural crashworthiness in ship collisions and grounding (part II: verification). Ships Offshore Struct. 2(1):81–85.

Santosa S, Wierzbicki T. 1998. On the modeling of crush behavior of closed-cell aluminum foam structure. J Mech Phys Solids. 46(4):645–669.

Simonsen BC. 1997. Mechanics of ship grounding [PhD thesis]. [Lyngby (Denmark)]: Department of Naval Architecture and Offshore Engineering, Technical University of Denmark.

Tornqvist R. 2003. Design of crashworthy ship structures [PhD thesis]. [Lyngby (Denmark)]: Department of Naval Architecture and Offshore Engineering, Technical University of Denmark.

Urban J. 2003. Crushing and fracture of lightweight structures [PhD thesis]. [Lyngby (Denmark)]: Department of Mechanical Engineering, Technical University of Denmark.

Wierzbicki T. 1983. Crushing behaviour of plate intersections. In: Jones N, Wierzbicki T, editors. Structural crashworthiness. London (UK): Butterworths. p. 66–95.

Wierzbicki T, Abramowicz W. 1983. On the crushing mechanics of thin-walled structures. J Appl Mech. 50:727–734.

Yamada Y, Pedersen P. 2008. A benchmark study of procedures for analysis of axial crushing of bulbous bows. Marine Struct. 21(2–3):257–293.

Yang PDC, Caldwell JB. 1988. Collision energy absorption of ship's bow structures. Int J Impact Eng. 7(2):181–196.

Zhang S. 1999. The mechanics of ship collisions [PhD thesis]. [Lyngby (Denmark)]: Department of Naval Architecture and Offshore Engineering, Technical University of Denmark.

Zhang XW, Su H, Yu TX. 2009. Energy absorption of an axially crushed square tube with a buckling initiator. Int J Impact Eng. 36(3):402–417.

Paper II

Haris S., Amdahl J.

An analytical model to assess a ship side during a collision

Published in:

Ships and Offshore Structures
Volume 7, Issue 4, pages 431-448, 2012

Ships and Offshore Structures
Vol. 7, No. 4, 2012, 431–448

Taylor & Francis
Taylor & Francis Group

An analytical model to assess a ship side during a collision

Sabril Haris* and Jorgen Amdahl

Department of Marine Technology, Norwegian University of Science and Technology, Trondheim, Norway

(*Received 7 June 2011; final version received 10 August 2011*)

During its lifetime, a ship may encounter collision or grounding and sustain permanent damage after these types of accidents. Crashworthiness has been based on two main methods: simplified plastic analysis and numerical simulation. In this paper, the resistance of a ship side hit by a rigid bow with two different shapes is investigated using the non-linear finite-element software LS-DYNA. All structural components of the ship side are analysed to determine their contribution to the total resistance. It is found that the shape of the striking bow affects the resistance of the ship. The outer shell plating and plate girders contribute significantly to the total ship resistance until a fracture occurs in the outer skin of the ship. The numerical findings are used as the basis of a new simplified procedure. The ship structure is divided into a shell plating and plate girder; the latter is further divided into cruciforms and web girders. A new analytical formula that can be used to calculate the axial force of shell plating loaded by the general shape of a striking bow is introduced, while the resistance of cruciforms and web girders is determined from the existing formula. The analytical calculations are compared with the numerical results, and good agreement is achieved.

Keywords: ship collision; analytical method; non-linear FEM; shape of bow; shell plating; plate girder

Introduction

A wide range of structural damage is possible during ship collision and grounding. Recently, a cargo ship, Cleantec, and a container carrier, Frisia Rotterdam, collided in the North Sea in December 2010 (Inquirer Global Nation 2010). The Cleantec's side hull sustained major damage, whereas the Frisia Rotterdam just suffered minor damage on its stern.

Since Minorsky's first work (1959), many have attempted to analyse the response of ship structures during collision and grounding. Simplified methods and numerical analysis using non-linear finite-element software have become valuable tools to measure the performance of ships in such accidents (Simonsen 1997a; Zhang 1999; Kitamura 2002; Urban 2003; Alsos 2008; Hong 2009). In the simplified methods, the ship structure is divided into basic structural elements: shell plating, cruciforms (girder intersections of transverse frame and horizontal stringer) and web girders (the remaining girders of transverse frame and horizontal stringer). The internal energy of each component is estimated based on kinematically admissible deformations, and the total energy is obtained by summing the energies for the whole structure. However, the non-linear finite-element method may be used to simulate ship collision and grounding with good results in a cost-effective way compared with experimental tests of real structures. Improvements in computer speed and material behaviour, especially with respect to fracture prediction, have made the computations more reliable.

Simplified methods still need further improvement, especially partitioning the girder system into a cruciform and a web girder. Further, the formula to determine the resistance of the shell plating is still based on a simplified shape of the striking part, which does not accurately represent the shape of the indenting. For example, the formula developed by Simonsen and Lauridsen (2000) used limited spherical indenters with a small radius.

In this paper, an analytical model to assess resistance and energy dissipation in the side of a ship structure subjected to collision is presented. The collision scenario is a rigid striking bow and a ductile ship side structure absorbing all strain energy. In practice, this scenario is relevant if the bow is relatively much stronger than the side of the struck ship, which is often the case.

The striking bow is modelled as an elliptical parabolic surface, which covers a wide range of shapes. Deformation mechanisms are studied by simulations with non-linear finite-element software, LS-DYNA, which generates virtual experiments. The internal energy of each component, i.e., shell plating, cruciform and web girder obtained in the numerical analysis, is used to assess their crashworthiness during collision process. Numerical results are compared to the simplified method. For this purpose, a new analytical formula to determine the crushing resistance of the shell

*Corresponding author. Email: sabril.haris@ntnu.no

ISSN: 1744-5302 print / 1754-212X online

http://dx.doi.org/10.1080/17445302.2012.614527
http://www.tandfonline.com

plating is described. The proposed formulae are applied to analyse the internal energy dissipation of the side of the ship. The analytical study is conducted until fracture occurs in the outer shell. To put the results of the analysis in perspective, the energy dissipation up to fracture is associated with the critical impact speed of the striking vessel.

Analytical crushing resistance formulae

A general double hull side of a ship is sketched in Figure 1. The structure consists of an inner and outer shell and plate girders, which are composed of a transverse frame and horizontal stringer. In simplified plastic analysis, the plate girder is split into a cruciform, which is the intersection between the transverse frame and horizontal stringer, and web girders, which are the remaining girders of the transverse frame and horizontal stringer. Haris and Amdahl (2011) proposed that the junction of a girder system is a cruciform with a breadth equal to half of the girder height. The remainder of the plate girders are analysed as web girders (Figure 1c, d).

Analytical formulae for the force crushing resistance of basic elements, such as cruciforms, web girders and shell plating, have been developed by several researchers. The resistance of a cruciform and web girder is commonly assumed to be constant during the deformation process. Meanwhile, the shell plating resistance increases with increasing displacement.

The resistance force is derived based on an assessment of the internal energy of the deformed structures. For that purpose, a kinematically admissible deformation is constructed, and the rate of internal energy dissipation is calculated assuming a rigid perfectly plastic material. The material is represented by a constant flow stress σ_0, which can be taken as the average of the yield and ultimate engineering stress.

Crushing resistance formulae for cruciforms have been proposed by several authors (Amdahl 1983; Hayduk and Wierzbicki 1984; Yang and Caldwell 1988; Santosa and Wierzbicki 1998; Abramowicz and Simonsen 2003). Haris and Amdahl (2011) found that the most suitable formula for the average crushing force of a cruciform with its breadth equal to half of the height of the cruciform was that proposed by Hayduk and Wierzbicki (1984):

$$P_{cf} = \frac{20.05}{\lambda} M_0 \left(\frac{C}{t_{\mathrm{cf}}}\right)^{1/2}, \tag{1}$$

where M_0 is the plastic moment capacity for a unit plate width, and C and t_{cf} are the width and thickness of the cruciform, respectively. The effective length factor λ is set to 0.73. The plastic moment capacity is defined as follows:

$$M_0 = \frac{\sigma_0 \cdot t_{\mathrm{cf}}^2}{4}. \tag{2}$$

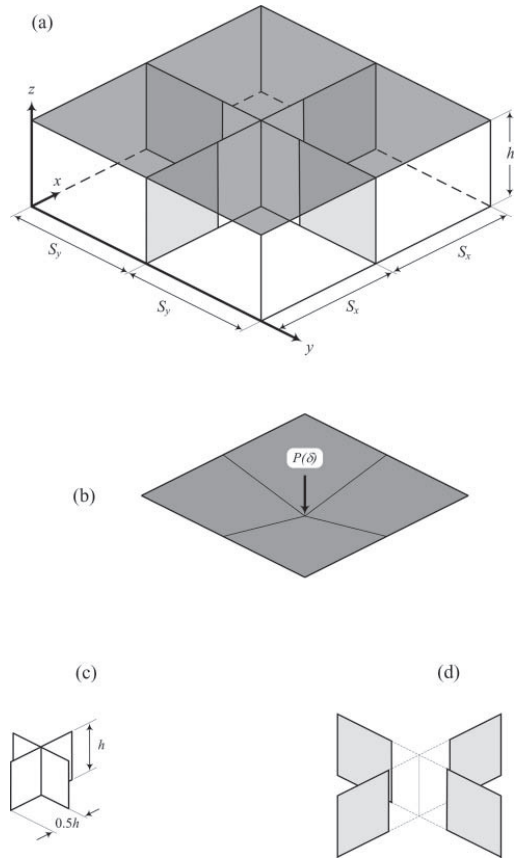

Figure 1. (a) An example of the structure of the side of a ship: shell plating and one plate girder intersection, (b) shell plating, (c) cruciform with a height equal to the girder height, (d) four remaining sections form a web girder.

Resistance formulae for a web girder have been suggested by many researchers (Wang and Ohtsubo 1997; Simonsen 1997b; Zhang 1999; Simonsen and Ocakli 1999; Hong and Amdahl 2008). Haris and Amdahl (2009) used a formula proposed by Zhang (1999), and good agreement with numerical results was achieved with the following formula:

$$P_{\mathrm{wg}} = \frac{11.26}{\lambda} M_0 \left(\frac{b}{t_{\mathrm{wg}}}\right)^{1/3}, \tag{3}$$

where b is half the span of the web girder, and t_{wg} is the thickness. The effective length factor λ is set to 0.73; the plastic moment capacity M_0 is analogous to the definition in Equation (2).

Zhang (1999) proposed a series of formulae to calculate the axial resistance of rectangular shell plating with various loading conditions and different plate thicknesses. For shell plating subjected to a central concentrated load (Figure 1a), the formula is given as follows:

$$P(\delta) = \frac{8}{3\sqrt{3}} \cdot \sigma_0 \cdot S_x \cdot S_y \left(\frac{t_{px}}{S_x^2} + \frac{t_{py}}{S_y^2} \right) \delta, \tag{4}$$

where S_x and S_y are the plate dimensions illustrated in Figure 1, t_{px} and t_{py} are the equivalent plate thicknesses that are determined by smearing the stiffener area in the x- and y-directions and δ is the indentation in the middle of the plate.

However, modelling the shape of the indenter as a point load or a distributed load is not appropriate when defining the force of the plate (Wang et al. 1998). Therefore, a more advanced formula is needed to predict the resistance if the shell plating is subjected to indenters with different shapes, e.g. an elliptical paraboloid bulbous bow. Simonsen and Lauridsen (2000) and Lee et al. (2004) derived a resistance formula for a circular plate loaded by a spherical indenter, while Zhang (1999) established a formula for a rectangular plate indented by a circular paraboloid. Both striking part models simplified the shape of the indenter and did not represent the actual geometry of the striking bows.

In the present work, a formula is derived for the resistance of a rigid bow of an elliptical paraboloid; its geometry is described by the following surface:

$$z = \frac{x^2}{\alpha \cdot S_x} + \frac{y^2}{\beta \cdot S_y}, \tag{5}$$

where α and β are the curvatures in the x- and y-directions. It is noted that the curvatures will be dependent not only on the bow shape but also on the dimensions of the analysed shell plating.

In the same spirit, the elliptical parabolic surface has been introduced by Nguyen et al. (2011) to describe the sea bed topology in the case of grounding using one girder spacing for both x- and y-directions. The resistance of the bottom plating was calculated using a formula proposed by Simonsen (1997a). However, the resistance formula was actually intended for the small radius of a spherical indenter; hence, it is not appropriate for a bow with large curvature which is possible using Equation (5).

A new formula is proposed to determine the resistance of shell plating subjected to an elliptic paraboloid indenter (see Equation (6)). The derivation is detailed in Appendix A1.

$$P(\delta) = \frac{8}{3\sqrt{3}} \cdot \sigma_0 \left(t_{px} \cdot \frac{S_y}{S_x} \left(1 - \frac{\alpha\delta}{S_x} \right)^{-1/2} + t_{py} \cdot \frac{S_x}{S_y} \left(1 - \frac{\beta\delta}{S_y} \right)^{-1/2} \right) \delta. \tag{6}$$

The new formula, Equation (6), coincides with Equation (4) by allowing the curvature parameters α and β to be zero.

The resistance force increases until its peak value is reached and the plate loses its capacity due to the occurrence of fracture. For shell plating subjected to a circular paraboloid indenter, i.e.: $\alpha = \beta$, failure displacement is given by

$$\delta_f = \left[1.316 \frac{S_x S_y}{\sqrt{S_x{}^2 + S_y{}^2}} \sqrt{\varepsilon_f} \right] \times \sqrt{\alpha}, \tag{7}$$

where ε_f is the failure strain. It is noted that, if indenter curvatures vary for each axis, linear multiplication is applied, and the total order is maintained using the square root. For example, if $\alpha \neq \beta$, then the function $\sqrt{\alpha}$ will be replaced by $(\sqrt{\alpha} \times \sqrt{\beta})^{1/2}$.

Various values of failure strain have been used, e.g. in the range of 5–10% (Amdahl 1995; Zhang 1999; McDermott et al. 1974 and Paik et al. 1999 cited in Wang et al. 2000, p.171) and 20% (Wang and Ohtsubo 1999; Wang et al. 2000). For shell plating supported by the girder system, early fracture occurs due to strain concentration in the area where the shell plating and girders meet. However, the analytical formula in Equation (7) is derived by considering membrane straining only, which neglects bending strain and may not consider all strain in the true conditions. Fracture is assumed to occur when the strain is 8% in this paper. This value gives the best agreement between the analytical solution and the finite-element analysis.

A comparison between two indenters having different curvatures is shown in Figure 2. The force–displacement curves, for the plating only, are given for an elliptical parabola ($\alpha = 0.5$, $\beta = 2$) and a circular parabola ($\alpha = \beta = 1$). Both indenters have an equivalent curvature which will give the same prediction of failure displacement (Equation 7), but different force–displacement curves (Equation 6). The analysed shell plating refers to Figure 1a; its dimensions are $S_x = S_y = 4000$ mm and $t_{px} = t_{py} = 20$ mm. The thickness of the plate girders is 15 mm. The same material properties and the failure criterion which are presented in the following section are applied on the comparison.

Figure 2 shows that there is a very good agreement between the analytical solution and the finite-element analysis. The maximum force differs about 3% and the failure displacement differs less than 2%.

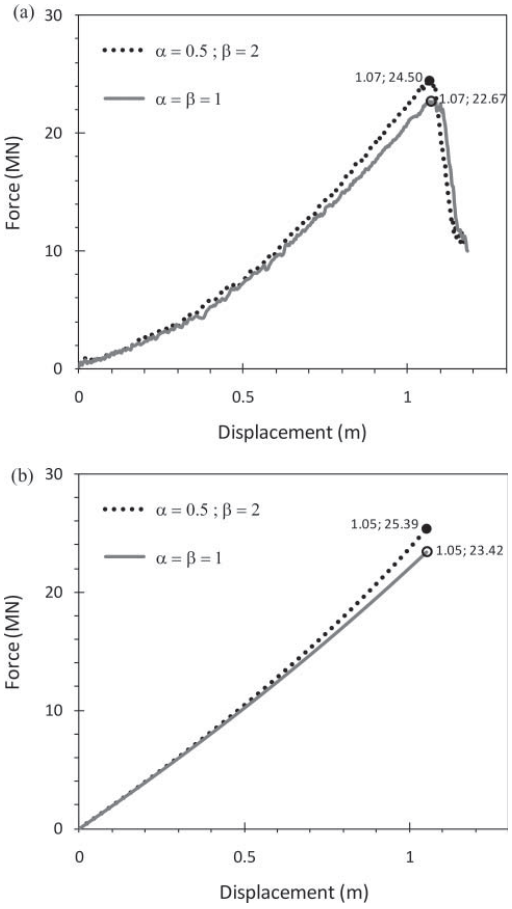

Figure 2. Force–displacement curves for different indenter curvatures: (a) the numerical results and (b) the proposed analytical formula.

Table 1. The main dimensions of the struck ship (in m).

Length P.P.	256.60
Breadth moulded	42.50
Depth moulded	22.00
Design draft	15.00
Tank length	32.00
Frame spacing	4.00
Double side width	2.56
Outer shell plating (mm)	17
Horizontal stringer (mm)	12

FE model of the struck ship side and the striking bow

A 120,000 DWT shuttle tanker with six double hull tanks is selected as the struck ship. The main dimensions of the ship are given in Table 1 and some details are presented in Figure 4. In the simulations, focus is placed on one tank section and on a half tank to each side (Figure 3).

The shape of two actual bows is used for the striking bow. One bow is sharp and has a smaller radius of curvature than the other one, the blunt bow (Figure 4). The tip of the ramming bow hits the side at the intersection of a middle stringer and middle frame. The bows are rigid and absorb no energy during the collision.

The non-linear finite-element software LS-DYNA (Hallquist 2006, 2007) is used to carry out virtual experiments of ship side collision. All structures are modelled with Belytschko-Tsay shell elements (Belytschko et al. 2006) with five integration points over the thickness. Three different mesh sizes are applied. A fine mesh with a size of approximately 100 mm is applied for the main area investigated, i.e., the tank between transverse bulkheads. A coarse mesh of 400 mm is used for the left-half tanks, whereas an intermediate mesh size, about 200 mm, is used for the transition parts. For the same area, mesh size of stiffeners follows the shell plating and girder's meshing element. The ratio of element length to thickness using the finest mesh is about six, which is within the limit of 5–10 suggested by Alsos and Amdahl (2007) and Tornqvist (2003) to achieve a consistent internal energy assessment by capturing the local stress and strain fields accurately.

Appropriate boundary conditions are needed to simulate the actual process of a ship collision. As it is not easy to identify them properly, a simplified but acceptably accurate model must be generated. In this study, fully fixed conditions are applied to the rear of the ship side model. At the ends of the side shell plating, axial displacements are restrained.

The material stress–strain curve is defined by the *power law plasticity* and is given as follows:

$$\sigma = k\left(\varepsilon_{yp} + \varepsilon^{p}\right)^{n}, \tag{8}$$

where ε_{yp} and ε^{p} are the elastic strain at the yield point and the effective plastic strain, respectively. The elastic modulus (E) is 207,000 MPa and the yield stress (σ_y) is assumed to be 235 MPa, which is the normal-grade steel material in ship building. The material constants in Equation (8), k and n, are determined from existing data for different yield stresses given by Alsos and Amdahl (2007) and Alsos et al. (2009); the constants are 740 and 0.24, respectively.

The failure criterion adopted is based on The Rice–Tracey and Cockcroft–Latham (RTCL) model, which captures the real fracture phenomenon during collision pretty well (Tornqvist 2003). The RTCL criterion was implemented in LS-DYNA subroutines by Alsos (2008).

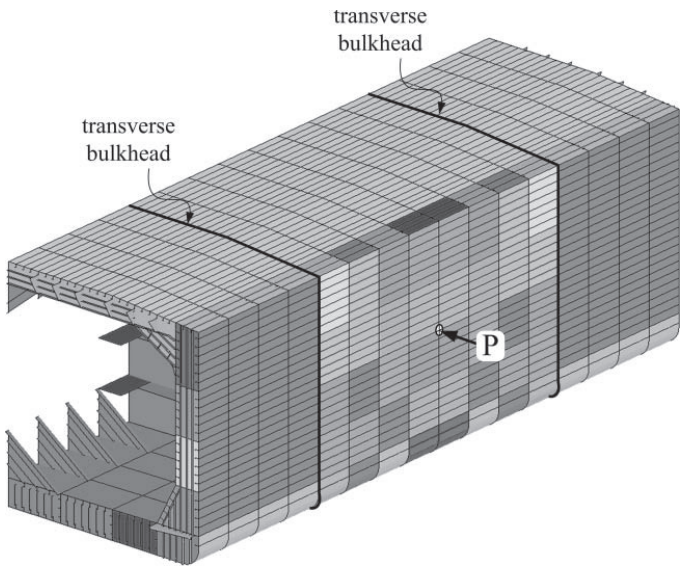

Figure 3. Model for the struck ship side. Point P represents the location of contact between the tip of the bow and the ship side.

Observations from numerical analyses

Global response

The response of ship side structures depends heavily on the resistance of the shell plating. Significant resistances may develop if the shell plating does not take fracture. The contact between the ramming bow and the struck side may spread over a large area. In that case, many parts of structures contribute to the resistance force. In the opposite case, early fracture may obstruct the distribution of the external load, which concentrates in the area in direct contact and causes early failure of the structure.

Force–indentation curves for different rigid bows are presented in Figure 5. The curves start with a resistance level of about 7 MN. The response is similar for both bows until a penetration of 0.60 m. A somewhat larger resistance is then achieved by the blunt bow. The difference in the resistance for the two bows becomes significant for further deformations.

The shape of the bow affects failure initiation in the outer shell. The sharp bow tears the shell plating after a 1.11-m indentation, while the blunt bow fractures the outer shell after a 2.56-m indentation. Because tearing of the shell plating happens early, the side struck by the sharp bow can only maintain its capacity of 30.42 MN during further loading. For the blunt bow impact, the resistance of the side reaches a peak value of 78.89 MN at the instant of rupture upon which it drops significantly.

Deformation pattern and load distribution

To analyse the deformation pattern and load distribution during penetration, the side of the struck ship is divided into two zones: the main zone, which is the panel area close to the first contact point between bow and ship side, and the extended zone, which is adjacent to the main zone (Figure 6). The main zone is forced to deform during penetration because it is in direct contact with the striking bow. Meanwhile, the extended zone may start to deform, either because it cannot support the forces from the main zone or because the striking bow is in direct contact.

For the sharp bow, deformation of the struck ship side is shown in Figure 7, where the contours represent effective plastic strain. Initially, the junction of the girders and the adjacent shell plating are deformed. For increasing penetration, the collision force is supported by the adjacent structure, and the extended zone undergoes very small deformations. When fracture occurs in the outer shell, the curvature of the striking bow is too small to create direct contact with the extended zone, and the striking bow only penetrates the main zone. The displacements of the adjacent junctions 2–4 confirm that deformation is limited to the main zone; these junctions displace only about 3% of the total bow indentation.

The internal energy dissipation of ship side when hit by the sharp bow is presented in Figure 8. It is observed that the energy dissipation is entirely dominated by deformations

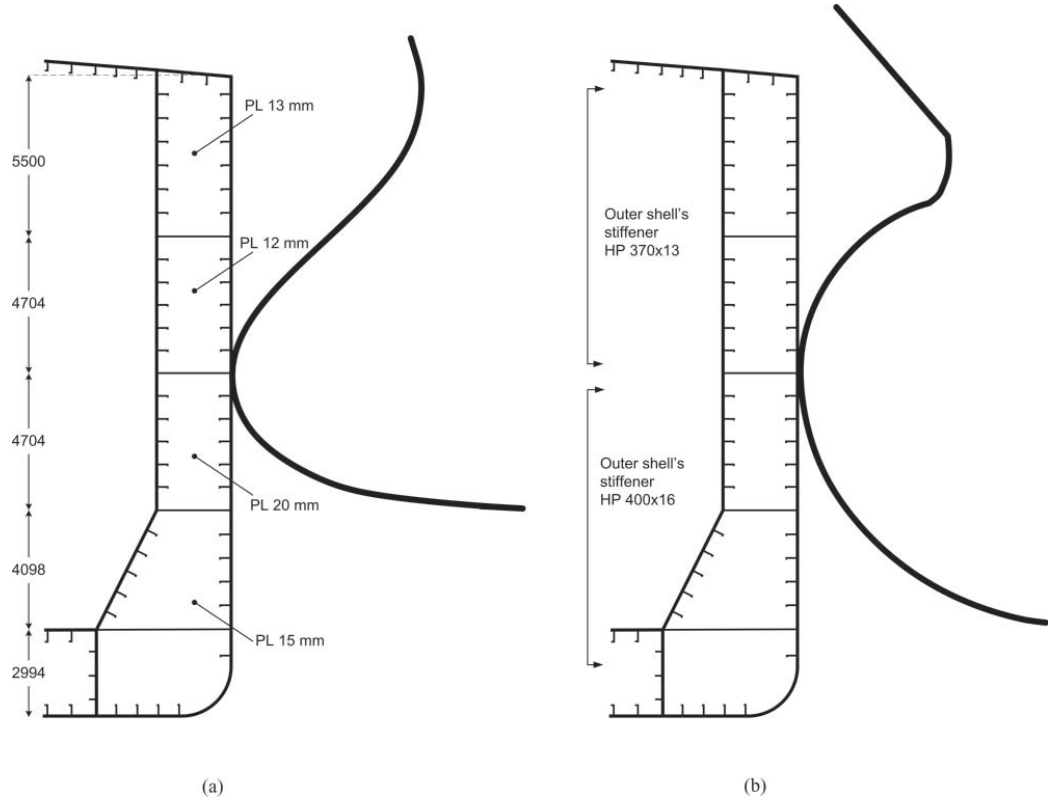

Figure 4. Bow models.

in the main zone, while the contribution from the extended zone is negligible.

When the ship side is indented by the blunt bow, both the main zone and the extended zone are mobilised prior to rupture of the outer shell (Figure 9). The plastic strain distribution in the outer shell shows that three transverse frames from the striking point undergo significant plastic strain.

The displacements of the junctions 1–9 are shown in Figure 10. The outer shell deforms at some junctions without being hit directly by the striking bow. The displacements spread to the extended zone when the adjacent junctions start to deform after 1 m of indentation. This happens when the adjacent members can no longer carry the reactions in the shell plating and the girders in the main zone. Moreover, the junctions on the inner shell start to deform after 1 m of indentation (Figure 10b), which shows that global deformation is an important contribution to the indentation.

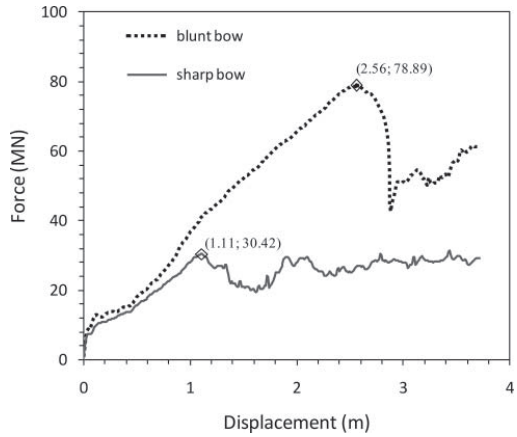

Figure 5. Total force–displacement for different bows. The points indicate when the outer shell fails.

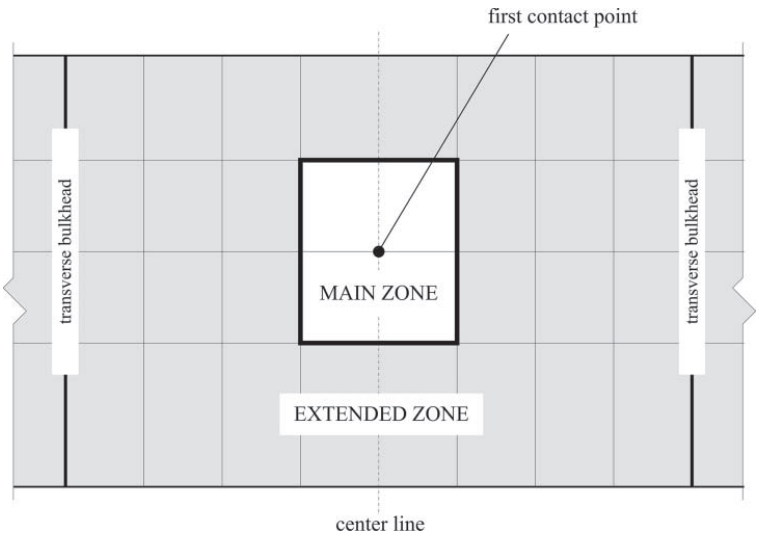

Figure 6. Main Zone and Extended Zone of ship side.

The internal energy dissipation when the side is struck by the blunt bow is shown in Figure 11. The internal energy is mainly absorbed by the main zone in the initial stage of loading. With increasing penetration, more areas are influenced by the bow surface, i.e. areas beyond the main zone. In addition, fracture does not take place early because strain concentrations in the shell plating are less pronounced due to this large indentation process. The increase in deformed

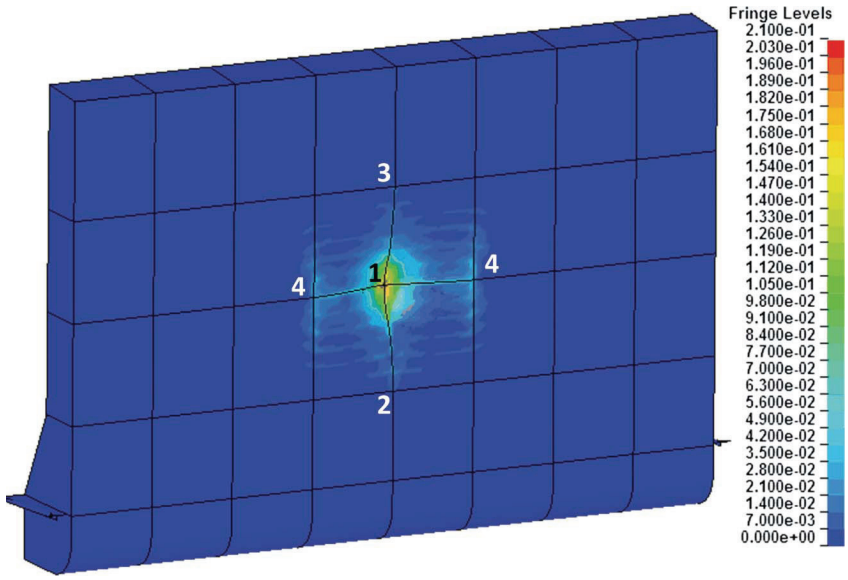

Figure 7. Ship side struck by the sharp bow; deformation is shown for frames between the transverse bulkhead at onset of failure of the outer shell. Numbers are given to identify junction position. (This figure is available in colour online.)

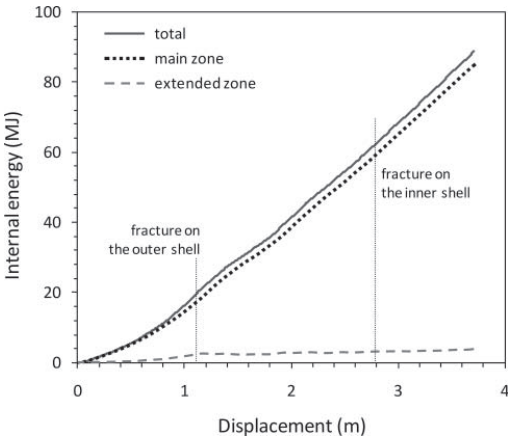

Figure 8. Internal energy absorbed by the ship side that was hit by the sharp bow.

areas at the late stage of loading and the absence of fracture in the outer shell are two factors that contribute significantly to internal energy dissipation from the extended zone.

Internal energy dissipation in the various components

The ship side structure consists of a shell plating, a girder system, and stiffeners. The total energy absorbed by the entire structure is found by summing the internal energy for all components. In Figure 12, the internal energy for each component in the main zone, inner and outer shell plating and girder system, is presented for the blunt bow case.

A significant contribution to the internal energy dissipation comes from the girder and the outer shell; the inner shell contributes virtually nothing (Figure 12a) for the indentation range analysed. The internal energy increases linearly in the girder system, which implies that the force is relatively constant. Meanwhile, the energy absorbed by the outer shell shows a quadratic increase before it changes to a linear relationship after a 1.40-m indentation. In Figure 12b, it is shown that the stiffeners attached at the outer shell contribute significantly to the total internal energy (about 50% relative to their primary part). Thus, the stiffeners on the outer shell must be considered for the total internal energy calculation. The contribution from the girder stiffeners is only 7% of the total internal energy of the main part, which implies that these stiffeners can be disregarded.

Simplified analysis

Key observations of the results of the finite-element analyses are used to develop a simplified analysis technique for ship side collisions. Focus is placed on assessing the resistance of the struck ship side using the analytical formulae presented in the previous sections (Equations (1)–(3), Equations (5)–(7)).

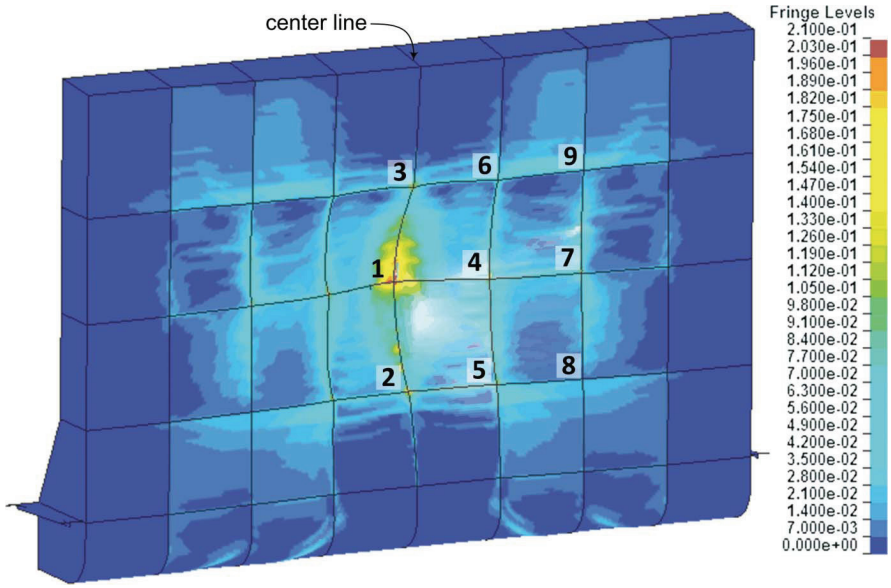

Figure 9. Deformation on ship side with a blunt bow at the onset of outer shell failure. Junctions are labelled as shown in the figure. (This figure is available in colour online.)

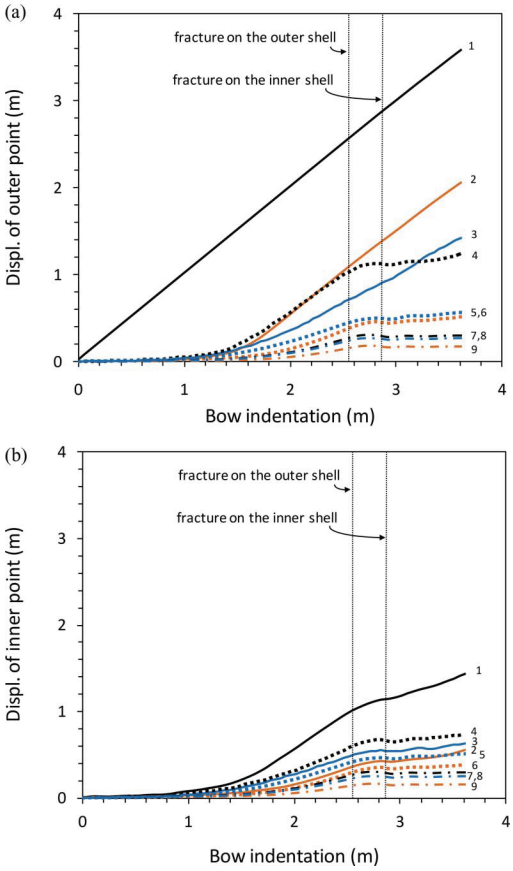

Figure 10. Deformation of junction: displacement of (a) outer points and (b) inner points. (This figure is available in colour online.)

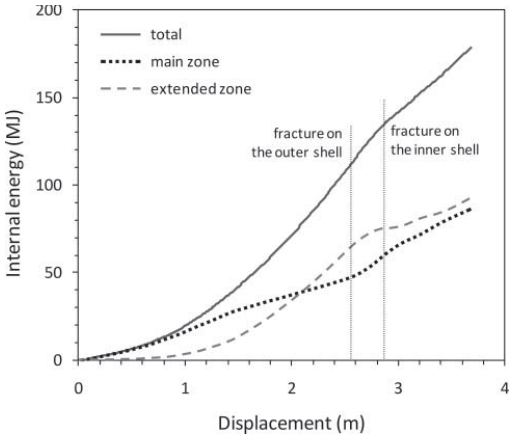

Figure 11. Internal energy dissipation of a ship side that collides with a blunt bow.

The collision process begins when the rigid bow indents the ship side at the contact point in the mid-junction. Initially, the external action is resisted by the contact area: the shell plating and the mid-intersection of the girders. By increasing the indentation, more elements are involved, and the process is greatly influenced by the shape of the striking bow.

The resistance for each component in the main zone, the shell plating, cruciform and web girder is calculated. Analysis is limited to this zone if fracture occurs in the shell plating before the external load is transferred to the extended zone. The transfer of the collision force may take place under one of two conditions: direct contact of the indenter to the next zone or collapse of the adjacent girder junctions due to excessive load through the action of membrane stresses. If the shell plating does not fracture, a similar procedure is applied in the next zone, which includes shell plating and adjacent girders.

The shape of the striking bow is described geometrically using the formula in Equation (5). In Figure 13, the blunt bow shape is quantified for the struck plate size: $S_x = 4000$ mm and $S_y = 4704$ mm. The bow curvatures are 1.98 and 2.95 in the vertical direction and 1.59 in the horizontal direction. For the sharp bow, which was analysed with the same struck plate size, the corresponding curvatures are 1.25, 1.06 and 0.79. If the analysed plate is expanded to the adjacent panels, the curvatures must be updated. In the following, the crushing processes for two shapes of the striking bow, the sharp and the blunt bow, are presented.

The sharp bow

It has been shown that only Junction-1 experiences significant displacement after impact from the sharp bow; therefore, the deformation model only involves the elements within the main zone. It is also shown that the energy absorbed in the main zone is close to the total energy dissipation of the whole side structure (Figure 8). Therefore, the simplified analysis of the sharp bow is only based on the main zone, which consists of the shell plating and the girder intersection system. The model is akin to the basic deformation model of a double hull structure, as described in Figure 1.

For the shell plating, only the outer shell and its stiffeners are considered; the inner one is disregarded both because of its diminutive deformation and its minimal contribution to internal energy dissipation. The girder system is split into one cruciform and four web girders following the proposition by Haris and Amdahl (2011); the cruciform is defined to have a flange width equal to a half of its height, and the

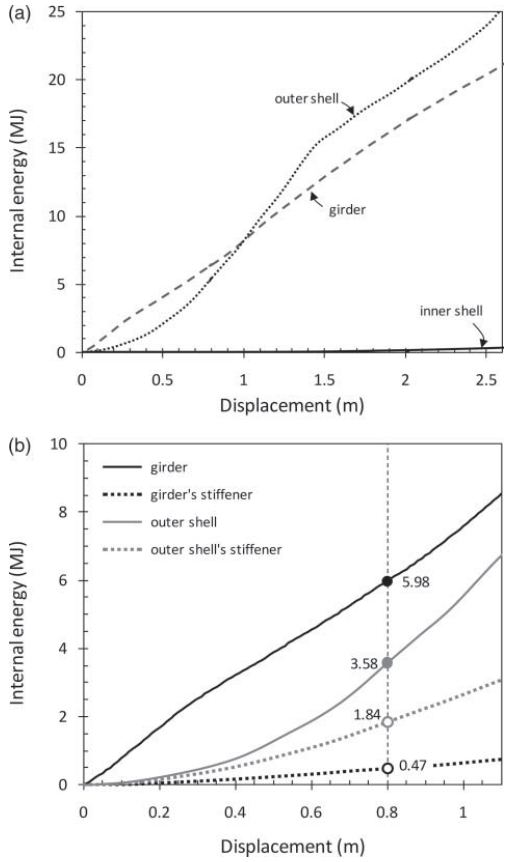

Figure 12. (a) Internal energy of each component of the ship side in the main zone for the blunt bow case, (b) contribution from the primary parts and their stiffener (the inner shell contribution is not shown).

web girder constitutes the rest of the frame. Based on the finding shown in Figure 12b, the stiffeners attached on the girder are not included in the calculation.

The shell plating has a 17-mm thickness with dimensions S_x and S_y equal to 4000 and 4704 mm, respectively. In the x-direction, stiffeners with an average area per panel of 7959 mm^2 are placed, and stiffener smearing on plate thickness is taken into account only for this direction. For the y-direction, the original plate thickness is applied in the plate formula. Based on the dimensions of the plate and the shape of the striking bow, the curvatures are determined. They are $\alpha = 0.79$ (x-axis) and $\beta_1 = 1.25$ and $\beta_2 = 1.06$ (y-axis). The resistance of the plate is then calculated using Equation (6).

The cruciform consists of four flanges; each flange has the same height and width, but their thicknesses depend on the thickness of the stringer and the transverse frame. Equation (1) is utilised to calculate the mean crushing force of the cruciform for each flange by considering its contribution to the unit of cruciform. The rest of the structure is four half web girders with different breadths and thicknesses; Equation (3) is used to compute the mean crushing force. The properties of the cruciform and the web girders are given in Table 2.

Table 2. The dimensions of the cruciform and web girders (in mm).

Cruciform			
Junction	C	t_{cf}	Contribution
1	1280	12	3/4
	1280	20	1/4
Web girder			
Junction	B	t_{wg}	Contribution
2	3424	20	1/2
3	3424	12	1/2
4 (2×)	2720	12	1/2

The total resistance of the struck ship side is obtained by summing the resistance of the shell plating, which is a function of the penetration depth δ, and constant resistance terms for the cruciform and the web girders. The procedure is applied until fracture occurs in the outer shell.

The displacement to failure is determined using Equation (7) with failure strain $\varepsilon_f = 0.08$. Because the curvatures of the indenter for each axis are different, linear multiplication of the square root of indenters is applied, and it replaces the single square root of $\sqrt{\alpha}$. The displacement to failure is $\delta_f = 1.11$ m, and the corresponding ultimate resistance is $P_{ult} = 35.08$ MN.

At this indentation level, there is no direct contact between the indenter and the extended zone. The collision force can also be resisted by the surrounding girders without the adjacent girder intersections collapsing. With these two conditions, it is confirmed that the crushing process is limited to the main zone, which agrees with the numerical results.

In Figure 14, the estimated resistance and the predicted point of failure are plotted together with the numerical result. It is shown that the analytic curve lies above the numerical one. The displacement at failure is estimated very well, while the prediction of the ultimate force is 15% larger than the numerical result.

The blunt bow

The deformation model of a ship side subjected to the blunt bow should include not only the main zone but also the extended zone. Therefore, the analysis is conducted in more than one stage, and a model for collapse of the adjacent frames and stringers is needed.

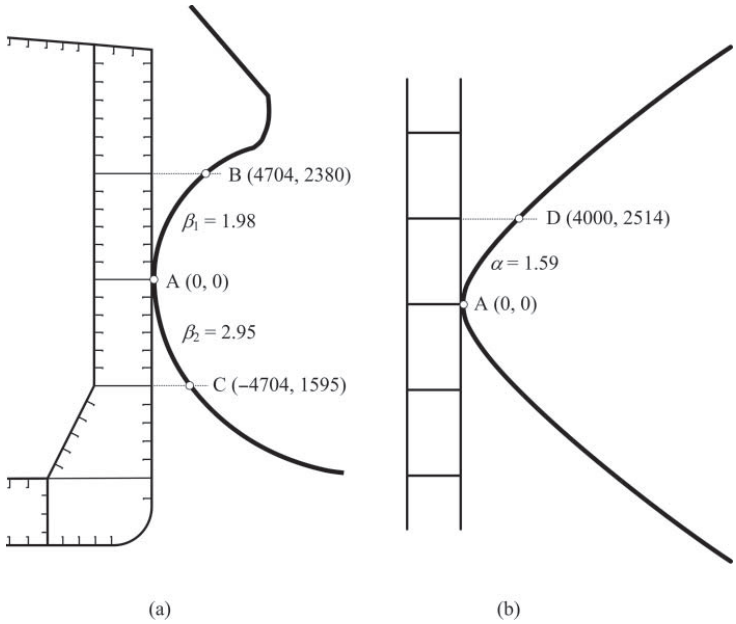

Figure 13. Curvatures of the blunt bow for (a) the vertical plane and (b) the horizontal plane.

As shown in Figure 9, six panels of the outer shell plating in a horizontal direction have significant plastic strain. Thus, the internal energies are absorbed by these parts. However, the inner shells contribute very little to the internal energy (Figure 12), although the inner junctions are displaced (Figure 10b). Thus, only the outer shell plating is accounted for in the calculation, and the inner shell is disregarded.

For the girder system, absorption of internal energy can be determined by observing the height of each

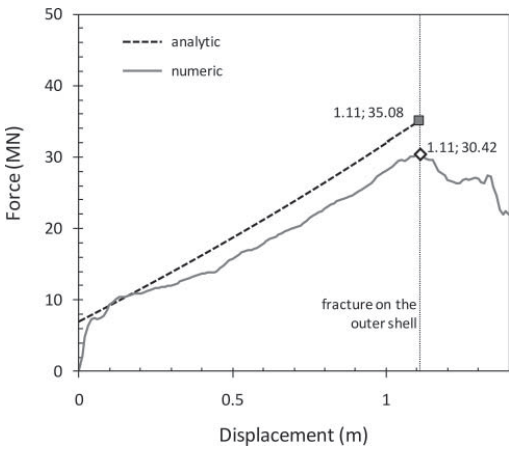

Figure 14. The sharp bow resistance force: predicted by analytical calculation and compared to the numerical result.

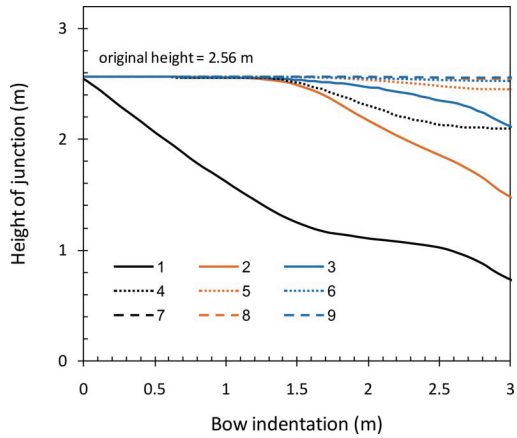

Figure 15. Junction height used to determine whether the junction absorbs energy. (This figure is available in colour online.)

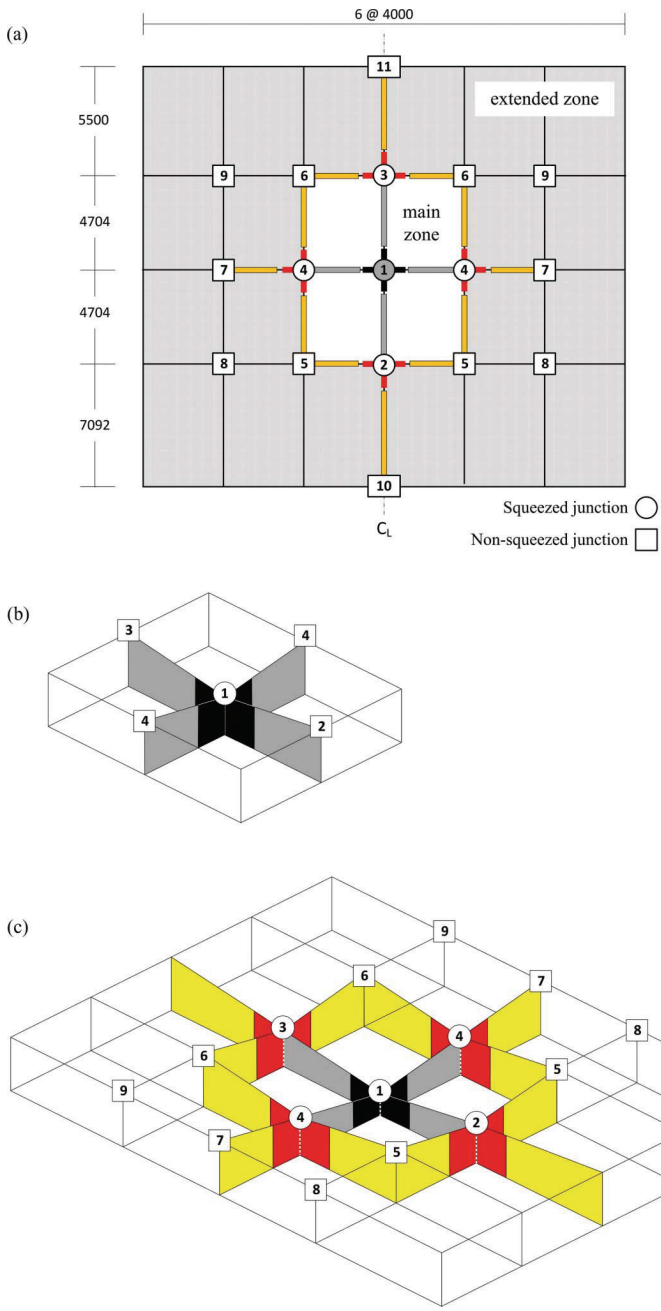

Figure 16. (a) The area of the ship side is used to analyse a collision with a blunt bow, (b) deformation of girders in Stage 1, (c) deformation of girders in Stage 2. (This figure is available in colour online.)

junction during the crushing process. Both figures in Figure 10 are utilised to obtain the height of the junctions; the results are presented in Figure 15. It is shown that there are four junctions that have significantly reduced heights. Junction 1 is squeezed from the beginning of loading, while Junctions 2–4 are compressed after about a 1.20-m indentation. The other junctions have minor reductions and are assumed to be still at their original height. Based on these results, contributions to absorb internal energy are only taken into account from frames and stringers connected to Junctions 1–4.

The area of the struck ship to be analysed is then determined (Figure 16a). Because the loading process is gradual, the analysis is conducted in two main stages: Stage 1 and Stage 2.

In Stage 1, the resistance force within the main zone is calculated. This process is analogous to analysis of the sharp bow. Only Junction 1 is defined to be squeezed; thus, one cruciform and four web girders are calculated (Figure 16b). The properties of the cruciform and web girder are similar to those given in Table 2. For the shell plating, a 2 × 2 panel is defined, and its resistance force is calculated using Equation (6) for the curvatures $\alpha = 1.59$, $\beta_1 = 1.98$, and $\beta_2 = 2.95$.

In Stage 2, resistance forces are computed for the main and extended zones. The process starts when the adjacent junctions collapse due to the excessive external load in the main zone. The external load is calculated using Equation (6) and assumed to transfer independently in the horizontal and vertical directions. A proportional load distribution is applied along the four surrounding girders.

For the horizontal direction, the first part within the outer bracket in Equation (6) is used, and the external force is compared with the resistance of the cruciforms in the Junction 4 (left and right of the centreline). Utilising the second part of Equation (6), the same procedures are carried out for the vertical direction, and the results are compared with the cruciform in Junctions 2 and 3.

The earliest collapse occurs when the cruciform in Junction 4 carries an external load greater than its capacity of 3.29 MN at a 1.16-m indentation. This indentation is close to the numerical result shown in Figure 15, which shows a displacement of 1.20 m, at which Junctions 2–4 start to deform. The junction collapses earlier than the shell plating fails, which is predicted to occur at an indentation of 1.59 m.

Stage 2 begins at a displacement of 1.16 m. The frames and stringers connected to Junctions 1–4 are involved in the crushing process (Figure 16c). Again, the frames and stringers to cruciforms and web girders are proportioned according to the parameters proposed by Haris and Amdahl (2011). In Appendix A2, the dimensions of the cruciforms and web girders are presented. The crushing resistance for each component can be calculated using Equations (1) and (3). The total resistance force for all components of the girder system is 26.69 MN.

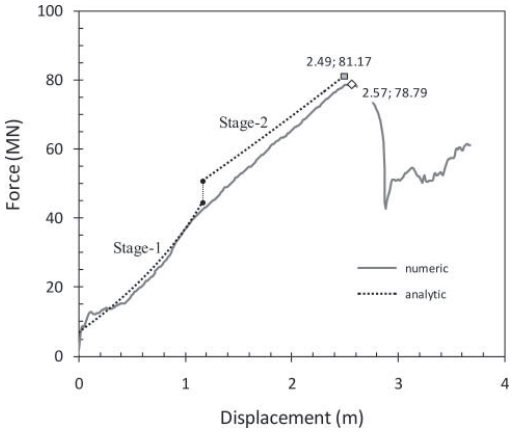

Figure 17. The blunt bow resistance force: predicted by analytical calculation and comparison to the numerical result.

The resistance of the shell plating in Stage 2 is now influenced by 6×4 panels. Because the dimension of the analysed shell plating has changed, the curvatures must be updated. Using the same coordinate data (Figure 13) with new plate dimensions ($S_x = 12000$ mm, $S_{y1} = 10204$ mm, $S_{y2} = 11796$ mm), the new curvatures are $\alpha = 0.53$, $\beta_1 = 0.91$ and $\beta_2 = 1.18$. The resistance force is then calculated using Equation (6).

Stage 2 ends if failure occurs on the outer shell. Equation (7) is utilised to determine the failure displacement: $\delta_f = 2.49$ m. This value agrees well with the numerical result: the maximum force before failure occurs at a displacement of 2.57 m.

In Figure 17, the results of the simplified method are plotted together with the numerical results. The predicted ultimate force at the point of failure onset is 81.17 MN, which constitutes more than 3% of the numerical results. Meanwhile, the analytical formula predicts 3% smaller failure displacement than the numerical result.

Critical striking vessel speed

The internal energy dissipated by the ship side structure is crucial when assessing the outcome of a collision. The total absorbed energy when fracture starts to occur in the outer shell is the primary focus. The amount of internal energy absorbed during a collision with a sharp bow and blunt bow is presented in Table 3; both numerical and analytical results are shown.

To give a perspective for the level of energy of the collision scenario, the critical striking vessel speed is determined by means of the external dynamics method. For

Table 3. Dissipated internal energy at onset of fracture of the outer shell (in MJ).

	Internal energy	
Bow type	Numeric	Analytic
Sharp bow	20	23
Blunt bow	113	114

this purpose, the principles of conservation of momentum and conversation of energy are utilised. The speed of the striking vessel corresponding to an internal energy dissipation is as given in Table 3 and can be calculated using the following assumptions:

- Only the side dissipates energy; the striking bow is rigid
- The initial velocity of struck ship is zero. At the end of collision, both ships will move together with the same speed.
- Displacement of the struck ship and the sharp striking bow are both 160,000 tons; the ship with the striking blunt bow is 185,000 tons.
- The collision is central (force vector through centre of gravity)
- The added mass is assumed to be 10% and 40% for the striking bow and the struck ship, respectively.

The critical vessel speed for fracture of the outer shell of the struck ship is found to be 0.7 m/s for the case of the sharp bow and 1.5 m/s for the blunt bow

Conclusions

An analytical model to assess the response of ship side structures struck by rigid bows is presented. The bow shape was parameterised with a formula for an elliptical parabolic surface. The energy dissipation caused by a sharp bow and a blunt bow striking a ship side was studied in detail. Virtual experiments were conducted with non-linear finite-element software LS-DYNA to visualise the crushing process for each component of the ship side structure, to obtain the resistance–indentation relationship, and to detect the onset of fracture in the outer shell.

To predict the response of the struck ship with the analytical method, the ship side was partitioned into shell plating and plate girders, which were further subdivided into cruciforms (transverse frames and horizontal stringer intersections) and web girders (transverse frame and stringer) with proportions suggested by Haris and Amdahl (2011). Existing formulae were used to calculate the constant crushing force of cruciforms and web girders. A new formula that includes the effect of stiffeners by smearing their area onto that of the shell plating was derived to estimate the resistance of the shell plating.

The stiffeners on the webs of the plate girders only have a minimal contribution to the total internal energy and were therefore disregarded. It is also found that the inner shell dissipates an insignificant amount of energy until failure occurs in the outer shell.

The force–displacement curve was obtained stepwise by increasing the deformations to take into account the contributions of all components. In the first stage, components in the main zone, i.e. the shell plating and web girder, in direct contact with the strike were considered. The calculation process stopped if fracture was initiated in the shell plating and continued if the adjacent frames and stringers could not support the collision force but started to collapse. If collapse occurred, the collision zone was extended to the next intact frames and stringers. This process continued until fracture occurred.

The analytical calculations were compared with the numerical results, and good agreements were achieved. The developed model allows for fast calculation of internal energy dissipation by the struck ship side during a collision and may be a useful tool for risk estimates or decision-making in accident situations.

Acknowledgement

The authors wish to thank the Research Council of Norway for financial support through the Strategic University Program (SUP) “ScenaRisC&G”, Norwegian University of Science and Technology.

References

Abramowicz W, Simonsen BC. 2003. Effect of fracture on crushing of ship structures. J Ship Res. 47(3):194–207.

Alsos HS. 2008. Ship grounding: Analysis of ductile fracture, bottom damage and hull girder response [PhD dissertation]. [Trondheim (Norway)]: Department of Marine Technology, Norwegian University of Science and Technology.

Alsos HS, Amdahl J. 2007. On the resistance of tanker bottom structures during stranding. Mar Struct. 20(4):218–237.

Alsos HS, Amdahl J, Hopperstad OS. 2009. On the resistance to penetration of stiffened plates, part II: Numerical analysis. Int J Impact Eng. 36(7):875–887.

Amdahl J. 1983. Energy absorption in ship-platform impacts [PhD dissertation]. [Trondheim (Norway)]: Department of Marine Technology, Norwegian University of Science and Technology.

Amdahl J. 1995. Side collision. Paper presented at: the 22nd WEGEMT Graduate School ‘Accidental Loadings on Marine Structures: Risk and Response’; Lyngby, Technical University of Denmark.

Belytschko T, Liu WK, Moran B. 2006. Nonlinear finite elements for continua and structures. Chichester (England): John Wiley & Sons.

Hallquist JO. 2006. LS-DYNA theory manual. Technical report. Livermore (CA): Livermore Software Technology Corporation.

Hallquist JO. 2007. LS-DYNA keyword user’s manual. Technical report. Livermore (CA): Livermore Software Technology Corporation.

Haris S, Amdahl J. 2009. Crushing mechanics of girder intersections in ship collision and grounding. Proceedings of the

3rd International Conference on Computational Methods in Marine Engineering (MARINE 2009); 2009 Jun 27–29; Oslo, Norway. Barcelona (Spain): International Center for Numerical Methods in Engineering (CIMNE).

Haris S, Amdahl J. 2011. Crushing resistance of a cruciform and its application to ship collision and grounding. Ships Offshore Struct. doi: 10.1080/17445302.2010.536392.

Hayduk RJ, Wierzbicki T. 1984. Extensional collapse modes of structural members. Comput Struct. 18(3):447–458.

Hong L. 2009. Simplified analysis and design of ships subjected to collision and grounding [PhD dissertation]. [Trondheim (Norway)]: Department of Marine Technology, Norwegian University of Science and Technology.

Hong L, Amdahl J. 2008. Crushing resistance of web girders in ship collision and grounding. Mar Struct. 21(4):374–401.

Inquirer Global Nation. 2010. Chinese, German ships collide in North Sea [Internet]; [cited 2011 Jan 20]. Available from: http://globalnation.inquirer.net/news/breakingnews/view/20101214-308833/Chinese-German-ships-collide-in-North-Sea

Kitamura O. 2002. FEM approach to the simulation of collision and grounding damage. Mar Struct. 15(4–5):403–428.

Kuroiwa T. 1993. Dynamic experiments and numerical simulations of failure of ship's side structure. Proceedings of the International Conference on Prediction Methodology of Tanker Structural Failure and Consequential Oil Spill; Tokyo, Japan. Japan: The Association for Structural Improvement of the Shipbuilding Industry (ASIS).

Lee YW, Woertz JC, Wierzbicki T. 2004. Fracture prediction of thin plates under hemi-spherical punch with calibration and experimental verification. Int J Mech Sci. 46:751–781.

Minorsky, VU. 1959. An analysis of ship collisions with reference to nuclear power plants. J Ship Res. 3(2):1–4.

Nguyen TH, Garre L, Amdahl J, Leira BJ. 2011. Benchmark study on the assessment of ship damage conditions during stranding. Ships Offshore Struct. doi:10.1080/17445302.2010.537087

Qvist S, Brian K, Schmidt MH, Madsen SH. 1995. Ship collision – experimental and numerical analysis of double hull models. Proceedings of the 9th DYMAT Technical Conference Material and Structural Modelling in Collision Research; 1995, Oct 10–11; Munich, Germany. Is-sur-Tille (France): DYMAT.

Santosa S, Wierzbicki T. 1998. On the modeling of crush behavior of closed-cell aluminum foam structure. J Mech Phys Solids. 46(4):645–669.

Simonsen BC. 1997a. Mechanics of ship grounding [PhD dissertation]. [Lyngby (Denmark)]: Department of Naval Architecture and Offshore Engineering, Technical University of Denmark.

Simonsen BC. 1997b. Ship grounding on rock – I. Theory Mar Struct. 10(7):519–562.

Simonsen BC, Lauridsen LP. 2000. Energy absorption and ductile failure in metal sheets under lateral indentation by a sphere. Int J Impact Eng. 24(10):1017–1039.

Simonsen BC, Ocakli H. 1999. Experiments and theory on deck and girder crushing. Thin-Walled Struct. 34:195–216.

Tornqvist R. 2003. Design of crashworthy ship structures [PhD dissertation]. [Lyngby (Denmark)]: Department of Naval Architecture and Offshore Engineering, Technical University of Denmark.

Urban J. 2003. Crushing and fracture of lightweight structures [PhD dissertation]. [Lyngby (Denmark)]: Department of Mechanical Engineering, Technical University of Denmark.

Wang G, Arita K, Liu D. 2000. Behavior of a double hull in a variety of stranding or collision scenarios. Mar Struct. 13(3):147–187.

Wang G, Ohtsubo H. 1997. Deformation of ship plate subjected to very large load. Proceedings of the 16th International Conference on Offshore Mechanics and Arctic Engineering (OMAE), Vol. 2; 1997 Apr 13–18; Yokohama, Japan. New York (NY): ASME.

Wang G, Ohtsubo H. 1999. Impact load of a supply vessel. Proceedings of 9th International Offshore and Polar Engineering Conference (ISOPE), Vol. 4; 1999 May 30–Jun 4; Brest, France. Cupertino (CA): ISOPE.

Wang G, Ohtsubo H, Arita K. 1998. Large deflection of a rigid-plastic circular plate pressed by a sphere. J Appl Mech. 65:533–535.

Yang PDC, Caldwell JB. 1988. Collision energy absorption of ship's bow structures. Int J Impact Eng. 7(2):181–196.

Zhang S. 1999. The mechanics of ship collisions [PhD dissertation]. [Lyngby (Denmark)]: Department of Naval Architecture and Offshore Engineering, Technical University of Denmark.

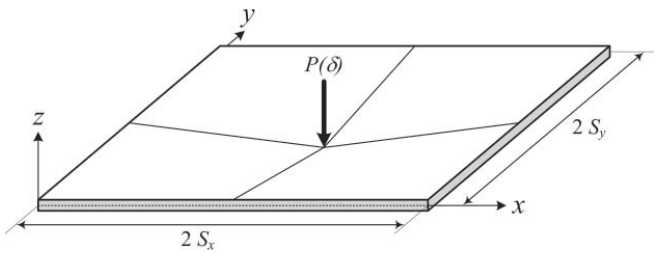

Figure A1. Deformation pattern of an indented rectangular plate.

Appendix 1: Resistance and failure of strip plate subjected by a parabolic indenter

A general deformation pattern for a rectangular plate sized $2S_x \times 2S_y$ that is subjected to a vertical load in the centre of the plate is shown in Figure A1. The deformation is defined as follows:

$$w(x, y, t) = f(x, y, \delta), \tag{A1}$$

where δ is the vertical deformation in the centre of the plate.

Normal and shear strains on the x–y plane can be calculated using the following equations:

$$\begin{aligned} \varepsilon_{xx} &= \frac{1}{2}\left(\frac{\partial w}{\partial x}\right)^2; \\ \varepsilon_{yy} &= \frac{1}{2}\left(\frac{\partial w}{\partial y}\right)^2; \\ \varepsilon_{xy} &= \frac{1}{2}\left(\frac{\partial w}{\partial x}\right)\left(\frac{\partial w}{\partial y}\right). \end{aligned} \tag{A2}$$

The effective strain rate is defined by applying the von Mises yield criterion as follows:

$$\dot{\bar{\varepsilon}} = \frac{2}{\sqrt{3}}\left((\dot{\varepsilon}_{xx})^2 + (\dot{\varepsilon}_{yy})^2 + (\dot{\varepsilon}_{xx} \cdot \dot{\varepsilon}_{yy}) + (\dot{\varepsilon}_{xy})^2\right)^{1/2}. \tag{A3}$$

Furthermore, for a constant flow stress σ_0, the rate of strain energy is defined as follows:

$$\dot{E}_{\text{int}} = \sigma_0 \int_V \dot{\bar{\varepsilon}} dV. \tag{A4}$$

The force can be determined by using the relationship between the rate of external work and the rate of internal energy:

$$P(\delta) \cdot \dot{\delta} = \dot{E}_{\text{int}}. \tag{A5}$$

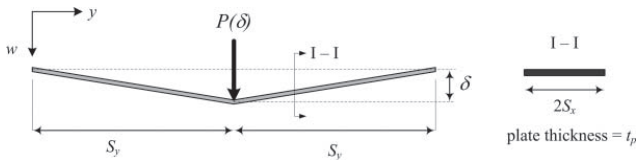

Figure A2. Deformation of a strip plate subjected to a line load in the mid-span.

Case 1: Strip plate subjected to a line load

Based on the general deformation pattern in Figure A2, a strip plate subjected to a vertical line load is analysed.

Assuming the plate deformation for one side is $w = \delta \frac{y}{S_y}$, the resistance for both sides is as follows:

$$P(\delta) = \frac{2}{\sqrt{3}} \cdot \sigma_0 \cdot t_p \cdot \frac{4S_x}{S_y} \cdot \delta. \tag{A6}$$

Case 2: Strip plate subjected to a point load

The deformation of plate in Figure A1 is defined as follows:

$$w = \delta \cdot \left(\frac{x}{S_x}\right) \cdot \left(\frac{y}{S_y}\right). \tag{A7}$$

The total resistance is (after Zhang 1999):

$$P(\delta) = \frac{1}{3}\frac{2}{\sqrt{3}} \cdot \sigma_0 \cdot t_p \cdot 4S_x S_y \left(\frac{1}{S_x^2} + \frac{1}{S_y^2}\right) \cdot \delta. \tag{A8}$$

Equation (A8) can be presented in the following form:

$$\begin{aligned} P(\delta) &= \frac{1}{3}\left(\frac{2}{\sqrt{3}} \cdot \sigma_0 \cdot t_p \cdot \frac{4S_x}{S_y} \cdot \delta\right) + \frac{1}{3}\left(\frac{2}{\sqrt{3}} \cdot \sigma_0 \cdot t_p \cdot \frac{4S_y}{S_x} \cdot \delta\right) \\ &= \frac{1}{3}\left(P_{\text{strip}-x} + P_{\text{strip}-y}\right). \end{aligned} \tag{A9}$$

The effective strain is calculated using the same manner in Equation (A3), which gives the following result:

$$\bar{\varepsilon} = \frac{\delta^2}{\sqrt{3}}\left(\frac{1}{S_x^2} + \frac{1}{S_y^2}\right). \tag{A10}$$

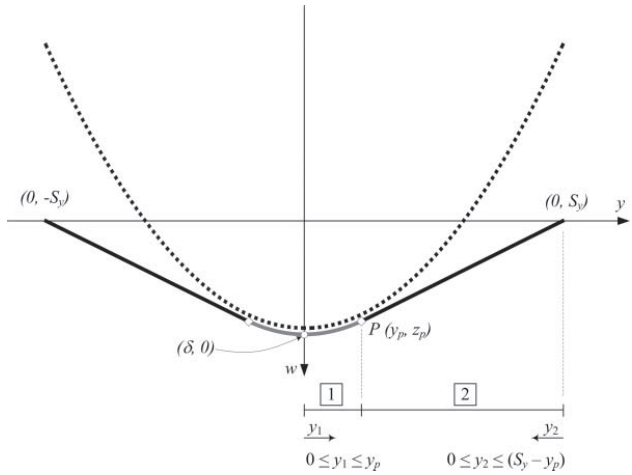

Figure A3. Deformation of a strip plate subjected to a parabolic indenter.

If the strain on the plate reaches the failure strain ε_f, the failure displacement is

$$\delta_f = 1.316 \frac{S_x S_y}{\sqrt{S_x^2 + S_y^2}} \sqrt{\varepsilon_f}. \tag{A11}$$

Case 3: Strip plate subjected to a parabolic indenter

A parabolic indenter is defined as follows:

$$z = \frac{y^2}{(\beta \cdot S_y)}. \tag{A12}$$

Based on experimental evidence (Kuroiwa 1993; Qvist et al. 1995; Zhang 1999) and numerical results presented by the authors, the deformation model for a strip plate that is loaded by a parabolic indenter is described in Figure A3.

The deformation functions for each part are as follows:

$$w_1 = \delta - \frac{x^2}{\beta \cdot b} \quad \text{for } 0 \le y_1 \le y_p; \tag{A13}$$

$$w_2 = \frac{2}{\beta} \frac{(x_p - 2\beta \cdot \delta)}{b - x_p} x \quad \text{for } 0 \le y_2 \le (S_y - y_p), \tag{A14}$$

where

$$y_p = S_y - S_y \left(1 - \frac{\beta \cdot \delta}{S_y}\right)^{1/2} \text{ and } z_p = \frac{2y_p}{\beta} - 2\delta.$$

After some derivation, the resistance of the strip plate becomes

$$P(\delta) = \frac{2}{\sqrt{3}} \cdot \sigma_0 \cdot t_p \cdot \frac{4S_x}{S_y} \delta \left(1 - \frac{\beta\delta}{S_y}\right)^{-1/2}. \tag{A15}$$

If $\beta = 0$, Equation (A15) is equal to Equation (A6) (the point load case).

Case 4: Strip plate subjected to an elliptical parabolic indenter

An elliptical parabolic indenter is defined as follows:

$$z = \frac{x^2}{(\alpha \cdot S_x)} + \frac{y^2}{(\beta \cdot S_y)}, \tag{A16}$$

where α and β are the curvatures on the x- and y-axes, respectively.

Because the case is quite complex, a linear simplification is proposed to determine the force. The idea is to combine Equation (A9) and Equation (A15).

The formula becomes

$$P(\delta) = \frac{8}{3\sqrt{3}} \cdot \sigma_0 \left(t_{px} \cdot \frac{S_y}{S_x} \left(1 - \frac{\alpha\delta}{S_x}\right)^{-1/2} + t_{py} \cdot \frac{S_x}{S_y} \left(1 - \frac{\beta\delta}{S_y}\right)^{-1/2} \right) \delta. \tag{A17}$$

The displacement at failure is affected by the shape of the indenter. Experimental data collected by Simonsen & Lauridsen (2000) showed that the failure displacement is proportional to the square root of the spherical indenter radius. The present numerical analysis for circular paraboloid indenters, i.e. $\alpha = \beta$, shows the same results: the failure deformation is proportional to the square root of the indenter curvature. Therefore, to accommodate the shape of the indenter, Equation (A11) is modified by including the effect of the indenter shape. The formula is as follows:

$$\delta_f = \left[1.316 \frac{S_x S_y}{\sqrt{S_x^2 + S_y^2}} \sqrt{\varepsilon_f} \right] \times \sqrt{\alpha}. \tag{A18}$$

It is noted that if indenter curvatures are different for each axis, linear multiplication is applied and the total order remains the square root.

Appendix 2: Component of girders in the Stage 2 for the case of blunt bow

Cruciform (all cruciforms have $C = 1280$ mm)

Junction	t_{cf}	Contribution
1	12	3/4
	20	1/4
2	12	2/4
	15	1/4
3	12	2/4
	13	1/4
4 (2×)	12	2/4
	20	1/4

Web girder (all contribution factors are 1/2)

Junction	b	t_{wg}
2	3424	20
3	3424	12
4 (2×)	2720	12
5 (2×)	2720	12
	3424	20
6 (2×)	2720	12
	3424	12
8 (2×)	2720	12
10	2798	12
11	4220	13

Paper III

Haris S., Amdahl J.

Analysis of ship–ship collision damage accounting for bow and side deformation interaction

Published in:

Marine Structures
Volume 32, pages 18-48, 2013

Marine Structures 32 (2013) 18–48

Contents lists available at SciVerse ScienceDirect

Marine Structures

journal homepage: www.elsevier.com/locate/marstruc

Analysis of ship–ship collision damage accounting for bow and side deformation interaction

Sabril Haris*, Jorgen Amdahl

Department of Marine Technology, Norwegian University of Science and Technology, Otto Nielsens V.10, Trondheim 7491, Norway

ARTICLE INFO

Article history:
Received 12 August 2012
Received in revised form 1 February 2013
Accepted 22 February 2013

Keywords:
Ship collision
Simplified analytical method
Non-linear FEM
Relative resistance
Damage interaction
Type of collision

ABSTRACT

This paper presents a procedure to analyse ship collisions using a simplified analytical method by taking into account the interaction between the deformation on the striking and the struck ships. Numerical simulations using the finite element software LS-DYNA are conducted to produce virtual experimental data for several ship collision scenarios. The numerical results are used to validate the method. The contributions to the total resistance from all structural components of the collided ships are analysed in the numerical simulation and the simplified method. Three types of collisions were identified based on the relative resistance of one ship to the other. They are denoted Collision Types 1 and 2, in which a relatively rigid ship collides with a deformable ship, and Collision Type 3, in which two deformable ships are involved. For Collision Types 1 and 2, estimates of the energy absorbed by the damaged ships differ by less than 8% compared to the numerical results. For Collision Type 3, the results differ by approximately 13%. The simplified method is applicable for right angle ship collision scenario, and it can be used as an alternative tool because it quickly generates acceptable results.

* Corresponding author. Tel.: +47 735 95648; fax: +47 735 95697.
E-mail address: sabril.haris@ntnu.no (S. Haris).

0951-8339/$ – see front matter © 2013 Elsevier Ltd. All rights reserved.
http://dx.doi.org/10.1016/j.marstruc.2013.02.002

1. Introduction

Inspired by Minorsky's empirical research [1], ship collision studies have been conducted by many researchers because the damage sustained during ship collisions can threaten human lives, the environment, and economic investments. According to Hong [2] the current approaches to analysing ship collisions can be generally categorised into three methods: experiments, numerical simulations, and simplified analytical methods. All methods can be applied from the local element level to the level of small-scale ship substructures. Experimental results are used as a reference against which the two other methods must be verified. If experiments are impracticable and costly, such as on global structure level, the use of numerical and simplified methods should be considered.

At the global structure level, experimental data are scarce and are limited to medium-scale structures. Most collision scenarios are based on a rigid bow striking the side structure of a deformable ship. A test series of rigid bow models colliding with the side of a small-scale deformable ship were conducted by Carlebur [3]. The maximum penetration depth and contact forces were presented and compared with numerical results. Ito et al. [4] presented more detailed experimental data for a test with a rigid stem and bow striking a ship side model. Numerical calculations were conducted and compared with test results. Using numerical simulations, Haris and Amdahl [5] analysed collisions between two types of rigid bows and a deformable double hull tanker. A simplified analytical method was proposed to determine the force history and the internal energy absorbed during collision.

Tests with deformable bows colliding into a rigid wall were reported in [6–9]. The experimental results were compared with the simplified method. Simple procedures to determine the forces created in a deformable bow were also developed by Yang and Caldwell [10] and Kierkegaard [11].

Ship collisions with two deformable bodies, the bow and the side ship, were tested by Endo et al. [8]. The crushing process consisted of two clearly different stages: denting of the side and crushing of the bow. For a one-to-one scale model of ship collisions, numerical simulations were conducted by Kitamura [12] and Yasuda and Imakita [13]. The deformations of the damaged structures were calculated, and the resistances and absorbed energies of the collided structures were determined. No comparisons with the simplified methods were made, so only the numerical results were discussed.

Most of the simplified analytical methods assume one of the ships to be rigid. This procedure may be unsatisfactory because damage interaction between the collided ships was not taken into account. A method to account for the mutual interaction between the striking and the struck ship was proposed by Lutzen et al. [14]. They used force–displacement curves obtained from bow collision against a rigid wall and a rigid bow hitting deformable ship side. Interaction between the two deformable ships was taken into account by applying the ratio of the bow cross sectional areas at two different stages of bow's penetration.

In this paper, an alternative method for the damage interaction analysis of ship collisions involving two deformable bodies is presented. Using the non-linear finite element software LS-DYNA [15,16], the method simulates the collision process to identify the deformation mechanisms, the resistance, and the internal energy dissipation. As stated by Kitamura [17], results from numerical simulations can be considered as virtual experimental data. The numerical simulation results can be used as a reference to verify the proposed analytical model by assessing the crushing forces, the deformations, and the internal energy dissipation. The analysis is limited to the elements in the impact zone, located on the bow and the impacted side.

2. Simplified plastic analysis method

To analyse a complex structure such as a ship, the structure is divided into several basic elements. The resistance of each basic element is evaluated, and all the resistances are added to obtain the total response of the entire structure. Normally, ship structures consist of plate girder intersections and a shell plating. The plate girder intersections can be further categorised into basic elements such as L-sections, T-sections, and cruciforms. Another type of basic element is the web girder, which has no girder intersections and is fixed at both ends.

The resistance of the basic structural elements is calculated by equilibrating the external and internal rates of energy dissipation. In plastic analysis methods, the rate of internal energy dissipation is

determined on the basis of a specified kinematically admissible displacement field. The material is assumed to have a constant flow stress σ_0. To account for the effect of strain hardening, the average value of the yield and ultimate engineering stresses is used.

2.1. Formulae for the basic elements

Formulae to determine the resistance values of basic elements have been proposed by many researchers. The deformation mode and the internal energy dissipation proposed by Wierzbicki and Abramowicz [18] for an L-section inspired many researchers to formulate similar models for other cross sections, such as a T-section and a cruciform (e.g., [6,10]).

Another type of basic element is the web girder with no plate intersections. Various researchers [19–22] have assumed different folding patterns to derive the internal energy, resulting in different mean crushing forces.

For the shell plating, Wang et al. [23] found that the response is strongly dependent on the shape and the strength of the striking bow. The two main indenter shapes used in the analysis were a sphere, which was used by Wang et al. [23], Simonsen and Lauridsen [24], and Lee et al. [25], and a circular parabola, which was used by Zhang [22] and Haris and Amdahl [5]. All the indenters were assumed to be rigid.

In this paper, resistance formulae for cruciforms, web girders, and the shell plating that have been used in previous studies to analyse collisions between a rigid bow and the side of a ship are presented [5]. For the basic T-section, a formula presented by Amdahl [6] is used.

In the following section, each formula is briefly presented.

a. Cruciform

The representative formula was proposed by Hayduk and Wierzbicki [26]:

$$P_c = \frac{20.05}{\lambda} M_0 \left(\frac{C_c}{t_c}\right)^{1/2}, \tag{1}$$

where M_0 is the plastic moment capacity for a unit plate width, and C_c and t_c are the width and thickness of the cruciform, respectively. The effective length factor λ is set to 0.73. The plastic moment capacity is defined as

$$M_0 = \frac{\sigma_0 \cdot t_c^2}{4}. \tag{2}$$

The cruciform resistance P_c in Eq. (1) applies to cruciforms with four identical flanges. In ship structures, cruciforms typically consist of flanges with different widths and thicknesses. The formula is therefore modified, assuming each flange contributes one-fourth of the amount associated with a cruciform with uniform flanges. This gives the following expression:

$$P_{cf} = \sum_{i=1}^{4} \left[\frac{5.01}{\lambda} M_{0i} \left(\frac{C_{cf-i}}{t_{cf-i}}\right)^{1/2} \right], \tag{3}$$

where P_{cf} is the cruciform resistance with unequal flanges, and $C_{cf\text{-}i}$ and $t_{cf\text{-}i}$ are the width and thickness of cruciform flange i, respectively.

b. T-section

For the T-section, a formula by Amdahl [6] is used. The formula is similar to one proposed by Yang and Caldwell [10] for their Mode-ii of a T-section. The crushing force is given by Eq. (4).

$$P_t = \frac{10.98}{\lambda} M_0 \left(\frac{C_t}{t_t}\right)^{1/2}, \tag{4}$$

where C_t and t_t are the width and thickness of the T-section, respectively, and λ and M_0 are as defined in Eqs. (1) and (2).

For T-sections with different flanges, the formula in Eq. (4) is modified as follows:

$$P_{tf} = \sum_{i=1}^{3} \left[\frac{3.66}{\lambda} M_{0i} \left(\frac{C_{tf-i}}{t_{tf-i}}\right)^{1/2}\right], \tag{5}$$

where P_{tf} is the resistance of the T-section, and $C_{tf\text{-}i}$ and $t_{tf\text{-}i}$ are the width and thickness of T-section flange i, respectively.

c. Web girder

The mean crushing force is determined by a formula developed by Zhang [22]:

$$P_w = \frac{11.26}{\lambda} M_0 \left(\frac{b}{t_w}\right)^{1/3}, \tag{6}$$

where b is half the span of the web girder; t_w is the thickness; and λ and M_0 are as described in (1) and (2).

The formula in Eq. (6) applies to web girders supported at both ends and loaded at the middle span. For a web girder with length b that is only supported at one end, the formula becomes

$$P_{wf} = \frac{5.63}{\lambda} M_0 \left(\frac{b}{t_w}\right)^{1/3}. \tag{7}$$

d. Shell plating

A formula for calculating the resistance of the shell plating based on the general shape of the indenter is proposed [5]. The indenter shape is represented by an elliptical paraboloid surface and may cover any bow shape. The resistance is given as follows:

$$P_s(\delta) = \frac{8}{3\sqrt{3}} \cdot \sigma_0 \left(t_{px} \cdot \frac{S_y}{S_x} \left(1 - \frac{\alpha\delta}{S_x}\right)^{-1/2} + t_{py} \cdot \frac{S_x}{S_y} \left(1 - \frac{\beta\delta}{S_y}\right)^{-1/2}\right)\delta \tag{8}$$

where t_{px} and t_{py} are the equivalent plate thicknesses for the x- and y-directions, respectively; S_x and S_y are the plate dimensions in the x- and y-directions, respectively; α and β are the curvatures of the indenter in the x- and y-directions, respectively; and δ is the displacement of the indenter (refer Fig. 1 in Section 2.2).

2.2. Application of the formulae

The resistance formulae for basic elements are applied to the structural components of the ship that are involved in the collision. The actual structures for the struck and striking ships are the ship side and the ship bow, respectively.

A typical double hull ship side is illustrated in Fig. 1. The structure can be divided into the shell plating, the cruciform, and the web girder. For the shell plating, the outer shell, which is in direct contact with the striking bow, is the main focus (Fig. 1b). Eq. (8) is used to calculate the resistance of the shell plating as a function of the displacement of the contact point. The cruciform consists of girder

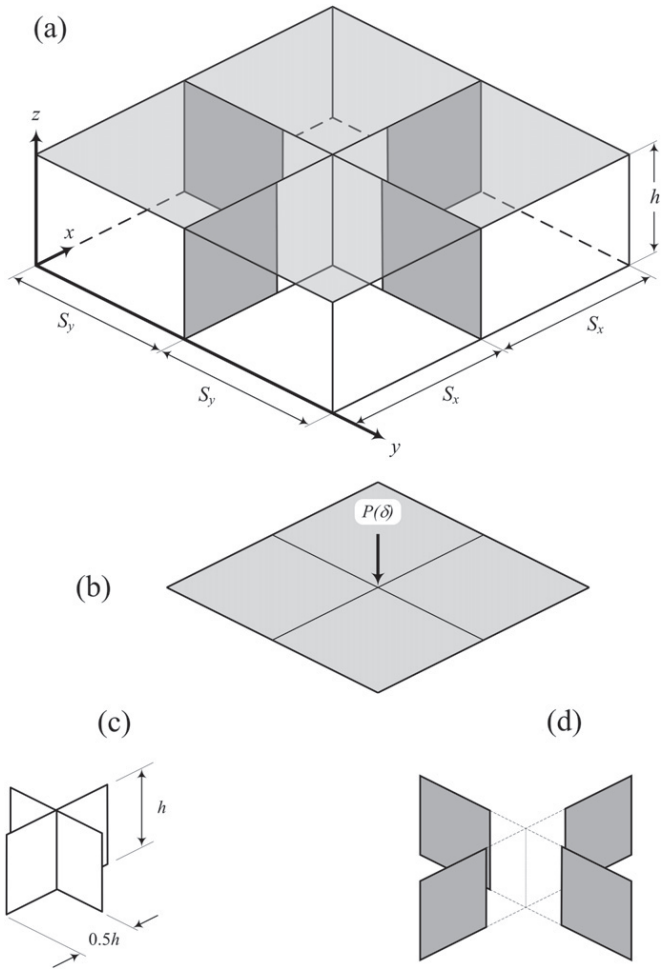

Fig. 1. (a) An example of the structure of the side of a ship: shell plating and one plate girder intersection, (b) shell plating, (c) cruciform with a height equal to the girder height, (d) four remaining sections form web girders.

intersections, and the width is defined to be half of the girder height [27] (Fig. 1c). The remainder of the plate girder is analysed as a web girder with no intersection (Fig. 1d). For these plate girder elements, a constant resistance using Eqs. (3) and (7) is assumed.

The total resistance of the ship side for the example illustrated in Fig. 1 is determined as follows:

$$P_{\text{side}} = P_{\text{cf}} + \sum_{i=1}^{4} P_{\text{wf}} + P_{\text{s}}, \tag{9}$$

where P_{cf}, P_{wf} and P_{s} are the resistances of the cruciform, the web girder and the shell plating as described in Eqs. (3), (7) and (8), respectively.

In the analysis of ship bows, the structure is partitioned into basic elements, as proposed by Amdahl [6], Yang and Caldwell [10], and Yamada and Pedersen [28]. For transverse sections, the total resistance force is determined by summing the resistance values of the cruciforms, the T-sections, and the L-sections. The longitudinal frame, including the longitudinal bulkheads and stringers, the bow shell plating, and its longitudinal stiffener are included in the calculation.

In this paper, the basic elements of a partitioned structure are simplified to consist of cruciforms and T-sections. L-sections, which are mostly L-stiffeners, are modelled as equivalent flat bars with the same height and correct cross section area.

The effect of a shell plating that is curved in the longitudinal and transverse directions is considered in the calculation. Due to the shell inclination, the crushing resistance force is reduced, and a reduction factor for the resistance developed by Wang et al. [29] is adopted. The reduction factor, α_I, is

$$\alpha_I = \frac{1-\sqrt{\sin^2\theta+(1-\lambda)^2\cos^2\theta}}{\lambda\cos\theta}, \tag{10}$$

where θ is the angle between the tangential line of the shell curve and the crushing direction at the instantaneous bow section, and λ is defined as in Eq. (1).

The total resistance of the bow for a given transverse section is calculated using the following formula:

$$P_{\text{bow}} = \sum_{i=1}^{m}\left[\sum_{j=1}^{4}\left[\frac{5.01}{\lambda}M_{0j}\left(\frac{C_{\text{cf}-j}}{t_{\text{cf}-j}}\right)^{1/2}\right]\right]_i + \sum_{p=1}^{n}\left[\sum_{q=1}^{3}\left[\frac{3.66}{\lambda}M_{0q}\left(\frac{C_{\text{tf}-q}}{t_{\text{tf}-q}}\right)^{1/2}\cdot\alpha_{\text{I}-q}\right]\right]_p \tag{11}$$

where m and n are the numbers of cruciforms and T-sections, respectively.

2.3. Verification of the simplified analytical method

The simplified analytical method was applied to the sides of a ship in [5]. Two rigid ship bows hit the same deformable side. The two bows had different curvatures in the vertical and transverse directions. Using the finite element software LS-DYNA, the collision process was simulated; the numerical results were considered as virtual experimental data and used as a reference for the simplified method. For both bow shapes, the results of the simplified method were similar to the numerical values in terms of force–displacement and energy dissipation. Predictions of the initial fracture on the outer shell were also in agreement.

The simplified method of the ship bow model is verified below. Experimental data from Yamada and Pedersen [28] are used as a reference. Tests were conducted with two types of bulbous bows: one with transverse stiffeners (Type-BCG) and one with longitudinal stiffeners (Type-BCL) (Fig. 2). The two models are similar from the top of the bow to the Ring Frame-1; after this structure, the configuration differs. Detailed material properties and specimen dimensions can be found in [28]. Bow crushing was simulated using LS-DYNA.

The experimental data, the simplified analyses and the numerical results for the resistance and the internal energy dissipation are presented in Fig. 3. The curves show that the results of the simplified method and the finite element simulation are similar to the experimental data.

For bow Type-BCG, the average force calculated by the simplified method approximately fits the experimental data for crushing up to Frame-1. After this section, the average force value is lower than the reference. The simplified method result agrees with the experimental data in terms of the internal energy dissipation; the difference is within 10–13%.

For bow Type-BCL, the numerical simulation results are similar to the experimental results at the beginning of crushing. The results deviate after 11 MN of force, corresponding to 300 mm of displacement. In the experiment, the force was continuously increased to 17.5 MN at 400 mm of displacement. For the numerical simulation, the force dropped significantly.

Further investigations to verify the experimental evidence provided by the first author of [28] were conducted. It was found that the portion of the experimental specimen above ring frame-1 did not deform. On the other hand, the numerical simulation shows that progressive folding occurs from the top of the bow, and the force drops earlier than in the experiment due to this folding. The results from two independent numerical simulations conducted by the present authors and the authors of [28] show similar force–displacement curves which indicate that the simulations will predict folding from the top.

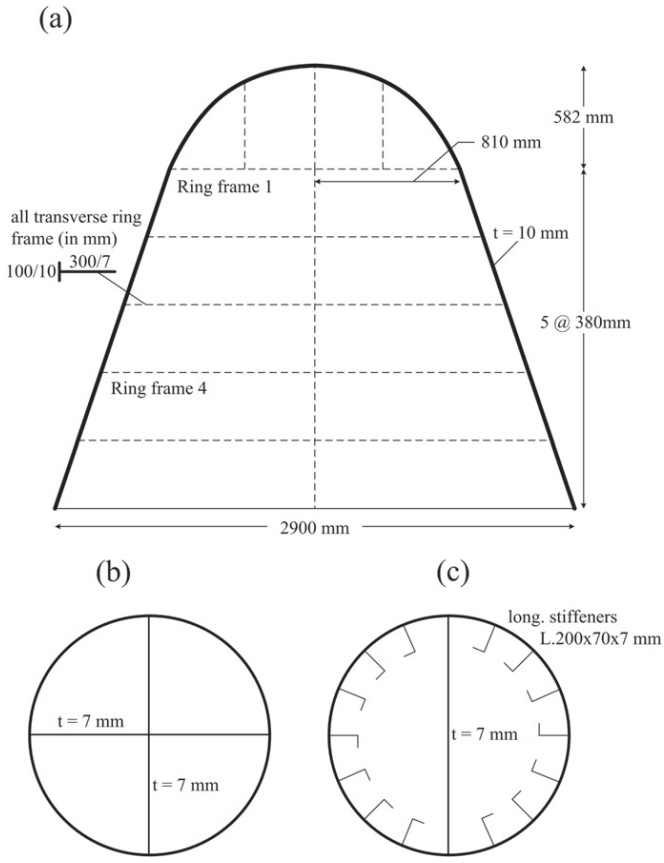

Fig. 2. (a) Bow models in [28]. Transverse ring frames were applied for Type-BCG, for Type-BCL only at Frame-1 and 4. Cross section from Ring Frame-1 until the end of the bow for: (b) Type-BCG, and (c) Type-BCL.

The estimated force at the beginning of crushing is similar with bow Type-BCG because the scantlings are identical until Frame-1. Although the average force does not accurately capture the force history of the experimental data, the internal energy absorbed during this stage is estimated satisfactorily. After Frame-1, longitudinal stiffeners are applied (Fig. 2c). As mentioned in Section 2.2, the free edge of the L-longitudinal stiffener is smeared. Hence, the L-stiffener becomes a plate with an adjusted thickness. During crushing, from Frame-1 to Frame-6, the contribution from the stiffeners to the resistance is constant. A small increase of the resistance between one ring frame and the following one is due to increases in the bow's diameter and the dimensions of the mid-plate. In terms of internal energy, the simplified method fits satisfactorily with the experimental data at the beginning of crushing. For the next indentation, the predictions deviate within 3–11%, on average.

The numerical results and the simplified method results for the resistance and the internal energy dissipation for both types of bows are similar to the experimental data. Consequently, in cases for which experimental data are not available, numerical simulations can be considered as virtual experiments that constitute a reference for the simplified method.

Numerical simulation analyses with the simplified method were conducted for two different bows colliding with a rigid wall. The bows are denoted the Sharp Bow and the Blunt Bow and are identical to the models used in [5] for the case of a rigid bow striking a deformable ship side.

The sharp bow and the blunt bow are shown in Figs. 4 and 5, respectively. The principal properties of the two bows are listed in Table 1. Due to computational time demands, a fine mesh element was

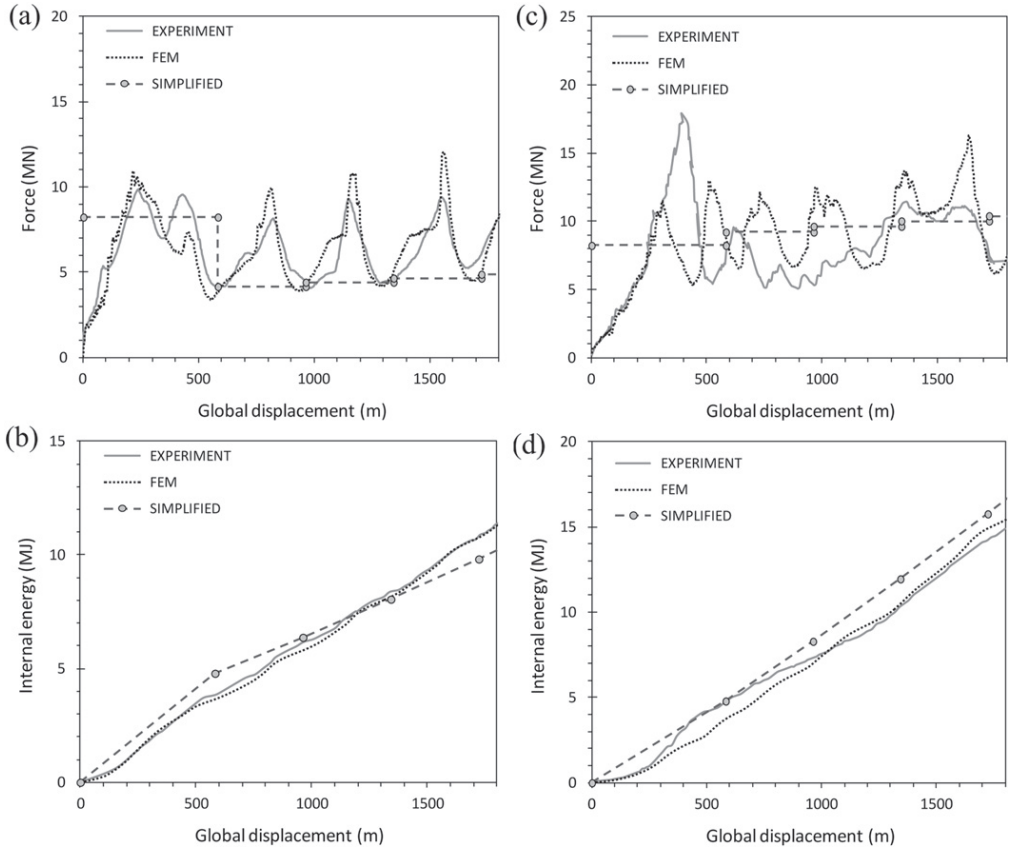

Fig. 3. Results for Bow Type-BCG: (a) resistance force and (b) internal energy. Results for Bow Type-BCL: (c) resistance force and (d) internal energy.

only applied to the front part of the bow where the collision occurs. A coarse mesh was used for the remainder of the structure. A more detailed description of the FE simulation is given in Section 4.

The results for the sharp bow are presented in Fig. 6. The average resistance and internal energy dissipation as estimated by the simplified method agree with the numerical results. The error for the internal energy dissipation is in the range of 7–8%.

The resistance and the internal energy curves for the blunt bow are given in Fig. 7. The results of the simplified method are similar to those of the numerical simulation, with a difference of 7–10%.

3. Ship collision scenarios for integrated analysis

The struck ship is a 120,000 DWT shuttle tanker with six double hull tanks (Fig. 8). The main dimensions are presented in Table 2.

The Sharp Bow and the Blunt Bow are used in the collision simulations. The ship with the sharp bow has a displacement of 126,000 DWT, while the ship with the blunt bow has a displacement of 148,000 DWT (refer Section 2.3).

The striking ships have a constant velocity of 5 m/s when they hit the other ship at a right angle. The first contact point is located at the intersection of the web frame and the stringer, as illustrated in Fig. 8b. For the struck ship, the area in the vicinity of the contact point is emphasised. If the striking bow is substantially crushed, the investigated area may be expanded. For the striking ships, only the

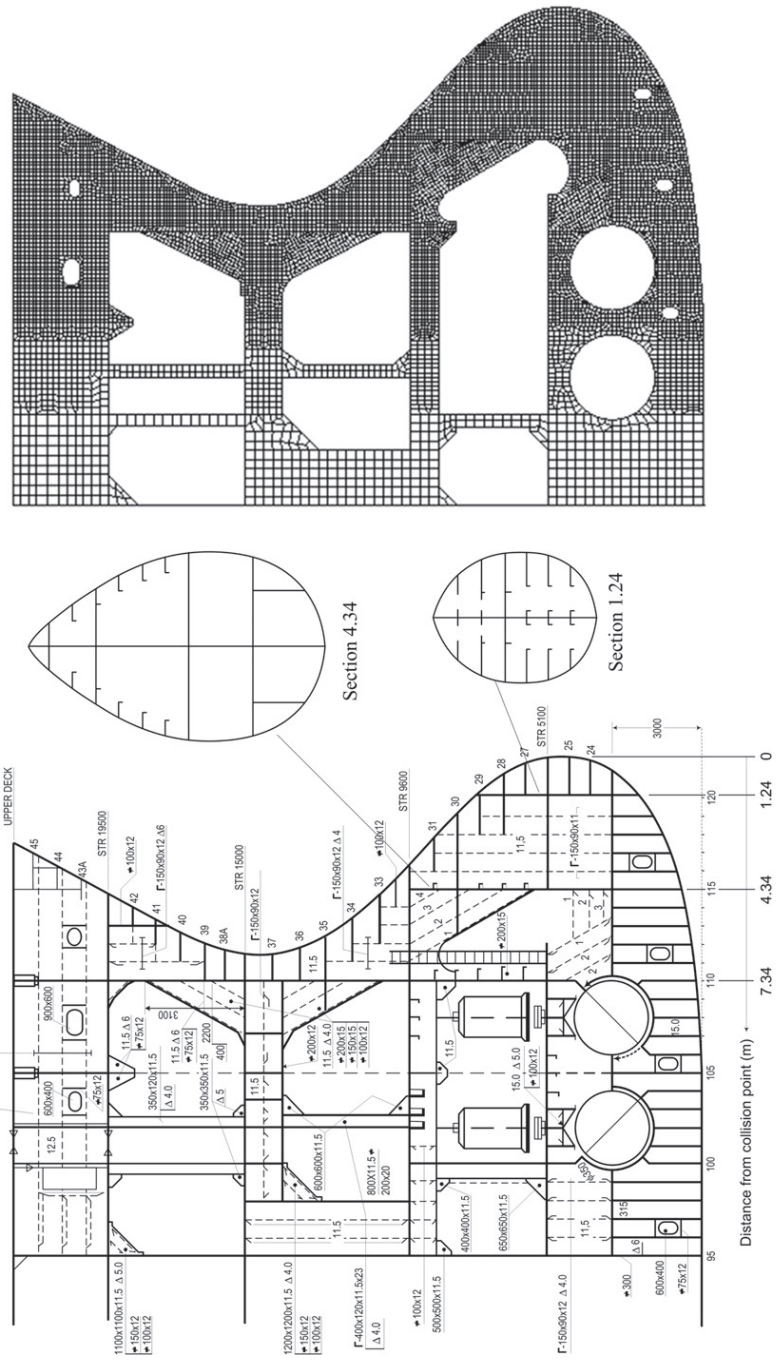

Fig. 4. The sharp bow model.

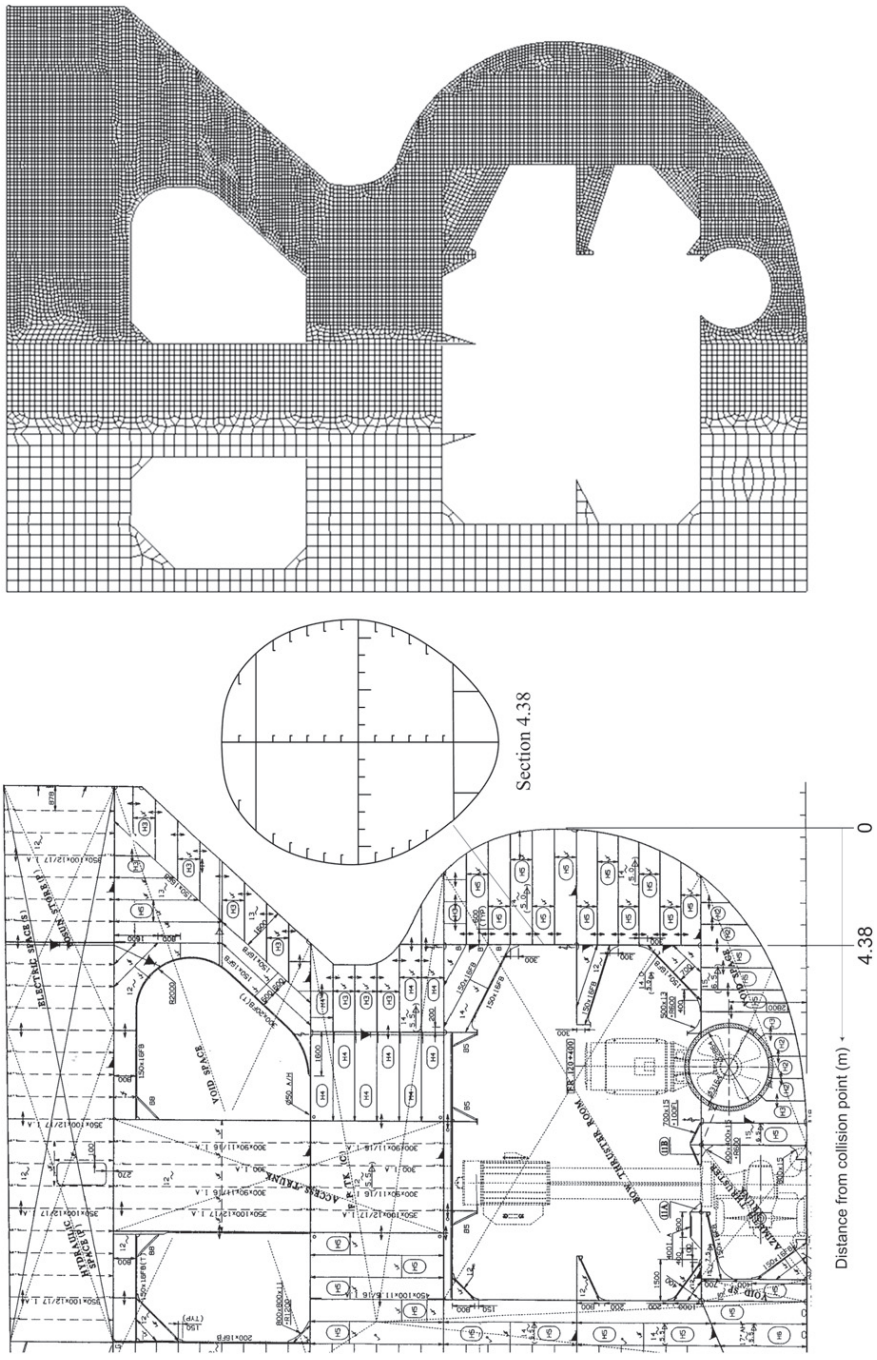

Fig. 5. The blunt bow model.

Table 1
The main properties of the striking ships.

	Sharp bow	Blunt bow
DWT (ton)	126,000	148,000
Length BPP (m)	251.26	262.00
Breadth moulded (m)	40.79	46.00
Depth moulded (m)	22.20	26.60
Draught (m)	16.76	17.00
Web frame-1 to contact point		
Distance (m)	1.24	4.38
Thickness of shell plating (mm)	16 & 18.5	20
Web frame-2 to web frame-1		
Distance (m)	3.10	3.20
Thickness of shell plating (mm)	16 & 18.5	20

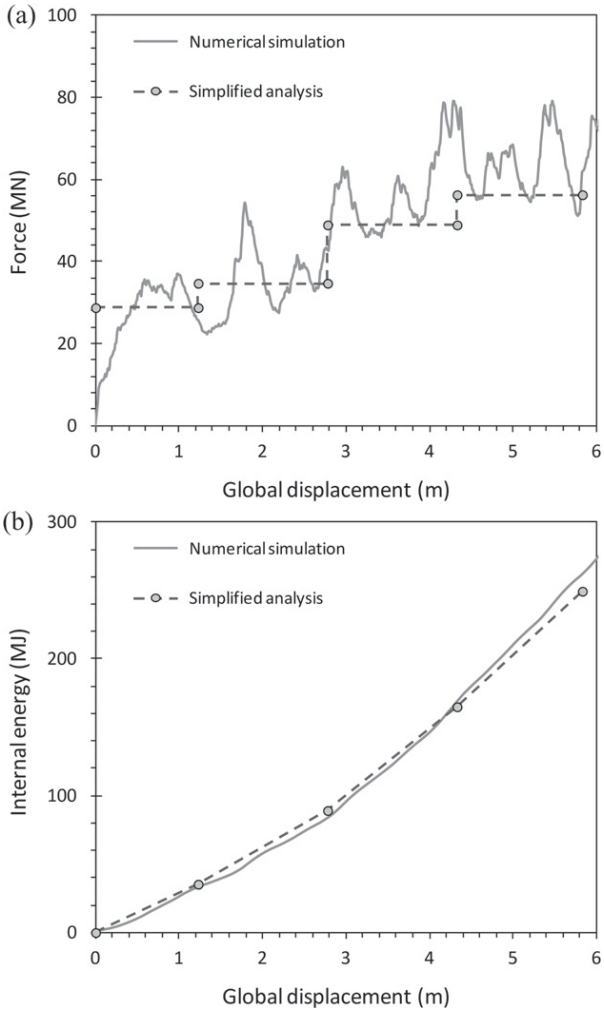

Fig. 6. Resistance force and internal energy dissipation for the sharp bow.

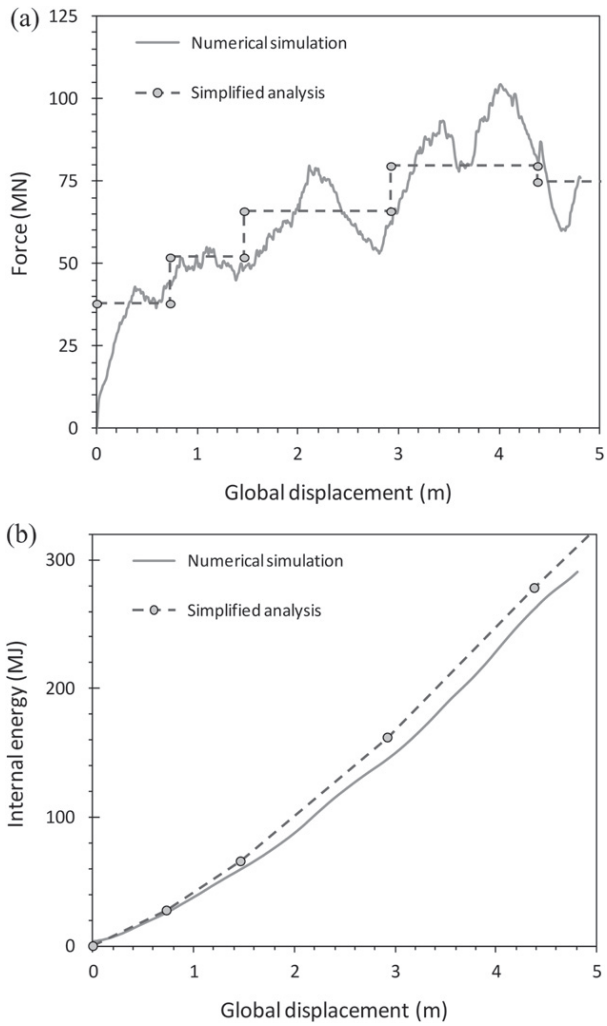

Fig. 7. Resistance force and internal energy dissipation for the blunt bow.

bulbous bow is assumed to be engaged in the collision, while possible contact with the bow superstructure is disregarded. The energy dissipated by the structural elements of the ship that are directly involved is considered.

4. Numerical analysis

4.1. Finite element model

Numerical simulations of the collisions are conducted with the finite element software LS-DYNA. The structures are discretised and modelled with Belytschko-Tsay shell elements [30]. The mesh size must be large enough to obtain a practical simulation time, but sufficiently small to capture the major deformation modes. For the main area in the ship bow and the struck tank between the transverse

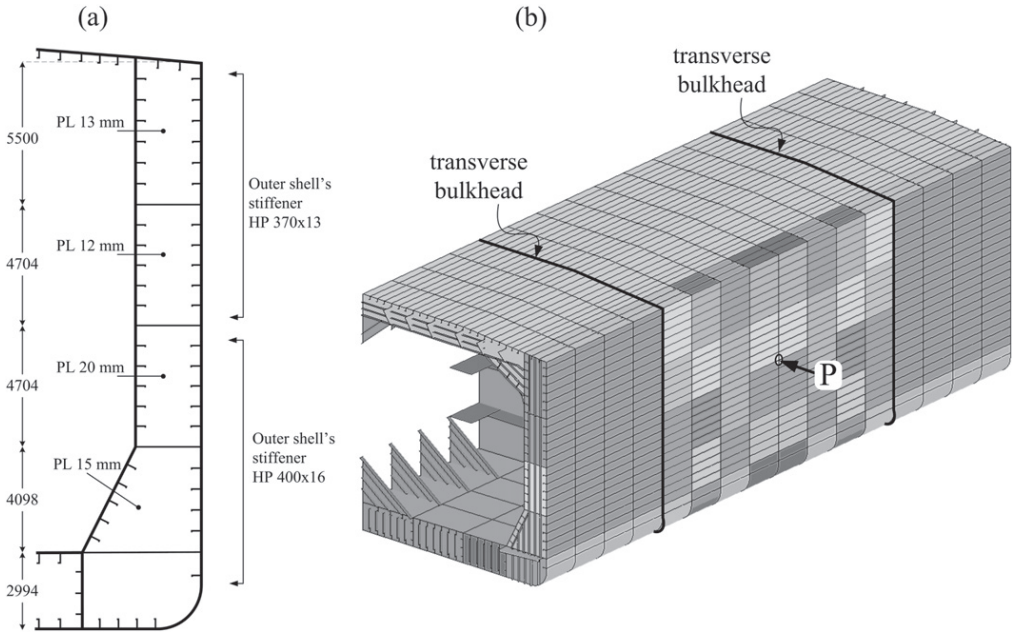

Fig. 8. The struck ship model: (a) cross section, (b) the middle tank of the ship, with two half tanks as the focus of the analysis. Point P is the first contact point with the upper most point of the striking bow.

bulkheads, a fine mesh with an approximate length of 120 mm is applied. For the area with no significant deformation or stress gradients, coarse meshes of 400–800 mm are used. Between the fine and the coarse mesh, transitional mesh sizes of 200 mm are used. Alsos and Amdahl [31] and Tornqvist and Simonsen [32] suggested that the element-length-to-thickness ratio should be within the range of 5–10 so that the local stress and strain fields can be captured well. The mesh in the core area has an element-length-to-thickness ratio of approximately 6–8. In the simulation which involves two deformable ships, the numerical model consists of about 660,000 elements, and the total computation time is three days on a high performance computer (Two Intel Xeon X5690 3.46 GHz, 24 GB RAM).

During the collision process, the displacement on the struck ship is set to be fixed at the centre line. In the side ship model illustrated in Fig. 8b, the fixation is applied for all web frames and two transverse bulkheads. At the ends of the side shell plating, axial displacements are restrained. On the back side of the striking ships, rigid elements that move with a constant velocity are attached.

The steel material is characterised by a power law stress–strain relationship:

$$\sigma = k\left(\varepsilon_{yp} + \varepsilon^{p}\right)^{n}, \tag{12}$$

Table 2
The main dimensions of the struck ship (in m).

Length P.P.	256.60
Breadth moulded	42.50
Depth moulded	22.00
Design draft	15.00
Tank length	32.00
Frame spacing	4.00
Double side width	2.56
Outer shell plating (mm)	17
Horizontal stringer (mm)	12

where ε_{yp} is the elastic strain at the yield point, and ε^{p} is the effective plastic strain. The modulus of elasticity (E) is 207,000 MPa. A nominal yield stress (σ_y) of 235 MPa is used in most of the simulations, with associated constants $k = 740$ and $n = 0.24$ [33]. Material rupture is taken into account according to the Rice-Tracey and Cockcroft–Latham (RTCL) model in [32]. The friction coefficient between the striking and the struck ships is set to 0.3; the same friction coefficient is applied to the internal structure contacts. Implementation of the failure model in LS-DYNA subroutines was conducted by Alsos in [33].

To vary the relative strengths of the colliding and struck ships, analyses are also conducted with augmented yield stresses of $\sigma_y = 355$ MPa and $\sigma_y = 460$ MPa.

4.2. Collision process

During the collision process, both structures are presumed to undergo crushing. Therefore, defining the indentation and crushing of each ship is essential. The displacement of the contact point of collision is defined as the reference for indentations (Fig. 9).

The collision starts at $T = 0$. At time $T = t$, the rigid body attached on the back side of the striking bow has moved forward a distance dRB_t, which is equal to the global displacement. If both the bow and the struck side ship are deformed and indented, as represented by db_t and ds_t, respectively, a simple relationship between the two indentations is obtained:

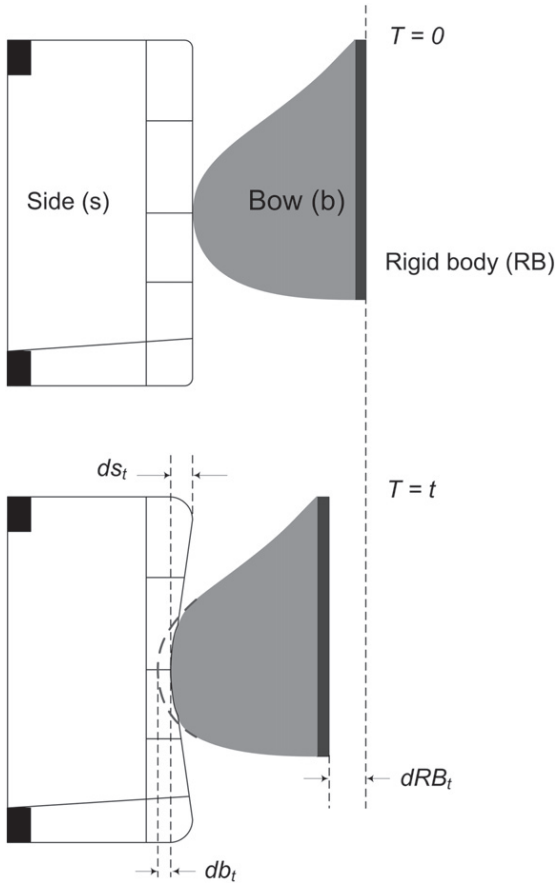

Fig. 9. Indentation measurement for the deformed collided structures.

$$db_t + ds_t = dRB_t, \tag{13}$$

If one of the colliding structures is relatively stronger than the other, the stronger structure undergoes no deformation. The indentation on the weaker structure is thus equal to the global displacement *dRB*.

4.2.1. The sharp bow

Fig. 10 shows the damage process for the collision with the sharp bow. In general, the collision process is categorised into four main stages according to the distribution of damage and the indentations of the striking bow and the struck ship. The deformations of the ships are illustrated in Fig. 11, and the stages are denoted by numbers 1–4. The force-indentation histories are given in Fig. 12.

The first stage is dominated by deformation of the striking bow until the bow has deformed approximately 0.18 m; the damage is mainly localised at the tip of the bow. The struck side is stronger than the bow in this stage. The contact force rises to 8 MN before the bow deformation stops and the damage changes to the side.

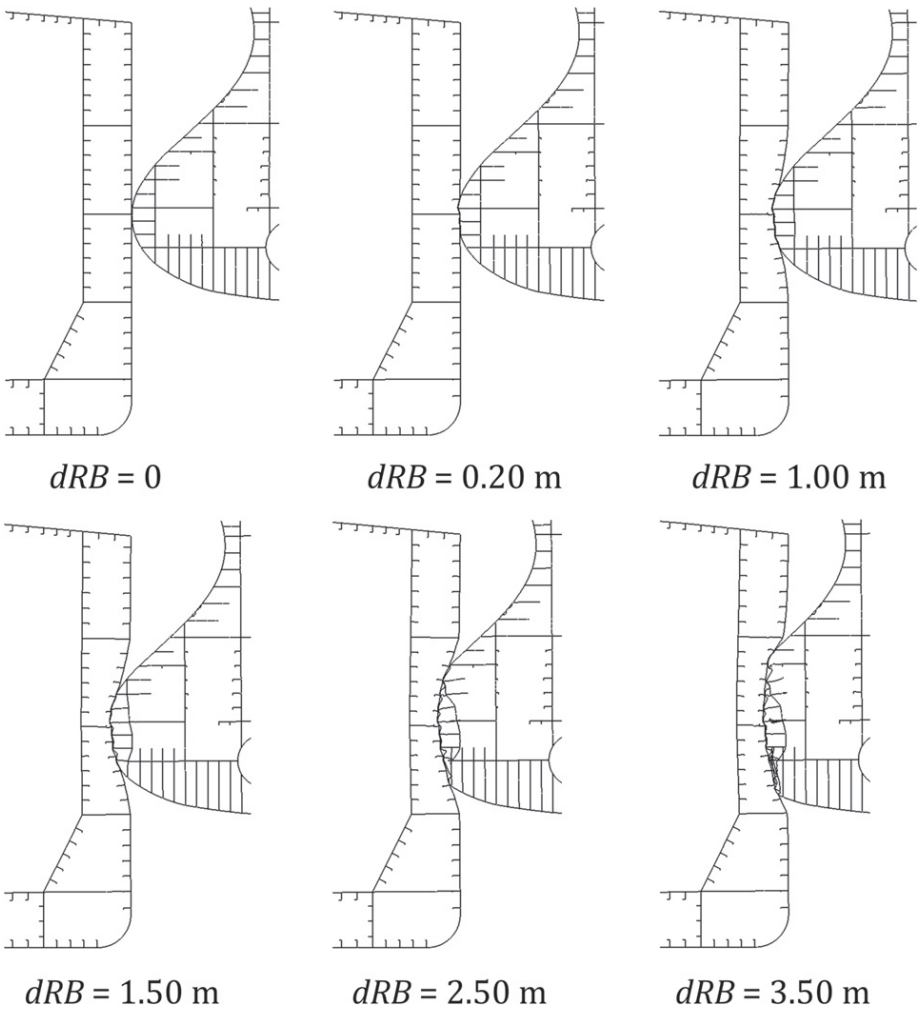

Fig. 10. Longitudinal section of deformed structures for the sharp bow impact.

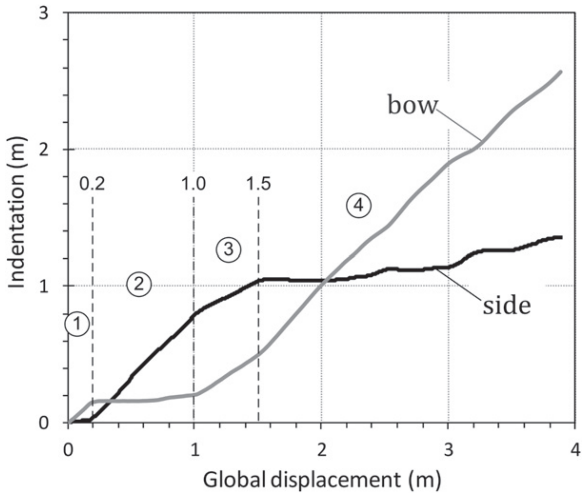

Fig. 11. Indentation histories for the sharp bow case.

Further deformation is specified by a continuous indentation on the ship side due to the increasing resistance of the bow to further deformation (Fig. 11, Stage 2). The stage lasts until the collision force reaches 30 MN, at which point the indentation of the struck side is 0.80 m and the deformation of the bow is 0.20 m. The total collision displacement is 1.00 m.

In the third stage, both structures undergo deformations, and the contact force increases to 40 MN. However, the struck side is relatively stronger than the striking bow, and the indentation of the striking bow increases faster than that of the struck side (Fig. 11, Stage 3). At the end of the third stage, the global displacement is 1.50 m, with the side and the bow being deformed by 1.00 m and 0.50 m, respectively.

In the last stage, the excessive resistance of the side causes the bow to become massively crushed. The bow force drops to 30 MN before rising again to 48 MN. At the end of the simulation, the side has been indented by 1.35 m, and the bow is crushed to 2.57 m (Fig. 13). The side can resist the maximum collision force of 56 MN without rupturing in the vicinity of the contact area. The maximum effective plastic strain for the side is 22%.

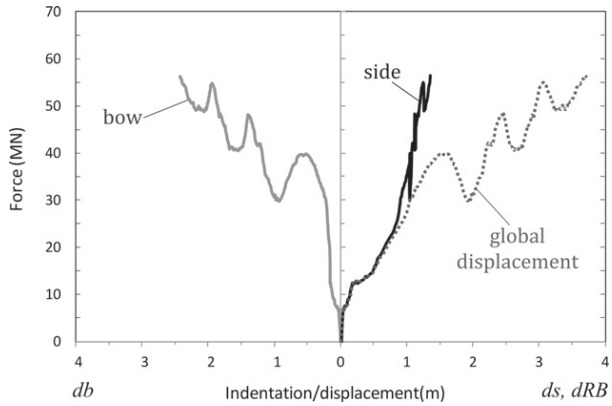

Fig. 12. Force-deformation histories for the sharp bow case.

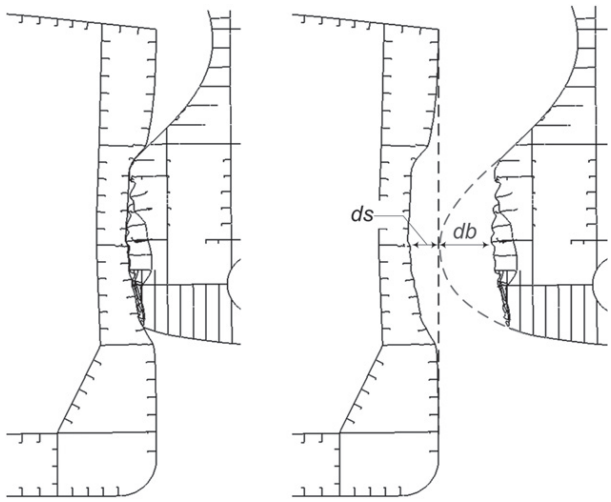

Fig. 13. Deformation at the end of the simulation for the sharp bow. The right figure illustrates the deformations of the bow and the side.

Because the striking bow is the weaker of the two structures, simulations with a relatively stronger bow are conducted by replacing the actual yield strength of the bow, $\sigma_y = 235$ MPa, with higher yield stress values, $\sigma_y = 355$ and 460 MPa. The new simulations show that the bow becomes virtually rigid for both yield stresses (Fig. 14), penetrating the side with minor damages to the bow.

Another simulation is also conducted to obtain a relatively rigid side ship by applying a higher yield stress of 460 MPa and by increasing the thicknesses of the shell plating and the web girders to 24 mm. The results of this scenario are used as an example of a collision between a relatively rigid side ship and a deformable bow.

4.2.2. The blunt bow

The damage process for the blunt bow collision is shown in Fig. 15, and the force-deformation histories are presented in Fig. 16. The bow is much stronger than the side and undergoes minor deformations at the beginning of the collision. The subsequent collision process is dominated by

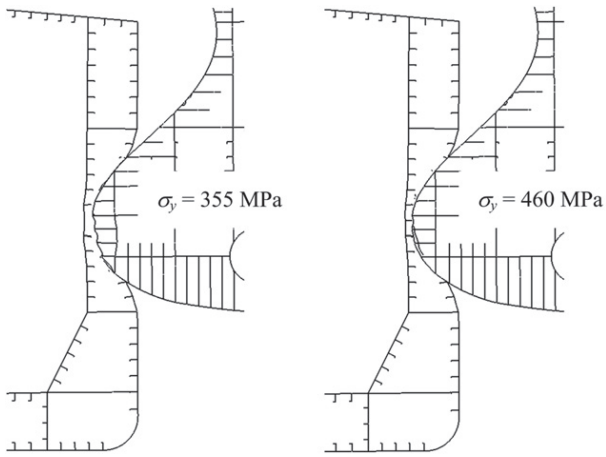

Fig. 14. Damage at 3.50 m of global displacement based on higher stresses on the bow.

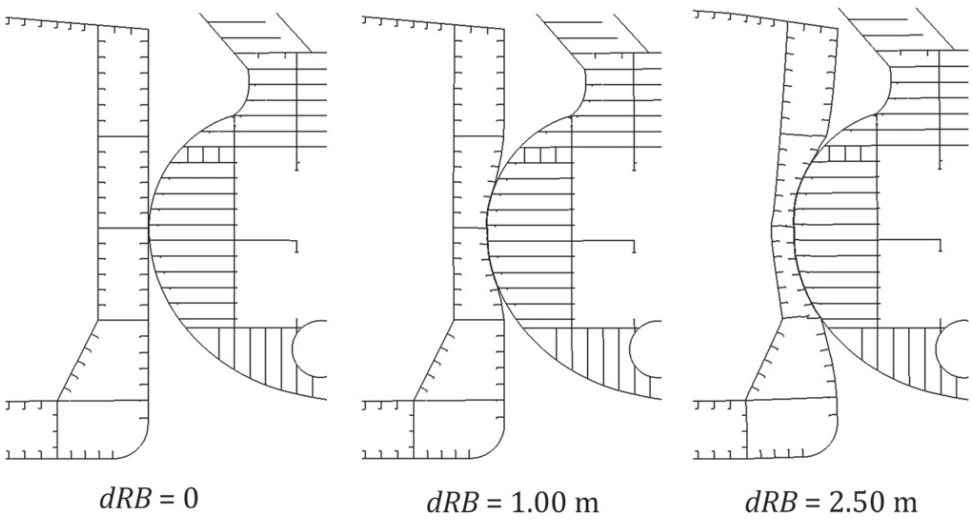

Fig. 15. Collision process of the blunt bow.

indentations on the side. At the late stages of the collision, a global collapse mechanism occurs in the struck side.

As shown in Fig. 17, the force-indentation history of the struck side is similar to the force–total displacement history because the striking bow can resist the collision forces and it behaves like a rigid body.

A new simulation in which the yield stress of the side structure is increased to 355 MPa is conducted to obtain a better balance between the resistance to deformation of the bow and the side. As shown in Fig. 18, the collision process is similar to the first case with the sharp bow, and both structures are damaged. In the beginning, the indentation of the bow is larger than the crushing of the side (Fig. 19). When the global displacement is between 0.20 and 0.95 m, the side is indented while the deformation

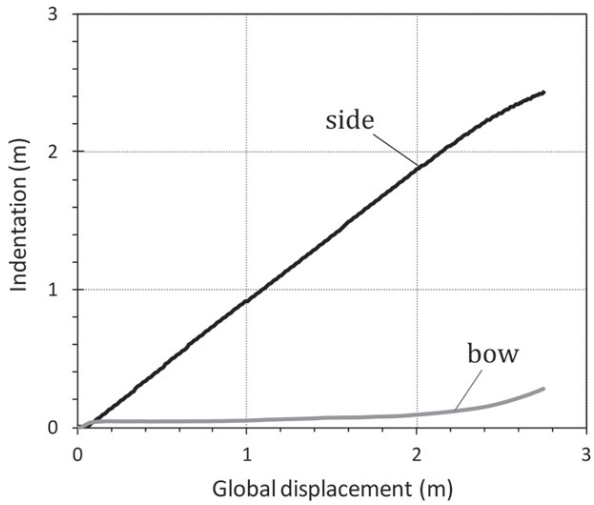

Fig. 16. Indentation history for the blunt bow case.

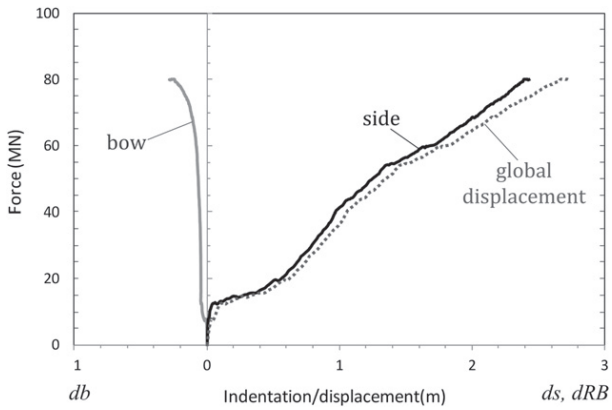

Fig. 17. Force-indentation history for the blunt bow case.

of the bow remains constant. In the next stage, both structures deform until the global displacement is 1.80 m. The last stage is characterised by massive crushing of the bow.

4.3. Type of collision

The collision processes obtained in the numerical simulations can be categorised into three types:

a. Type 1: a relatively rigid bow colliding with a deformable side. In the NORSOK N-004 [34] for the design of offshore structures against ship impacts, this is denoted as *ductile design*.

The bow suffers a minor indentation. The force-indentation of the side is similar to the force-global displacement. This type is observed in the simulations with the blunt bow and the side with the actual yield stress and with the sharp bow with increased yield stresses.

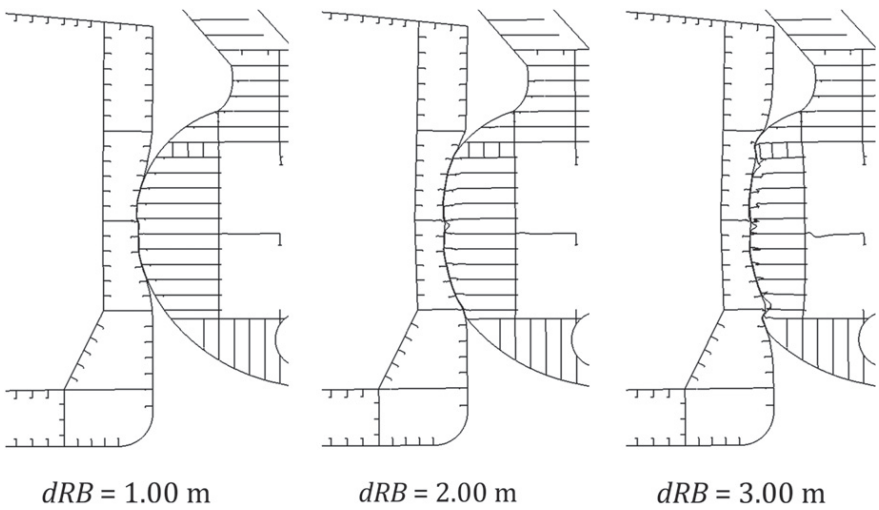

Fig. 18. Collision between the blunt bow and the higher yield stress side ($\sigma_y = 355$ MPa).

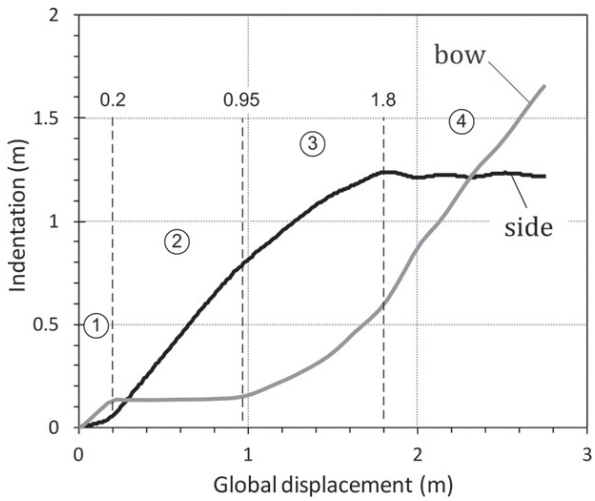

Fig. 19. Indentation history for the blunt bow case with the higher yield stress side ($\sigma_y = 355$ MPa).

b. Type 2: a relatively rigid side colliding with a deformable bow (*strength design* according to NORSOK N-004 [34]).

Small deformations occur in the side. The force-deformation of the bow is similar to the force-global displacement. The collision between the sharp bow and the side with the increased yield stress resulted in this type of collision.

c. Type 3: a deformable bow colliding with a deformable side (*shared energy design* according to NORSOK N-004 [34]).

Both ships are deformed, and the striking and the struck ships deform simultaneously. This category includes the cases in which the damage process may switch between the two structures. The simulation with the sharp bow and the side, both with the actual yield stresses, is an example of this type.

As mentioned, the collision involving one relatively rigid ship, Types 1 and 2, generates a force–deformation relationship in the weak structure that is similar to the force–global displacement. In terms of internal energy, the energy dissipated by the deformed ship is similar to the total collision energy.

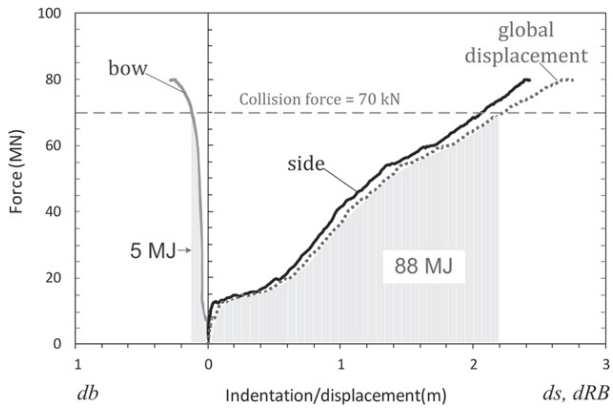

Fig. 20. Energy absorbed for the case of a deformed side ship hit by a relatively rigid bow. Energy dissipated by the side is not shown.

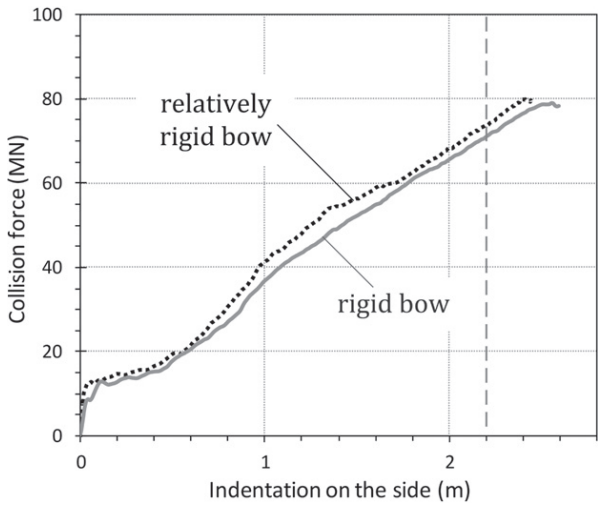

Fig. 21. Force-indentation profile for the relatively rigid and rigid bows.

For example, the deformed side ship that was hit by the relatively rigid bow absorbed 83 MJ of energy for a collision force of 70 kN; the total collision energy was approximately 88 MJ (Fig. 20). This resulted in an energy allocation 94% and 6% for the deformed side and the relatively rigid bow, respectively. Furthermore, replacing the relatively rigid bow with an infinitely rigid bow shows that the force-indentations on the deformed side for both cases are similar (Fig. 21). For a side indentation of 2.20 m, the absorbed energy difference is only 6%.

For Collision Type 3, in which both ships deform, the energy dissipation is shared by the striking bow and the side. The indentation and force history of the sharp bow are shown in Figs. 11 and 12 can be used to determine the internal energy for each stage. The results are presented in Table 3. The predominant energy absorption site switches in each stage between the side and the bow.

5. Simplified analytical method

5.1. Determining type of collision

The collision process is characterised by mutually dependent deformations of the colliding ships. The deformation of each ship is determined by the relative resistance to further deformations. One of the ships may consistently dominate, resulting in Collision Types 1 or 2.

The force created by the blunt bow hitting a rigid wall and the resistance of the side subjected to indentations from the blunt, rigid bow are plotted in Fig. 22. The blunt bow has more resistance to

Table 3
Energy absorption for Collision Type 3.

Global displ. (m)	Stage	Indentation	Energy absorbed (MJ)			% Energy	
			Side	Bow	Total	Side	Bow
0.2	End of Stage 1	Major on bow	0.4	1.2	1.6	26%	74%
0.6	Stage 2	Major on side	6.1	1.4	7.4	82%	18%
1.0	End of Stage 2	Major on side	14.2	2.4	16.6	86%	14%
1.4	Stage 3	Both ships	20.9	10.3	31.2	67%	33%
1.8	Stage 4	Major on bow	22.9	24.4	47.3	48%	52%
2.2	Stage 4	Major on bow	23.2	37.2	60.5	38%	62%

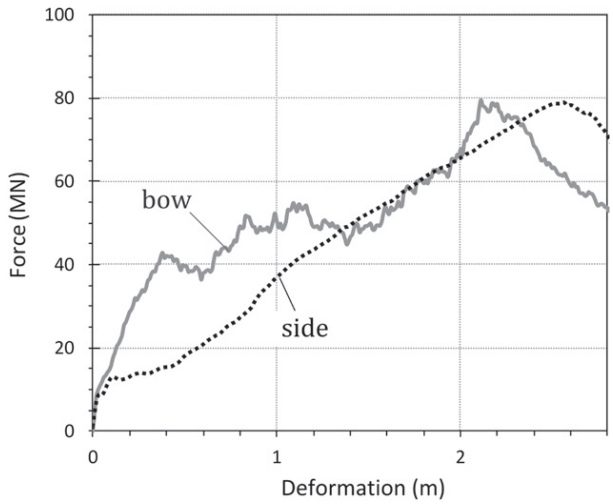

Fig. 22. Force-deformation for the deformable blunt bow hitting a rigid wall and the ship side subjected to indentation by the rigid blunt bow.

deformations than the side for deformations up to 1.30 m. For deformations in the range of 1.30–2.00 m, the resistances of the two structures are approximately equal.

We postulate that the bow will be relatively stronger than the side, resulting in a Type 1 collision. This assumption was proven to be correct, as shown in Fig. 17, which also shows that the bow started to undergo significant deformation when the force reached 60 MN and the side indentation reached 1.80 m. This behaviour is confirmed by the histories in Fig. 22.

In Fig. 23, the resistance of the sharp bow colliding with a rigid wall and the resistance of the side subjected to penetration by the sharp, rigid bow are shown. The resistance of the bow is greater than the side until an indentation of 1.10 m. After this point, the side is stronger than the bow. Because the

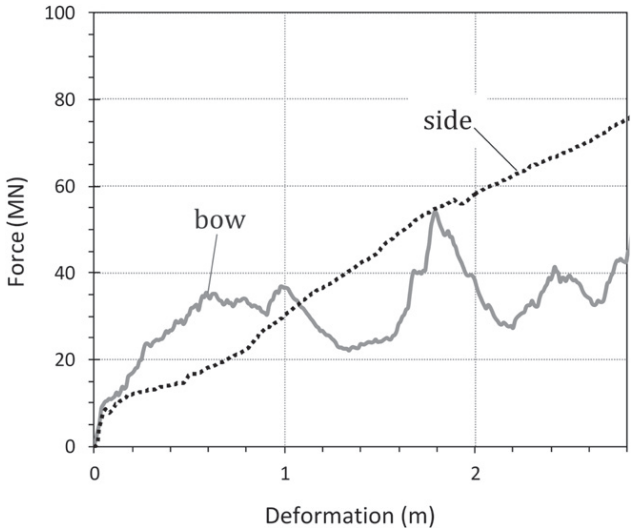

Fig. 23. Force-deformation for the deformable sharp bow colliding with a rigid wall and the side subjected to indentation by the rigid sharp bow. Rupture of ship side is disregarded.

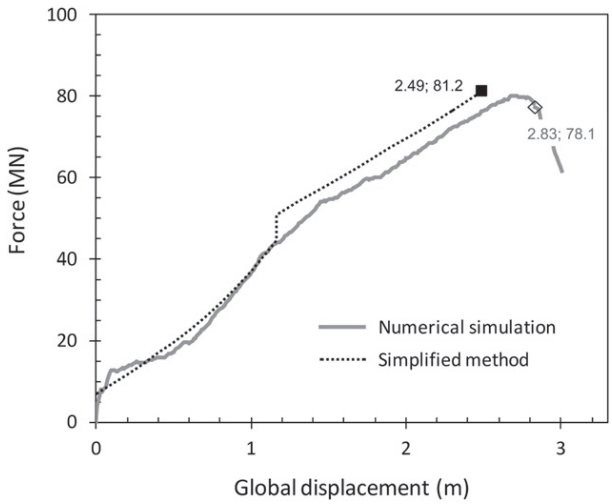

Fig. 24. Resistance of the struck side ship: Numerical simulation and simplified method.

maximum strength values switch from one ship to the other, it is expected that the indentation process will also change ships, resulting in a Type 3 collision.

5.2. Application of the simplified method

The simplified analytical method can be applied when the resistance values of the striking bow and the struck ship are determined and compared.

In the following section, an application for each type of collision is presented. Collision Types 1 and 2, in which one of the ships involved is relatively rigid, are simplified to consider a fully rigid ship colliding with a deformable ship. For Collision Type 3, in which both ships are deformed, a simplified calculation model is used for the striking bow and the struck ship. The virtual experimental data from the FE simulations, described in Section 4, is used as the reference.

5.2.1. Collision Type 1

The collision case between the blunt bow and the realistic side using the FE simulation is presented as an example. In the simplified method, the bow is assumed to be rigid. The side dissipates all collision energy through plastic deformations.

The response of the ship side hit by a rigid bow was discussed by Haris and Amdahl [5]; the procedure and the results for the rigid blunt bow are used in this paper. The resistance of the side was calculated in two stages based on the area of the side plating involved in the collision.

In Fig. 24, the force–displacement histories from the FE simulation and the simplified analytical method are presented. The force predicted with the analytical method agrees with the FE results. The

Table 4
Results for Collision Type 1.

Method	Ship	Displacement (m)	Point of failure force (MN)	Energy (MJ)
FE simulation	Total	2.83	78.1	134
	Ship side	2.46	78.1	112
Analytical method	Ship side	2.49	81.2	114

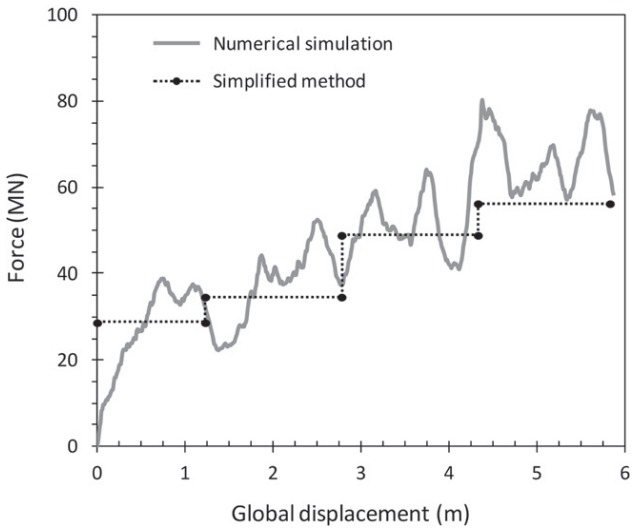

Fig. 25. Resistance of the deformable bow colliding with the strong side ship.

calculations are stopped when the outer shell fails, causing a significant decrease in the side resistance. Table 4 presents a comparison between the two methods at the point of failure.

The outer shell fails at a global displacement of 2.83 m. The displacement predicted by the simplified method is 12% smaller than that predicted by the numerical simulation. The indentation of 0.37 m on the relatively rigid bow is substantial at the failure point, and a more accurate comparison can be made if this indentation is taken into account. The resistance is predicted well, and it is 4% larger than that of the numerical simulation.

Because the bow is assumed to be rigid in Collision Type 1, the side ship only contributes to the internal energy. The side ship absorbs an estimated 114 MJ of energy, of approximately 85% of the total energy during collision. The estimated energy dissipation differs by only 2% from that of the simulation.

5.2.2. Collision Type 2

The collision between the strengthened side and the sharp bow with the actual yield stress is used as an example of Collision Type 2. The strong side is assumed to be rigid, and all energy is absorbed by the deformable bow.

In Section 2.3, the mean crushing force history of the sharp bow that hit a rigid wall is analysed. The results presented in Fig. 6 are compared with the FE simulation for Collision Type 2. The force–displacement histories from both methods are given in Fig. 25, which shows that the simplified method yields a relatively accurate estimate of the mean crushing force.

In Table 5, the internal energy dissipation versus the crushing distances of the frames is presented. Except for the final stage, the difference between the simplified method and the FE results is 3%.

Table 5
Results for Collision Type 2.

Crushing distance	Internal energy		
	FE (MJ)	Simplified (MJ)	Difference
1.23 m	34	35	+3%
2.78 m	92	89	−3%
4.33 m	171	165	−3%
5.83 m	272	249	−8%

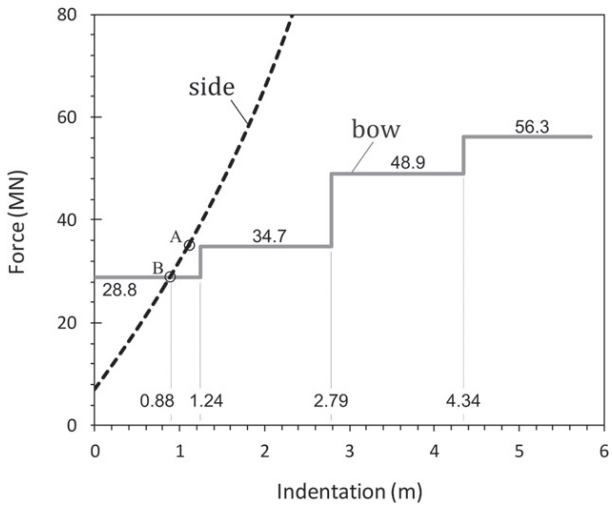

Fig. 26. Independent resistance values of the two ships when colliding with the rigid ones.

5.2.3. Collision Type 3

In Collision Type 3, two deformable ships are involved. The case is represented by a collision between the sharp bow and the ship side with the actual yield stresses applied. As described in Section 4.2.1, the damages occur on both ships, and the damage evolution is governed by the relative resistance of the two ships.

The resistance of the sharp bow hitting a rigid wall (refer Section 2.3) is used for this type of collision. The resistance of the ship side struck by the similar rigid sharp bow was calculated by Haris and Amdahl [5]. Relevant formulae for the cruciform (Eq. (3)), the web girder (Eq. (7)), and the shell plating (Eq. (8)) were used. The resistance of the shell plating is a function of the shape of the bow. Because the bow is indented during the collision, its effective shape changes, and the curvatures of the shape in Eq. (8) must be updated.

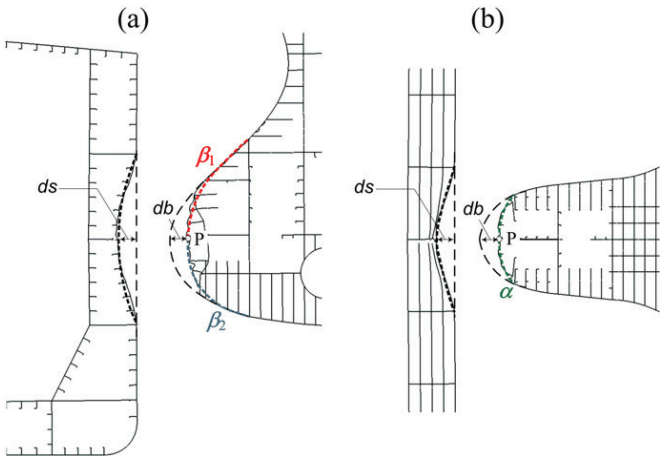

Fig. 27. Indentation at the global displacement $dRB = 2.12$ m: (a) Side view and (b) top view. The bold dashed lines are simplified deformation patterns.

Table 6
Curvatures of the bow.

Direction	Initial curvatures	New curvatures
Horizontal (α)	0.79	2.19
Vertical upper (β_1)	1.25	3.47
Vertical lower (β_2)	1.06	2.93

In Fig. 26, the sole resistances of the two colliding ships are presented. The resistance of the side ship is calculated based on the initial shape of the sharp bow. Failure on the ship side occurs at point A (1.10 m; 35.1 MN) if fracture is considered.

The simplified method calculates the resistance of the bow as a step-wise curve. The bow is thus assumed to have a constant resistance for each web frame spacing. From the beginning of the collision until the indentation is at web frame-1, the resistance of the bow is 28.8 MN, which is greater than that of the side. The indentation will therefore initially occur in the ship side. In this stage, the global displacement *dRB* is equal to the side indentation *ds*.

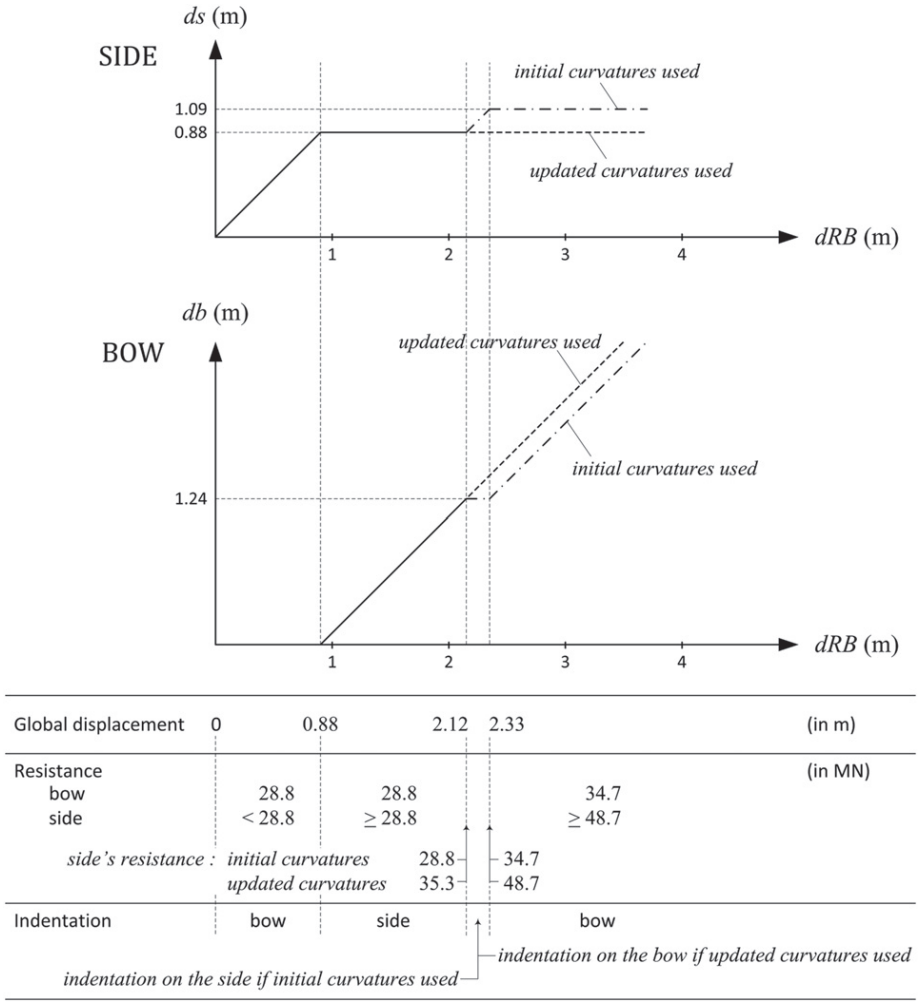

Fig. 28. Indentation process in Collision Type 3.

The resistance of the ship side increases as the indentation increases, and it is equal to the resistance of the bow at an indentation of 0.88 m (Point B in Fig. 26). At this point, the resistance of the side ship becomes greater than that of the bow. Consequently, the indentation process now switches to the bow.

As long as the ship side is stronger than the bow, the indentation occurs in the bow. Due to the deformation, the shape of the bow changes progressively; the effective curvature of the bow gradually increases. As the curvature of the bow increases, the resistance of the side ship also increases (refer Eq. (8)).

The analysis of the bow curvature focuses on the deformation state correspondence, which occurs at 1.24 m. At this deformation, the resistance of the bow shifts from 28.8 MN to 34.7 MN, and the indentation can switch back to the bow.

The indentations on both ships are illustrated in Fig. 27. The side has been indented to 0.88 m, and the global displacement is $dRB = 2.12$ m. The bow indentation is 1.24 m. This gives the new coordinate of the bow tip, *P*, which is used to calculate new effective curvatures of the bow shape using the elliptical paraboloid formula proposed by Haris and Amdahl in [5]. The resistance of the side ship is calculated using these new curvatures.

The initial curvatures based on the original shape of the bow and the new curvatures based on the deformed bow are presented in Table 6. The curvatures change significantly after indentation of the bow. The resistance of the ship side is calculated for the current indentation and curvatures to be 35.3 MN, which is slightly greater than the bow's resistance of 34.7 MN.

The indentation switches to the side if the side resistance using the initial curvatures (28.8 MN) is used. This occurs until the side's resistance rises to 34.7 MN at 1.09 m. Beyond this, the bow is indented again because the side becomes stronger.

However, the actual resistance of the side is 35.3 MN because the bow shape has changed. Because the side is continuously stronger than the bow, the indentation process does not switch to the side; rather, it remains on the bow.

The bow is continuously damaged for the next indentation steps, creating an even larger curvature of the bow shape. This causes the side to have a larger resistance than the bow for the rest of collision. In Fig. 28, the indentation process is summarised.

Failure does not occur in the side because the indentation stops at a deformation of 0.88 m. This is less than the displacement for which failure is predicted, 1.10 m. If the indentation of the side is assumed to continue until 1.09 m, which is near the failure level, the updated failure displacement is calculated using the new shape of the bow. Larger bow curvatures correspond to larger failure displacements (refer to the formula by Haris and Amdahl [5]). The failure is predicted to occur at a side indentation of 1.84 m.

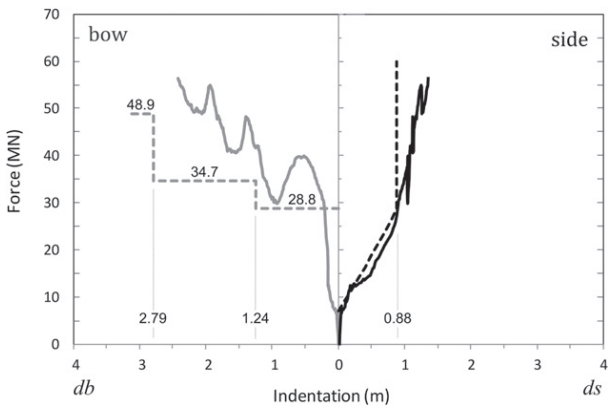

Fig. 29. Force-indentation curves for each collided ship. The dashed and the bold lines represent the simplified and numerical curves, respectively.

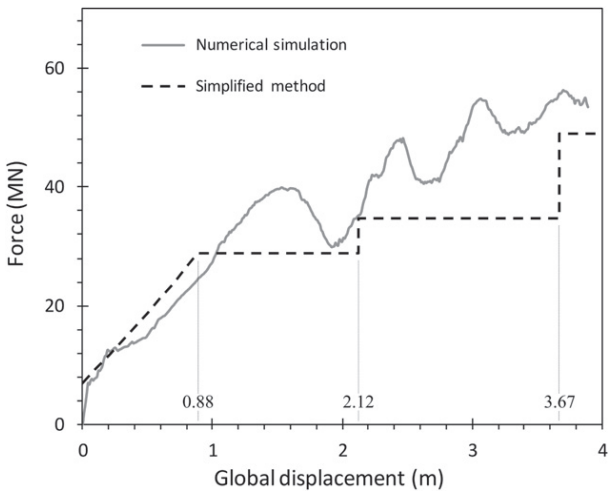

Fig. 30. Force-global displacement for Collision Type 3: Numerical and simplified methods.

The illustration in Fig. 28 shows the force-indentation curves for both ships, with the updated curvatures for the bow. The collision process is simplified into two stages: in the first, a side indentation is considered for a global displacement of less than 0.88 m, and in the second, a bow indentation is considered for the remainder of the collision.

The force-indentation curves are presented with the numerical results in Fig. 29. For the side (right curves), the force increases to 28.8 MN for a displacement of 0.88 m, similar to the side curve in Fig. 26. After this point, no further indentation occurs on the side, and the curve resistance is represented by the vertical line in this stage. The force-indentation curve for the bow is identical to the one given in Fig. 26.

The contact force during collision is plotted against the global displacement in Fig. 30. The contact forces for each stage are taken as the minimum values of the resistances of the side and the bow. In the first stage, the contact force is equal to the side resistance, and the bow is stronger than the side and has no indentation. The bow starts to deform after the first stage, and the side is rigid, resulting in a contact force equal to the resistance of the bow.

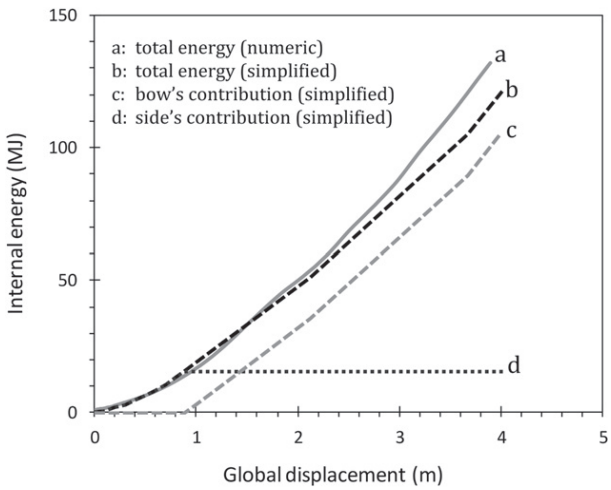

Fig. 31. Internal energy for Collision Type 3.

In Fig. 31, the internal energies from the numerical simulation and the simplified method are presented. The side contributes to energy dissipation only in the beginning of the collision; it stops after 0.88 m of displacement. After this point, only the bow contributes to energy dissipation. The side does not absorb any energy.

In general, the two methods agreed well, especially for global displacements of less than 2.00 m. The predictions deviate for larger displacements because the side suffers some indentations in the numerical simulations. At the end of the simulation, the simplified method under predicts the energy by roughly 13%.

6. Conclusions

An integrated analysis of ship-to-ship collisions was presented in this paper. Numerical simulations using the finite element software LS-DYNA were conducted to produce virtual experimental data, which were used as the reference for the proposed simplified analytical method. In the numerical simulation, the collision process for each of the colliding ships can be visualised, and the individual contributions to the total energy dissipation can be determined.

The numerical simulations were verified against existing experimental data in the literature. The damage and energy dissipation of the ship predicted by the simplified analytical method were compared with both numerical simulations and experimental data. The three methods agreed for the model of the ship bow. Therefore, the finite element simulation is a reliable reference when experimental data are not available.

In the proposed simplified analytical method, the structural system is partitioned into four basic elements, the shell plating, the cruciform, the T-section, and the web girder. Existing analytical formulae are used to determine the resistance to deep deformations of the basic elements. For the ship side, the total resistance, which varies with the indentation of the side, is based on the shell plating, cruciforms, and web girders. For the bow, the resistance increases in a step-wise manner based on the cruciforms and web girders for each space web frame.

Two actual ship bows striking a ship side were analysed. The yield stresses were varied artificially to obtain variations in the relative strength of the bow and the side. Generally, ship collisions can be categorised into three types: Type 1 – collisions between a relatively rigid bow and a deformable side, Type 2 – collisions between a relatively rigid side and a deformable bow, and Type 3 – collisions in which both ships deform and share the energy absorption.

The analytical method and the numerical simulations showed good agreement for Type 1 and 2 collisions. For Type 3 collisions, the damage and energy dissipation can switch between ships during the collision, and the proposed method was able to account for such switches satisfactorily.

The simplified method can be adopted and modified if the relative resistance between two ships changes. By applying the proposed method, ship-to-ship right angle collisions can be quickly and accurately conducted. Compared to the numerical simulation which can take days to complete, the simplified method needs only a few hours. Regarding the accuracy, the simplified method differs in the range of 2–13% to the numerical simulation. In the future, the proposed simplified method should be further developed to account for varying angles of collision.

Acknowledgement

The authors wish to thank the Research Council of Norway for financial support through the Strategic University Program (SUP) “ScenaRisC&G”, Norwegian University of Science and Technology. The authors would also like to thank Dr. Yasuhira Yamada from the National Maritime Research Institute of Japan for his valuable discussions and supporting materials.

References

[1] Minorsky VU. An analysis of ship collisions with reference to nuclear power plants. J Ship Res 1959;3(2):1–4.
[2] Hong L. Simplified analysis and design of ships subjected to collision and grounding. Doctoral thesis. Department of Marine Technology, Norwegian University of Science and Technology, Trondheim, Norway; 2009.
[3] Carlebur AFC. Full-scale collision tests. Saf Sci 1995;19(2, 3):171–8.

[4] Ito H, Kondo K, Yoshimura N, Kawashima M, Yamamoto S. A simplified method to analyse the strength of double hulled structures in collision. J Soc Naval Architects Jpn 1984;156:283–96.
[5] Haris S, Amdahl J. An analytical model to assess a ship side during a collision. Ships Offshore Struct 2012;7(4):431–48.
[6] Amdahl J. Energy absorption in ship-platform impacts. Doctoral thesis. Department of Marine Technology, Norwegian University of Science and Technology, Trondheim, Norway; 1983.
[7] Hagiwara K, Takanabe H, Kawano H. A proposed method of predicting ship collision damage. Int J Impact Eng 1983;1(3): 257–79.
[8] Endo H, Yamada Y, Kitamura O, Suzuki K. Model test on the collapse strength of the buffer bow structures. Marine Struct 2002;15(4, 5):365–81.
[9] Yamada Y, Endo H. Collapse mechanism of the buffer bow structure on axial crushing. Int J Offshore Polar Eng 2005;15(2): 147–54.
[10] Yang PDC, Caldwell JB. Collision energy absorption of ships' bow structures. Int J Impact Eng 1988;7(2):181–96.
[11] Kierkegaard H. Ship bow response in high energy collisions. Marine Structures 1993;6(4):359–76.
[12] Kitamura O. Buffer bow design for the improved safety of ships. In: Ship structure symposium on ship structures for the new millennium. Arlington, VA: Supporting Quality in Shipbuilding; 2000.
[13] Yasuda A, Imakita A. Numerical study on structural arrangement effects on collision resistance of hull girders. In: Proceedings of the 4th international conference on collision and grounding of ships, Hamburg, Germany; 2007. p. 117–122.
[14] Lutzen M, Simonsen BC, Pedersen PT. Rapid prediction of damage to struck and striking vessels in a collision event. In: Ship structure symposium on ship structures for the new millennium. Arlington, VA: Supporting Quality in Shipbuilding; 2000.
[15] Hallquist JO. LS-DYNA theory manual. Technical report. Livermore, CA: Livermore Software Technology Corporation; 2006.
[16] Hallquist JO. LS-DYNA keyword user's manual. Technical report. Livermore, CA: Livermore Software Technology Corporation; 2007.
[17] Kitamura O. FEM approach to the simulation of collision and grounding damage. Marine Struct 2002;15(4, 5):403–28.
[18] Wierzbicki T, Abramowicz W. On the crushing mechanics of thin-walled structures. J Appl Mech 1983;50:727–34.
[19] Hong L, Amdahl J. Crushing resistance of web girders in ship collision and grounding. Marine Struct 2008;21(4):374–401.
[20] Simonsen BC, Ocakli H. Experiments and theory on deck and girder crushing. Thin-walled Struct 1999;34(3):195–216.
[21] Wang G, Ohtsubo H. Deformation of ship plate subjected to very large load. In: Proceedings of sixteenth international conference on offshore mechanics and arctic engineering, Yokohama, Japan, vol. II; 1997. p. 173–80.
[22] Zhang S. The mechanics of ship collisions. Doctoral thesis. Department of Naval Architecture and Offshore Engineering, Technical University of Denmark, Lyngby, Denmark; 1999.
[23] Wang G, Ohtsubo H, Arita K. Large deflection of a rigid-plastic circular plate pressed by a sphere. J Appl Mech 1998;65(2): 533–5.
[24] Simonsen BC, Lauridsen LP. Energy absorption and ductile failure in metal sheets under lateral indentation by a sphere. Int J Impact Eng 2000;24(10):1017–39.
[25] Lee YW, Woertz JC, Wierzbicki T. Fracture prediction of thin plates under hemi-spherical punch with calibration and experimental verification. Int J Mech Sci 2004;46(5):751–81.
[26] Hayduk RJ, Wierzbicki T. Extensional collapse modes of structural members. Comput Struct 1984;18(3):447–58.
[27] Haris S, Amdahl J. Crushing resistance of a cruciform and its application to ship collision and grounding. Ships Offshore Struct 2012;7(2):185–95.
[28] Yamada Y, Pedersen P. A benchmark study of procedures for analysis of axial crushing of bulbous bows. Mar Struct 2008; 21(2, 3):257–93.
[29] Wang G, Katsuyuki S, Ohtsubo H. Predicting collision strength of bow structure. In: International conference on technologies for marine environment preservation, Tokyo, Japan; 1995. p. 40–43.
[30] Belytschko T, Liu WK, Moran B. Nonlinear finite elements for continua and structures. Chichester (England): JohnWiley & Sons; 2006.
[31] Alsos HS, Amdahl J. On the resistance of tanker bottom structures during stranding. Mar Struct 2007;20(4):218–37.
[32] Tornqvist R, Simonsen BC. Safety and structural crashworthiness of ship structures; Modelling tools and application in design. In: the third international conference on collision and grounding of ships, Izu, Japan; 2004. p. 285–294.
[33] Alsos HS, Amdahl J, Hopperstad OS. On the resistance to penetration of stiffened plates, part II: numerical analysis. Int J Impact Eng 2009;36(7):875–87.
[34] NORSOK N-004. Design of steel structures, appendix A. Design Against Accidental Actions; 2004.

Glossary

b: half span of web girder
db: indentation on the bow
dRB: global displacement
ds: indentation on the ship side
k, n: constants in the steel material model
t_c: thickness of identical flanges of cruciform
t_t: thickness of identical flanges of T-section
$t_{cf\text{-}i}$: thickness of flange ith of cruciform
$t_{tf\text{-}i}$: thickness of flange ith of T-section
$t_{px,y}$: equivalent plate thickness for x- and y-directions of the shell plating
t_w: thickness of web girder
C_c: width of identical flanges of cruciform

$C_{cf\text{-}i}$: width of flange ith of cruciform
C_t: width of identical flanges of T-section
$C_{tf\text{-}i}$: width of flange ith of T-section
M_0: plastic moment capacity for a unit plate width
$M_{0\text{-}i}$: plastic moment capacity of flange ith for a unit plate width
P_{bow}: total resistance of bow
P_c: resistance of cruciform with four identical flanges
P_{cf}: resistance of cruciform with different thickness and width flanges
P_s: resistance of shell plating
P_{side}: total resistance of ship side
P_t: resistance of T-section with three identical flanges
P_{tf}: resistance of T-section with different thickness and width flanges
P_w: resistance of web girder which its span is $2b$ and supported at both ends
P_{wf}: resistance of web girder which its span is b and supported at one end
S_x, S_y: half dimension of shell plating in x- and y-directions
α, β: indenter curvatures in x- and y-directions
α_1: reduction factor for curved shell plating on the bow cross section
δ: displacement of indenter, indentation on the shell plating
ε^P: effective plastic strain
ε_{yp}: elastic strain at yield point
λ: effective length factor of crushed section
θ: angle between tangential line of shell curve and crushing direction at bow cross section
σ_0: flow stress, $\sigma_0 = (\sigma_y + \sigma_u)/2$
σ_y: yield stress of material
σ_u: ultimate stress of material

Appendix B

Calculation of the resistance of the double hull model and the bows

Appendix B-1

Application of the resistance formula to a double hull of ship side model

Experimental data from Wang et al (2000a)

- Model of the test

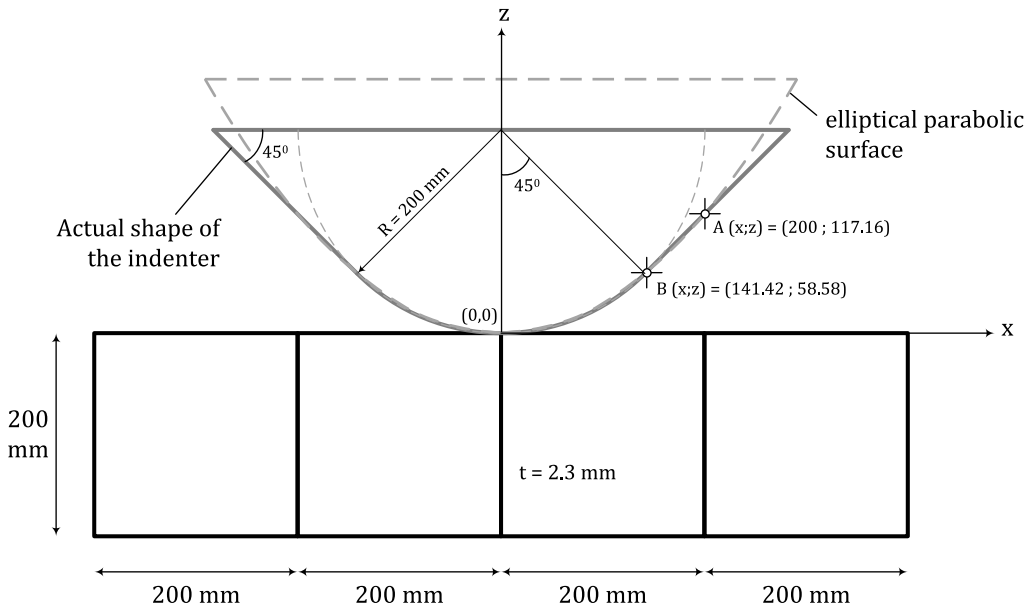

Material properties:

$\sigma_y = 282$ MPa; $\sigma_u = 400$ MPa; $\sigma_0 = 341$ MPa.

$M_0 = 451$ N.mm/mm , $\lambda = 0.73$

- Loading process

STEP-1

S_x = 200 mm; S_y = 200 mm

Deformation of the 2x2 Panels, i.e., 400 x 400 mm:

Basic elements are 1 cruciform, 4 half web girders, and shell plating.

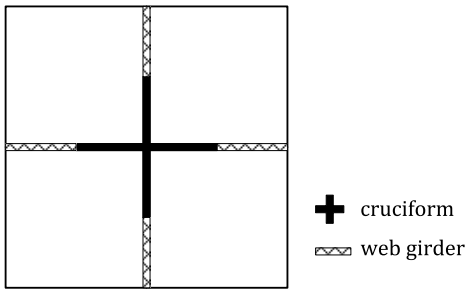

1. Cruciform $P_c = \frac{20.05}{\lambda} M_0 \left(\frac{100}{2.3}\right)^{1/2} = 81673$ N

2. Web girder $P_{wf} = 4 \cdot \left[\frac{5.63}{\lambda} M_0 \left(\frac{100}{2.3}\right)^{1/3} \right] = 48920$ N

3. Shell plating $P_s(\delta) = \frac{8}{3\sqrt{3}} \cdot \sigma_0 \left(t_{px} \cdot \frac{S_y}{S_x} \left(1 - \frac{\alpha\delta}{S_x}\right)^{-1/2} + t_{py} \cdot \frac{S_x}{S_y} \left(1 - \frac{\beta\delta}{S_y}\right)^{-1/2} \right) \delta$

At the *x*-*z* plane, Eq. 3.9 (page 29) becomes

$$z = \frac{x^2}{(\alpha \cdot S_x)}. \qquad \text{B1.1}$$

By using Eq. B1.1 for point A, the curvature is determined as $\alpha_1 = 1.707$.

For the *y*-*z* plane, a similar procedure is conducted to obtain $\beta_1 = 1.707$.

We obtain the resistance of the shell plating as

$$P_s(\delta) = \frac{8}{3\sqrt{3}} \cdot \sigma_0 \left(\left(2.3 \cdot \left(1 - \frac{1.707\delta}{200}\right)^{-1/2} \right) \times 2 \right) \delta \qquad \text{B1.2}$$

End of Step-1

- Case 1: the indenter has direct contact with the side model ($\delta = 117.16$ mm).
- Case 2: significant tension forces in the non-ruptured shell plating may cause collapse at the next girder intersections.

  The resistance of the next girder intersections has contributions from 4 cruciforms which have three remaining flanges, and 12 half web girders, i.e.,

$$P_{next-girder} = 4\left(3\times\frac{5.01}{\lambda}M_0\left(\frac{100}{2.3}\right)^{1/2}\right)+12\left(\frac{5.63}{\lambda}M_0\left(\frac{100}{2.3}\right)^{1/3}\right) = 391778 \text{ N}$$

  Collapse at the next girder intersections:

$$P_{next-girder} = P_s(\delta)$$

$$391778 = 7.082\cdot\sigma_0\cdot\left(1-\frac{1.707\delta}{200}\right)^{-1/2}(\delta)$$

$$\delta_{collapse} = 85 \text{ mm}.$$

- Case 3: failure occurs in the shell plating before deformation of the next girder intersections and panels.

  Eq. 3.11

$$\delta_f = \left[1.316\frac{200\times200}{\sqrt{200^2+200^2}}\sqrt{0.2}\right]\times\sqrt{1.707} = 109 \text{ mm}$$

The smallest indentation among the three cases:

$$\delta_{min} = 85 \text{ mm}.$$

Deformation continues to the next panels and girder intersections.

STEP-2

S_x = 400 mm; S_y = 400 mm

Deformation of the 4x4 Panels, i.e., 800 x 800 mm.

Basic elements are 1 full cruciform, 4 cruciforms which have three flanges, 16 half web girders, and shell plating.

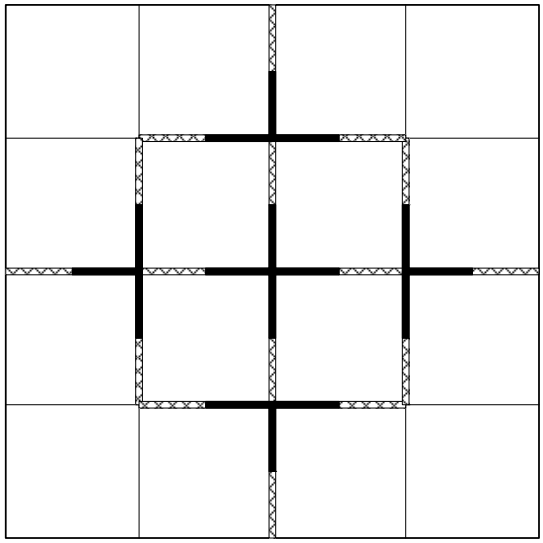

1. Cruciforms and web girders: P_c = 522371 N

2. Shell plating: $$P_s(\delta) = \frac{8}{3\sqrt{3}} \cdot \sigma_0 \left(t_{px} \cdot \frac{S_y}{S_x} \left(1 - \frac{\alpha\delta}{S_x} \right)^{-1/2} + t_{py} \cdot \frac{S_x}{S_y} \left(1 - \frac{\beta\delta}{S_y} \right)^{-1/2} \right) \delta$$

The change in the curvatures of the indenter is estimated by substituting the value of coordinate A (200;117.16) to Eq B1.1, but S_x is now 400.

We obtain the updated curvatures: $\alpha_2 = \beta_2 = 0.854$.

The resistance of the shell plating is

$$P_s(\delta) = \frac{8}{3\sqrt{3}} \cdot \sigma_0 \left(\left(2.3 \cdot \left(1 - \frac{0.854\ \delta}{200} \right)^{-1/2} \right) \times 2 \right) \delta \qquad \text{B1.3}$$

End of Step-2

- Case 1: the indentation process ends at $\delta = 200$ mm which is equal to the depth of the double hull model; no failure occurs in the shell plating.
- Case 2: failure occurs in the shell plating.

  Eq. 3.11

$$\delta_f = \left[1.316 \frac{400 \times 400}{\sqrt{400^2 + 400^2}} \sqrt{0.2} \right] \times \sqrt{0.854} = 154 \text{ mm} < 200 \text{ mm}$$

Appendix B-2

Application of the resistance formula to a bow model

Experimental data from Yamada and Endo (2005) and Yamada and Pedersen (2008)

A. BCG bow

- Model of the test (all dimensions in mm)

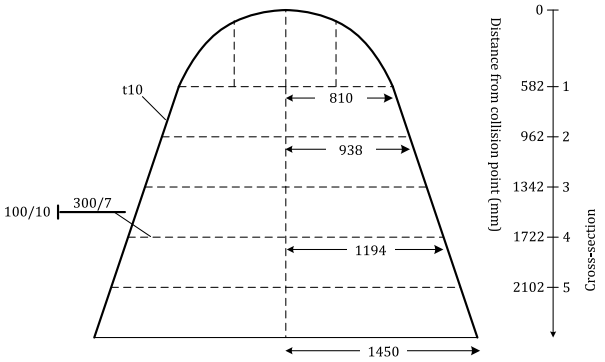

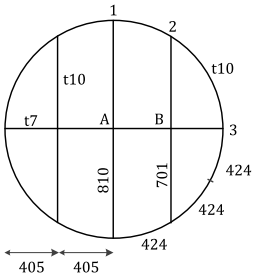

SECTION-1

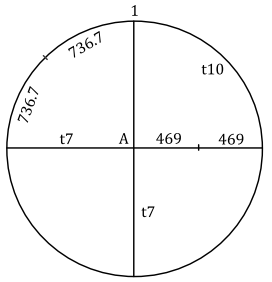

SECTION-2

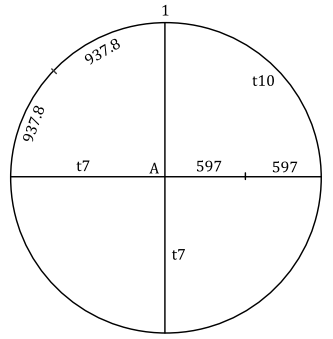

SECTION-4

- Calculation

	shell	web	long
t	10	7	7
σ_y	361	226	326
σ_u	451	322	498
σ_0	406	274	412

SECTION-01			distance		582 mm		
			force		8.233 MN		
JOINT	CRUCIFORM						
	i	C_{cf}	t_{cf}	θ	P_{cf}	$P_{cf\text{-}tot}$	
A	2	202.5	7	0	0.248	0.545	2.691
	2	291	7	0	0.297		
B	4	202.5	7	0	0.496	2.146	
	4	350.5	10	0	1.650		
JOINT	T-SECTION						
	j	C_{tf}	t_{tf}	θ	P_{tf}	$P_{tf\text{-}tot}$	
1	4	424	10	18.62	1.132	1.313	5.541
	2	202.5	7	0	0.181		
2	4	424	10	18.62	1.132	3.138	
	4	212	10	18.62	0.801		
	4	350.5	10	0	1.205		
3	4	212	10	18.62	0.801	1.090	
	2	519	7	0	0.290		
SECTION-02			distance		962 mm		
			force		4.161 MN		
JOINT	CRUCIFORM						
	i	C_{cf}	t_{cf}	θ	P_{cf}	$P_{cf\text{-}tot}$	
A	4	190	7	0	0.480	0.480	0.480
JOINT	T-SECTION						
	j	C_{tf}	t_{tf}	θ	P_{tf}	$P_{tf\text{-}tot}$	
1	8	736.7	10	18.62	2.985	3.680	3.680
	4	748	7	0	0.696		

SECTION-03			distance		1342 mm		
			force		4.415 MN		
JOINT	CRUCIFORM						
	i	C_{cf}	t_{cf}	θ	P_{cf}	$P_{cf\text{-}tot}$	
A	4	190	7	0	0.480	0.480	0.480
JOINT	T-SECTION						
	j	C_{tf}	t_{tf}	θ	P_{tf}	$P_{tf\text{-}tot}$	
1	8	837.2	10	18.62	3.182	3.935	3.935
	4	876	7	0	0.753		
SECTION-04			distance		1722 mm		
			force		4.654 MN		
JOINT	CRUCIFORM						
	i	C_{cf}	t_{cf}	θ	P_{cf}	$P_{cf\text{-}tot}$	
A	4	190	7	0	0.480	0.480	0.480
JOINT	T-SECTION						
	j	C_{tf}	t_{tf}	θ	P_{tf}	$P_{tf\text{-}tot}$	
1	8	937.8	10	18.62	3.367	4.173	4.173
	4	1004	7	0	0.806		
SECTION-05			distance		2102 mm		
			force		4.880 MN		
JOINT	CRUCIFORM						
	i	C_{cf}	t_{cf}	θ	P_{cf}	$P_{cf\text{-}tot}$	
A	4	190	7	0	0.480	0.480	0.480
JOINT	T-SECTION						
	j	C_{tf}	t_{tf}	θ	P_{tf}	$P_{tf\text{-}tot}$	
1	8	1038	10	18.62	3.543	4.399	4.399
	4	1132	7	0	0.856		

B. BCL bow

- Model of the test (all dimensions in mm)

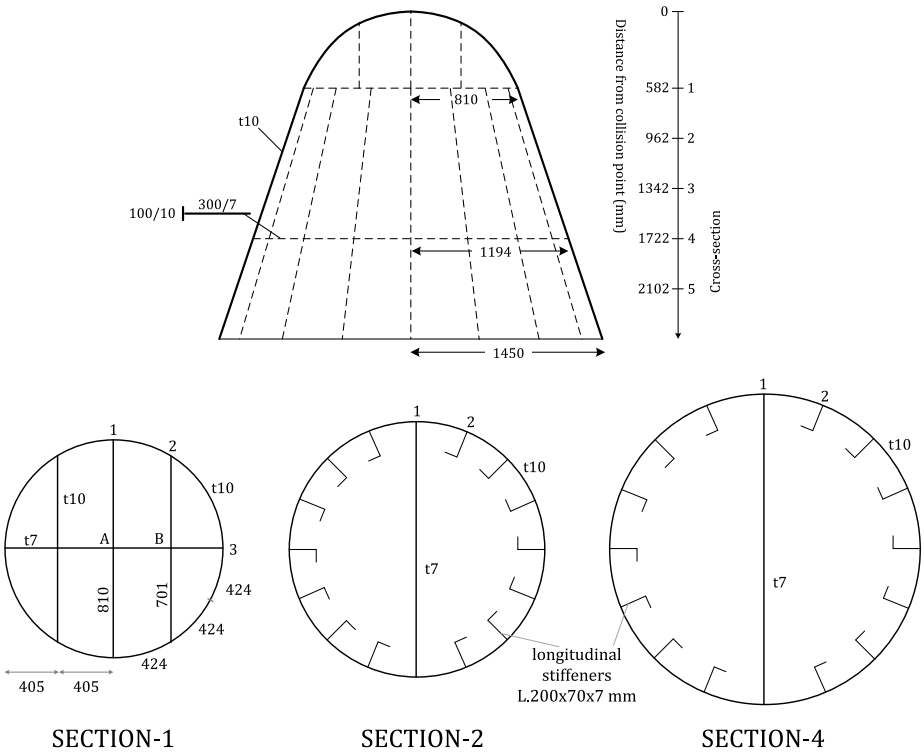

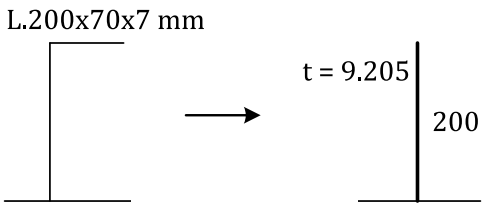

- Calculation

	shell	web	long
t	10	7	7
σ_y	361	226	326
σ_u	451	322	498
σ_0	406	274	412

SECTION-01			distance		582 mm		
			force		8.233 MN		
JOINT	CRUCIFORM						
	i	C_{cf}	t_{cf}	θ	P_{cf}	$P_{cf\text{-}tot}$	
A	2	202.5	7	0	0.248	0.545	2.691
	2	291	7	0	0.297		
B	4	202.5	7	0	0.496	2.146	
	4	350.5	10	0	1.650		
JOINT	T-SECTION						
	j	C_{tf}	t_{tf}	θ	P_{tf}	$P_{tf\text{-}tot}$	
1	4	424	10	18.62	1.132	1.313	5.541
	2	202.5	7	0	0.181		
2	4	424	10	18.62	1.132	3.138	
	4	212	10	18.62	0.801		
	4	350.5	10	0	1.205		
3	4	212	10	18.62	0.801	1.090	
	2	519	7	0	0.290		
SECTION-02			distance		962 mm		
			force		9.214 MN		
JOINT	T-SECTION						
	j	C_{tf}	t_{tf}	θ	P_{tf}	$P_{tf\text{-}tot}$	
1	2	938	7	0	0.390	1.136	9.214
	4	184	10	18.62	0.746		
2	14	200	9.205	0	2.855	8.078	
	28	184	10	18.62	5.223		

SECTION-03			distance		1342 mm		
			force		9.634 MN		
JOINT	T-SECTION						
	j	C_{tf}	t_{tf}	θ	P_{tf}	$P_{tf\text{-}tot}$	
1	2	1066	7	0	0.415	1.211	9.634
	4	209	10	18.62	0.795		
2	14	200	9.205	0	2.855	8.423	
	28	209	10	18.62	5.568		
SECTION-04			distance		1722 mm		
			force		10.030 MN		
JOINT	T-SECTION						
	j	C_{tf}	t_{tf}	θ	P_{tf}	$P_{tf\text{-}tot}$	
1	2	1194	7	0	0.440	1.281	10.030
	4	234	10	18.62	0.842		
2	14	200	9.205	0	2.855	8.748	
	28	234	10	18.62	5.893		
SECTION-05			distance		2102 mm		
			force		10.404 MN		
JOINT	T-SECTION						
	j	C_{tf}	t_{tf}	θ	P_{tf}	$P_{tf\text{-}tot}$	
1	2	1322	7	0	0.463	1.348	10.404
	4	260	10	18.62	0.886		
2	14	200	9.205	0	2.855	9.056	
	28	260	10	18.62	6.201		

Appendix B-3

Resistance of the Sharp Bow which collides with a rigid wall

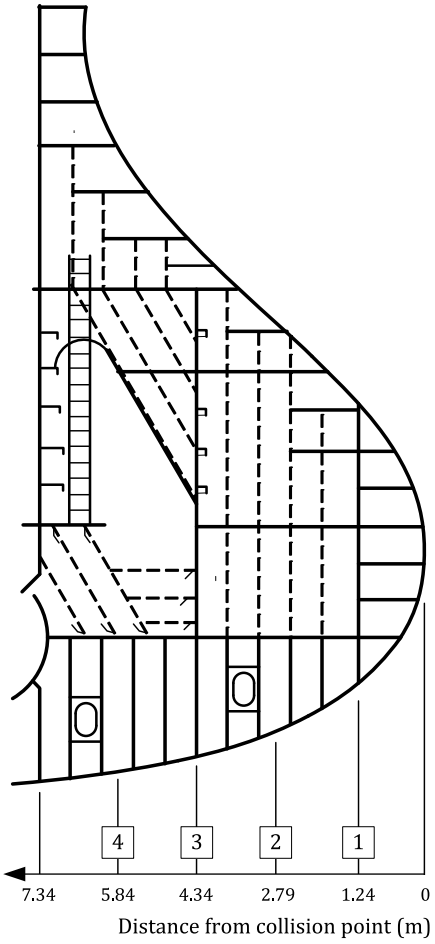

Material properties:

$\sigma_y = 235$ MPa; $\sigma_u = 385$ MPa; $\sigma_0 = 310$ MPa.

Cross-sections (all dimensions in mm)

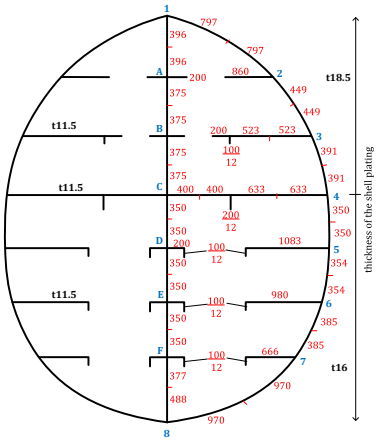

SECTION-01

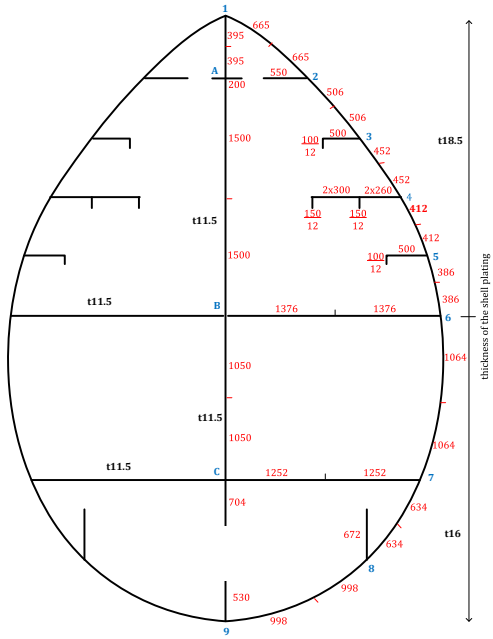

SECTION-02

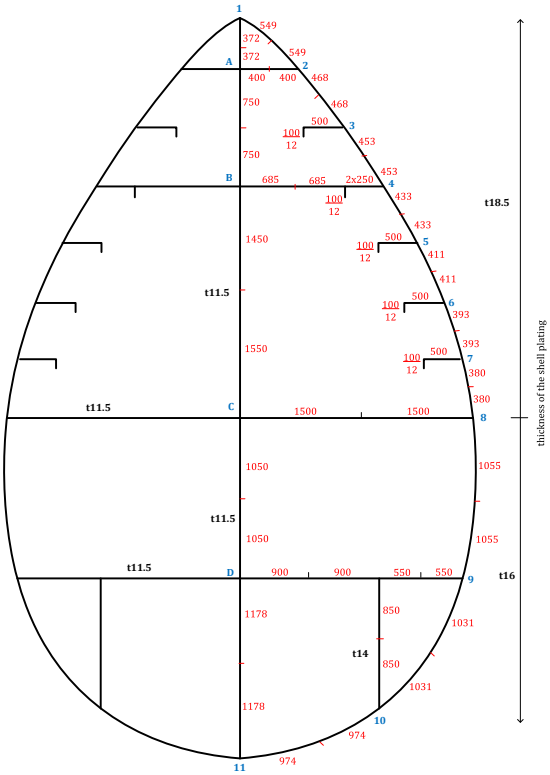

SECTION-03

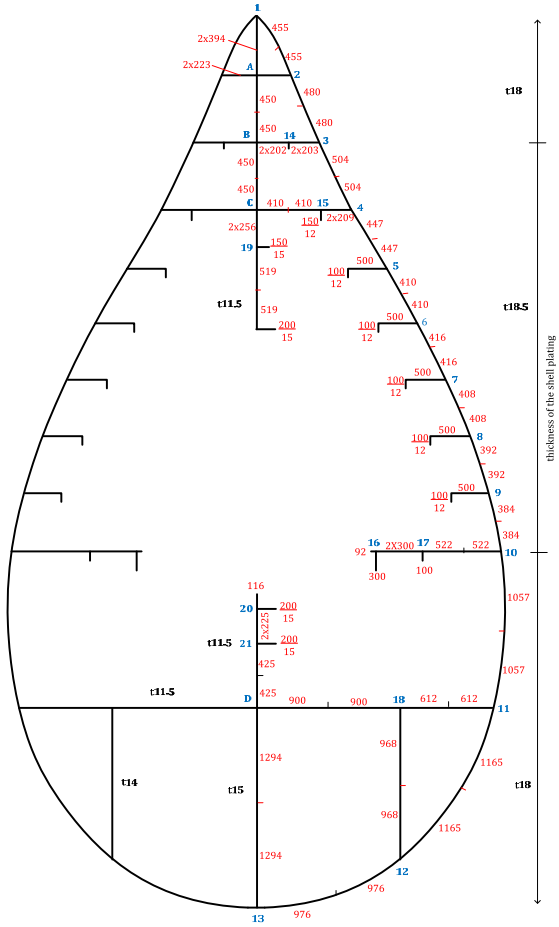
1
2x394
455
455
2x223
A
2
480
450
480
B
450
14
3
2x202
2x203
504
450
504
C
410
410
15
4
2x256
150
12
2x209
447
19
150
15
447
519
500
100
12
5
t11.5
410
519
410
500
200
15
100
12
6
416
416
500
100
12
7
408
408
500
100
12
8
392
392
500
100
12
9
384
384
16
2X300
17
522
522
10
92
300
100
116
1057
20
200
15
2x225
t11.5
21
200
15
425
1057
t11.5
425
D
900
900
18
612
612
11
968
1165
t14
t15
t18
1294
968
1165
1294
12
976
13
976
t18
t18.5
thickness of the shell plating

SECTION-04

Calculation

SECTION-01				distance 1.24 m				
				force 28.776 MN				
JOINT	CRUCIFORM							
	i	C_{cf}	t_{cf}	θ	α_I	P_{cf}	$P_{cf\text{-}tot}$	
A	2	200	11.5	0	1	0.587	1.403	10.071
	1	396	11.5	0	1	0.413		
	1	375	11.5	0	1	0.402		
B	2	200	11.5	0	1	0.587	1.392	
	2	375	11.5	0	1	0.804		
C	2	400	11.5	0	1	0.831	1.622	
	1	350	11.5	0	1	0.389		
	1	375	11.5	0	1	0.402		
D, E	4	200	17.5	0	1	2.205	3.760	
	4	350	11.5	0	1	1.554		
F	2	200	17.5	0	1	1.103	1.895	
	1	350	11.5	0	1	0.389		
	1	377	11.5	0	1	0.403		
JOINT	T-SECTION							
	j	C_{tf}	t_{tf}	θ	α_I	P_{tf}	$P_{tf\text{-}tot}$	
1	1	396	11.5	0	1	0.302	1.095	18.705
	2	797	18.5	0.88	0.45	0.793		
2	2	860	11.5	0	1	0.889	2.305	
	2	797	18.5	0.86	0.46	0.809		
	2	449	18.5	0.86	0.46	0.607		
3	2	523	11.5	0	1	0.694	2.179	
	2	449	18.5	0.69	0.59	0.768		
	2	391	18.5	0.69	0.59	0.717		
4	2	633	11.5	0	1	0.763	2.085	
	2	391	18.5	0.65	0.61	0.751		
	2	350	16	0.65	0.61	0.571		
5	2	1083	12.61	0	1	1.146	2.249	
	2	350	16	0.68	0.59	0.550		
	2	354	16	0.68	0.59	0.553		
6	2	980	12.72	0	1	1.105	2.166	
	2	354	16	0.73	0.55	0.519		
	2	385	16	0.73	0.55	0.541		
7	2	666	13.30	0	1	0.974	2.178	
	2	385	16	0.84	0.48	0.466		
	2	970	16	0.84	0.48	0.739		
8	1	488	11.5	0	1	0.335	1.175	
	2	970	16	0.75	0.54	0.840		
9	2	100	12	0	1	0.323	1.446	
	2	200	11.5	0	1	0.429		
	2	523	11.5	0	1	0.694		
10	2	200	12	0	1	0.457	1.827	
	2	400	11.5	0	1	0.607		
	2	633	11.5	0	1	0.763		

SECTION-02				distance 2.79 m				
				force 34.721 MN				
JOINT	CRUCIFORM							
	i	C_{cf}	t_{cf}	θ	α_I	P_{cf}	$P_{cf\text{-}tot}$	
A	1	395	11.5	0	1	0.413	1.805	7.787
	1	1500	11.5	0	1	0.804		
	2	200	11.5	0	1	0.587		
B	1	1500	11.5	0	1	0.804	3.018	
	1	1050	11.5	0	1	0.673		
	2	1376	11.5	0	1	1.541		
C	1	1050	11.5	0	1	0.673	2.964	
	1	704	15	0	1	0.821		
	2	1252	11.5	0	1	1.470		
JOINT	T-SECTION							
	j	C_{tf}	t_{tf}	θ	α_I	P_{tf}	$P_{tf\text{-}tot}$	
1	1	395	11.5	0	1	0.301	1.164	26.935
	2	665	18.5	0.75	0.54	0.863		
2	2	550	11.5	0	1	0.711	2.771	
	2	665	18.5	0.55	0.69	1.100		
	2	506	18.5	0.55	0.69	0.960		
3	2	500	13.9	0	1	0.901	3.087	
	2	506	18.5	0.39	0.81	1.124		
	2	452	18.5	0.39	0.81	1.062		
4	2	260	11.5	0	1	0.489	2.723	
	2	452	18.5	0.3	0.87	1.143		
	2	412	18.5	0.3	0.87	1.091		
5	2	500	13.9	0	1	0.901	3.130	
	2	412	18.5	0.25	0.9	1.133		
	2	386	18.5	0.25	0.9	1.096		
6	2	1376	11.5	0	1	1.125	3.748	
	2	386	18.5	0.22	0.92	1.123		
	2	1064	16	0.22	0.92	1.500		
7	2	1252	11.5	0	1	1.073	3.507	
	2	1064	16	0.34	0.85	1.373		
	2	634	16	0.34	0.85	1.060		
8	2	672	14	0	1	1.056	3.095	
	2	998	16	0.51	0.72	1.135		
	2	634	16	0.51	0.72	0.904		
9	1	530	15	0	1	0.520	1.773	
	2	998	16	0.4	0.8	1.253		
10	2	150	12	0	1	0.396	1.937	
	2	600	14.5	0	1	1.052		
	2	260	11.5	0	1	0.489		

SECTION-03				distance 4.34 m				
				force 48.934 MN				
JOINT	CRUCIFORM							
	i	C_{cf}	t_{cf}	θ	α_1	P_{cf}	$P_{cf\text{-}tot}$	
A	1	372	11.5	0	1	0.401	1.800	10.326
	1	750	11.5	0	1	0.569		
	2	400	11.5	0	1	0.831		
B	1	750	11.5	0	1	0.569	2.446	
	1	1450	11.5	0	1	0.791		
	2	685	11.5	0	1	1.087		
C	1	1550	11.5	0	1	0.818	3.099	
	1	1050	11.5	0	1	0.673		
	2	1500	11.5	0	1	1.609		
D	1	1050	11.5	0	1	0.673	2.981	
	1	1178	15	0	1	1.062		
	2	900	11.5	0	1	1.246		
JOINT	T-SECTION							
	j	C_{tf}	t_{tf}	θ	α_1	P_{tf}	$P_{tf\text{-}tot}$	
1	1	372	11.5	0	1	0.292	1.024	38.609
	2	549	18.5	0.81	0.5	0.731		
2	2	400	11.5	0	1	0.607	3.068	
	2	549	18.5	0.28	0.88	1.280		
	2	468	18.5	0.28	0.88	1.181		
3	2	500	13.9	0	1	0.901	3.276	
	2	468	18.5	0.27	0.89	1.197		
	2	453	18.5	0.27	0.89	1.178		
4	2	250	11.5	0	1	0.480	3.005	
	2	453	18.5	0.13	0.97	1.277		
	2	433	18.5	0.13	0.97	1.248		
5	2	500	13.9	0	1	0.901	3.412	
	2	433	18.5	0.08	0.99	1.272		
	2	411	18.5	0.08	0.99	1.239		
6	2	500	13.9	0	1	0.901	3.357	
	2	411	18.5	0.07	0.99	1.242		
	2	393	18.5	0.07	0.99	1.214		
7	2	500	13.9	0	1	0.901	3.315	
	2	393	18.5	0.07	0.99	1.217		
	2	380	18.5	0.07	0.99	1.197		
8	2	1500	11.5	0	1	1.175	3.948	
	2	380	18.5	0.1	0.98	1.185		
	2	1055	16	0.1	0.98	1.588		
9	2	550	11.5	0	1	0.711	3.886	
	2	1055	16	0.08	0.99	1.597		
	2	1031	16	0.08	0.99	1.578		
10	2	850	11.5	0	1	0.884	3.916	
	2	1031	16	0.15	0.96	1.538		
	2	974	16	0.15	0.96	1.495		
11	1	1178	11.5	0	1	0.520	1.996	
	2	974	16	0.17	0.95	1.476		
12	2	100	12	0	1	0.323	1.597	
	2	685	11.5	0	1	0.794		
	2	250	11.5	0	1	0.480		
13	2	850	14	0	1	1.188	2.809	
	2	900	11.5	0	1	0.910		
	2	550	11.5	0	1	0.711		

SECTION-04				distance 5.84 m				
				force 41.842 MN				
JOINT	CRUCIFORM							
	i	C_{cf}	t_{cf}	θ	α_1	P_{cf}	$P_{cf\text{-}tot}$	
A	1	394	11.5	0	1	0.412	1.473	7.389
	1	450	11.5	0	1	0.441		
	2	223	11.5	0	1	0.620		
B	1	450	11.5	0	1	0.441	1.471	
	1	450	11.5	0	1	0.441		
	2	202	11.5	0	1	0.590		
C	1	450	11.5	0	1	0.441	1.614	
	1	256	11.5	0	1	0.332		
	2	410	11.5	0	1	0.841		
D	1	425	11.5	0	1	0.428	2.832	
	1	1400	15	0	1	1.157		
	2	900	11.5	0	1	1.246		
JOINT	T-SECTION							
	j	C_{tf}	t_{tf}	θ	α_1	P_{tf}	$P_{tf\text{-}tot}$	
1	1	394	11.5	0	1	0.301	0.738	34.453
	2	455	18	1.04	0.34	0.437		
2	2	223	11.5	0	1	0.453	2.274	
	2	455	18	0.52	0.71	0.898		
	2	480	18	0.52	0.71	0.922		
3	2	203	11.5	0	1	0.432	2.460	
	2	480	18	0.44	0.77	1.002		
	2	504	18	0.44	0.77	1.026		
4	2	209	11.5	0	1	0.438	2.715	
	2	504	18	0.31	0.86	1.149		
	2	447	18.5	0.31	0.86	1.127		
5	2	500	13.9	0	1	0.901	3.289	
	2	447	18.5	0.21	0.93	1.220		
	2	410	18.5	0.21	0.93	1.168		
6	2	500	13.9	0	1	0.901	3.311	
	2	410	18.5	0.16	0.96	1.201		
	2	416	18.5	0.16	0.96	1.209		
7	2	500	13.9	0	1	0.901	3.369	
	2	416	18.5	0.1	0.98	1.240		
	2	408	18.5	0.1	0.98	1.228		
8	2	500	13.9	0	1	0.901	3.351	
	2	408	18.5	0.07	0.99	1.237		
	2	392	18.5	0.07	0.99	1.213		
9	2	500	13.9	0	1	0.901	3.320	
	2	392	18.5	0.07	0.99	1.215		
	2	384	18.5	0.07	0.99	1.203		
10	2	522	11.5	0	1	0.693	3.781	
	2	384	18.5	0.1	0.98	1.191		
	2	1057	18	0.1	0.98	1.897		
...								
16	2	300	12	0	1	0.560	1.376	
	2	92	11.5	0	1	0.291		
	2	300	11.5	0	1	0.525		
17	2	100	12	0	1	0.323	1.542	
	2	300	11.5	0	1	0.525		
	2	522	11.5	0	1	0.693		
18	2	900	11.5	0	1	0.910	2.928	
	2	612	11.5	0	1	0.750		
	2	968	14	0	1	1.268		

Appendix C

List of previous PhD theses

Previous PhD theses published at the Departement of Marine Technology
(earlier: Faculty of Marine Technology)

NORWEGIAN UNIVERSITY OF SCIENCE AND TECHNOLOGY

Report No.	Author	Title
	Kavlie, Dag	Optimization of Plane Elastic Grillages, 1967
	Hansen, Hans R.	Man-Machine Communication and Data-Storage Methods in Ship Structural Design, 1971
	Gisvold, Kaare M.	A Method for non-linear mixed -integer programming and its Application to Design Problems, 1971
	Lund, Sverre	Tanker Frame Optimalization by means of SUMT-Transformation and Behaviour Models, 1971
	Vinje, Tor	On Vibration of Spherical Shells Interacting with Fluid, 1972
	Lorentz, Jan D.	Tank Arrangement for Crude Oil Carriers in Accordance with the new Anti-Pollution Regulations, 1975
	Carlsen, Carl A.	Computer-Aided Design of Tanker Structures, 1975
	Larsen, Carl M.	Static and Dynamic Analysis of Offshore Pipelines during Installation, 1976
UR-79-01	Brigt Hatlestad, MK	The finite element method used in a fatigue evaluation of fixed offshore platforms. (Dr.Ing. Thesis)
UR-79-02	Erik Pettersen, MK	Analysis and design of cellular structures. (Dr.Ing. Thesis)
UR-79-03	Sverre Valsgård, MK	Finite difference and finite element methods applied to nonlinear analysis of plated structures. (Dr.Ing. Thesis)
UR-79-04	Nils T. Nordsve, MK	Finite element collapse analysis of structural members considering imperfections and stresses due to fabrication. (Dr.Ing. Thesis)
UR-79-05	Ivar J. Fylling, MK	Analysis of towline forces in ocean towing systems. (Dr.Ing. Thesis)
UR-80-06	Nils Sandsmark, MM	Analysis of Stationary and Transient Heat Conduction by the Use of the Finite Element Method. (Dr.Ing. Thesis)

UR-80-09	Sverre Haver, MK	Analysis of uncertainties related to the stochastic modeling of ocean waves. (Dr.Ing. Thesis)
UR-81-15	Odland, Jonas	On the Strength of welded Ring stiffened cylindrical Shells primarily subjected to axial Compression
UR-82-17	Engesvik, Knut	Analysis of Uncertainties in the fatigue Capacity of Welded Joints
UR-82-18	Rye, Henrik	Ocean wave groups
UR-83-30	Eide, Oddvar Inge	On Cumulative Fatigue Damage in Steel Welded Joints
UR-83-33	Mo, Olav	Stochastic Time Domain Analysis of Slender Offshore Structures
UR-83-34	Amdahl, Jørgen	Energy absorption in Ship-platform impacts
UR-84-37	Mørch, Morten	Motions and mooring forces of semi submersibles as determined by full-scale measurements and theoretical analysis
UR-84-38	Soares, C. Guedes	Probabilistic models for load effects in ship structures
UR-84-39	Aarsnes, Jan V.	Current forces on ships
UR-84-40	Czujko, Jerzy	Collapse Analysis of Plates subjected to Biaxial Compression and Lateral Load
UR-85-46	Alf G. Engseth, MK	Finite element collapse analysis of tubular steel offshore structures. (Dr.Ing. Thesis)
UR-86-47	Dengody Sheshappa, MP	A Computer Design Model for Optimizing Fishing Vessel Designs Based on Techno-Economic Analysis. (Dr.Ing. Thesis)
UR-86-48	Vidar Aanesland, MH	A Theoretical and Numerical Study of Ship Wave Resistance. (Dr.Ing. Thesis)
UR-86-49	Heinz-Joachim Wessel, MK	Fracture Mechanics Analysis of Crack Growth in Plate Girders. (Dr.Ing. Thesis)
UR-86-50	Jon Taby, MK	Ultimate and Post-ultimate Strength of Dented Tubular Members. (Dr.Ing. Thesis)
UR-86-51	Walter Lian, MH	A Numerical Study of Two-Dimensional Separated Flow Past Bluff Bodies at Moderate KC-Numbers. (Dr.Ing. Thesis)

UR-86-52	Bjørn Sortland, MH	Force Measurements in Oscillating Flow on Ship Sections and Circular Cylinders in a U-Tube Water Tank. (Dr.Ing. Thesis)
UR-86-53	Kurt Strand, MM	A System Dynamic Approach to One-dimensional Fluid Flow. (Dr.Ing. Thesis)
UR-86-54	Arne Edvin Løken, MH	Three Dimensional Second Order Hydrodynamic Effects on Ocean Structures in Waves. (Dr.Ing. Thesis)
UR-86-55	Sigurd Falch, MH	A Numerical Study of Slamming of Two-Dimensional Bodies. (Dr.Ing. Thesis)
UR-87-56	Arne Braathen, MH	Application of a Vortex Tracking Method to the Prediction of Roll Damping of a Two-Dimension Floating Body. (Dr.Ing. Thesis)
UR-87-57	Bernt Leira, MK	Gaussian Vector Processes for Reliability Analysis involving Wave-Induced Load Effects. (Dr.Ing. Thesis)
UR-87-58	Magnus Småvik, MM	Thermal Load and Process Characteristics in a Two-Stroke Diesel Engine with Thermal Barriers (in Norwegian). (Dr.Ing. Thesis)
MTA-88-59	Bernt Arild Bremdal, MP	An Investigation of Marine Installation Processes – A Knowledge - Based Planning Approach. (Dr.Ing. Thesis)
MTA-88-60	Xu Jun, MK	Non-linear Dynamic Analysis of Space-framed Offshore Structures. (Dr.Ing. Thesis)
MTA-89-61	Gang Miao, MH	Hydrodynamic Forces and Dynamic Responses of Circular Cylinders in Wave Zones. (Dr.Ing. Thesis)
MTA-89-62	Martin Greenhow, MH	Linear and Non-Linear Studies of Waves and Floating Bodies. Part I and Part II. (Dr.Techn. Thesis)
MTA-89-63	Chang Li, MH	Force Coefficients of Spheres and Cubes in Oscillatory Flow with and without Current. (Dr.Ing. Thesis
MTA-89-64	Hu Ying, MP	A Study of Marketing and Design in Development of Marine Transport Systems. (Dr.Ing. Thesis)
MTA-89-65	Arild Jæger, MH	Seakeeping, Dynamic Stability and Performance of a Wedge Shaped Planing Hull. (Dr.Ing. Thesis)
MTA-89-66	Chan Siu Hung, MM	The dynamic characteristics of tilting-pad bearings

MTA-89-67	Kim Wikstrøm, MP	Analysis av projekteringen for ett offshore projekt. (Licenciat-avhandling)
MTA-89-68	Jiao Guoyang, MK	Reliability Analysis of Crack Growth under Random Loading, considering Model Updating. (Dr.Ing. Thesis)
MTA-89-69	Arnt Olufsen, MK	Uncertainty and Reliability Analysis of Fixed Offshore Structures. (Dr.Ing. Thesis)
MTA-89-70	Wu Yu-Lin, MR	System Reliability Analyses of Offshore Structures using improved Truss and Beam Models. (Dr.Ing. Thesis)
MTA-90-71	Jan Roger Hoff, MH	Three-dimensional Green function of a vessel with forward speed in waves. (Dr.Ing. Thesis)
MTA-90-72	Rong Zhao, MH	Slow-Drift Motions of a Moored Two-Dimensional Body in Irregular Waves. (Dr.Ing. Thesis)
MTA-90-73	Atle Minsaas, MP	Economical Risk Analysis. (Dr.Ing. Thesis)
MTA-90-74	Knut-Aril Farnes, MK	Long-term Statistics of Response in Non-linear Marine Structures. (Dr.Ing. Thesis)
MTA-90-75	Torbjørn Sotberg, MK	Application of Reliability Methods for Safety Assessment of Submarine Pipelines. (Dr.Ing. Thesis)
MTA-90-76	Zeuthen, Steffen, MP	SEAMAID. A computational model of the design process in a constraint-based logic programming environment. An example from the offshore domain. (Dr.Ing. Thesis)
MTA-91-77	Haagensen, Sven, MM	Fuel Dependant Cyclic Variability in a Spark Ignition Engine - An Optical Approach. (Dr.Ing. Thesis)
MTA-91-78	Løland, Geir, MH	Current forces on and flow through fish farms. (Dr.Ing. Thesis)
MTA-91-79	Hoen, Christopher, MK	System Identification of Structures Excited by Stochastic Load Processes. (Dr.Ing. Thesis)
MTA-91-80	Haugen, Stein, MK	Probabilistic Evaluation of Frequency of Collision between Ships and Offshore Platforms. (Dr.Ing. Thesis)
MTA-91-81	Sødahl, Nils, MK	Methods for Design and Analysis of Flexible Risers. (Dr.Ing. Thesis)
MTA-91-82	Ormberg, Harald, MK	Non-linear Response Analysis of Floating Fish Farm Systems. (Dr.Ing. Thesis)

MTA-91-83	Marley, Mark J., MK	Time Variant Reliability under Fatigue Degradation. (Dr.Ing. Thesis)
MTA-91-84	Krokstad, Jørgen R., MH	Second-order Loads in Multidirectional Seas. (Dr.Ing. Thesis)
MTA-91-85	Molteberg, Gunnar A., MM	The Application of System Identification Techniques to Performance Monitoring of Four Stroke Turbocharged Diesel Engines. (Dr.Ing. Thesis)
MTA-92-86	Mørch, Hans Jørgen Bjelke, MH	Aspects of Hydrofoil Design: with Emphasis on Hydrofoil Interaction in Calm Water. (Dr.Ing. Thesis)
MTA-92-87	Chan Siu Hung, MM	Nonlinear Analysis of Rotordynamic Instabilities in Highspeed Turbomachinery. (Dr.Ing. Thesis)
MTA-92-88	Bessason, Bjarni, MK	Assessment of Earthquake Loading and Response of Seismically Isolated Bridges. (Dr.Ing. Thesis)
MTA-92-89	Langli, Geir, MP	Improving Operational Safety through exploitation of Design Knowledge - an investigation of offshore platform safety. (Dr.Ing. Thesis)
MTA-92-90	Sævik, Svein, MK	On Stresses and Fatigue in Flexible Pipes. (Dr.Ing. Thesis)
MTA-92-91	Ask, Tor Ø., MM	Ignition and Flame Growth in Lean Gas-Air Mixtures. An Experimental Study with a Schlieren System. (Dr.Ing. Thesis)
MTA-86-92	Hessen, Gunnar, MK	Fracture Mechanics Analysis of Stiffened Tubular Members. (Dr.Ing. Thesis)
MTA-93-93	Steinebach, Christian, MM	Knowledge Based Systems for Diagnosis of Rotating Machinery. (Dr.Ing. Thesis)
MTA-93-94	Dalane, Jan Inge, MK	System Reliability in Design and Maintenance of Fixed Offshore Structures. (Dr.Ing. Thesis)
MTA-93-95	Steen, Sverre, MH	Cobblestone Effect on SES. (Dr.Ing. Thesis)
MTA-93-96	Karunakaran, Daniel, MK	Nonlinear Dynamic Response and Reliability Analysis of Drag-dominated Offshore Platforms. (Dr.Ing. Thesis)
MTA-93-97	Hagen, Arnulf, MP	The Framework of a Design Process Language. (Dr.Ing. Thesis)

MTA-93-98	Nordrik, Rune, MM	Investigation of Spark Ignition and Autoignition in Methane and Air Using Computational Fluid Dynamics and Chemical Reaction Kinetics. A Numerical Study of Ignition Processes in Internal Combustion Engines. (Dr.Ing. Thesis)
MTA-94-99	Passano, Elizabeth, MK	Efficient Analysis of Nonlinear Slender Marine Structures. (Dr.Ing. Thesis)
MTA-94-100	Kvålsvold, Jan, MH	Hydroelastic Modelling of Wetdeck Slamming on Multihull Vessels. (Dr.Ing. Thesis)
MTA-94-102	Bech, Sidsel M., MK	Experimental and Numerical Determination of Stiffness and Strength of GRP/PVC Sandwich Structures. (Dr.Ing. Thesis)
MTA-95-103	Paulsen, Hallvard, MM	A Study of Transient Jet and Spray using a Schlieren Method and Digital Image Processing. (Dr.Ing. Thesis)
MTA-95-104	Hovde, Geir Olav, MK	Fatigue and Overload Reliability of Offshore Structural Systems, Considering the Effect of Inspection and Repair. (Dr.Ing. Thesis)
MTA-95-105	Wang, Xiaozhi, MK	Reliability Analysis of Production Ships with Emphasis on Load Combination and Ultimate Strength. (Dr.Ing. Thesis)
MTA-95-106	Ulstein, Tore, MH	Nonlinear Effects of a Flexible Stern Seal Bag on Cobblestone Oscillations of an SES. (Dr.Ing. Thesis)
MTA-95-107	Solaas, Frøydis, MH	Analytical and Numerical Studies of Sloshing in Tanks. (Dr.Ing. Thesis)
MTA-95-108	Hellan, Øyvind, MK	Nonlinear Pushover and Cyclic Analyses in Ultimate Limit State Design and Reassessment of Tubular Steel Offshore Structures. (Dr.Ing. Thesis)
MTA-95-109	Hermundstad, Ole A., MK	Theoretical and Experimental Hydroelastic Analysis of High Speed Vessels. (Dr.Ing. Thesis)
MTA-96-110	Bratland, Anne K., MH	Wave-Current Interaction Effects on Large-Volume Bodies in Water of Finite Depth. (Dr.Ing. Thesis)
MTA-96-111	Herfjord, Kjell, MH	A Study of Two-dimensional Separated Flow by a Combination of the Finite Element Method and Navier-Stokes Equations. (Dr.Ing. Thesis)
MTA-96-112	Æsøy, Vilmar, MM	Hot Surface Assisted Compression Ignition in a Direct Injection Natural Gas Engine. (Dr.Ing. Thesis)

MTA-96-113	Eknes, Monika L., MK	Escalation Scenarios Initiated by Gas Explosions on Offshore Installations. (Dr.Ing. Thesis)
MTA-96-114	Erikstad, Stein O., MP	A Decision Support Model for Preliminary Ship Design. (Dr.Ing. Thesis)
MTA-96-115	Pedersen, Egil, MH	A Nautical Study of Towed Marine Seismic Streamer Cable Configurations. (Dr.Ing. Thesis)
MTA-97-116	Moksnes, Paul O., MM	Modelling Two-Phase Thermo-Fluid Systems Using Bond Graphs. (Dr.Ing. Thesis)
MTA-97-117	Halse, Karl H., MK	On Vortex Shedding and Prediction of Vortex-Induced Vibrations of Circular Cylinders. (Dr.Ing. Thesis)
MTA-97-118	Igland, Ragnar T., MK	Reliability Analysis of Pipelines during Laying, considering Ultimate Strength under Combined Loads. (Dr.Ing. Thesis)
MTA-97-119	Pedersen, Hans-P., MP	Levendefiskteknologi for fiskefartøy. (Dr.Ing. Thesis)
MTA-98-120	Vikestad, Kyrre, MK	Multi-Frequency Response of a Cylinder Subjected to Vortex Shedding and Support Motions. (Dr.Ing. Thesis)
MTA-98-121	Azadi, Mohammad R. E., MK	Analysis of Static and Dynamic Pile-Soil-Jacket Behaviour. (Dr.Ing. Thesis)
MTA-98-122	Ulltang, Terje, MP	A Communication Model for Product Information. (Dr.Ing. Thesis)
MTA-98-123	Torbergsen, Erik, MM	Impeller/Diffuser Interaction Forces in Centrifugal Pumps. (Dr.Ing. Thesis)
MTA-98-124	Hansen, Edmond, MH	A Discrete Element Model to Study Marginal Ice Zone Dynamics and the Behaviour of Vessels Moored in Broken Ice. (Dr.Ing. Thesis)
MTA-98-125	Videiro, Paulo M., MK	Reliability Based Design of Marine Structures. (Dr.Ing. Thesis)
MTA-99-126	Mainçon, Philippe, MK	Fatigue Reliability of Long Welds Application to Titanium Risers. (Dr.Ing. Thesis)
MTA-99-127	Haugen, Elin M., MH	Hydroelastic Analysis of Slamming on Stiffened Plates with Application to Catamaran Wetdecks. (Dr.Ing. Thesis)
MTA-99-128	Langhelle, Nina K., MK	Experimental Validation and Calibration of Nonlinear Finite Element Models for Use in Design of Aluminium Structures Exposed to Fire. (Dr.Ing. Thesis)

MTA-99-129	Berstad, Are J., MK	Calculation of Fatigue Damage in Ship Structures. (Dr.Ing. Thesis)
MTA-99-130	Andersen, Trond M., MM	Short Term Maintenance Planning. (Dr.Ing. Thesis)
MTA-99-131	Tveiten, Bård Wathne, MK	Fatigue Assessment of Welded Aluminium Ship Details. (Dr.Ing. Thesis)
MTA-99-132	Søreide, Fredrik, MP	Applications of underwater technology in deep water archaeology. Principles and practice. (Dr.Ing. Thesis)
MTA-99-133	Tønnessen, Rune, MH	A Finite Element Method Applied to Unsteady Viscous Flow Around 2D Blunt Bodies With Sharp Corners. (Dr.Ing. Thesis)
MTA-99-134	Elvekrok, Dag R., MP	Engineering Integration in Field Development Projects in the Norwegian Oil and Gas Industry. The Supplier Management of Norne. (Dr.Ing. Thesis)
MTA-99-135	Fagerholt, Kjetil, MP	Optimeringsbaserte Metoder for Ruteplanlegging innen skipsfart. (Dr.Ing. Thesis)
MTA-99-136	Bysveen, Marie, MM	Visualization in Two Directions on a Dynamic Combustion Rig for Studies of Fuel Quality. (Dr.Ing. Thesis)
MTA-2000-137	Storteig, Eskild, MM	Dynamic characteristics and leakage performance of liquid annular seals in centrifugal pumps. (Dr.Ing. Thesis)
MTA-2000-138	Sagli, Gro, MK	Model uncertainty and simplified estimates of long term extremes of hull girder loads in ships. (Dr.Ing. Thesis)
MTA-2000-139	Tronstad, Harald, MK	Nonlinear analysis and design of cable net structures like fishing gear based on the finite element method. (Dr.Ing. Thesis)
MTA-2000-140	Kroneberg, André, MP	Innovation in shipping by using scenarios. (Dr.Ing. Thesis)
MTA-2000-141	Haslum, Herbjørn Alf, MH	Simplified methods applied to nonlinear motion of spar platforms. (Dr.Ing. Thesis)
MTA-2001-142	Samdal, Ole Johan, MM	Modelling of Degradation Mechanisms and Stressor Interaction on Static Mechanical Equipment Residual Lifetime. (Dr.Ing. Thesis)
MTA-2001-143	Baarholm, Rolf Jarle, MH	Theoretical and experimental studies of wave impact underneath decks of offshore platforms. (Dr.Ing. Thesis)

MTA-2001-144	Wang, Lihua, MK	Probabilistic Analysis of Nonlinear Wave-induced Loads on Ships. (Dr.Ing. Thesis)
MTA-2001-145	Kristensen, Odd H. Holt, MK	Ultimate Capacity of Aluminium Plates under Multiple Loads, Considering HAZ Properties. (Dr.Ing. Thesis)
MTA-2001-146	Greco, Marilena, MH	A Two-Dimensional Study of Green-Water Loading. (Dr.Ing. Thesis)
MTA-2001-147	Heggelund, Svein E., MK	Calculation of Global Design Loads and Load Effects in Large High Speed Catamarans. (Dr.Ing. Thesis)
MTA-2001-148	Babalola, Olusegun T., MK	Fatigue Strength of Titanium Risers – Defect Sensitivity. (Dr.Ing. Thesis)
MTA-2001-149	Mohammed, Abuu K., MK	Nonlinear Shell Finite Elements for Ultimate Strength and Collapse Analysis of Ship Structures. (Dr.Ing. Thesis)
MTA-2002-150	Holmedal, Lars E., MH	Wave-current interactions in the vicinity of the sea bed. (Dr.Ing. Thesis)
MTA-2002-151	Rognebakke, Olav F., MH	Sloshing in rectangular tanks and interaction with ship motions. (Dr.Ing. Thesis)
MTA-2002-152	Lader, Pål Furset, MH	Geometry and Kinematics of Breaking Waves. (Dr.Ing. Thesis)
MTA-2002-153	Yang, Qinzheng, MH	Wash and wave resistance of ships in finite water depth. (Dr.Ing. Thesis)
MTA-2002-154	Melhus, Øyvin, MM	Utilization of VOC in Diesel Engines. Ignition and combustion of VOC released by crude oil tankers. (Dr.Ing. Thesis)
MTA-2002-155	Ronæss, Marit, MH	Wave Induced Motions of Two Ships Advancing on Parallel Course. (Dr.Ing. Thesis)
MTA-2002-156	Økland, Ole D., MK	Numerical and experimental investigation of whipping in twin hull vessels exposed to severe wet deck slamming. (Dr.Ing. Thesis)
MTA-2002-157	Ge, Chunhua, MK	Global Hydroelastic Response of Catamarans due to Wet Deck Slamming. (Dr.Ing. Thesis)
MTA-2002-158	Byklum, Eirik, MK	Nonlinear Shell Finite Elements for Ultimate Strength and Collapse Analysis of Ship Structures. (Dr.Ing. Thesis)

IMT-2003-1	Chen, Haibo, MK	Probabilistic Evaluation of FPSO-Tanker Collision in Tandem Offloading Operation. (Dr.Ing. Thesis)
IMT-2003-2	Skaugset, Kjetil Bjørn, MK	On the Suppression of Vortex Induced Vibrations of Circular Cylinders by Radial Water Jets. (Dr.Ing. Thesis)
IMT-2003-3	Chezhian, Muthu	Three-Dimensional Analysis of Slamming. (Dr.Ing. Thesis)
IMT-2003-4	Buhaug, Øyvind	Deposit Formation on Cylinder Liner Surfaces in Medium Speed Engines. (Dr.Ing. Thesis)
IMT-2003-5	Tregde, Vidar	Aspects of Ship Design: Optimization of Aft Hull with Inverse Geometry Design. (Dr.Ing. Thesis)
IMT-2003-6	Wist, Hanne Therese	Statistical Properties of Successive Ocean Wave Parameters. (Dr.Ing. Thesis)
IMT-2004-7	Ransau, Samuel	Numerical Methods for Flows with Evolving Interfaces. (Dr.Ing. Thesis)
IMT-2004-8	Soma, Torkel	Blue-Chip or Sub-Standard. A data interrogation approach of identity safety characteristics of shipping organization. (Dr.Ing. Thesis)
IMT-2004-9	Ersdal, Svein	An experimental study of hydrodynamic forces on cylinders and cables in near axial flow. (Dr.Ing. Thesis)
IMT-2005-10	Brodtkorb, Per Andreas	The Probability of Occurrence of Dangerous Wave Situations at Sea. (Dr.Ing. Thesis)
IMT-2005-11	Yttervik, Rune	Ocean current variability in relation to offshore engineering. (Dr.Ing. Thesis)
IMT-2005-12	Fredheim, Arne	Current Forces on Net-Structures. (Dr.Ing. Thesis)
IMT-2005-13	Heggernes, Kjetil	Flow around marine structures. (Dr.Ing. Thesis
IMT-2005-14	Fouques, Sebastien	Lagrangian Modelling of Ocean Surface Waves and Synthetic Aperture Radar Wave Measurements. (Dr.Ing. Thesis)
IMT-2006-15	Holm, Håvard	Numerical calculation of viscous free surface flow around marine structures. (Dr.Ing. Thesis)
IMT-2006-16	Bjørheim, Lars G.	Failure Assessment of Long Through Thickness Fatigue Cracks in Ship Hulls. (Dr.Ing. Thesis)
IMT-2006-17	Hansson, Lisbeth	Safety Management for Prevention of Occupational Accidents. (Dr.Ing. Thesis)

IMT-2006-18	Zhu, Xinying	Application of the CIP Method to Strongly Nonlinear Wave-Body Interaction Problems. (Dr.Ing. Thesis)
IMT-2006-19	Reite, Karl Johan	Modelling and Control of Trawl Systems. (Dr.Ing. Thesis)
IMT-2006-20	Smogeli, Øyvind Notland	Control of Marine Propellers. From Normal to Extreme Conditions. (Dr.Ing. Thesis)
IMT-2007-21	Storhaug, Gaute	Experimental Investigation of Wave Induced Vibrations and Their Effect on the Fatigue Loading of Ships. (Dr.Ing. Thesis)
IMT-2007-22	Sun, Hui	A Boundary Element Method Applied to Strongly Nonlinear Wave-Body Interaction Problems. (PhD Thesis, CeSOS)
IMT-2007-23	Rustad, Anne Marthine	Modelling and Control of Top Tensioned Risers. (PhD Thesis, CeSOS)
IMT-2007-24	Johansen, Vegar	Modelling flexible slender system for real-time simulations and control applications
IMT-2007-25	Wroldsen, Anders Sunde	Modelling and control of tensegrity structures. (PhD Thesis, CeSOS)
IMT-2007-26	Aronsen, Kristoffer Høye	An experimental investigation of in-line and combined inline and cross flow vortex induced vibrations. (Dr. avhandling, IMT)
IMT-2007-27	Gao, Zhen	Stochastic Response Analysis of Mooring Systems with Emphasis on Frequency-domain Analysis of Fatigue due to Wide-band Response Processes (PhD Thesis, CeSOS)
IMT-2007-28	Thorstensen, Tom Anders	Lifetime Profit Modelling of Ageing Systems Utilizing Information about Technical Condition. (Dr.ing. thesis, IMT)
IMT-2008-29	Berntsen, Per Ivar B.	Structural Reliability Based Position Mooring. (PhD-Thesis, IMT)
IMT-2008-30	Ye, Naiquan	Fatigue Assessment of Aluminium Welded Box-stiffener Joints in Ships (Dr.ing. thesis, IMT)
IMT-2008-31	Radan, Damir	Integrated Control of Marine Electrical Power Systems. (PhD-Thesis, IMT)
IMT-2008-32	Thomassen, Paul	Methods for Dynamic Response Analysis and Fatigue Life Estimation of Floating Fish Cages. (Dr.ing. thesis, IMT)

IMT-2008-33	Pákozdi, Csaba	A Smoothed Particle Hydrodynamics Study of Two-dimensional Nonlinear Sloshing in Rectangular Tanks. (Dr.ing.thesis, IMT/ CeSOS)
IMT-2007-34	Grytøyr, Guttorm	A Higher-Order Boundary Element Method and Applications to Marine Hydrodynamics. (Dr.ing.thesis, IMT)
IMT-2008-35	Drummen, Ingo	Experimental and Numerical Investigation of Nonlinear Wave-Induced Load Effects in Containerships considering Hydroelasticity. (PhD thesis, CeSOS)
IMT-2008-36	Skejic, Renato	Maneuvering and Seakeeping of a Singel Ship and of Two Ships in Interaction. (PhD-Thesis, CeSOS)
IMT-2008-37	Harlem, Alf	An Age-Based Replacement Model for Repairable Systems with Attention to High-Speed Marine Diesel Engines. (PhD-Thesis, IMT)
IMT-2008-38	Alsos, Hagbart S.	Ship Grounding. Analysis of Ductile Fracture, Bottom Damage and Hull Girder Response. (PhD-thesis, IMT)
IMT-2008-39	Graczyk, Mateusz	Experimental Investigation of Sloshing Loading and Load Effects in Membrane LNG Tanks Subjected to Random Excitation. (PhD-thesis, CeSOS)
IMT-2008-40	Taghipour, Reza	Efficient Prediction of Dynamic Response for Flexible and Multi-body Marine Structures. (PhD-thesis, CeSOS)
IMT-2008-41	Ruth, Eivind	Propulsion control and thrust allocation on marine vessels. (PhD thesis, CeSOS)
IMT-2008-42	Nystad, Bent Helge	Technical Condition Indexes and Remaining Useful Life of Aggregated Systems. PhD thesis, IMT
IMT-2008-43	Soni, Prashant Kumar	Hydrodynamic Coefficients for Vortex Induced Vibrations of Flexible Beams, PhD thesis, CeSOS
IMT-2009-43	Amlashi, Hadi K.K.	Ultimate Strength and Reliability-based Design of Ship Hulls with Emphasis on Combined Global and Local Loads. PhD Thesis, IMT
IMT-2009-44	Pedersen, Tom Arne	Bond Graph Modelling of Marine Power Systems. PhD Thesis, IMT
IMT-2009-45	Kristiansen, Trygve	Two-Dimensional Numerical and Experimental Studies of Piston-Mode Resonance. PhD-Thesis, CeSOS

IMT-2009-46	Ong, Muk Chen	Applications of a Standard High Reynolds Number Model and a Stochastic Scour Prediction Model for Marine Structures. PhD-thesis, IMT
IMT-2009-47	Hong, Lin	Simplified Analysis and Design of Ships subjected to Collision and Grounding. PhD-thesis, IMT
IMT-2009-48	Koushan, Kamran	Vortex Induced Vibrations of Free Span Pipelines, PhD thesis, IMT
IMT-2009-49	Korsvik, Jarl Eirik	Heuristic Methods for Ship Routing and Scheduling. PhD-thesis, IMT
IMT-2009-50	Lee, Jihoon	Experimental Investigation and Numerical in Analyzing the Ocean Current Displacement of Longlines. Ph.d.-Thesis, IMT.
IMT-2009-51	Vestbøstad, Tone Gran	A Numerical Study of Wave-in-Deck Impact usin a Two-Dimensional Constrained Interpolation Profile Method, Ph.d.thesis, CeSOS.
IMT-2009-52	Bruun, Kristine	Bond Graph Modelling of Fuel Cells for Marine Power Plants. Ph.d.-thesis, IMT
IMT 2009-53	Holstad, Anders	Numerical Investigation of Turbulence in a Sekwed Three-Dimensional Channel Flow, Ph.d.-thesis, IMT.
IMT 2009-54	Ayala-Uraga, Efren	Reliability-Based Assessment of Deteriorating Ship-shaped Offshore Structures, Ph.d.-thesis, IMT
IMT 2009-55	Kong, Xiangjun	A Numerical Study of a Damaged Ship in Beam Sea Waves. Ph.d.-thesis, IMT/CeSOS.
IMT 2010-56	Kristiansen, David	Wave Induced Effects on Floaters of Aquaculture Plants, Ph.d.-thesis, CeSOS.
IMT 2010-57	Ludvigsen, Martin	An ROV-Toolbox for Optical and Acoustic Scientific Seabed Investigation. Ph.d.-thesis IMT.
IMT 2010-58	Hals, Jørgen	Modelling and Phase Control of Wave-Energy Converters. Ph.d.thesis, CeSOS.
IMT 2010- 59	Shu, Zhi	Uncertainty Assessment of Wave Loads and Ultimate Strength of Tankers and Bulk Carriers in a Reliability Framework. Ph.d. Thesis, IMT/ CeSOS
IMT 2010-60	Shao, Yanlin	Numerical Potential-Flow Studies on Weakly-Nonlinear Wave-Body Interactions with/without Small Forward Speed, Ph.d.thesis,CeSOS.

IMT 2010-61	Califano, Andrea	Dynamic Loads on Marine Propellers due to Intermittent Ventilation. Ph.d.thesis, IMT.
IMT 2010-62	El Khoury, George	Numerical Simulations of Massively Separated Turbulent Flows, Ph.d.-thesis, IMT
IMT 2010-63	Seim, Knut Sponheim	Mixing Process in Dense Overflows with Emphasis on the Faroe Bank Channel Overflow. Ph.d.thesis, IMT
IMT 2010-64	Jia, Huirong	Structural Analysis of Intect and Damaged Ships in a Collission Risk Analysis Perspective. Ph.d.thesis CeSoS.
IMT 2010-65	Jiao, Linlin	Wave-Induced Effects on a Pontoon-type Very Large Floating Structures (VLFS). Ph.D.-thesis, CeSOS.
IMT 2010-66	Abrahamsen, Bjørn Christian	Sloshing Induced Tank Roof with Entrapped Air Pocket. Ph.d.thesis, CeSOS.
IMT 2011-67	Karimirad, Madjid	Stochastic Dynamic Response Analysis of Spar-Type Wind Turbines with Catenary or Taut Mooring Systems. Ph.d.-thesis, CeSOS.
IMT 2011-68	Erlend Meland	Condition Monitoring of Safety Critical Valves. Ph.d.-thesis, IMT.
IMT 2011-69	Yang, Limin	Stochastic Dynamic System Analysis of Wave Energy Converter with Hydraulic Power Take-Off, with Particular Reference to Wear Damage Analysis, Ph.d. Thesis, CeSOS.
IMT 2011-70	Visscher, Jan	Application of Particla Image Velocimetry on Turbulent Marine Flows, Ph.d.Thesis, IMT.
IMT 2011-71	Su, Biao	Numerical Predictions of Global and Local Ice Loads on Ships. Ph.d.Thesis, CeSOS.
IMT 2011-72	Liu, Zhenhui	Analytical and Numerical Analysis of Iceberg Collision with Ship Structures. Ph.d.Thesis, IMT.
IMT 2011-73	Aarsæther, Karl Gunnar	Modeling and Analysis of Ship Traffic by Observation and Numerical Simulation. Ph.d.Thesis, IMT.
IMT 2011-74	Wu, Jie	Hydrodynamic Force Identification from Stochastic Vortex Induced Vibration Experiments with Slender Beams. Ph.d.Thesis, IMT.
IMT 2011-75	Amini, Hamid	Azimuth Propulsors in Off-design Conditions. Ph.d.Thesis, IMT.

IMT 2011-76	Nguyen, Tan-Hoi	Toward a System of Real-Time Prediction and Monitoring of Bottom Damage Conditions During Ship Grounding. Ph.d.thesis, IMT.
IMT 2011-77	Tavakoli, Mohammad T.	Assessment of Oil Spill in Ship Collision and Grounding, Ph.d.thesis, IMT.
IMT 2011-78	Guo, Bingjie	Numerical and Experimental Investigation of Added Resistance in Waves. Ph.d.Thesis, IMT.
IMT 2011-79	Chen, Qiaofeng	Ultimate Strength of Aluminium Panels, considering HAZ Effects, IMT
IMT 2012-80	Kota, Ravikiran S.	Wave Loads on Decks of Offshore Structures in Random Seas, CeSOS.
IMT 2012-81	Sten, Ronny	Dynamic Simulation of Deep Water Drilling Risers with Heave Compensating System, IMT.
IMT 2012-82	Berle, Øyvind	Risk and resilience in global maritime supply chains, IMT.
IMT 2012-83	Fang, Shaoji	Fault Tolerant Position Mooring Control Based on Structural Reliability, CeSOS.
IMT 2012-84	You, Jikun	Numerical studies on wave forces and moored ship motions in intermediate and shallow water, CeSOS.
IMT 2012-85	Xiang ,Xu	Maneuvering of two interacting ships in waves, CeSOS
IMT 2012-86	Dong, Wenbin	Time-domain fatigue response and reliability analysis of offshore wind turbines with emphasis on welded tubular joints and gear components, CeSOS
IMT 2012-87	Zhu, Suji	Investigation of Wave-Induced Nonlinear Load Effects in Open Ships considering Hull Girder Vibrations in Bending and Torsion, CeSOS
IMT 2012-88	Zhou, Li	Numerical and Experimental Investigation of Station-keeping in Level Ice, CeSOS
IMT 2012-90	Ushakov, Sergey	Particulate matter emission characteristics from diesel enignes operating on conventional and alternative marine fuels, IMT
IMT 2013-1	Yin, Decao	Experimental and Numerical Analysis of Combined In-line and Cross-flow Vortex Induced Vibrations, CeSOS

IMT 2013-2	Kurniawan, Adi	Modelling and geometry optimisation of wave energy converters, CeSOS
IMT 2013-3	Al Ryati, Nabil	Technical condition indexes doe auxiliary marine diesel engines, IMT
IMT 2013-4	Firoozkoohi, Reza	Experimental, numerical and analytical investigation of the effect of screens on sloshing, CeSOS
IMT 2013-5	Ommani, Babak	Potential-Flow Predictions of a Semi-Displacement Vessel Including Applications to Calm Water Broaching, CeSOS
IMT 2013-6	Xing, Yihan	Modelling and analysis of the gearbox in a floating spar-type wind turbine, CeSOS
IMT-7-2013	Balland, Océane	Optimization models for reducing air emissions from ships, IMT
IMT-8-2013	Yang, Dan	Transitional wake flow behind an inclined flat plate----- Computation and analysis, IMT
IMT-9-2013	Abdillah, Suyuthi	Prediction of Extreme Loads and Fatigue Damage for a Ship Hull due to Ice Action, IMT
IMT-10-2013	Ramìrez, Pedro Agustìn Pèrez	Ageing management and life extension of technical systems- Concepts and methods applied to oil and gas facilities, IMT
IMT-11-2013	Chuang, Zhenju	Experimental and Numerical Investigation of Speed Loss due to Seakeeping and Maneuvering. IMT
IMT-12-2013	Etemaddar, Mahmoud	Load and Response Analysis of Wind Turbines under Atmospheric Icing and Controller System Faults with Emphasis on Spar Type Floating Wind Turbines, IMT
IMT-13-2013	Lindstad, Haakon	Strategies and measures for reducing maritime CO2 emissions, IMT